

Integrated widely tunable laser systems at 1300 and 1550 nm as swept sources for optical coherence tomography

Citation for published version (APA):

Hazan, J. (2023). *Integrated widely tunable laser systems at 1300 and 1550 nm as swept sources for optical coherence tomography*. [Phd Thesis 1 (Research TU/e / Graduation TU/e), Electrical Engineering]. Eindhoven University of Technology.

Document status and date:

Published: 31/05/2023

Document Version:

Publisher's PDF, also known as Version of Record (includes final page, issue and volume numbers)

Please check the document version of this publication:

- A submitted manuscript is the version of the article upon submission and before peer-review. There can be important differences between the submitted version and the official published version of record. People interested in the research are advised to contact the author for the final version of the publication, or visit the DOI to the publisher's website.
- The final author version and the galley proof are versions of the publication after peer review.
- The final published version features the final layout of the paper including the volume, issue and page numbers.

[Link to publication](#)

General rights

Copyright and moral rights for the publications made accessible in the public portal are retained by the authors and/or other copyright owners and it is a condition of accessing publications that users recognise and abide by the legal requirements associated with these rights.

- Users may download and print one copy of any publication from the public portal for the purpose of private study or research.
- You may not further distribute the material or use it for any profit-making activity or commercial gain
- You may freely distribute the URL identifying the publication in the public portal.

If the publication is distributed under the terms of Article 25fa of the Dutch Copyright Act, indicated by the "Taverne" license above, please follow below link for the End User Agreement:

www.tue.nl/taverne

Take down policy

If you believe that this document breaches copyright please contact us at:

openaccess@tue.nl

providing details and we will investigate your claim.

Integrated widely tunable laser systems at 1300 and 1550 nm as swept sources for optical coherence tomography

Proefschrift

ter verkrijging van de graad van doctor aan de Technische Universiteit Eindhoven, op gezag van de rector magnificus prof.dr.S.K.Lenaerts, voor een commissie aangewezen door het College voor Promoties, in het openbaar te verdedigen op woensdag 31 Mei 2023 om 16:00 uur

door

Joel Hazan
geboren te Milaan, Italië

Dit proefschrift is goedgekeurd door de promotoren en de samenstelling van de promotiecommissie is als volgt:

voorzitter:	prof.dr.ir. S.M. Heemstra	
promotor:	dr. E.A.J.M. Bente	
co-promotor:	prof.dr. K.A. Williams	
leden:	dr. O. Raz	
	prof.dr. A.G.J.M. van Leeuwen	(Universiteit van Amsterdam)
	prof.dr. S. Garcia-Blanco	(Universiteit Twente)
	prof.dr. G. Carpintero Del Barrio	(Universidad Carlos III de Madrid)
adviseur:	dr. L. Augustin	(SMART Photonics B.V.)

Het onderzoek of ontwerp dat in dit proefschrift wordt beschreven is uitgevoerd in overeenstemming met de TU/e Gedragscode Wetenschapsbeoefening.

Copyright © 2023 by Joel Hazan. All Rights Reserved.

Integrated widely tunable laser systems at 1300 and 1550 nm as swept sources for optical coherence tomography

Keywords: photonic integrated circuits, indium phosphide, widely tunable lasers, optical coherence tomography.

A catalogue record is available from the Eindhoven University of Technology Library.

ISBN: 978-94-6419-804-1



This work is part of the research program 'An integrated Optical Coherence Tomography system for medical imaging at 1300nm' with project number 16251, which is (partly) financed by the Dutch Research Council (NWO).

Printed by Gildeprint, typeset using WORD

SUMMARY

This work concerns the development of monolithically integrated InP widely tunable laser systems at 1300 and 1550 nm, suitable to achieve multispectral optical coherence tomography (OCT) imaging in biological tissues. The research aim is to investigate a variety of integrated laser configurations and optimize their wavelength scanning performance to meet OCT requirements. In terms of wavelength scan, 50 to 100 nm range swept at hundred microseconds speed is needed together with a coherence length of several centimeters, at least.

The laser systems here investigated make use of an optical amplifier combined with intra-cavity tunable filters biased by voltage-controlled phase modulators. In all designs but one the wavelength scan is performed in a stepwise manner over a set of equally spaced optical frequencies. The research has been carried out starting from the existing InP active-passive integration technology in which active components such as amplifiers, and passive components are combined with a monolithic approach. To realize 1300 nm lasers on chip, a new InP integration platform was developed in collaboration with a III-V semiconductor foundry company. The thesis consists of four main parts. The first part focuses on the design, the characterization, and the modeling of a new 1300 nm InP active-passive integration platform, with minimized active-passive interface reflections. Such reflections inside the laser cavity can cause problems with tuning the laser to specific wavelengths. The processing in this platform is compatible with the already established processing pipeline in the 1550 nm integration platform. The active and passive layer stack were designed and tested on a fully passive and fully active device fabrication run respectively. The active and passive layer stack designs were optimized to have >99% mode overlap, less than 0.5% difference in refractive index, a sufficiently low propagation loss (<3 dB/cm), a wide gain bandwidth (>80 nm), and an efficient ($20^\circ/\text{V}\cdot\text{mm}$) phase modulation. Design, characterization, and modeling of specific building blocks such as multimode interference (MMI) couplers, semiconductor optical amplifiers (SOA), absorbers and reverse bias driven electro refractive modulators (ERM), led to the development of a photonic design kit (PDK) which can be used by users of multi-project wafer runs (MPW). To test the active quantum well based layer stack, high power diode lasers (>2 W for broad area devices) and amplifiers were fabricated. The dependency of the measured gain spectrum on the current density has been successfully modelled using amplifier rate equations and has been validated further with material transparency and optical saturation measurements.

The second part of the thesis focuses on the realization of laser systems on this new 1300 nm InP monolithic integration platform. Pulsed sources and continuous wave (CW) widely

tunable laser systems have been investigated experimentally. Quantum well based passively mode-locked lasers have been realized on a fully active wafer. Mode locking and Q-switching dynamics have been characterized and investigated by studying the repetition rate change with current and the optical pulse duration. This is aimed to evaluate a gain and absorption parametrization of a new quantum well based 1300 nm amplifier. Laser designs utilizing active-passive integration raise the opportunity of having optical filters in the passive part inside the laser cavity. Intracavity electro-optically tunable bandpass filters for the laser to meet the OCT application requirements of tuning range, spectral quality, and scan speed, have been simulated, designed and characterized. To simulate the tuning capabilities, a rate equation model of the 1300 nm quantum well amplifier has been extended into a steady state laser spectral model.

The third part concerns the study of a 1550 nm laser system as an OCT tunable laser source. An investigation of the intracavity filter and the laser tuning improved insight into the stability limitations of the wavelength scanning control. A detailed analysis of the influence of the control settings on the wavelength tuning of one laser design is presented together with the demonstration of a wavelength calibration process that ensures the control of the laser system through a real-time wavelength monitoring unit.

In the fourth part, the suitability for OCT of an integrated Fourier domain mode locked (FDML) laser is investigated. In particular, the lasing output is produced through a sinusoidal RF driving signal which is applied to an electro-optic modulator to tune an intra-cavity bandpass filter within the round-trip time of the laser light. The fixed phase relation between the optical modes inside the frequency comb led to a CW laser output which can be used as an OCT source with a calculated coherence length of 35 mm according to simulations. Preliminary experiments with a FDML fiber-based laser and an integrated asymmetric Mach-Zehnder Interferometer on InP as a fast tunable bandpass filter reveal promising results since a FDML operation has been demonstrated and highly chirped optical pulse have been observed. This confirms the viability to use an integrated electro-optic filter in an FDML and even fully integrate the device for an OCT imaging scan at high scan rates and with electronic waveforms that are different than the sinusoidal ones currently used in FDML lasers.

The results achieved in this thesis show that a laser system at 1300 nm can be accomplished and controlled with a calibration scheme to properly tune the output emission. The step wise scan demonstrated in the chapter 6 highlights the current limitation of the continuous wave single mode laser systems based on cascaded asymmetric Mach-Zehnder interferometers. Therefore, an alternative approach relying on a FDML lasers has been searched towards enabling the use of monolithically integrated lasers on InP in OCT systems.

CONTENTS

Summary	i
1. Introduction	1
1.1 Optical Coherence Tomography	1
1.2 Tunable laser source requirements for OCT	3
1.3 Generic integration technology on InP	4
1.4 Integrated lasers for OCT	6
1.5 Motivation	7
1.6 Thesis Outline	8
2. 1300 nm Passive Components design and Characterization	11
2.1 Introduction	11
2.2 Passive Layer Stack Design.....	12
2.2.1 Waveguiding layer thickness	13
2.2.2 Quaternary alloy material composition	14
2.3 Waveguide fabrication.....	16
2.4 Passive components characterization	17
2.4.1 Passive waveguide measurements	17
2.4.2 Curved waveguides	24
2.4.3 Multimode interference coupler	25
2.4.4 Multimode interference reflector.....	31
2.5 Conclusions	33
3. 1300 nm amplifier compatible with an InP monolithic active/passive integration technology.....	35
3.1 Introduction	35
3.2 Active layer stack design.....	37
3.3 Device Fabrication	39
3.4 Active layer stack quality evaluation	39
3.5 Compact model for SOA gain.....	43
3.5.1 Unsaturated modal gain	43
3.5.2 Amplifier Rate equation and Carrier density at Transparency	46
3.5.3 Optical Gain Saturation.....	49
3.6 Conclusions	52
4. Two-section passively Mode-locked laser as a test for amplification and absorption parameters of a quantum well based InP optical amplifier at 1300 nm	55
4.1 Introduction	56
4.2 Simulator model and parameters	57
4.2.1 SOA gain parametrization	58

4.2.2	Absorption characterization and parametrization.....	59
4.3	Device design and fabrication.....	62
4.4	Laser device characterization	62
4.5	Passive Mode-Locking.....	66
4.5.1	Pulse duration and relative phase measurements	66
4.5.2	Laser repetition rate	67
4.6	Q-switching	68
4.7	Conclusions	70
5.	Active/Passive integration technology on InP at 1300 nm.....	71
5.1	Introduction	71
5.2	Electro refractive phase modulators	72
5.2.1	Theory and Simulations	73
5.2.2	Measurements and Analysis	74
5.3	Optical tunable bandpass filters	76
5.3.1	Asymmetric Mach Zehnder Interferometers	76
5.3.2	Tunable micro-ring resonators	77
5.4	Tunable Laser Systems at 1300 nm.....	79
5.4.1	Steady state spectral model.....	79
5.4.2	Linear laser design with loop mirror including micro-rings	81
5.4.3	Tunable laser simulation.....	82
5.4.4	Laser tuning measurements	84
5.5	Conclusions	87
6.	Control settings optimization and step-wise wavelength scanning of an InP monolithically integrated tunable laser at 1550 nm	89
6.1	Introduction	89
6.2	Tunable laser design	91
6.3	Laser tuning	93
6.3.1	Intra-cavity filters tuning	93
6.3.2	Laser stability over time.....	96
6.4	Calibration strategy for the laser sweep.....	97
6.4.1	Equally spaced wavelengths Look-Up Table	98
6.4.2	Wavelength measurements with a fast read-out unit.....	100
6.4.3	Tunable laser scan.....	102
6.5	Conclusions	105
6.6	Design improvements to increase the laser tuning range.....	106
6.6.1	Laser design	106
6.6.2	Output coupler characterization.....	107
6.6.3	Tuning range measurements	110

7.	Fourier-domain Mode-locked semiconductor laser for Optical Coherence Tomography	113
7.1	Introduction	113
7.2	Fourier-domain Mode-locked laser design	115
7.3	Laser simulations	117
7.3.1	Optical simulations	117
7.3.2	SS-OCT simulation	121
7.4	Fiber-based Fourier-Domain Mode-locked laser with an InP integrated filter....	123
7.4.1	Asymmetric Mach-Zehnder Interferometer tunable filter	123
7.4.2	Laser Design and DC Operation	125
7.4.3	Fourier Domain Mode-Locking operation.....	125
7.4.4	Use of multiple driving waveforms	129
7.5	Conclusions	130
8.	Conclusions and Outlook	133
8.1	1300 nm active/passive integration platform	133
8.2	Laser Sources for OCT	135
	Appendix A.....	137
	Rate Equation for the SOA description	137
	References	141
	List of publications	155
	Journal articles.....	155
	international Conferences	155
	Regional Conferences / Workshops.....	156
	Acknowledgments	159
	Biography.....	162

1. INTRODUCTION

1.1 OPTICAL COHERENCE TOMOGRAPHY

Detailed and informative imaging on the internal structure human body is crucial for an effective medical diagnosis and treatment [1]. Several diagnostic imaging techniques such as X-ray radiography [2], computed tomography (CT) [3], ultrasonic imaging [4] and magnetic resonance imaging (MRI) [5], are being already developed over the past decades. These techniques aim for different applications, depending on specific application requirements, mainly on the imaging depth and resolution. The optical tomography techniques are nowadays taking off, especially in the field of optical medical imaging. In particular Optical coherence tomography (OCT) can have several specific advantages over the other techniques [6]. It is non-invasive, as uses light waves to produce detailed images of internal body structures. Contrary to X-ray based techniques, it is not harmful to biological tissues and there is no need for physical contact with the sample under investigation. Therefore, it is possible to perform OCT imaging in-vivo. OCT also allows a high-resolution image, compared to the other techniques. Due to its micrometer level resolution and millimeter level imaging depth, OCT is widely used in diagnostic inspections, such as in ophthalmology to obtain three-dimensional images of retinas [7]. OCT can be beneficial also to other medical applications such as dermatology [8], or to non-medical applications such as art conservation [9]. This technique is developed from one-dimensional interferometric measurements, based on the information on the attenuation coefficient coming from a sample [10]. Two- or three-dimensional OCT images can be obtained through repetition of one-dimensional in-depth measurements in different positions over a surface. The working principle of an OCT system is a Michelson interferometer, and it is depicted in Figure 1.1 a). The phase and the intensity information of the backscattered light are obtained in an interferometer configuration where the reference arm uses a portion of the input light. The information on the position and the intensity of the reflections can be derived from the optical interference signal that is recorded into a photodetector as a function of wavelength. In Figure 1.1 b) a real OCT system implemented by Topcon is shown. It is possible to observe that the machinery is composed by several different units, making the system rather costly and bulky.

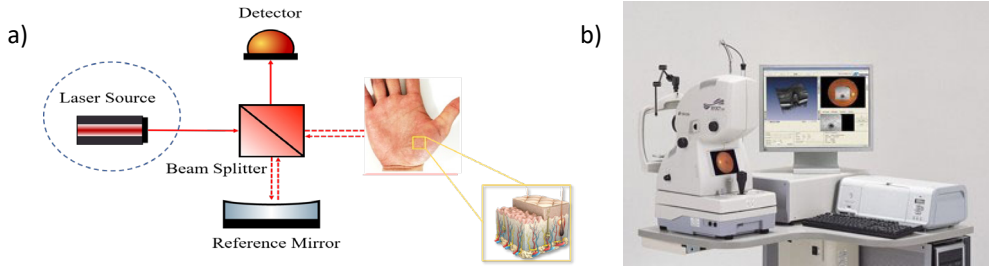


Figure 1.1: a) The schematic diagram of a basic OCT system. The hand image is taken from [11]. b) Topcon OCT imaging system for ophthalmology [12].

The frequency domain or Fourier domain OCT (FD-OCT) is a promising technique to achieve fast scanning speed because, differently than the time domain OCT (TD-OCT), it does not involve any mechanical movement of the reference mirror [6]. In FD-OCT, the OCT image along the penetration depth is obtained through the inverse Fourier transformation (FT) of the interferometer transmission spectrum. The interference spectrograms are detected either with a broad band light source and a high speed spectrometer (i.e. spectral domain OCT (SD-OCT)) [7], [13], [14] or with a wavelength swept laser and an ultrahigh speed photodetector (i.e. swept source OCT (SS-OCT)) [15]. SD-OCT uses a fast CCD camera to achieve high acquisition speed [16], and can get over 100,000 A-scans per second. On the other hand, SS-OCT uses a swept source (i.e. a tunable laser system) and a dual balanced photodetector to obtain higher resolution in the signal detection [17]. The swept laser with a sufficiently narrow linewidth in an SS-OCT setup can lead to higher OCT resolution than the SD-OCT setup. The major advantage of SS-OCT over SD-OCT is the lower sensitivity roll-off along the imaging depth [18]. The sensitivity roll-off is the minimum detectable signal along the depth which depends on the amount of power impinging the sample and on the acquisition resolution of the spectrum. In both techniques the speed of the data acquisition systems (DAQs) is the limiting factor to the imaging speed. High definition live 3D-OCT imaging has been performed using Fourier domain mode locked (FDML) lasers and ultra-fast (2.5 GS/s) analog to digital converters (ADC) [19].

Different monolithically integrated laser systems discussed in this thesis are designed to be used as source for the FD-OCT setup, with the aim of achieving high-performance OCT imaging. These widely tunable laser systems are conceived to be stepwise swept sources in SS-OCT schemes. Finally, options for Fourier Domain Mode Locked (FDML) lasers based on monolithic integrated circuits for both SS and SD-OCT are investigated. The performance of both type of integrated lasers will be discussed with particular focus on the impact of the tunable laser scan speeds.

1.2 TUNABLE LASER SOURCE REQUIREMENTS FOR OCT

In OCT there is a clear link between the tunable laser systems specifications and the associated OCT image quality. The four different aspects of a tunable laser source that influence the performance metric of an OCT system are described here below.

1. The laser tuning range is linked to the axial resolution of the images in SS-OCT systems. The axial resolution in vacuum of the OCT imaging (ΔL) is defined as [20]:

$$\Delta L = 2 \ln 2 \frac{\lambda_0^2}{\pi \Delta \lambda} \quad (1.1)$$

where λ_0 is the central wavelength and $\Delta \lambda$ is the tuning range. Note that this equation assumes a Gaussian intensity distribution of the laser output power over the laser scan range. It is possible to observe from this equation that the axial resolution is mainly limited by the tuning range of the laser around a central wavelength.

2. The spectral sampling of the laser determines the maximum imaging depth in vacuum from the zero path length difference point, as [21]:

$$z_{max} = \frac{\lambda_0^2}{4 \delta \lambda} \quad (1.2)$$

where $\delta \lambda$ is the spectral sampling interval of the tunable laser system.

3. The coherence length of the laser influences the fringe visibility of OCT measurements [22]. The longer the coherence length the lower the interference fringe visibility roll-off, so the image quality does not decrease with increasing the imaging depth. The coherence length is strictly related to the spectral linewidth of the laser as [23]:

$$L_c = \frac{\lambda_0}{2 \pi d \lambda} \quad (1.3)$$

where $d \lambda$ is the laser linewidth or the full width at half maximum (FWHM) of the laser peak.

4. The sweep speed is a crucial factor to obtain high-definition OCT images. Since FD-OCT for clinical purposes needs to be performed in-vivo, the motion of the cells inside the tissue can lead to image blurriness in 3D imaging. For this reason, the OCT scan needs to be at least 100 kHz to distinguish the motion of the particles, from the interferometric signal [24].

As defined from the equations above ((1.1)(1.2) (1.3)), the choice of the operating wavelength influences the performance of an OCT system. Longer wavelengths lead to deeper penetrations and longer coherence lengths for the same spectral sampling and FWHM. On the other hand, shorter wavelengths can obtain higher axial resolution for the same laser tuning range. However, when choosing the operating wavelength is important to consider the properties of the sample that needs to be imaged, such as the absorption spectrum of water to perform OCT imaging biological tissues. The water absorption is the

main limiting factor of this technique. Figure 1.2 shows the water absorption spectrum between 800 and 2500 nm. It is possible to notice that two strong absorption bands are present (1400-1500 nm 1900-2200 nm). This research focuses on the realization of a tunable laser source operating at 1300 nm for its use as a swept source in a SS-OCT system. The choice of this wavelength is based on the presence of a local minimum of 1.12 cm^{-1} in the water absorption spectrum at 1270 nm. Moreover, the use of a dual wavelength OCT system, with swept sources around 1300 and 1500 nm, enables an interleaved OCT imaging [25]. In this way, it is possible to derive the water content of a biological tissue, i.e. a human hand, from the analysis of the different wavelengths, which yield different water absorption coefficients.

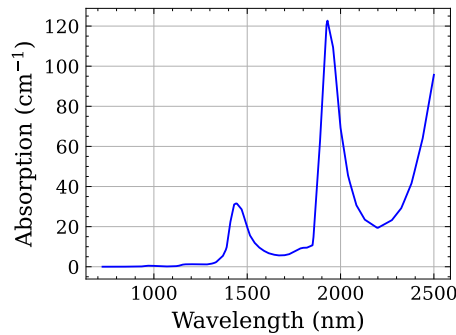


Figure 1.2: Water absorption spectrum taken from [26].

1.3 GENERIC INTEGRATION TECHNOLOGY ON INP

A photonic integration technology platform for generic purposes refers to a design and fabrication system for photonic integrated circuits that can be used for a wide range of applications, as opposed to being specifically designed for a single application or use case. It is typically made up of a combination of various photonic components like optical amplifiers, lasers, modulators, detectors, and waveguides integrated onto a single chip or substrate using a single process [27]. This allows for the creation of compact and versatile systems that can be adapted to a wide range of applications.

Examples of applications that can benefit from a generic photonic integration platform include telecommunications, sensing, and imaging. In telecommunications, for example, a generic photonic integration platform can be used to create compact and efficient optical transmitters and receivers for high-speed data communication [28]. In sensing and imaging, a generic photonic integration platform can be used to create compact and versatile devices for a wide range of applications, such as spectroscopy [29], interferometry, and optical coherence tomography [30].

The design of a generic photonic integration platform can be challenging as it requires a balance between flexibility and performance. The platform must be able to accommodate

different applications, while providing necessary functionality and performance. The platform discussed in this thesis is based on the InGaAsP/InP material system, with a monolithic active-passive integration technology [31]. The generic platform is based on wafer material produced using three different epitaxial steps with metalorganic vapor phase epitaxy. The first step is the growth of an active wafer stack for an active waveguide on a highly n-doped InP substrate up to the first low p-doped InP layer. The active gain material is then etched away everywhere, except where the optical amplifiers are needed on the wafer. The second growth step refers to a passive bulk quaternary InGaAsP and first undoped InP layer that restores the wafer in the areas that have been etched away to a passive waveguiding stack. The active and the passive material have then the same height again and are connected. This is called a butt-joint active/passive integration scheme. The third step involves the growth of p-doped cladding InP layer and the contact to supply forward or reverse bias to the InP pin diodes. The active and the passive material layer stack must be designed to optimize the interface between the two different layer stacks. This is done to ensure minimal losses (<0.1 dB) and reflections (<-50 dB) at the transitions in the ridge waveguides that are realized at the active-passive interfaces. In Figure 1.3 a) is depicted a schematic representation of the different cross-sections of the basic building blocks which compose the 1500 nm library of photonic components. This technology is since 2013 commercially available through Smart Photonics in the forms of multi-project wafer (MPW) runs, where the designers can submit their PIC designs and share the processing costs (Figure 1.3 b) [31]. After the fabrication, the wafer is diced into separate photonic chips. The extension of this generic integration platform towards the 1300 nm wavelength range is broadly described in this thesis. This first 1300 nm InP monolithic integration platform with active/passive capabilities is crucial to realize tunable laser systems. Different approaches to realize 1300 nm integration platforms, such as heterogeneous [35] or heteroepitaxial III-V integration on Si [36] have been reported in literature. These approaches have encountered difficulties in requiring tailored processes with high precision alignment and high control over the formation of defects at the interfaces between different materials. With a monolithic integration platform on InP, modulators, passive components and amplifiers can be integrated together with a single regrowth process. In this way the risk of defects and impurities is minimized. Moreover, this new monolithic 1300 nm platform on InP can exploit a well-established process [34], which, in turn, can lead to robust 1300 nm photonics components.

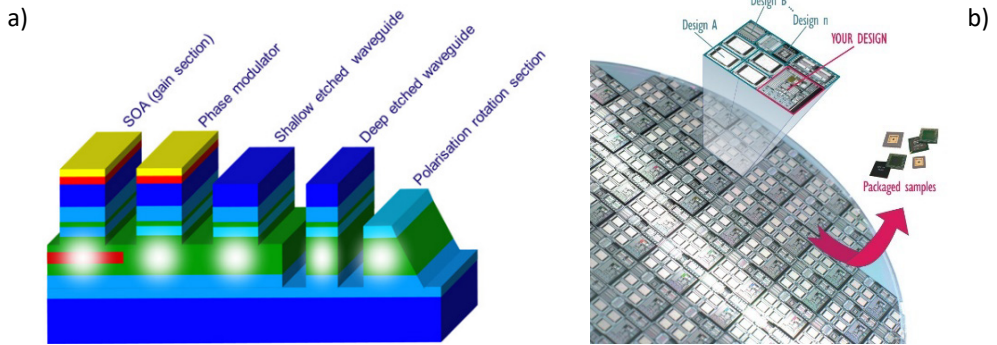


Figure 1.3: a) Examples of different cross sections realized on the generic integration technology on InP with active passive capabilities, this picture is taken from [27] b) Multi project wafer where the mask area is shared among different users. After manufacturing, each die is further sub-diced and the chips containing the different designs are delivered to the customers. After [32].

1.4 INTEGRATED LASERS FOR OCT

Most of the OCT systems developed so far are realized using bulk-optical components or fiber-optic components. Photonic integrated circuits (PICs) have the potential to satisfy the need of miniaturization e.g., by combining the light source with interferometer optics. Such miniaturization is increasingly of interest in OCT technology to perform diagnostics of internal organs in a minimal invasive way [8]. Photonic integration in OCT is also used for endoscopic devices, as it allows for miniaturization of the system and integration of the source, detector and optics into a small probe [33]. In addition, an OCT system on a chip would not suffer from misalignment and optical path instability such as free-space and fiber-optics based OCT systems. The compact size also allows for options such as multi-channel OCT systems that accelerate image acquisition through parallelization [34]. Efforts to integrate parts of an OCT system on a photonic integrated circuit (PIC) have resulted in the integration of widely tunable light sources on an InP chip [11, 15]. The development of optical sources for SS-OCT is focused on the development of a tunable laser system which can be tuned over a wide range with fast stepwise scan rates (20 kHz-100 MHz). High quality OCT imaging can be obtained using a uniform frequency grid of around 1000 lasing wavelengths within 100 nm. The feasibility of a 1.7 μm source for OCT has been studied [21]. This source was based on a long ring cavity (43.5 mm) with two electro-optically tuned arrayed waveguide gratings and a quantum dot (QD) amplifier. Two main limitations were highlighted. The first limitation is the low gain in the QD amplifiers. This in turn leads to slow wavelength switching time (500 ns) with respect to what has been predicted by theory (10 ns), due to the fact that the laser could not be operated further above threshold [21]. The second limitation was related to the complexity of the control settings needed to operate the laser with 36 reverse bias voltage

electro-optic modulators, which results in a need of more complex electronics driving. A different approach based on the use of asymmetric Mach-Zehnder interferometers inside the laser cavity is investigated in this thesis. This laser with shorter integrated cavity length can lead to faster switching times (50 ns) [36] and stronger single mode selection between adjacent longitudinal cavity modes, leading to side mode suppression ratio >40 dB [29]. These laser type have still to be demonstrated suitable to achieve OCT scans with sufficiently high sweep rate. To improve the speed of SS-OCT scans, the integration of FDML laser sources can lead to hundreds of MHz scan speeds in OCT systems [37]. The use of 1300 nm tunable laser systems are fundamental in OCT setup schemes, to obtain imaging from biological tissues which present a high-water content. The absorption in water at 1300nm is approximately 1.1 cm^{-1} and this can be tolerated over a propagation distance of a few millimeters. Moreover, the 1300 nm wavelength range is currently used in multiple clinical applications [24].

1.5 MOTIVATION

This main goal of the work presented in this thesis is to search and develop a 1300 nm monolithically integrated InP extended cavity widely tunable laser that is to be used as a light source in a swept source OCT system. The focus of this goal can be divided into two main research questions:

1. How to realize a 1300 nm InP integration platform that is technologically as similar as possible as an established 1550nm platform, and that can support a widely tunable laser system?
2. Is it possible to achieve high-performance OCT by means of a monolithically integrated InP widely tunable laser as a swept source?

The first four chapter of this thesis are dedicated to addressing the realization of a 1300 nm generic integration platform. The main objective is to develop electro optic modulators on InP with sufficient efficiency ($<8.5 V_\pi \text{ mm}$) and speed ($< \text{several ns}$) to be able to integrate widely tunable lasers that can have a stable output power while operating at high scanning rates. The design, realization and test of passive and active components has been done first. That is followed by their integration using the butt-joint integration scheme, and the realization of active-passive integrated complex circuits. The main challenges are to develop optimum passive components (i.e., single mode and low loss waveguides), and to design compatible amplifiers (i.e. high mode overlap and minimal modal index difference with the passive waveguide) without compromising their performance (i.e. high characteristic temperatures and wide modal gain bandwidth). Parametrized models are set-up, which describe the different photonic building blocks in a simple but complete way and are used in the development of steady state and dynamics laser simulation tools at 1300 nm.

The remaining chapters of the thesis focus on the study of laser sources for OCT schemes. The main challenge is to realize a tunable laser system that is able to maintain a stable laser operation for OCT experiments. This problem is approached from two different perspectives and using different laser sources. The first approach involves the integration of a single mode widely tunable laser system for OCT with a real-time wavelength monitoring system to obtain a complete laser calibration strategy. The wavelength monitoring system also enables frequent measurements of all the laser emission wavelengths and the compensation for any calibration drift due to environmental condition changes.

The second approach is to use active/passive integration in the development of a FDML laser for OCT. The use of FDML laser for OCT allows to obtain wide emission frequency comb with equally spaced optical frequency and tens of MHz scan speeds. Moreover, the use of integrated filters in FDML laser cavities, allows one to obtain uniform power distributions over a broad range of emission wavelengths. This is achieved through the application of different electronic waveforms rather than sinusoidal to the modulators used in the filter arms. This power uniformity over the full wavelength tuning range is a critical requirement for SS-OCT applications.

The laser calibration systems for OCT lasers are performed at 1500 nm due to the higher maturity of the technology and availability of equipment in the lab. Since the control strategy mostly involves optimization methods for the electronic control settings, similar consideration can be done on tunable laser systems at 1300 nm.

1.6 THESIS OUTLINE

In the following paragraphs, the thesis outline is detailed.

Chapter 2 focuses on the definition of a passive waveguide component which is single mode and with sufficiently low amount of propagation loss in the 1300 nm wavelength range. The description of the choices made on the material composition and the geometry of the ridge waveguide are followed by the characterization results of passive components such as straight and bend waveguides, and multimode interference couplers (MMI) and reflectors (MIR) that were fabricated by the company Smart Photonics.

In **Chapter 3** the performance of quantum well based semiconductor optical amplifier (SOA) based on a multiple Quantum well active layer stack on InP is presented. The SOA stack was designed to be compatible with the passive waveguides for an active/passive but-joint integration scheme at 1300 nm. The SOAs were fabricated at Smart Photonics. The dimensions and material composition of the active layer stack were chosen to maximize the mode overlap (>99%) and minimize the interface reflections (<-50 dB) with the passive waveguide defined in **Chapter 2**. Moreover, we present a compact description of the SOA, which can be used in the modeling of more complex circuits.

Chapter 4 describes the behavior of a two-section passively mode locked laser at 1300 nm realized in the newly designed gain layer stack, and its modeling. The model description is based on the gain and absorption parametrization of the SOA. The parameters for gain and absorption are tested on a sensitive device such as a Mode-Locked laser to verify their goodness for a use inside a 1300 nm laser simulator. The different Q-switching and Mode-Locking laser dynamics and the output pulses observed are compared with the simulation results of a time domain travelling wave simulator using the parameters of the SOA described in Chapter 3.

Chapter 5 discusses the characterization results of the full active/passive 1300 nm monolithic integration technology on InP substrate. The description of a phase modulator utilizing electro-optic effects, is followed by the analysis of its use in bandpass optical filters and a widely tunable laser system at 1300nm.

In **Chapter 6** a possible control strategy for a scanning monolithically integrated tunable laser system on InP at 1500 nm is presented and tested. Fast wavelength monitoring of the different control parameter configurations in the scan is used to monitor the laser performance. Wavelength drift of the initial laser calibration and small changes in the control settings obtained using an optimization algorithm, could be monitored. This allowed for the correction of the data recorded in a laser scan. Such a system is necessary to be able to use this type of widely tunable laser as a swept source for OCT setup schemes.

In **Chapter 7** a new design for an integrated Fourier domain mode locked (FDML) laser system, intended as an FD-OCT source is described in detail. The simulation results of a 2.5 GHz fully integrated FDML laser design with asymmetric Mach-Zehnder integrated filter are presented and its use as an OCT source is discussed. The use of such AMZI in a 12 MHz fiber based FDML is described, and initial characterization results are presented. The results demonstrate that integrated optical devices show potential use in such FDML lasers.

2. 1300 NM PASSIVE COMPONENTS DESIGN AND CHARACTERIZATION

In this chapter, the design and performance of passive integrated optical components for a new active/passive generic integration platform on InP at 1300 nm are discussed. This new platform aims to extend the capabilities of a 1550 nm integration platform towards the 1300 nm wavelength regime without increasing the fabrication complexity. To design and realize a platform for 1300 nm, the development was started with the optimization of passive components separately. In this chapter, the design of a new passive layer stack is introduced. The geometry and the material composition of shallow and deep etched ridge waveguides have been chosen from the analysis of optical simulations. This is followed by the characterization of different passive components such as straight waveguides, multimode interference coupler (MMI) and reflectors (MIR) that were fabricated. A deep etched waveguide with propagation loss of 2 dB/cm at 1310 nm, limited by p cladding InP absorption losses, has been realized as well as an MMI with a minimized wavelength dependency (<1 dB), less than 0.2 dB imbalance and 1 dB insertion loss over 100 nm between 1260 and 1360 nm. This MMI has been realized engineering the input and output waveguide geometries.

These passive components form the foundation of a 1300 nm active/passive integration platform as functional building blocks to be used in complex optical circuits that will be described in the following chapters. The parametrized models describing the different passive components can be used inside complex circuit simulators, to describe the steady state behavior of tunable laser systems, realized on a 1300 nm active/passive integration platform on InP.

2.1 INTRODUCTION

Photonic integrated circuit technology allows for the miniaturization of complex optical systems. This can enable the reduction of cost and allows for larger production volumes, being able to serve several different applications. An Indium Phosphide (InP) monolithic active/passive integration platform in the 1300 nm range (O-band), with low reflections at the active/passive interfaces (<40 dB) such as those available at 1550 nm [27], will enhance the use of photonic integration in a larger number of applications such as optical data communication and medical optical imaging techniques. This platform is useful for applications in broad band circuits such as wavelength division multiplexing [38] or for realizing widely tunable laser systems [29]. A generic integration platform uses a standard set of building blocks which brings the benefit of being able to create a large variety of complex circuits with the same integration process. This allows for fast and cost-effective prototyping, since many different applications, i.e. circuits, can be served at the same time and the cost can be shared.

This chapter explores the capabilities of an integration platform at 1300 nm platform on InP with low propagation loss (≈ 2 dB/cm). The passive layer stack needs to be compatible with an active layer stack through a butt-joint active/passive integration scheme. The passive stack is formed by growing several different layers on a InP based substrate. From the analysis of the geometry and the material of the layers is possible to derive the properties of the passive components. The choice for the layer stack to be used in this new 1300 nm InP passive platform is justified by the analysis of two-dimensional simulation output for straight waveguide structures as described in section 2.2. The fabrication of two different waveguide geometries which are distinguished by the different etch stop levels is then addressed in section 2.3. Section 2.4 describes the characterization methods and the results obtained for different passive functional building blocks such as straight passive waveguides, and multi-mode interference couplers and reflectors.

2.2 PASSIVE LAYER STACK DESIGN

The starting point in the design of a passive layer stack monolithically grown on InP is the definition of a straight passive ridge waveguide which presents single mode propagation and a low amount of optical loss per unit length (cm). This passive layer stack needs to be compatible with a butt-joint active/passive integration to maximize the mode overlap with an active InP layer stack defined in the same thesis [39]. The waveguide is also used as an electro-refractive modulator when contacted. In this way it is possible to design and realize intra-cavity bandpass optical filters inside monolithically integrated widely tunable laser systems.

These requirements lead to the presence of p and n-doping above and below the waveguiding layer. The passive components are grown on a n-type (100) InP substrate. In the waveguide, light is guided by a quaternary alloy, made of InGaAsP lattice matched to InP and sandwiched by n- and p-doped InP. The bandgap of InGaAsP is properly engineered to be almost transparent in the O-band (1260-1360 nm). Both n- and p- type doping influence the real and imaginary part of the refractive index of InP [40]. While the change in the real part of the refractive index is almost negligible, the doping has a strong effect on the imaginary part of the refractive index and on the wavelength dependent material absorption. In particular, inside the p-doped InP layers, the absorption occurs due to the excitation of the light and heavy holes, which has been measured to be dependent on the doping concentration in InP [41] as:

$$\alpha_p(N) = 4.25 * 10^{-16} N e^{-\frac{4.53}{\lambda}} \quad (2.1)$$

Since the p-doping levels should be maintained sufficiently high to ensure a low series resistance in the active components, the design challenge is to minimize the mode power fraction in the p-doped regions to keep low value for the optical losses.

Simultaneously, the geometry of the waveguide can also influence the number of transverse modes that the waveguide supports. It is important to design a waveguide with a limited number of guided modes to avoid the propagation of higher order modes. The higher order modes propagation could lead to the propagation of hybrid modes inside the waveguide during the light transmission, leading to higher optical losses and a scrambling of the phase. It is highly important to avoid the propagation of the second order mode (TE_{02}) since it can easily couple with the fundamental one (TE_{00}) being both symmetric over both the horizontal and the vertical directions.

To meet those requirements, the design of the layer stack for the fabrication of the passive structures arises from the optimization of two different parameters, through two dimensional MODE simulations [42], which are:

1. The waveguiding layer thickness (t)
2. The composition (InGaAsP) of the waveguide core layer (Q)

2.2.1 WAVEGUIDING LAYER THICKNESS

The first parameter studied in the simulations is the thickness of the waveguiding core layer. Finite difference element (FDE) 2-D numerical simulations were performed varying the thickness of the waveguiding layer for a small range of ridge widths. The number of modes together with their effective refractive indices as function of the waveguide thickness are calculated. The optimum waveguiding layer thickness arises from the trade-off between the optical loss and the number of propagating modes. Waveguiding layers as thick as possible maximize the TE_{00} confinement but, at the same time, thinner waveguiding layers avoid the propagation of high order modes. Furthermore, during the design phase it is important also to account for the fabrication tolerance on the layer thickness ($\pm 5\%$) and more importantly on the waveguide width ($\pm 0.2 \mu m$). An increase of $0.2 \mu m$ in the ridge width can lead to the propagation of higher order modes for thinner waveguides. Figure 2.1 a) and b) show the simulation results of the fundamental mode effective index on shallow and deep etched waveguides, for ridge widths of 2 and $1.5 \mu m$. These widths are chosen as references for the analysis of the waveguiding layer thickness. Further in this chapter, we will study the influence of the waveguide width from the measurements of the waveguide propagation losses. A thickness equal to $t = 400 \text{ nm}$ is selected for the waveguiding layer thickness. In this way it is possible to obtain a deeply etched single mode waveguide at $1.5 \mu m$. For shallow etched waveguides with ridge widths as wide as $2 \mu m$ the waveguide propagates the TE_{00} and the TE_{01} modes which in a straight waveguide do not couple to each other.

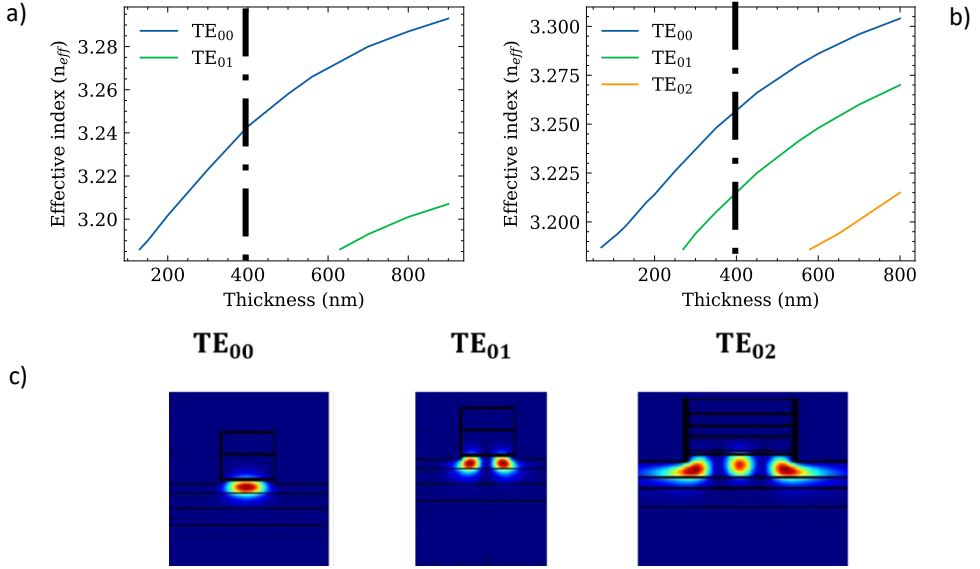


Figure 2.1: a) Effective Index of the different order TE modes as function of the waveguiding layer thickness at 1310 nm for a) the deep ($W=1.5 \mu\text{m}$) and b) the shallow ($W=2 \mu\text{m}$) etched ridge waveguides. c) Intensity of the TE modes of different orders from 2-dimensional simulations

2.2.2 QUATERNARY ALLOY MATERIAL COMPOSITION

The quaternary alloy composition (Q-value) refers to the bandgap energy in μm of the InGaAsP contained inside the waveguide core layer [40]. The optimization of this parameter considers the optical mode confinement and the intrinsic absorption of the quaternary layer itself (Q-layer). The higher the Q-value, the more the optical mode is confined inside the Q-layer, due to a higher refractive index contrast with respect to the InP layers. On the other hand, the amount of intrinsic absorption of a semiconductor depends on its composition [43]. The intrinsic absorption at 1300 nm increases for higher Q-values since the bandgap energy will then be closer to the photon energy. The intrinsic absorption in quaternary alloy semiconductor below the bandgap can be approximated to [44]:

$$\alpha = A \exp\left[\frac{\sigma(\hbar\omega - \hbar\omega_0)}{k_b T}\right] \quad (2.2)$$

where $\hbar\omega_0$ is the bandgap energy, $\hbar\omega$ is the photon energy, T the temperature and σ and A are parameters that depend on the quaternary alloy material composition. The parameter σ in this work has been obtained from the measurement of the absorption tail of a straight waveguide with a Q-value=1.25 μm when the photon energy is close to the band edge (i.e., 1300 nm) at 20°C. The σ parameter is then assumed to be almost constant within 10% of accuracy ($\sigma = 2 \pm 0.2$), for similar quaternary alloy compositions (InGaAsP). $A = \alpha$ at the bandgap energy. The total waveguide losses are then simulated as function of photon

wavelength, including the free carrier absorption (equation (2.1)) and the intrinsic absorption (equation (2.2)). Please note that the free carrier absorption wavelength dependence is negligible compared to the intrinsic absorption. The simulation results for the propagation loss of the waveguides with different material compositions are presented in Figure 2.2. Optical propagation loss of the passive layer stack design as function of wavelength for two different bandgaps of the quaternary alloy material composition of the waveguiding layer. From this figure it is possible to observe how for a Q-value=1.1 μm , the overall waveguide propagation losses are simulated to be lower than 2 dB/cm with a 0.2 dB/cm change over the whole wavelength range. Higher Q-values (Q=1.15 μm) make the intrinsic absorption ($\approx 0.3 \frac{1}{\text{cm}}$ @1300 nm) the predominant source of losses, leading to higher losses variations (> 1 dB) over the whole 1260-1360 nm wavelength range.

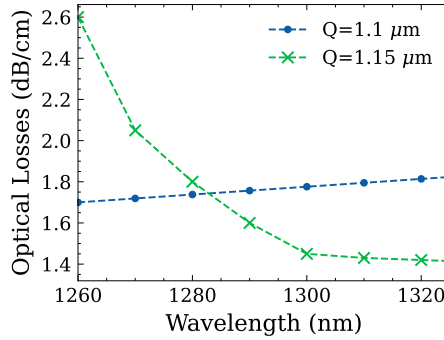


Figure 2.2 Optical propagation loss of the passive layer stack design as function of wavelength for two different bandgaps of the quaternary alloy material composition of the waveguiding layer.

For a Q-value equal to 1.1 μm the fundamental TE_{00} mode has an optical confinement of 67% inside the waveguiding layer. Lower Q-values do not improve the optical losses, because they reduce the refractive index contrast at the boundaries of the waveguiding layer resulting in a poorer mode confinement (<50%). A Q value equals to 1.1 μm is also the lower technological limit given by the Smart Photonics foundry which performs the epitaxial layers growth and the waveguide lithography. This is due to the increasing percentage of Phosphorus (>70%) needed to decrease the Q-value below 1.1 μm .

The choice of the different layer thicknesses, doping profiles and bandgap energies, for the passive layers are summarized in Table 2.1.

Table 2.1 Epitaxial layer thicknesses and composition which arises as optimum design from simulation. (n.i.d. is non-intentionally doped).

Name	Material	Bandgap (nm)	Thickness (nm)	Strain (%)	Dopant (n-type)	Dop. level (1/cm ³)	Dopant (p-type)	Dop. level (1/cm ³)
III-4	InP	920	700	0			Zn	5.0E+17-1.0E+18
III-3	InP	920	300				Zn	5.0E+17
III-2	InP	920	300	0			Zn	3.0E+17
III-1	InP	920	140	0	n.i.d.			
II-1 Grating	InGaAsP	1100	30	0	n.i.d.			
III-1	InP	920	30	0	n.i.d.			
II-1 Waveguide	InGaAsP	1100	400	0	n.i.d.			
I-2	InP	920	500	0	S	3,00E+17		
I-1	InP	920	500	0	S	1,00E+18		
substrate	InP	920	-	0	S	4,00E+18		

2.3 WAVEGUIDE FABRICATION

The passive layer stack is fabricated following the design considerations on the material compositions, the thicknesses of the epitaxial layers and the dopant materials for the n and p-doped layers as shown in table 1 by Smart Photonics. The layers are fabricated with a metal organic chemical vapor deposition method (MOCVD), with p and n doped InP layer definition. The waveguide ridges are then written through Ultraviolet (UV) scanner lithography technique [45], following a mask design implemented from an open-source design framework [46]. The waveguides are all etched using an Inductively Coupled Plasma (ICP) dry etch process. In Figure 2.3 one can see two different cross sections following from the use of two different etching stop levels, which are called shallow and deep etched waveguides. The shallow etched waveguides in Figure 2.3 a) have ridges that are etched down to 100 nm above the waveguiding core layer. This is done to obtain wider mode dimensions and a lower amount of propagation losses. The losses are lower due to less optical confinement in the p doped InP cladding. As a downside, this waveguide shows a smaller lateral confinement, and a high sensitivity to the in-plane surface roughness.

The deeply etched waveguides, shown in Figure 2.3 b) have an etching depth of more than 150 nm below the waveguiding core layer. In this way the light is more confined inside the waveguide, due to the high index contrast at the lateral sides. This allows for sharper bending radii and narrower ridges. The narrow ridge in the deep etched waveguide of $W=1.5\text{ }\mu\text{m}$ leads

to the propagation of the single mode for a waveguiding layer thickness of 400 nm. As a downside, the narrower ridges of the deep etched waveguides provoke higher propagation losses due to the sidewall roughness.

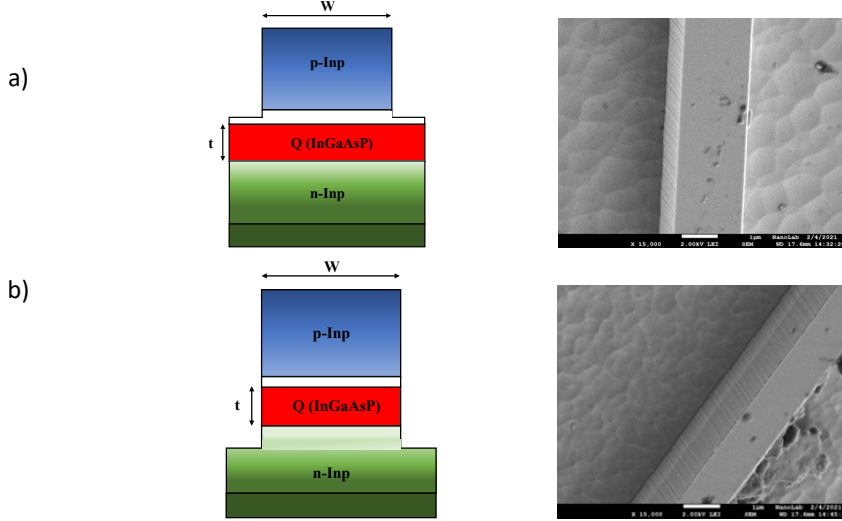


Figure 2.3: Schematics of the cross section for shallow (a) and deep (b) etched waveguides where the n-doped layers (green) the intrinsic quaternary layer (red) and the p-doped InP layers (blue) are highlighted. A darker color means higher doping concentration. On the side we report Scanning Electron Microscope (SEM) pictures, where we highlight the etch depth by showing different colors (materials) behind the ridge waveguide.

2.4 PASSIVE COMPONENTS CHARACTERIZATION

To verify the suitability of the fabricated passive layer-stack, characterization tests are performed on straight and curved waveguides to assess their performance. Following from that, the design, and the characterization of MMI couplers and MIR are described in this section.

2.4.1 PASSIVE WAVEGUIDE MEASUREMENTS

The passive waveguide propagation losses per unit length are measured for a wavelength of 1310 nm. The waveguide dispersion between 1260 and 1350 nm is measured to assess the group index n_g dispersion as function of wavelength.

2.4.1.1 PASSIVE WAVEGUIDE LOSS

The propagation losses are measured using the Fabry-Perot (FP) interferometric method [47]. This method is enabled by the fact that the wafer has been cleaved into a 4 x 4.6 mm dies, and the cleaved ends of each die act as mirrors trapping the light in a FP cavity. The analysis of both the transmitted and the reflected light from the FP cavity, allows to perform

the analysis of the optical losses through two different methods. The losses extracted from these two methods are then compared to cross-validate the two different methods. The transmission from a FP cavity is given by [48]:

$$\frac{I_t}{I_i} = \frac{e^{-\alpha L(1-R)^2}}{(1-e^{-\alpha L R})^2 + 4GR \sin^2\left(\frac{\delta}{2}\right)} \quad (2.3)$$

where $R=32\%$ is the facet reflectivity for the fundamental transverse mode calculated with an academic software developed by the ETH in Zurich, α the optical loss per unit length and $\delta = \frac{4\pi}{\lambda} n_g L$ is the argument of the sinusoidal, which contains the wavelength dependence. Looking at the equation (2.3), it is possible to distinguish between maxima and minima of the transmission, where the $\sin^2(\delta/2)$ function is either 1 or 0. From the contrast ratio between the maxima and the minima of the interferometric fringes it is possible to calculate the optical losses per unit length as [48]:

$$\alpha = \frac{1}{L} \ln \left(\frac{1}{r} \frac{\sqrt{r}-1}{(\sqrt{r}+1)} \right) \quad (2.4)$$

where r is the ratio between the maxima and the minima of the sinusoidal transmission curve.

The reflected signal from the Fabry-Perot cavity can be also used to calculate the waveguide propagation losses. The reflected signal presents higher contrast ratio and transmission, being more tolerant with respect to lower fiber to chip coupling. However, the difficulty of using this method arises from the need to distinguish between the amount of light reflected from the facet without entering the FP cavity and the light traveling inside the cavity for at least one roundtrip. As suggested by Y.He et al [49] the intensity of the total reflected light detected by the power-meter has been calculated to be:

$$I_r = c^2 + \frac{e^{-2\alpha L R(1-R)^2} + 2cR^2(1-R)e^{-2\alpha L} - 2ce^{-\alpha L} R^{\frac{1}{2}}(1-R) \cos(\delta)}{1 + R^2 e^{-2\alpha L} - 2Re^{-\alpha L} \cos(\delta)} \quad (2.5)$$

where c is a fitting parameter which refers to the amount of optical signal collected by the power meter that does not contribute to any resonant mode of the Fabry-Perot cavity. The fit of the reflected signal, applying equation (2.5), with a group index value $n_g=3.6$, is implemented to retrieve a value for the optical loss per unit length and a fitting parameter c .

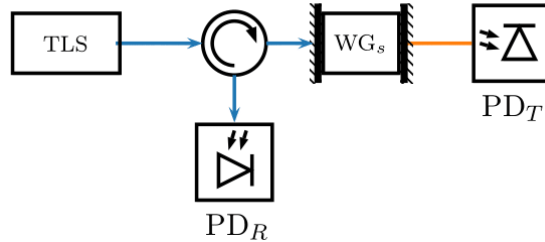


Figure 2.4: Experimental setup for the Waveguide Loss and Dispersion Measurements.

The experimental setup used to perform those measurements is schematically shown in Figure 2.4. The light from a tunable laser source (TLS) (Santec TSL-550) enters the waveguide through a polarization maintained lensed fiber, which is calibrated to ensure the injection of TE-polarized light only. An optical circulator is used to capture the reflected light which is guided to a power meter. The transmitted light is monitored simultaneously on the second channel of the power meter (Agilent 8163B). The TLS and the detectors are synchronized through electronic triggering. The input light from the laser is swept over 10 nm with a resolution of 1 pm around the central wavelength of the O-band (1310 nm). Figure 2.5 a) and b) show the two resulting signals from these measurements (blue dots). Figure 2.5 a) shows the transmission of the FP cavity. In the graph it is possible to notice that the contrast ratio is not constant over 1 nm between 1309 and 1310 nm. This can be due to the change in fiber to chip coupling during the measurement time of several minutes. To remove noise from the signal, a Savitzky-Golay digital filter (red curve) is applied to the transmitted output power to smoothen the measurement data [50]. After that, an average contrast ratio (r) and a standard deviation are calculated over a certain number of smoothed interferometric ripples (≈ 20) around 1310 nm. Figure 2.5 b) shows the reflected signal which is fitted (red curve) with equation (2.5). The number for the propagation loss α and the measurement error on the propagation losses are then calculated. The error is extracted as the χ^2 of the fitted curve.

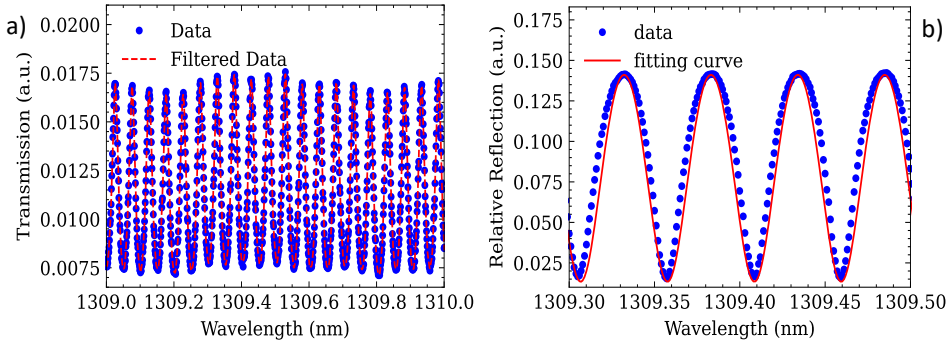


Figure 2.5: Fabry-Perot interferometric measurements to extract the shallow etched waveguide propagation losses. (a) Transmission curve: blue empty dots are measurement data, and the red curve is the smoothed curve.

(b) Reflection curve: blue dots are the data, and the red curve is the fit performed with Eq (2.5).

In table 2.2 we report the optical loss values for different waveguides obtained from the analysis of the reflected and the transmitted power respectively. Please note that for all the measurements the same cavity length of $L=4.6$ mm is used in the calculations.

Table 2.2 Waveguide optical loss per unit length, measured from two different signals over 4 different waveguides with different geometric parameters

Waveguide width	W=1.5 μm Deep Etched	W=1.6 μm Deep Etched	W=1.8 μm Shallow Etched	W=2.0 μm Shallow Etched
Transmission Loss (dB/cm)	3.00 ± 0.07	2.95 ± 0.15	9.96 ± 0.2	6.11 ± 0.25
Reflection Loss (dB/cm)	3.10 ± 0.12	3.17 ± 0.25	10.29 ± 1	6.30 ± 0.5

It is possible to notice two different things. First the fact that the loss values measured from the two power detectors and analyzed with the two different methods are similar, which indicates the robustness of the two methods of analysis. Then it is worth to notice how the measurements of the shallow etched waveguide present a higher standard deviation and higher fit uncertainty. This can be explained by the fact that the shallow etched waveguides can support the TE_{01} mode, which lead to higher losses due to the propagation of hybrid modes in the lensed fiber. On the other hand, the deep etched waveguides can support only the fundamental transverse mode. For this reason, in Figure 2.6 we report the amount of optical propagation losses as function of the ridge waveguide width, for the deeply etched waveguides. Please note that the coupling losses affect the contrast ratio of the FP fringes. The increase in coupling losses leads to the overestimation of the loss in some measurements due to a smaller contrast ratio in the FP methods. The propagation losses as function of waveguide width have not been described in this thesis referring to optical simulations, because the amount of measured optical losses is highly dependent on the sidewall roughness. This parameter is highly fabrication specific and needs to be investigated with experimental data. The propagation losses are then analyzed considering two different contributions to the optical propagation loss inside deeply etched InP based waveguides. The first contribution is the scattering at the sidewalls, which decreases exponentially with increasing the ridge width of the waveguide as shown in the red solid line in Figure 2.6. This can be explained using optical simulations which reveal that the fraction of the fundamental optical mode intensity at the edges of the ridge drops from 24% to 8% for a waveguide width between 1 μm and 2.4 μm . The main contribution to the scattering loss is the sidewall roughness of the edges of the waveguide, which leads to propagation losses, according to [51] as:

$$\alpha(m^{-1}) = \frac{16\sigma^2}{2k_0 n_s W^4} g \quad (2.6)$$

where $k_0 = \frac{2\pi}{\lambda_0}$, is the wavevector in vacuum, n_s is the slab index, W is the waveguide width, σ represents the magnitude of the surface roughness ($\approx 3.1 \text{ nm}$) from [52], and g is a fitting

parameter which depend on the waveguide geometry ($g \approx 15$). This expression suggests that wider waveguides will induce lower scattering losses explaining partly the trend of the optical loss with the waveguide width.

The second contribution to the optical loss is given by the effect of free carrier absorption, due to holes, which takes place in the p-doped layers of InP. This is expressed as a linear term increasing with the width and is represented by the solid yellow line in Figure 2.6. Increasing the width, we increase the presence of p-doped material which will induce higher propagation losses. As explained in the previous sections, the p-doping should be maintained high to ensure a low resistance series in the active components such as amplifiers or electro-optic modulators.

In Figure 2.6 the total prediction of the propagation loss and the waveguide width given by the sum of these two effects is represented with a purple solid line.

Following from those consideration an optimum width of $W=1.5 \mu\text{m}$ can be considered because of these two different effects.

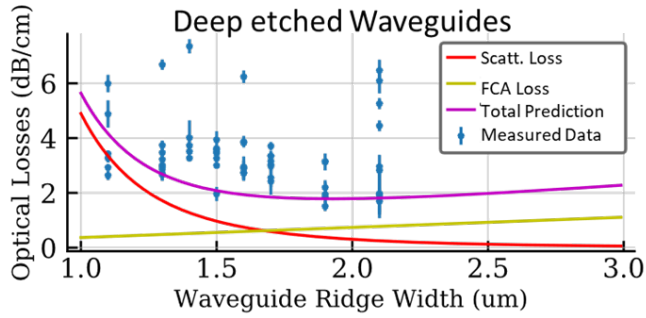


Figure 2.6: Deep Etched Waveguide optical Losses as function of waveguide width. The Blue points represent the measured data, and the solid line represents the individual contribution of scattering (red) free carrier absorption (yellow) to the optical loss. The purple curve is the sum of the two terms, and it is used to predict the optical loss values [53].

2.4.1.2 PASSIVE WAVEGUIDE DISPERSION

The passive waveguide dispersion can be determined by accurately measuring the effective index of the guided modes as a function of transmitted wavelength [54]. The first step is to measure the fundamental mode group index n_g as function of wavelength. With n_g , it is possible to calculate the modal effective index n_{eff} change as function of wavelength. The measurement of the waveguide dispersion, is important mainly for three reasons:

1. To calculate the waveguide propagation constants.
2. To model the field induced effective index change as a function of wavelength inside an electro-optical phase modulator at 1300 nm (see Chapter 5).

3. To increase the spatial resolution of interferometric measurements needed to calculate the reflections from integrated components on-chip.

To measure the group index dispersion we used the optical frequency domain reflectometry (OFDR) measurement technique, taking advantage of the chips facets reflectivity to create FP interferometers [55]. The spatial resolution of such OFDR measurements is linked to the group index and the external tunable laser wavelength span, according to [56]:

$$\delta L = \frac{c}{2n_g \Delta f} \quad (2.7)$$

where c is the speed of light in vacuum n_g is the group index of the waveguide (set to 3.6) and Δf is the frequency span of the laser. For example, in a dispersion free waveguide, a wavelength span of 90 nm around 1300 nm should result in a high spatial resolution of 2.65 μm .

However, due to the presence of waveguide dispersion, the measured spatial resolution with OFDR is significantly lower than the theoretical limit, as demonstrated by Glombitza and Brinkmeyer [57]. Therefore, it is firstly necessary to calculate the wavelength dependency of the group index, to increase the spatial resolution through the dispersion compensation, as reported by Zhao et al. [58] for 1550 nm InP based waveguides. In this way, it is possible to obtain a spatial resolution close to the theoretical limit determined by equation (2.7).

The group index is extracted from the FP transmission measurements using the experimental setup reported in Figure 2.4, and the numerical algorithm developed in [58]. The tunable laser wavelength steps are first rescaled into equally spaced optical frequencies. Then the FFT is applied to a rectangular frequency window of the optical spectrum, thus obtaining the temporal trace at the central frequency f of the rectangular window. After having re-scaled the temporal axis, with the introduction of the group delay interval $\delta\tau = \frac{1}{\delta f}$, it is possible to obtain the temporal traces as function of wavelength by moving the rectangular window over the full width of the spectrum. The group index of the dispersive medium is extracted according to [56] as:

$$n_g(\lambda) = c \frac{(\tau_b(\lambda) - \tau_f(\lambda))}{L_{cavity}} \quad (2.8)$$

where c is the light speed in vacuum, τ_b and τ_f are the group delays of the front and back facet reflection, and L_{cavity} is the cavity length.

To evaluate $n_g(\lambda)$, the external tunable laser is swept over a wavelength window of 90 nm, from 1260 to 1340 nm, with a step-size of 10 pm. This coarser step size is chosen due to the limitation on the number of data points that can be recorded by the photodetector's main frame over a single wavelength sweep (i.e., 60000). The group index measurement resolution is limited by the wavelength step (10 pm), and by the variations of the cavity length between different dies, which was around 15 μm over 4 different dies.

Figure 2.7 a) shows the extracted group index dispersion, measured over 5 transmission measurements of different waveguides with same parameters. A linear fit to the measurements has been applied with [59]:

$$n_g(\lambda) = a - b\lambda_0 - c\lambda_0(\lambda - \lambda_0) \quad (2.9)$$

where $\lambda_0 = 1310 \text{ nm}$ and $a = 3.235$, $b = -2.978 \cdot 10^5 \text{ m}^{-1}$, and $c = 1.127 \cdot 10^{12} \text{ m}^{-2}$ are three fitting parameters.

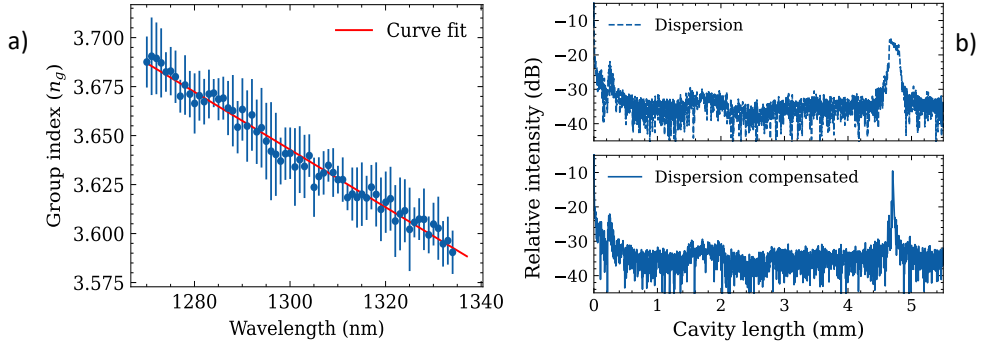


Figure 2.7: a) Group index measurement averaged over 5 different deep etched waveguides with the same ridge width ($1.5 \mu\text{m}$) (blue) together with a linear curve fit (red) following from eq. (8). b) Fourier Transform for the signal containing dispersion (top) and the signal after the dispersion is de-embedded (bottom)

From the group index dispersion fit with equation (2.9), it is then possible to extract the effective index wavelength dispersion, which is approximated as a second order polynomial of the type:

$$n_{eff}(\lambda) = n_{eff}(\lambda_0) + n'_{eff}(\lambda_0)(\lambda - \lambda_0) + \frac{1}{2}n''_{eff}(\lambda_0)(\lambda - \lambda_0)^2 \quad (2.10)$$

where $n_{eff}(\lambda_0) = a$, $n'_{eff}(\lambda_0) = b$ and $n''_{eff}(\lambda_0) = c$.

Figure 2.7 b) shows the FFT for a transmission signal when the dispersion is compensated, i.e., $F\left(\frac{\lambda}{n_{eff}}\right)$ and when it is not, i.e., $F(\lambda)$. It is evident how in the corrected signal on Figure 2.7 b), the spatial resolution is highly improved going from hundreds to only few μm ($\approx 10 \mu\text{m}$). However, this improved spatial resolution is still lower than the theoretical limit ($< 3 \mu\text{m}$). The limitations to this spatial resolution have several causes. The uncertainty on the cavity length used in the calculation of the group index, the coarser resolution of the wavelength step size and the parabolic approximation in the calculation of the effective index are just few examples of the causes that can limit the spatial resolution of the cavity length created by the straight waveguide. Looking at the relative intensity of Figure 2.7 b) it is possible to extract the propagation losses of the waveguide as [60]:

$$RI \approx Re^{-\alpha L} \quad (2.11)$$

Where $R=0.32$ is the facet reflectivity previously calculated and $L=4.6$ mm is the FP cavity length. From the $RI=-9$ dB, it is possible to extract losses of 3.6 dB/cm which agrees with the measured values for deep etched waveguides with $W=1.5$ μm .

2.4.2 CURVED WAVEGUIDES

A curved waveguide is a waveguide which propagates over a radius of curvature R . The deep etched waveguides are the best candidate to have smaller bending radii, due to their higher lateral mode confinement. In a model proposed by Melloni et al. [61], the fundamental mode in a curved waveguide is described as a linear superposition of fundamental and first order modes of a straight waveguide. This approximation holds if the radiation losses are low (< 0.1 dB/90°), which is generally the case for R much bigger than the width of the waveguide and the wavelength.

It is also important to include an offset at the straight to bend interface to ensure optimum overlap between the mode propagating in a straight and a bend waveguide. This helps to minimize the insertion losses at the straight-bend interfaces. In this subsection we will present:

- The design and the simulations of two-dimensional curved waveguides to obtain indication on a minimum bending radius and on the straight to curve offset value.
- The characterization of curved waveguides with different angles.

2.4.2.1 DESIGN AND SIMULATION

Two-dimensional optical simulations have been performed on curved waveguides for a fixed angle of 90°, to obtain a relation between the optical confinement inside the waveguiding layer and the radius of curvature. The waveguide radius for a fixed angle is strongly related to the amount of light that is confined inside a waveguiding layer during a propagation over a bend. Simulation results reveal that for bend radii smaller than 100 μm the optical confinement inside the waveguiding layer strongly decreases from 66% at 100 μm to 51% at 40 μm of radius. For radii larger than 100 μm the optical confinement barely changes, reaching a 67% confinement at $R=500$ μm . This value corresponds to the straight ridge waveguide optical confinement. Following from these simulations, a radius of 100 μm has been chosen as a minimum value for the design of curved deep-etched waveguides.

Furthermore, the interface between the straight and the curved waveguide need to be optimized, to avoid any insertion loss. A standard way to maximize the optical overlap at a straight to bend interface is ensured by the application of a small lateral offset [62]. This offset depends on both the bending radius and the waveguide ridge width. In Figure 2.8 a) the black dots are the simulated optimum lateral offset for a fixed angle of 90° and different bending radii between 50 and 500 μm . The blue curve represents a polynomial fit of the

lateral offset as function of the deep etched waveguide ridge width ($W=1.5 \mu\text{m}$) and the radius R as described by [52]:

$$\hat{o} = \pi^2 n_s^2 \frac{c_0 W^4 + c_1}{(c_2 \lambda^2 + c_3)(c_4 R + c_5)} \quad (2.12)$$

where n_s is the slab index, and $\lambda=1310 \text{ nm}$ the wavelength. The $c_0 - c_5$ terms are fitting constant to match equation (2.12) with the two-dimensional optical simulation results. For a nominal value of $R=100 \mu\text{m}$, which is the minimum bending radius used in the platform for deep etched waveguides, a lateral offset of 48 nm is applied.

2.4.2.2 MEASUREMENTS AND CONCLUSIONS

Several curved waveguides on different passive wafers were measured with the same FP method explained in section 2.4.1, and the bend waveguide losses are extracted using as reference the propagation over a straight deep etched waveguide. Figure 11 b) shows the measured losses of several different deep etched curved waveguides with radius $R=100 \mu\text{m}$, and propagation angles between 15° and 90° with 15° steps. The waveguide lengths have been designed to be identical to neglect the propagation losses from straight waveguide in the analysis. The measurements reveal a linear dependence of the loss with the angle, for a fixed $100 \mu\text{m}$ radius. Value as low as 0.1 dB are obtained for a $\frac{\pi}{2}$ angle of propagation with a standard deviation smaller than 0.01 dB , which agrees to what has been found in literature for an InP waveguides operating in the C-band [63].

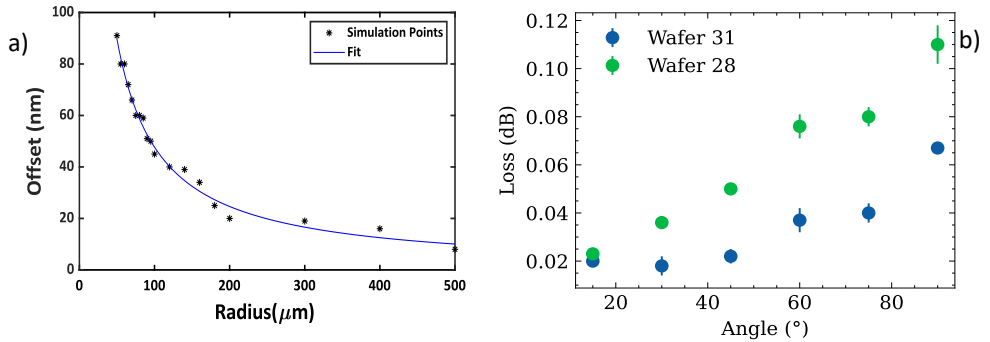


Figure 2.8 a) Optical simulations of the optimum offset between a deep etched straight and a curved waveguide with angle of 90° as function of the radius of curvature (black dots). Fit of the offset with equation (2.11) with a $W=1.5 \mu\text{m}$ and a $n_s = 3.26$. b) Loss measurements of curved waveguide losses as function of the bending angle for deep etched waveguides from two different wafers.

2.4.3 MULTIMODE INTERFERENCE COUPLER

In this sub-section, the design, and the characterization of 1300 nm 2×2 3-dB multimode interference (MMI) couplers on InP substrate are presented. Please note that inside integrated tunable laser systems on InP, to ensure the same performance over the whole

frequency range it is crucial to have low wavelength dependence of passive components. For this reason, the MMI is optimized during the design phase, to decrease the wavelength dependency of the splitting ratio and of the insertion loss in the whole 1300 nm range. This is done by varying the geometry parameters such as the multimode region width (W_{MMI}) and the access waveguide widths (W_{io}). A schematic, where the different regions are highlighted, together with a picture of the realization of such MMI are presented in Figure 2.9.

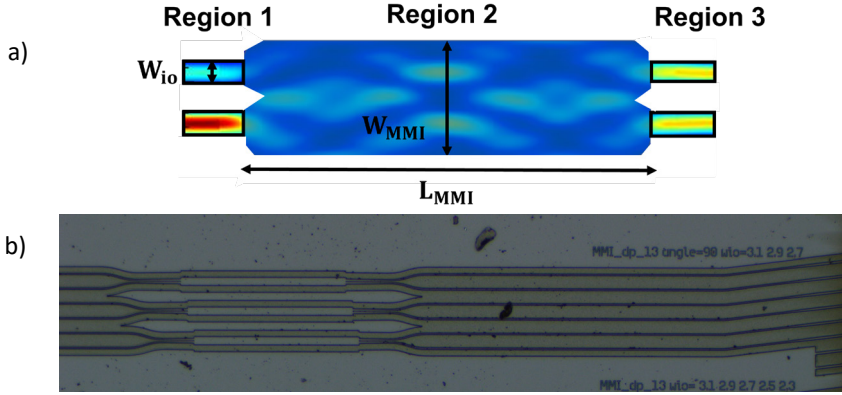


Figure 2.9 a) Schematics of a 2x2 MMI coupler layout, with distinguish the input (region 1) the interference (region 2) and the output (region 3) regions. b) A microscope picture of the 2x2 MMI with deep etched waveguides and different input and output waveguide ridge widths is shown. In the picture above the parameters that are varied in this work are highlighted (W_{MMI} , W_{io})

2.4.3.1 THEORY AND DEVICE DESIGN

In a 2x2 3-dB MMI coupler, the input light is split in a two-fold image after a length of $L = \frac{L_\pi}{2}$ [64], where the beat length L_π is referred as the imaging length. L_π shows a dependence over the MMI coupler geometry of the form [64]:

$$L_\pi(\lambda) = \frac{4n_{eff}(\lambda)W_{MMI}^2(\lambda)}{3\lambda} \quad (2.13)$$

As indicated in the equation, the beat length of an MMI depends on the wavelength through three different factors:

1. the effective multimode width W_{MMI}
2. the wavelength dependent effective mode index (n_{eff})
3. the wavelength λ .

Resulting from these three different factors, the beat or imaging length changes with wavelength [65]. This defocusing effect can lead to a decrease in the MMI performance. As an option, from (2.13), it is possible to increase the MMI wavelength tolerance by decreasing drastically the width of the multimode region (W_{MMI}). However, too narrow W_{MMI} would reduce the number of modes propagated in the MMI. This results in a lower image definition due to poorer multimode interference. A valid alternative to reduce the MMI wavelength

dependence is to increase the tapered [66] access waveguide widths (W_{io}), to reduce the amount of light lost due to the defocusing effect. Beam propagation mode (BPM) simulations revealed that increasing the width of the input and output waveguides, the insertion loss of the MMI as function of wavelength decreases (see Figure 2.10 b). For a wavelength of 1270 nm, the insertion loss of the MMI decreases from -1.2 dB for a $W_{io} = 2 \mu\text{m}$, to -0.7 dB for a $W_{io} = 3.1 \mu\text{m}$, for the same multimode section width of $12 \mu\text{m}$. In the meanwhile, the overall splitting ratio imbalance between the two different ports of the MMI remains below 0.15 dB for W_{io} between 2.7 and $3.1 \mu\text{m}$ (see Figure 2.10 a). Moreover, the input and output corners of the MMI have been designed with a corner angle of 53° (see Figure 2.9). This leads to the reduction of any spurious reflection, which can be detrimental for the laser operation [67]. As shown in Figure 2.9, the MMI coupler consists of three regions: the input where single mode waveguides adiabatically tapered to W_{io} (region 1), is followed by a wide multimode waveguide where the interference between different guided mode occurs (region 2). The output region consists of adiabatic tapers which shrinks the waveguide back to the standard deep etched ridge width of $1.5 \mu\text{m}$ (region 3). Different MMI couplers with various W_{MMI} (10 – $13 \mu\text{m}$) and different shallow and deep W_{io} (1.9 – $3.7 \mu\text{m}$), are realized and tested to identify the optimum geometrical configuration for broadband wavelength response.

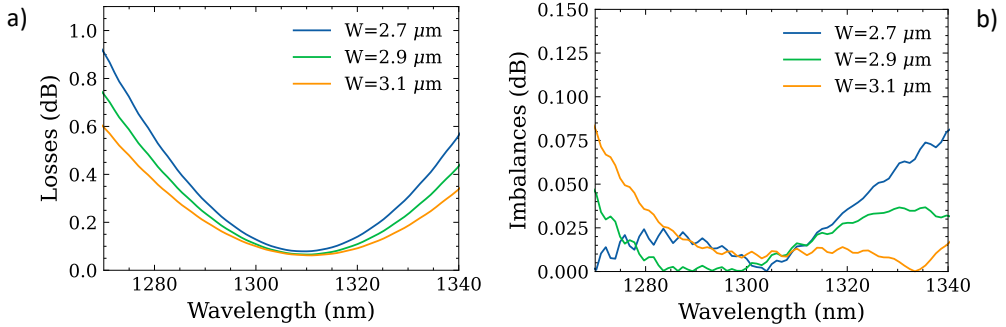


Figure 2.10 Optical simulations of the splitting Imbalances (a) and the insertion loss (b) for an MMI width of $12 \mu\text{m}$ and different deep etched access waveguide widths (W_{io}).

2.4.3.2 MEASUREMENTS AND ANALYSIS

The measurements and the analysis of the different MMI combinations are performed to extract the splitting imbalances (IMB) and the insertion loss (IL). The results follow from the analysis of transmission measurement over 100 different devices. To reduce the reflection from the interface between the InP waveguide and the single mode lensed fiber, an anti-reflection coating layer is applied to the chip's facets. During the measurements the MMI is defined as a 2×2 S-matrix of a 4-port reciprocal device with no reflections. For every device we can store the measurement referring to the device port numbers. As an example, the measurements with input port x and output port y can be referred as $P_{yx} = S_{yx}^2$. For a 2×2

MMI the measurements can be referred as P_{31}, P_{41}, P_{32} and P_{42} . In this way we can obtain the splitting imbalance (IMB) and the insertion loss (IL) of the device as:

$$IMB = \frac{S_{bar}}{S_{cross}} \quad (2.14)$$

$$IL = S_{bar} + S_{cross} \quad (2.15)$$

where $S_{bar} = S_{31}^2 = S_{42}^2$ and $S_{cross} = S_{32}^2 = S_{41}^2$. This analysis assumes that the ports of the MMIs are identical and lossless. Unfortunately, within the same device waveguides can have different transmissions due to their fabrication tolerances and different amounts of sidewall roughness. During the measurements, every MMI port transmission is normalized with the transmission power through a straight waveguide (P_{ref}). In this way, the power measured with input port x and output port y will result to be:

$$P'_{yx} = \frac{P_{yx}}{P_{ref}} = \eta_x S_{yx}^2 \eta_y \quad (2.16)$$

where η_x and η_y are used to express any excess loss of input and output ports. We end up with four different formulas as function of four different port combinations. The four different measurements are then used to evaluate six different variables ($\eta_1, \eta_2, \eta_3, \eta_4, S_{bar}, S_{cross}$). To solve the problem, it is necessary to constrain one of the inputs and one of the outputs to be lossless. This allows to obtain four different cases (CASE A-D in Table) and four possible IMB and IL for a single device. Only one case will be valid since we assume that $0 < \eta_i \leq 1$.

The transmission measurements are performed when a tunable laser (Santec TSL-550) is swept over the whole frequency range, from 1260 nm to 1360 nm, with a wavelength step of 10 pm. At the input, a polarization maintaining fiber is used to ensure the propagation of the TE polarized light only. The output optical power is measured by a photodetector that is electronically synchronized with the laser. Automated alignment routines and motorized 3-axis stages both at the input and at the output are used to optimize the coupling between optical fibers and the waveguides. This enables one to measure all devices automatically and with a reproducible and accurate fiber to waveguide coupling [68]. Transmission from straight waveguides on the same chip are used as reference for optical losses in the analysis of the MMI performance. Small reflections in the waveguide transmission can lead to ± 0.03 dB oscillations on the analyzed signals. Four different transmission measurements are performed on a single MMI device to analyze all the different splitting combinations from the different ports of the 2x2 3-dB coupler as explained above.

The imbalance and the losses are firstly evaluated from the average powers along the wavelength range between 1260 and 1360 nm. Some trends can be evaluated as function of the different etching levels of the input and output waveguides to the multimode region. Figure 2.11 shows the increase of the average splitting imbalance with the W_{io} of the shallow etched input waveguide for a fixed $W_{MMI} = 13 \mu m$. This dramatic IMB increase can be

explained by the optical coupling between the two input ports before entering the multimode region. This creates different interference conditions in the MMI structure and different splitting ratios. This feature is a direct consequence of the etching depth. In shallow etched waveguides, the waveguiding layer remains completely unetched, leading to poorer lateral confinement to the optical modes. This leads to a higher mode coupling between adjacent waveguides when they are close. The wider the input waveguides the stronger this effect, increasing the IMB of the MMI. This problem is hampering the use of wider W_{io} in the 2x2 MMI, resulting in a strong wavelength dependence of the MMI performance with shallow etched input waveguides.

Table 2.3 Complete List of all the four possible cases to calculate the IMB and IL. The η coefficients account for extra losses of the MMI structure with respect to the reference waveguide on the same chip. The matrix element for the cross and the bar state are the ones used in the calculation of the imbalances and the insertion loss.

	CASE A	CASE B	CASE C	CASE D
η_1	1	1	$\sqrt{\frac{P'_{41}P'_{31}}{P'_{32}P'_{42}}}$	$\sqrt{\frac{P'_{41}P'_{31}}{P'_{32}P'_{42}}}$
η_2	$\sqrt{\frac{P'_{42}P'_{32}}{P'_{31}P'_{41}}}$	$\sqrt{\frac{P'_{42}P'_{32}}{P'_{31}P'_{41}}}$	1	1
η_3	1	$\sqrt{\frac{P'_{32}P'_{31}}{P'_{41}P'_{42}}}$	1	$\sqrt{\frac{P'_{32}P'_{31}}{P'_{41}P'_{42}}}$
η_4	$\sqrt{\frac{P'_{42}P'_{41}}{P'_{31}P'_{32}}}$	1	$\sqrt{\frac{P'_{42}P'_{41}}{P'_{31}P'_{32}}}$	1
S_{bar}^2	P'_{31}	$\sqrt{\frac{P'_{31}P'_{41}P'_{42}}{P'_{32}}}$	$\sqrt{\frac{P'_{31}P'_{32}P'_{42}}{P'_{41}}}$	P'_{42}
S_{cross}^2	$\sqrt{\frac{P'_{31}P'_{32}P'_{41}}{P'_{42}}}$	P'_{41}	P'_{32}	$\sqrt{\frac{P'_{32}P'_{41}P'_{42}}{P'_{31}}}$

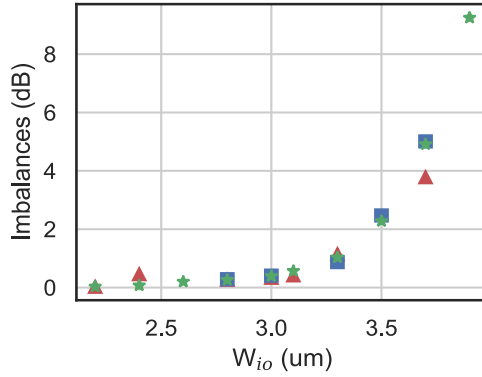


Figure 2.11 Imbalances (a) for an MMI ($W=13\ \mu\text{m}$), with Shallow etched input and output waveguides with different ridge widths.

On the other hand, deep etched waveguides present a completely etched waveguiding layer which leads to a stronger lateral mode confinement. For this reason, wider W_{io} do not negatively influence the splitting ratio. It is possible then to obtain MMI couplers with reduced insertion loss and less sensitive to the wavelength. The trend predicted from the beam propagation mode optical simulations is in this case confirmed by the experimental measurements. Figure 2.12 a) and b) reveal the wavelength-dependent imbalance and insertion loss for a multimode section width of $W_{MMI} = 12\ \mu\text{m}$, for two different W_{io} . The optical simulation results that were used to design and fabricate the MMI are also visible in the graphs (dashed lines). A reduction in imbalance and losses is visible increasing W_{io} for a fixed W_{MMI} . The measurements of MMI couplers with deeply etched access waveguides with $W_{io}=3\ \mu\text{m}$ reveal a response with $<1\ \text{dB}$ loss and $<0.12\ \text{dB}$ splitting imbalance over the 1260-1360 nm wavelength range. We presented the design, fabrication, and demonstration of the first multimode interference 3dB coupler on InP for 1300 nm light splitting with a minimized wavelength dependence.

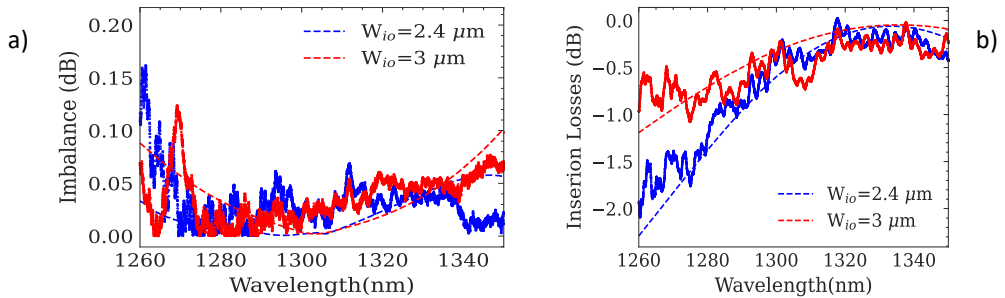


Figure 2.12: Measured (dotted) and theoretical (dashed line) imbalance and insertion loss as function of wavelength for two different input waveguide widths [69].

2.4.4 MULTIMODE INTERFERENCE REFLECTOR

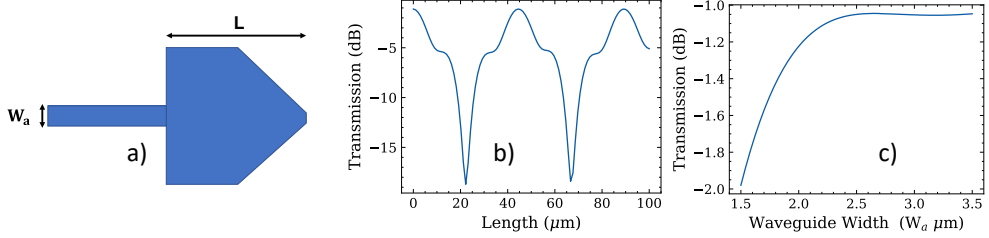


Figure 2.13: Schematics (a), analytical simulations of the reflected power (b), and (c) of the reflection power losses of the 1-port multi-mode interference reflector (MIR) with width $W=6$ μm , as function of multimode region length L and input waveguide width W_a

Multi-mode interference reflectors (MIR) are designed to reflect all or part of the input light, acting as an on-chip mirrors [70]. Their use as broadband reflective elements is helpful to create FP or ring resonator-based laser avoiding the use of cleaved facets of the semiconductor, distributed Bragg reflectors [71] or loop mirrors [72]. MIRs presents several advantages with respect to the other options for on chip mirrors such as the ones mentioned above. A MIR is quite compact, has a high fabrication tolerance and presents a broadband response.

In this sub-section the design and the characterization of 1-port MIRs are presented. The design of the mirror is like the design of a 1x1 MMI device. The length is halved to obtain a full imaging at the input since it corresponds to the beating length L_π . The presence of a triangular tip at the end of the MIR geometry, is realized by creating a 45° angle at the end of the MIR. This tip is aimed to obtain the full reflection of the light that enters in the MIR. However, the rounding of the tip during the fabrication processing induces some insertion losses for a MIR. For this purpose, during in the MIR simulations we added a 1 dB of insertion loss to the analytical simulation results, as experimentally evidenced on a MIR on average [70]. The simulation results suggest that the highest reflected power is achieved when the MIR length is 44.5 μm or a multiple of that for a MIR width of 6 μm (Figure 2.13 b). Thus, this length was selected for the design of the 1-port MIR. Figure 2.13 c) shows the simulated MIR optical insertion loss as a function of the input waveguide width (W_a). The results show that when W_a is greater than 2.2 μm , the insertion losses are below 1.1 dB. Further increasing the width of the waveguide does not result in any significant improvement. Moreover, a longer adiabatic taper is required to couple the input to the deep etched standard waveguide width of 1.5 μm , leading to a bigger MIR total footprint. The characterization of MIR with $W=6$ μm , $L = 44.5$ μm and $W_a = 2.2$ μm , is performed to measure the reflections and losses of such components.

The technique used to measure such devices is the optical frequency domain reflectometry (OFDR), which is the one used to measure the group index dispersion. From the transmission of a FP interferometer built out of a MIR, it is possible to obtain the reflectivity R as:

$$R = \frac{\frac{1}{G}(\sqrt{r}-1)}{\sqrt{r}+1} \quad (2.17)$$

Where $G = e^{-\alpha L}$ and r is the contrast ratio between the on resonance and the off-resonance power of the FP cavity. Sweeping the tunable laser wavelength, it is possible to obtain the contrast ratio as function of wavelength and calculate the R . The losses of the MIR are assumed as the difference with respect to a 100% of light back reflected. The experimental setup used is depicted in Figure 2.4, but the interferometric structure inside the device under test (DUT) is different than the linear FP cavity given by the chip's facets. In a Michelson interferometer configuration (Figure 2.14 a), the reflection from the MIR interferes with the reflection of the end facet of the chip. Figure 2.14 b) shows the power reflections. It is possible to see the fast fringes coming from the MIR reflections, due to their path length difference of 2 mm. However, some additional slow modulation is present. This modulation can be due to some small spurious reflections inside the 2x2 MMI, or between the left-hand side facet and the fiber tip. The MIR reflectivity varies due to this slow modulation. Figure 2.14 c) shows the calculated reflectivity from the analysis of the interference fringes. To extract the MIR reflectivity and insertion loss, it is needed to include the MMI insertion losses (1 dB) and the propagation loss through the passive waveguide (3 dB/cm). A reflectivity of around 0.78% has been calculated which leads to insertion loss of 1.27 ± 0.36 dB for a MIR. These values agree with what has been predicted during the design and the simulation phase, leading to an amount of insertion loss slightly bigger than 1 dB in the overall 1300 nm wavelength range.

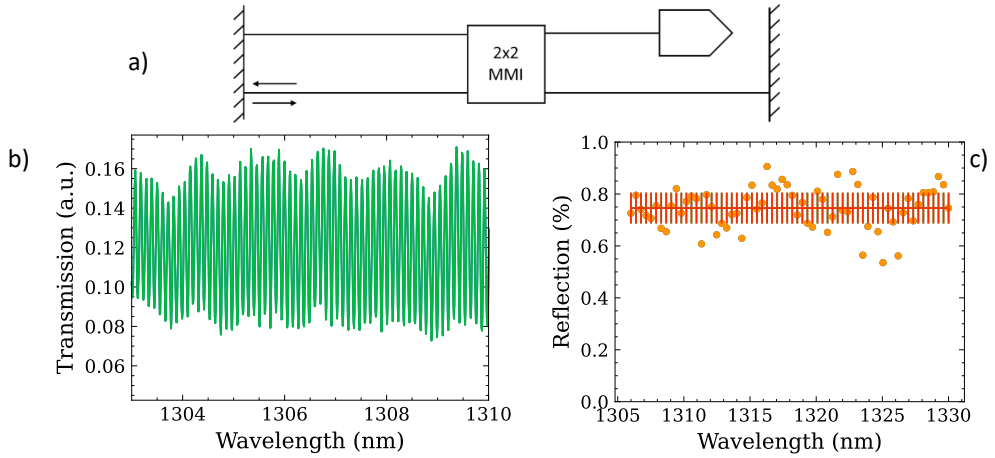


Figure 2.14 a) Schematics of the Michelson Interferometer on chip. it has been reproduced from [70]. b) Reflection over the MIR port as function of the input laser wavelength. c) Estimation of the reflection from the contrast ratio of Fig. 16 b). Such reflections will induce a 1.27 ± 0.36 dB of insertion loss inside the MIR.

2.5 CONCLUSIONS

In this chapter, the design considerations, the simulation results, and the basic performance of several passive components in InP at 1300 nm have been described and summarized. The considerations made during the 1300 nm layer stack design phase have been tested with the measurements of several passive building blocks (BBs). Straight (2 dB/cm) and curved waveguides (0.1 dB/90°) propagation loss for a 100 μm curvature radius have been evaluated. The group index dispersion has also been measured to be smaller than 3% of its value within 70 nm between 1270 and 1340 nm. Insertion loss for MMIs and MIRs have been measured (1 dB), engineering their geometries to ensure flat wavelength response. In the following chapter, the realization of an InP based 1300 nm active layer stack to be integrated with a butt-joint coupling scheme with the passive waveguide will be presented. The aim is to maximize the overlap between these two different layer stack and in this way to reduce the spurious reflections at the active/passive interface. The combination of such passive and active BBs leads to the design of more complex circuits with several functionality, such as lasers or optical switches. By making this 1300 nm passive technology generic, multiple applications can be targeted at the same time and several different photonic integrated circuits can be realized. With the help of SMART Photonics, a component library is made available to the users of this 1300 nm monolithic platform where a designer can use such functional passive building blocks to design complex photonic circuits. The study of the wavelength characteristics of such components is crucial during the development of laser circuit simulators which will be described in the following chapters. The propagation

CHAPTER 2

constants and the insertion loss of the components are fundamental characteristics to address the building blocks with as transfer matrices (T-matrices), inside a steady state laser simulator.

3.1300 NM AMPLIFIER COMPATIBLE WITH AN INP MONOLITHIC ACTIVE/PASSIVE INTEGRATION TECHNOLOGY

In monolithic photonic integrated circuits (PICs), an optimized active/passive integration is needed to provide efficient coupling and low amount of interface reflections between amplifiers and passive components. A 1300 nm semiconductor optical amplifier (SOA) on InP substrate and optimized for butt-joint coupling with the passive components described in Chapter 1 is investigated. Material performances were assessed from measurements of broad area lasers. Room temperature operation reveals 1.2 W single facet output power with threshold current around 100 A/cm² per well. Characteristic temperatures of $T_0=75$ K and $T_1=294$ K were obtained. A compact model description of the SOA, suitable for the design of PICs and rate equation analysis, was applied to parametrize the unsaturated gain measurements. Current injection efficiency of 0.65, transparency carrier density of $0.57 \cdot 10^{18}$ cm⁻³, and free carrier absorption losses up to 15 cm⁻¹ were extracted from fitting the data. The model is verified with measurements of optical gain saturation. A modal gain of 15 dB for a 600 μ m long narrow ridge SOA leads to output saturation power higher than 30 mW at 7 kA/cm². This building block contributes to the development of an InP monolithic integration technology in the 1300 nm range, which can enable the use of photonic integrated circuits in many kinds of applications.

3.1 INTRODUCTION

Semiconductor optical amplifiers (SOAs) are a critical component for numerous kinds of photonic integrated circuits (PICs). SOAs are the basis for the development of light sources such as light emitting diodes [73] and tunable laser systems [74]. These components are also used to increase output power and to maintain sufficiently high signal levels as the signal propagates throughout many optical components [75]. Extensive studies have been performed on 1300 nm SOA [76], [77], since commercial fibers present near zero dispersion in this spectral region [78]. SOAs in this wavelength range are widely used in data centers since high bit rates can be achieved without the need of dispersion compensation. O-band SOAs can then be included in more complex systems such as dual wavelength division

multiplexers for high bit rate and capacity transmission systems [79]. 1300 nm SOA are commonly used for their low temperature dependence [80] and high efficiency [81], [82]. Different InP SOA were designed as discrete components and optimized for low polarization dependence [77], high operating temperatures [83] and wide gain bandwidth [84].

The introduction of active-passive integration technologies creates the opportunity of using 1300 nm SOAs in more complex circuits such as extended cavity widely tunable laser systems [85] or optical switches [86]. Both hybrid integration [87] and hetero-epitaxial growth [88] technologies at 1300 nm have been developed to integrate SOA with passive waveguide on Si substrates. Threshold current as low as 450 A/cm^2 has been reported for quantum dot laser grown on Si (001) [89]. Narrow width ridge SOA revealed gain as high as 45 cm^{-1} and on chip optical power of 25 dBm at room temperature [90]. However, these “III-V on Si” approaches face the challenge of the creation of some bonding defects at the interface between the different materials [91]. The development of a new quantum well-based InP SOA in the 1300 nm wavelength regime is a crucial step in the development of a 1300 nm monolithic integration platform on InP. This 1300 nm platform on InP is designed to have minimized active passive interface reflections and optical loss [41] with the same integration process. Moreover, the introduction of a 1300 nm InP generic integration platform, based on the already existing one [31], brings the benefit of being able to use a standard set of building blocks to create various complex circuits and optical functionalities. The platform will allow fast and cost-effective prototyping in the 1300 nm band, giving the opportunity to serve many different applications. In this chapter, we present the design and the characterization of a new InGaAsP/InP SOA that will be integrated with a low propagation loss passive waveguide via a butt-joint integration scheme with a single regrowth step, to further develop a new monolithic generic integration technology at 1300 nm. The analysis of the fundamental properties of active devices such as temperature and current dependent emissions reveals that the requirement of being compatible with an active/passive butt-joint integration technology does not lead to any major downgrades in the optical performance of the active layer stack chosen. First, the active layer stack design is presented together with the considerations made to meet the requirement of compatibility with an active passive monolithic integration technology on InP at 1300 nm. Then, the overall material quality is addressed through measurements of broad area Fabry-Perot lasers and the analysis of parameters which highlight the device performance. The description of a compact model for a narrow ridge width optical amplifier is presented and verified through experimental data of gain spectra and optical gain saturation. This SOA model description can be then use in the design and simulation of photonic integrated circuits fabricated on a 1300 nm generic InP integration technology.

3.2 ACTIVE LAYER STACK DESIGN

To develop a generic platform for photonic integration at 1300 nm, active devices such as lasers and amplifiers need to be integrated with passive components such as propagation waveguides, splitters, and reflectors. One of the main challenges of the integration technology is to engineer the active and the passive components so that the best coupling and the lowest amount of interface reflections are ensured. In this work, an InGaAsP-based optical amplifier with photoluminescence (PL) targeted at 1310 nm, is designed, and simulated with the commercial simulator HAROLD licensed from Photon Design. In active-passive integration it is important to minimize reflections from the butt-joint active passive area transitions to at least -50dB. The reflections can lead to poor side mode suppression inside tunable laser systems or instabilities when causing feedback to the laser. Therefore, an important requirement during the design of the active layer stack was to match the fundamental mode effective index of the SOA to that of the InP passive waveguide designed for 1300 nm light propagation. The change in the effective index with respect to the passive waveguide has been limited to $\Delta n_{eff} < 5 \cdot 10^{-3}$ and the mode overlap has been kept to >99% in simulations, to keep reflections at the active passive interfaces <50 dB. This requirement is targeted as follows. Firstly, the total active region thickness is chosen to be 400 nm and both the separate confinement heterostructure and the barriers present a quaternary energy bandgap (Q-value) of 1.1 μm , to match the passive waveguide dimensions and composition. Inside the active region four InGaAsP based quantum wells are embedded. A low number of wells does not lead to very uneven carrier densities in the different wells and in this way, the material gain can be reasonably approximated as four times the gain arising from a single quantum well. Moreover, low number of quantum well is a good compromise between having sufficient high small signal gain and a limited modal effective index mismatch with a passive waveguide with the same geometry. The second aspect concerns the design of the quantum wells in which compressive strain is used, and the design of the barrier layers which are needed to compensate the strain. It turns out the compressive strain level that can be used in the quantum wells is limited by the requirement to maintain a sufficiently low effective index mismatch with the passive waveguide. The introduction of compressive strain leads to an increase in the transverse electric (TE) gain which is beneficial for achieving lower threshold current levels [92], [93] in lasers and improves high temperature performance [80].

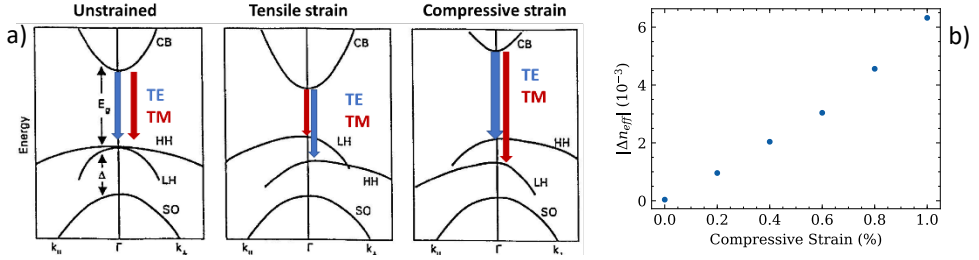


Figure 3.1: a) Explanation of the degeneracy removal of the energy bands due to the application of the strain. The picture is taken from [94]. b) Difference in the effective index of an active shallow etched ridge waveguide with respect of a passive waveguide with ridge width $W=2\ \mu\text{m}$ as function of compressive strain applied to the quantum wells. The effective index of a $2\text{-}\mu\text{m}$ -wide passive shallow etched waveguide is 3.26.

The compressive strain removes the degeneracy in the valence sub-bands at the Γ point. The splitting of the heavy and light holes degenerate bands decreases significantly the Auger recombination and the intervalence band absorption [82], increasing the TE polarized light optical emission of the SOA (Figure 3.1 a). On the other hand, the introduction of strain induces a change in the refractive index of the well, and a change in the Q-value of the barriers from the targeted value ($Q=1.1\mu\text{m}$) which can lead to an effective index change in the active region of the waveguide and a smaller mode overlap with the passive waveguide. The fundamental TE mode effective index of a straight waveguide with same single mode ridge width of $2\ \mu\text{m}$ is equal to 3.26. The introduction of strain increases the effective index change with respect to a passive waveguide with the same ridge width. This is depicted in Figure 3.1 b) which shows the calculated modal refractive index as function of different compressive strain in a four quantum well structure using HAROLD software licensed from Photon Design.

Therefore, it is possible to imply that the more the strain is the higher the effective index difference is which can increasingly deteriorate the mode overlap at the active passive interface. This will introduce higher coupling loss and strong reflections at the butt-joint interfaces which can compromise the performance of integrated laser systems. Moreover, simulations show that strain values higher than 0.8% do not noticeably increase the TE material gain. A smaller than 10% increase in the material gain occurs when the amount of compressive strain in the quantum wells is doubled in the simulation from 0.7% to 1.4%. For this reason, we limit the amount of compressive strain at 0.8%, to ensure the butt-joint reflection is smaller than -50 dB inside our extended cavity tunable laser systems. At room temperature, isothermal one-dimensional simulations of the optimized layer stack design, shown schematically in Figure 3.2 a), reveal a threshold current of 300 A/cm^2 and minimum internal loss of the amplifier as low as 4 cm^{-1} . A material gain for TE polarized light of 2200 cm^{-1} is predicted at 5 kA/cm^2 . Finite difference element mode simulations calculate an optical

confinement of around 4% inside the active region for a shallow etched 2 μm wide ridge waveguide. This value is approximately 1% for every quantum well present inside the SOA.

3.3 DEVICE FABRICATION

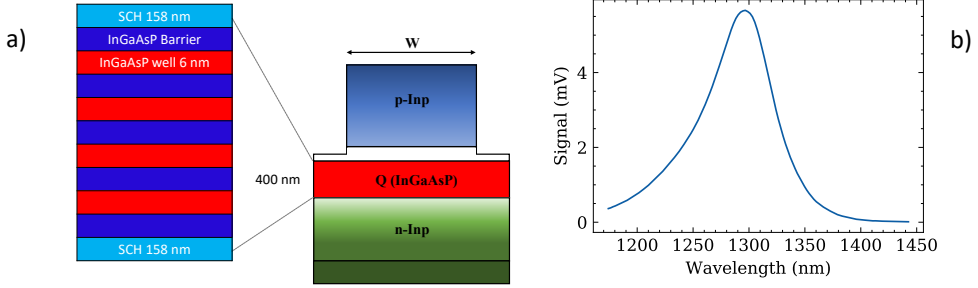


Figure 3.2: a) Cross-sectional view of the fabricated SOA active layer stack. b) Measured photoluminescence spectrum of the wafer with this layer stack design.

The InP based fully active test structures were fabricated by Smart Photonics following a well-established processing technique [31]. The layers are grown on top of a heavily n-doped ($5 \cdot 10^{18} \text{ cm}^{-3}$) InP (100) substrate. The active layers are grown using Metal Organic Chemical Vapor Deposition (MOCVD). After the epitaxial growth the waveguides are defined to obtain the shallow waveguide cross section as depicted in Figure 3.2 a). The waveguides are all etched using an Inductively Coupled Plasma (ICP) dry etch process. The different waveguide ridge widths are defined in a single lithography step to ensure good alignment and fabrication reproducibility. After etching, the waveguides are passivated and planarized through the deposition of a Polyimide layer. The contact and a metallization layer are applied on top and on bottom of the structure to allow current conduction. The photoluminescence signal of the four quantum well amplifier is measured using a technique described in [95]. The results, shown in Figure 3.2 b), reveal that the maximum emission targeted at 1300 nm during the design phase, was achieved during the fabrication. A photoluminescence peak at 1290 nm with a 70 nm wide 3-dB bandwidth is reported in the graph measured for a 3-inch wafer.

3.4 ACTIVE LAYER STACK QUALITY EVALUATION

To establish the quality of the layer stack used in the fabrication of optical amplifier first the following, generally published, parameters are determined. These results to be the transparency current density J_0 , the internal quantum efficiency η_i and the amplifier internal loss α_i . It is possible to extract these parameters, using a well-established method as published in [96], [97], from the analysis of the output optical power as function of the injected current density. Since these parameters are generally independent on the geometry

of the device, they could provide the gain material performance of a SOA at any operating temperature. These parameters can be used to compare the designed device with 1300 nm amplifiers available in literature and with the simulated device predictions. To identify the temperature dependence of these SOA parameters, it is needed to evaluate the characteristic temperatures T_0 and T_1 . Those can be obtained from the analysis of the light intensity (L-I) curves at different operating temperatures as described by [98]. Higher characteristic temperatures T_0 and T_1 reflect lower temperature dependence and this indicates that the amplifiers performance deteriorates less at high operating temperatures. In this work we are investigating the temperature dependence of the broad area lasers from length-independent parameters. Thus, the analysis to extract T_0 and T_1 is applied to the transparency current density J_{tr} and the internal quantum efficiency η_i and not to the threshold current J_{th} and the external quantum differential efficiency η_d as often reported in literature.

For this purpose, a set of Fabry-Perot lasers with uncoated cleaved facets and different lengths between 500 and 1200 μm , and ridge widths between 1 and 100 μm have been fabricated. The cleaved facets leave reflections of approximately 30% at both ends. These lasers have been characterized over a range of operating temperatures between 20 and 80°C. Broad area stripes, with width of 100 μm , lasers are tested. On devices with this wide ridge area, it is possible to approximate that all the current that is going through the metallic contact is reaching the active region inside the waveguide. In this way, it is possible to neglect the effect of the ridge and measure the material property only. Pulse current measurements, with pulse width of 10 μs and 1% duty cycle (DC), are performed to avoid thermal effect inside the lasers. Measurements with shorter pulse duration reveal constant output power at current density higher than 3 kA/cm^2 . We believe this is since very short pulses do not leave sufficient time to the current to heat the active region. The pulsed operation L-I measurements of the broad area Fabry-Perot cavity lasers reveal high output powers and high temperature of operation. In Figure 3.3 a), averaged L-I curves are shown for measurements over 10 identical devices on the same wafer for 1300 μm long amplifiers with broad area stripes. The current is swept between 0 and 5 A reaching up to 4.8 kA/cm^2 in density. We can notice the output power from a single facet of 1200 μm long devices at room temperature ($T=20^\circ\text{C}$) goes up to 1.25 W, with standard deviation of around 30 mW. Threshold current density as low as 350 A/cm^2 has been measured at room temperature. The wall plug efficiency (WPE) exhibits a drop from 20% to 8% from room temperature to 80°C, as depicted in Figure 3.3 b). In Figure 3.3 a) it is possible to notice that the relative change in the threshold current and in the slope of the L-I curve is constant between 20 and 60°C. The increase in the threshold current is estimated around 10 $\text{mA}/^\circ\text{C}$, ranging from 400 up to 800 mA between 20 and 60°C. When the substrate is set to 80°C, it is possible to note that the stimulated emission slope is slightly lower. This can be due to the lower performance of the

active material at high heat sink temperature. Moreover, at 80°C we can notice some roll-over at around 4 A of injected current, which is due to the relatively long pulse duration of 10 μ s that accumulates heat in the active region.

By measuring the threshold current density of broad area lasers of different cavity lengths, it is possible to evaluate the material without the effect of the ridge, as function of laser temperature of operation.

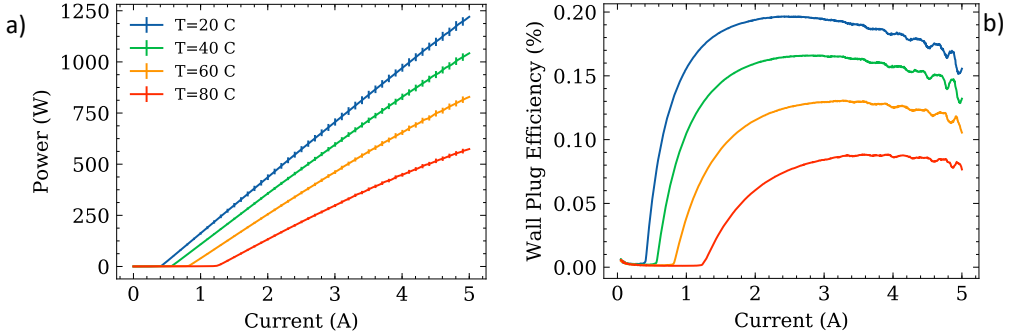


Figure 3.3: a) Total output power per facet and b) wall plug efficiency, for a 1200 μ m long and 100 μ m wide Fabry-Perot laser at different heat sink operating temperatures. The output power a) is averaged over 10 different measurements on identical devices, and we can observe the standard deviation (error bars). The measurements were performed using pulsed current with 10 μ s of pulse duration and 1% duty cycle.

In Figure 3.4 a) the fit of the threshold current density as function of the inverse cavity length is shown. The transparency current density is calculated as the intercept of the fit line which corresponds to an infinitely long cavity with zero reflections at the mirrors, as stated in [96]. The uncertainty over the J_{tr} parameter is given by the covariance matrix of the fit and can vary between 10% and 20%, depending on the temperature as can be seen in Figure 3.4 b). The observed temperature dependency of the transparency current density shows a mean value of 140 A/cm² for 20°C and around 310 A/cm² for 80°C. These values, as shown in Figure 3.4 b) are in accordance with those reported in [98] for III-V broad area lasers. At higher temperature, the statistical carrier distribution across the states of the quantum wells becomes broader and this results in an increase in the transparency current density due to the reduction in the differential gain [98]. From the exponential fit with equation from [98], the characteristic temperature T_0 is calculated to be 75 K, which is comparable to what found in literature for Al-based lasers on InP substrate [99].

From the stimulated emission part of the curve above threshold, it is possible to obtain the external differential efficiency η_d . The slope is determined from the threshold current up to 1 A above threshold to avoid the range where thermal roll-over occurs. Figure 3.5 a) shows η_d as a function of the laser cavity length. By fitting the data to the equation in [96], the internal efficiency η_i and the scattering loss α_i are extracted. The amplifier losses are the

sum of the free carrier absorption loss [83] and carrier independent loss mechanism such as photon scattering [100] or intervalence band absorption [82]. It is noticeable how at higher temperature the measurement of η_d is less accurate than the threshold current density value since the slope of the L-I curves is evaluated at higher current levels.

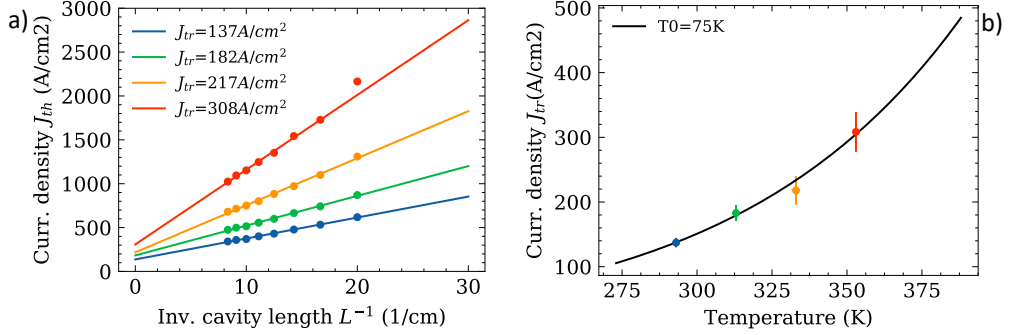


Figure 3.4: a) Threshold current density as function of inverse cavity length and linear fit to obtain J_{tr} for different heat sink T . b) J_{tr} as function of temperature and measurement fit to obtain the characteristic temperature $T_0 = 75\text{ K}$ of broad area lasers. Legend same as 3a).

This leads to higher contribution of thermal effects due to the active region heating. In this way we have a much higher uncertainty over the estimation of η_i and α_i at higher operating temperatures. Internal losses are increasing with the temperature due to the increase intervalence band absorption in the quantum wells [101].

They are determined to vary from 5 cm^{-1} to 16 cm^{-1} in a temperature range of 20 to 80 °C. The fitted internal efficiency as function of temperature shown in Figure 3.5 b) allows to calculate the characteristic temperature $T_1 = 294\text{ K}$, which identifies the temperature dependence of the stimulated emission slope. T_1 lies in the reported ‘state of the art’ characteristic temperatures around 300 K for 1300 nm broad area lasers on InP substrate [99]. The measurements of Fabry-Perot broad area lasers demonstrate that the device performance agree with the one-dimensional simulations.

The amplifier internal losses were observed to be lower than 5 cm^{-1} at room temperature, as was expected from the simulation. Furthermore, the thermal dependence of the extracted parameters is very close to what is presented in literature for InP based amplifiers. This suggests that the requirement of being compatible for an active-passive butt-joint integration does not lead to major compromises in the active material performance at low carrier density values. The broad area laser analysis has been performed to establish whether the designed active material meets the desired specification. In the following section a detailed analysis of the performance of single mode ridge width SOA, will be addressed together with a compact model to include into laser circuits. Before that the study of J_{tr} as function of the amplifier ridge width, shows how the ridge width affects the SOA parameters.

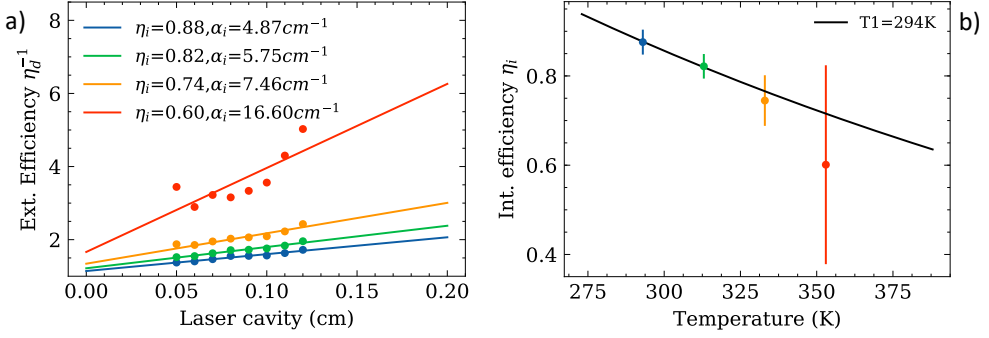


Figure 3.5: a) External differential quantum efficiency as function of laser cavity length (dots) and fit (line) from [96] to extract the injection efficiency η_i and the internal loss α_i at different heat sink Temperature. b) η_i as function of heat sink temperature and measurement fit to obtain the characteristic temperature $T_1 = 294\text{K}$ of broad area lasers. Legend in 3a) is also valid here.

3.5 COMPACT MODEL FOR SOA GAIN

The amplifier structure has been developed to be used in a monolithic InP active-passive integration platform. The goal is to obtain a compact model description of the SOA suitable for the design of photonic integrated circuits. This is done by measuring the modal gain $g(f, N)$ of the SOA and analyzing the results using a simplified analytical theory. This theory leads to a set of parameters that can be used to describe the modal gain and a relation between the current density and a scaled carrier density. An analysis is then applied using the rate equation for the carrier density to obtain a value for the scaling factor of the scaled carrier density. The scaling of the carrier density can then be checked by the study of the material transparency and the gain saturation of the SOA. The measurements are compared with the predicted behavior using the determined parameters from the unsaturated gain analysis. It is possible to obtain important parameters for single mode ridge amplifiers by fitting them to the measurement results. The parameters representative of the SOA performance are the transparency carrier density N_0 , the passive loss α , the injection efficiency η_i and the input saturation power $P_{in,sat}$.

3.5.1 UNSATURATED MODAL GAIN

There are several ways the unsaturated modal gain of the optical amplifier can be measured. There are methods based on the contrast ratio of each cavity mode of the amplified spontaneous emission (ASE) [102]. However, this method is sensitive to the measurement equipment resolution due to the small light intensity at the minimum. This has led researchers to study multiple electrodes methods. In this work, the unsaturated gain spectra of the 1300 nm SOA are determined by the analysis of the ASE spectra from different

amplifier lengths as described by Thompson et al. and Pustakhod et al. [103],[104]. The measurements of different amplifier stripes with different lengths are needed to reduce the effect of the coupling loss to the chip facets which are hard to control due to variations in the fabrication of optical waveguides. Averaging measurements with different SOA lengths and different coupling loss it is possible to link the gain and the ASE power density at each wavelength λ . To measure the unsaturated modal gain a series of shallowly etched ridge waveguide optical amplifiers, divided into two sections of different lengths, were processed on a single $2 \times 2.5 \text{ mm}^2$ chip with anti-reflection (AR) coated facets. The two sections are addressed by different electrodes and are separated by $20 \text{ }\mu\text{m}$ isolation sections where $1 \text{ }\mu\text{m}$ of highest p doped top-cladding InP is removed to ensure electrical isolation between the two sections. One section is reversely biased to prevent any optical feedback into the amplifier to avoid unwanted laser operations, while the other one is being driven by current. The amplified spontaneous emission (ASE) spectra are detected using an optical spectrum analyzer connected to a lensed single mode output fiber. Automated alignment routines are performed to optimize the chip to fiber coupling as described in [68]. Multiple spectra from different amplifier lengths between 50 and $600 \text{ }\mu\text{m}$ are measured. Measuring ASE from multiple SOA lengths allows us to identify some experimental points that deviate more than 10% from the overall averaged values. Those measurements were discarded in the fit, if they derived from fabrication imperfections. In Figure 3.6 the modal gain spectra for current densities between 1 and 8 kA/cm^2 , are shown. A 3-dB gain bandwidth greater than 80 nm is observed for a current density of $J=5 \text{ kA/cm}^2$, together with a gain peak of 60 cm^{-1} . A wide gain bandwidth is of high importance in the realization of widely tunable laser systems, since the gain spectrum at the laser threshold is the ultimate limitation to the tuning range. The modal gain from a quantum well based SOA can be described using only few parameters using analytical approximations for the material gain. The model used here is derived by Balle [105]. Under the assumptions of parabolic energy bands and temperature equal to zero, the material gain spectrum $g_m(f, N)$ as function of carrier density N inside the amplifier can be written as [105]:

$$g_m(f, N) = \chi \left[\text{atan} \left(\frac{f - f_0(N)}{\gamma} \right) - 2 \text{atan} \left(\frac{f - f_0(N)}{\gamma} - \frac{N}{N_0} \right) - \frac{\pi}{2} \right] \quad (3.1)$$

where $f_0(N)$ is the bandgap frequency which depends on the carrier density, γ is the homogenous line width, N_0 is the carrier density at transparency at the bandgap energy and χ is a gain scaling factor.

Hence the net modal gain g_{mod} will be:

$$g_{mod}(f, N) = \Gamma g_m(f, N) - \alpha(N) \quad (3.2)$$

where $\alpha(N)$ represents the amount of free carrier absorption losses inside the amplifier, due to the excitations of the light and heavy holes inside the valence band and Γ refers to the

gain confinement factor in the quantum wells. The fit of the parameters in equation (3.1) and (3.2)

to the experimental net modal gain spectra with, are depicted by the dashed lines in Figure 3.7 b). Figure 3.7 a), b) and c) show respectively the fitted values found for the scaled carrier density ratio $N_r = N/N_0$ as function of injection current density, the bandgap frequency shift, and the free carrier absorption losses as function of carrier density ratio.

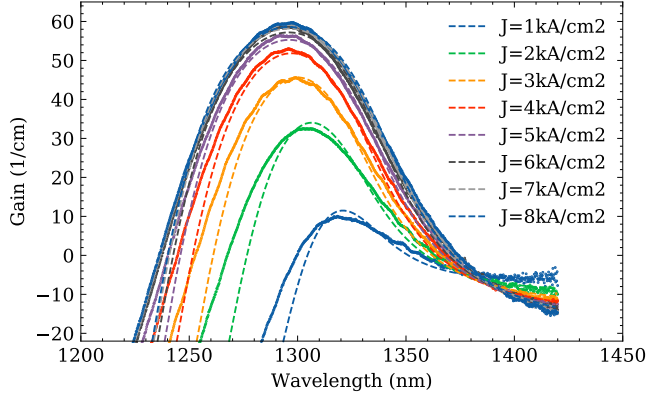


Figure 3.6: Modal gain spectra from the fit of ASE measurements (dots) and calculated from the parametrized model (dashed) for different injected current densities.

The fit is obtained for all current densities with the same value for the homogenous linewidth $\gamma = 5.0 \text{ THz}$, and a scaling factor of $\chi = 1050 \text{ cm}^{-1}$. It is interesting to note that the values of γ and χ are near identical to those determined for 1550 nm quantum well amplifiers. The confinement factor of 4% for a single mode ridge width amplifier is calculated using PicWave software from Photon Design®.

In Figure 3.7 a), the carrier density increases with the injected current density, until it reaches its maximum at approximately 4 times the transparency carrier density value N_0 . This suggests the presence of a carrier overshoot mechanisms, which arises from the fact that more injected carriers are recombining in the InP outside of the active region. In this way, the gain spectra remain constant for higher current densities. This can be improved either by increasing the number of the well in the active region, which will affect the SOA optical saturation, or by applying a graded index structure in the spatial confinement heterostructure to better confine the carriers inside the SOA active region. This can however create issues for the active passive integration reflection and mode overlap. Figure 3.7 b) depicts the bandgap frequency shift f_0 as function of the carrier density inside the amplifier. The bandgap follows a square-root or a cubic-root dependence on the carrier density ratio as suggested by Tomita et al. [106] and Kleinman et al. [107]. In Figure 3.7 c) the fitted values for the optical loss α as a function of the scaled carrier density are presented. The linear relation between the carrier density and losses indicates these are absorption losses due to the absorption of light from the holes present in the active region. The values found here are

lower than those determined in 1550 nm InP quantum well-based amplifiers [105]. This indicates the higher efficiency of 1300 nm quantum wells amplifier with respect to C and L-band InP amplifiers. Fitted polynomial functions, as shown in Figure 3.7 a) b) and c), can be used to parametrize these three single mode ridge width amplifier properties that will be used to model the SOA performance. Note that this parametrization underestimates the gain at higher energies, due to some approximations on which the model in [105] is based.

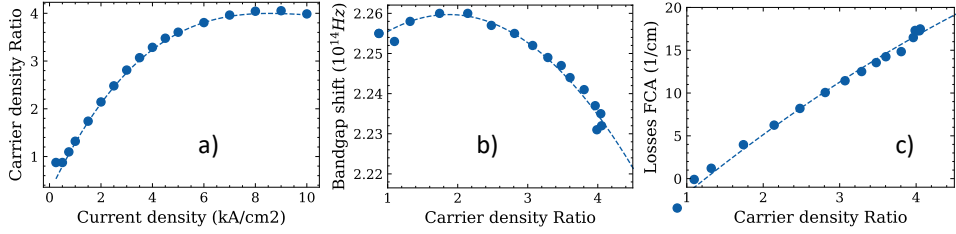


Figure 3.7: a) Carrier density ratio as function of injected current. b) Frequency bandgap shift and c) free carrier absorption losses as function of carrier density ratio. The dashed lines show polynomial parametrized fit of the dots.

3.5.2 AMPLIFIER RATE EQUATION AND CARRIER DENSITY AT TRANSPARENCY

The relation between the current density and the scaled carrier density can be analyzed further to determine a value of N_0 . For this purpose, the rate equation for the carrier density in an optical amplifier can be used.

The time evolution of the carrier density inside the active region of an optical amplifier is described by [108]:

$$\frac{dN}{dt} = -v_g g_{mat}(f, N)P + \frac{Jw\eta_i}{qS_{mode}\Gamma} - R(N) \quad (3.3)$$

Where the first right hand side term describes the carrier depletion due to stimulated emission, the second one is the pump rate, which determines the number of carriers injected in the active region and the third one refers to possible recombination mechanisms. The second right hand side term, which corresponds to the pump rate, directly depends on the current density J , the ridge width w and the injection efficiency η_i and it is inversely proportional to the optical confinement Γ times the modal area S_{mode} . For the S_{mode} parameter, which is dependent on the geometry of the structure, the effective mode size [109] was used. This was calculated to be $1.63 \mu m^2$ using a commercial mode solver MODE from Lumerical Inc®. Assuming that the photon number inside the active region is negligible during the modal gain measurements which implies there is no significant carrier loss due to ASE, it is possible to set to zero the stimulated recombination term and equation (3) becomes:

$$\frac{dN}{dt} = \frac{\eta_i J w_r}{q S_{mode}\Gamma} - AN - BN^2 - CN^3 - DN^{5.5} \quad (3.4)$$

Where the recombination processes are expressed as a polynomial function of the carrier density N . The A,B,C,D coefficients represent the probability to occur of each recombination mechanism [110], [111]. A, B, and C are extracted from [97] and [111], while D has been kept as a fitting parameter. At steady state conditions, under which the measurements were done, the carriers are at equilibrium and the rate equals zero. It is then possible to find solutions that link the carrier density inside the active region to the injected current density into the device. When we compare the solution of equation (3.4) with the carrier density ratio extracted from equation (3.1), it is possible to determine the transparency carrier density N_0 , the injection efficiency η_i and the D term that corresponds to the carrier leakage inside the amplifier due to current drift as explained in [111]. Table summarizes all the values that were used to obtain the solutions of equations (3.3) and (3.4).

Table 3.1: Coefficients in the carrier rate equation

Coefficient	Value	Units
A [97]	$1.68 \cdot 10^{-8}$	s^{-1}
B [97]	$2.6 \cdot 10^{-10}$	$cm^3 s^{-1}$
C [43]	$1.417 \cdot 10^{-28}$	$cm^6 s^{-1}$
D	$2.5 \cdot 10^{-90}$	$cm^{13.5} s^{-1}$
v_g	$0.83 \cdot 10^8$	$m s^{-1}$
S_{mode}	1.63	μm^2
Γ	0.04	-
η_i	0.65	-
N_0	$0.575 \cdot 10^{18}$	cm^{-3}

The values of $\eta_i = 0.65$ and $N_0 = 0.575 \cdot 10^{18} cm^{-3}$, are calculated through the agreement between the two curves for current densities between 1 and 7 kA/cm^2 . At higher injected current densities, the two curves start to slightly deviate from each other. The highest carrier dependence of the recombination mechanisms in equation (3.4) is referring to the leakage due to the carrier drift as explained in [31], but from the parametrization of the unsaturated gain measurements, it is evident that the carrier density is clamped at a maximum value of four times the carrier density at transparency for current densities of 7 kA/cm^2 and higher. This behavior indicates that inside the SOA, the injected carriers can easily escape from the low energy barriers and spatial confinement heterostructures (SCH). This limitation comes from a particular design choice for the active layers' epitaxial growth since the barriers were chosen to minimize reflections at the active passive butt-joint integration interfaces and not as an optimized energy barrier layer for the carriers escape.

The calculation of N_0 and η_i are verified through the measurements of material transparency and optical saturation. Measurements of the material transparency current density have

been performed by recording the change in voltage over the SOA induced by an external laser as function of current density. An external laser is on/off modulated at 300 kHz and coherent light at a particular frequency is injected into a 2 μm wide shallow etched ridge SOA. The current bias is swept over a range that includes the material transparency point and both the amplitude (mV) and the phase (degrees) of the voltage change over the amplifier are detected with the lock-in amplifier (LIA) as also described in [112]. For lower injection currents the amplifier is absorbing the external laser light, thus generating carriers, and increasing conductivity which reduces the voltage over the diode structure. While for higher currents the quantum well material starts to provide gain which reduces the carrier concentration when the light is in the SOA, the conductivity is reduced and the voltage over the SOA increases. The minimum value in the amplitude of the voltage modulation corresponds to π phase jump which means that the voltage modulation over the SOA is changing its electrical polarity. The current at which this transition occurs is described as the material transparency current at the input wavelength.

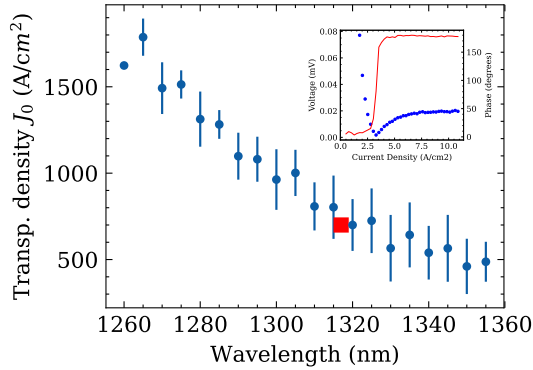


Figure 3.8: Transparency current density as function of input laser wavelength (blue). Results are obtained from measurements of three different device lengths of 300, 560, and 1100 μm . The (red) dot is the transparency current density derived from the analysis with equation (4) of the unsaturated gain parametrized model. An example of a detected signal (inset) is shown where both the amplitude (blue) and the phase (red) are detected.

Figure 3.8 shows the material transparency current density as function of the external laser wavelength. In the inset graph a measurement example is presented. Lower wavelengths present higher transparency current densities as suggested by the modal gain spectra on Figure 3.6. The red dot in Figure 3.8 is coming from the N_0 determination from the carrier density rate equation. J_0 is defined as the current density at transparency, which refers to the transparency carrier density N_0 at the bandgap frequency $f_0(N_0)$. The model predicts $J_0 = 707 \text{ A/cm}^2$ at 1317 nm, which agrees with the material transparency.

3.5.3 OPTICAL GAIN SATURATION

When light enters the SOA with photon density $P \neq 0$, we need to introduce a second equation that describes the time evolution of the photon density inside the amplifier. In an optical amplifier the rate of photons generated through stimulated recombination can be expressed as:

$$\frac{dP}{dt} = v_g(f)g_{mod}(f, N)P(t), \quad (3.5)$$

where v_g is the group velocity g_{mod} is the modal gain of equation (2) and P is the photon density at a time t . In a one-dimensional device, the signal power P in the SOA is determined from the travelling-wave equation [113] as:

$$\frac{dP}{dx} = g_{mod}P \quad (3.6)$$

Applying a fixed current and fixed input optical power at a single wavelength λ , it is possible to obtain the output photon number of an amplifier as function of injected current and length of the device. This is done by solving the system of coupled differential equations (3.3) and (3.6) at the steady state condition (i.e. $dN/dt=0$ and $dP/dt=0$), using the Runge-Kutta method [114]. Thus, it is possible to determine amplification $G = P_{out}/P_{in}$, for a particular photon frequency and injection current density. The calculated gain decreases as function of input power due to the significant increase of the carrier depletion inside the active region. This mechanism leads to the optical gain saturation of the SOA. The input saturation power is identified as the input power for which the amplifier gain drops to half of its value and it is linked to the maximum output power by Davenport [115]:

$$P_{in,sat} = \frac{P_{out,max}}{G_0 - 2} \quad (3.7)$$

where G_0 is the unsaturated linear amplification and $P_{out,max}$ is the output saturation power. It is important to state that the saturation power is dependent on current, wavelength and amplifier length. To determine the saturation input power levels and to check the prediction of the gain saturation using the measured unsaturated gain data and the extracted carrier density values, the optical saturation of a series of shallowly etched ridge waveguide optical amplifiers was measured. These were special devices where the waveguide on the chip was divided into two sections of different length. The two sections are addressed by different electrodes and are separated by 20 μm electrical isolation sections where 1 μm of top cladding highly p doped InP is removed to ensure electrical isolation between the two sections. The first section, where the laser light enters, is operated as an SOA. The second section is reversely biased to detect the light amplified by the first section. A reverse bias voltage of -1V is applied to the second section amplifier to increase the detector absorption. Since the resistance of the isolation section is lower than 1 k Ω , it becomes possible to extend the carrier detection area to the isolation section. Thus, the light absorbed in the isolation section is included in the signal measured at the detector. The

reference input power is obtained by shorting the two electrodes at the same reverse bias V_b and extracting the amplifier photocurrent with the LIA as function of input power from a modulated external laser with different attenuation settings. The opportunity to use an integrated solution for light amplification and detection can lead to the full on-chip characterization of the amplifier optical properties [116]. The devices were processed on a single $2 \times 2.5 \text{ mm}^2$ chip with anti-reflection (AR) coated facets.

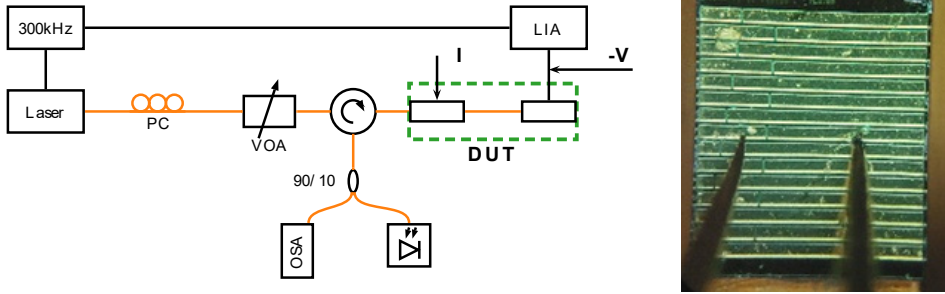


Figure 3.9: Setup schematics and microscope image of the device under test (DUT). Variable optical attenuator (VOA), lock-in amplifier (LIA) and optical spectrum analyzer (OSA).

The experimental setup used to characterize the optical amplifiers is shown in Figure 3.9. When the first section optical amplifier is driven with forward bias and no light is injected from an external source, it is possible to perform automated alignment through the maximization of the power reading from an external detector (Agilent81636B) [68] and read the current dependent ASE from an optical spectrum analyzer (OSA) (ANDO AQ6315A). When we inject an on/off modulated (300kHz) TE polarized light from a tunable laser source (Santec TSL-520) into the amplifier, the second amplifier section is used as a detector. The first section amplification is detected as function of input laser power, which is controlled through a variable optical attenuator (VOA). This is done after a polarization controller (PC), used to optimize the polarization of the input light to TE. A LIA (Stanford SR865A) is connected to the photodetector section to increase the sensitivity of the measurements and avoid any effect from the current leakage or the electrical crosstalk between the two SOA segments. In Figure 10, it is possible to see how the device under test (DUT) looks like under an optical microscope, when the two sections are probed.

The device temperature is stabilized to 20°C with a temperature-controlled copper mount. The optical gain saturation measurements are performed to verify the evaluation of the injection efficiency parameter η_i inside the optical amplifier model. The first section amplifier is biased with current densities J between 2 and 7 kA/cm^2 . The lower current density limit is chosen to ensure a current density above material transparency. The upper current density limit has been chosen as the one that ensures matching between the carrier

density obtained from the gain parametrization with equation (3.1) and the solution of the amplifier rate equation (3.4).

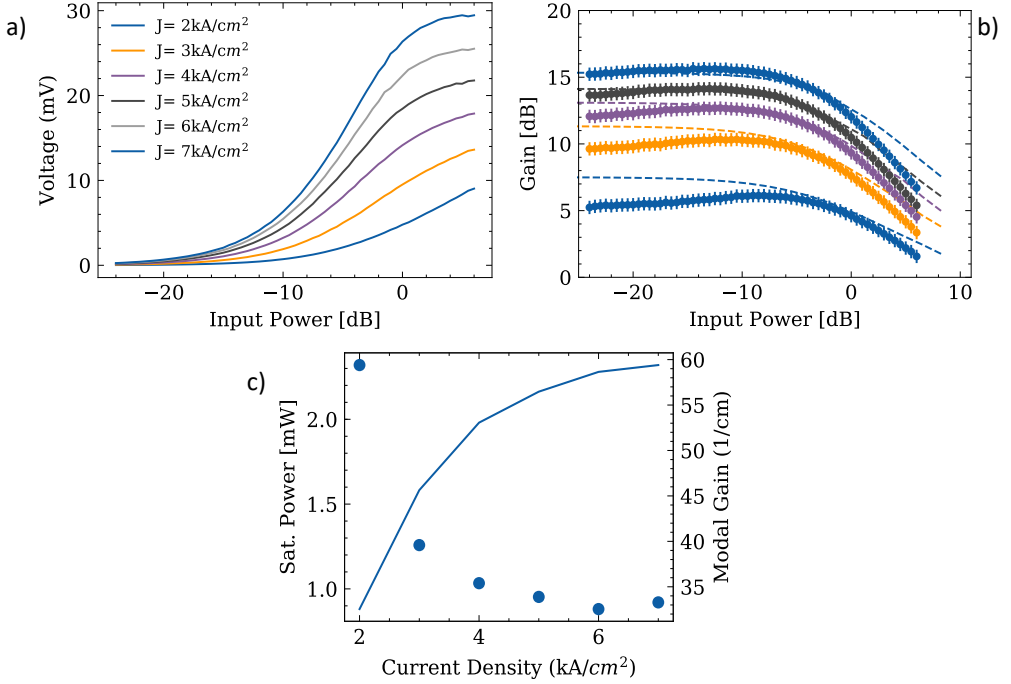


Figure 3.10: a) Measured signal on the detector at different current density b) Measured gain saturation (dotted) and predictions based on the parametrized model (dashed). c) saturation input power and small signal gain as function of current density. Measurements performed on a $600 \mu\text{m}$ long SOA with laser lighth at 1300 nm . Legend in a) is valid in all plots.

Figure 3.10 a) shows an example of a measurement results for a $600 \mu\text{m}$ long SOA for different currents as function of external laser power at a particular wavelength $\lambda = 1300 \text{ nm}$. The detector voltage as function of input power clearly shows for high optical power the presence of gain saturation. Figure 3.10 b) shows the amplifier gain as function of the laser power in a logarithmic plot. The dashed line represents the optical gain saturation predicted by the model. The error bars of $\pm 0.5 \text{ dB}$ in the measurement points represent the error due to the uncertainty on the coupling loss due to variations in the fiber to waveguide alignment, which can be between 3 and 4 dB. The deviation of the measurement curves with the model prediction are an artifact due to the dynamic range of the LIA. Since the LIA input range is maximized to the highest value obtained at high input photon density, at low input power its sensitivity is decreased and in this way it underestimates the ratio of the output power with respect to input power. This also explains why before saturation, the small signal gain increases instead of slightly decreasing with the increase in optical power. This artifact

is more prominent at low injected current densities since the optical amplification is lower. From the gain curves is possible to extract the $P_{in,sat}$ from [115] as in Figure 3.10 c). It is identified as the input power when the gain decreases to half of its unsaturated value G_0 , i.e when any increase in the optical input power does not produce any increase in the output power. From Figure 3.10 c), it is visible how the input saturation power decreases with current density. It varies between 2 and 0.5 mW for a 600 μm long SOA. This lead to approximately 30 mW maximum output power at 1300 nm for a 600 μm long SOA with 7 kA/cm^2 injected current.

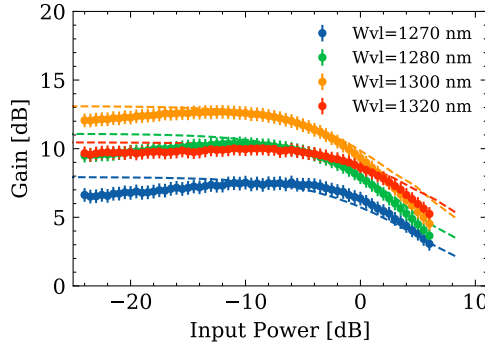


Figure 3.11: Optical gain saturation measurements (dotted) and model (dashed) at 4 kA/cm^2 for different input laser wavelengths.

In Figure 3.11 the gain saturation curves are plotted as function of wavelength for the same device length and an injected current of 4 kA/cm^2 . It is shown how the highest gain is at the center of the gain spectrum for that particular current. Moreover, for wavelength closer to the modal gain maximum the gain is higher but at the same time $P_{in,sat}$ is lower, keeping an approximately constant maximum optical power with wavelength for the same current density. The optical saturation predicted by the model (dashed line) can be used to predict the amplifier gain behavior as function of input wavelength as well as for different lengths.

3.6 CONCLUSIONS

In this chapter, we have designed, fabricated, and characterized a new InGaAsP/InP semiconductor optical amplifier that is optimize for a monolithic active/passive integration technology aty 1300 nm. This SOA is compatible with a butt-joint integration scheme with low active/passive interface reflections, and it shows high performance in terms of efficiency ($\eta_i=0.82$) and temperature dependence compared to what available in literature. Fabry-Perot laser measurements reveal output power levels as high as 2.5 W and characteristic temperature $T_0 = 75$ K. A self-consistent compact model for the description of ridge width amplifier has been described and validated. The analysis indicates a reduced free carrier

absorption loss compared to 1550 nm InP based SOAs, a gain bandwidth as broad as 80 nm, limited by the carrier density, and a 30 mW output saturation power from single mode ridge waveguide amplifier 600 μm long. Therefore, this building block contributes to the development of an InP monolithic integration technology in the 1300 nm range, which can be utilized for the development of photonic integrated circuits for data communication, biomedical imaging and other applications.

4. TWO-SECTION PASSIVELY MODE-LOCKED LASER AS A TEST FOR AMPLIFICATION AND ABSORPTION PARAMETERS OF A QUANTUM WELL BASED INP OPTICAL AMPLIFIER AT 1300 NM

The semiconductor optical amplifier (SOA) described in the previous chapter is tested in a monolithic passively mode locked laser operating at 1300 nm. The different laser dynamics are investigated in detail and the gain and absorption parametrization of the SOA as used in a laser simulator is described. Simulation outcomes are compared with the characterization results of a passively mode-locked two-section laser that was realized using a fully active quantum well layer stack. The different laser dynamic regimes are identified by recording light intensity characteristics for a range of operating conditions with 50 GHz bandwidth in real time as well as the high frequency electrical spectra from a photodetector. Passive mode-locking has been achieved with a 20.4 GHz repetition rate with a 0.32% detuning by increasing the current, where a 0.25% detuning was predicted by the parametrized model. The stepped heterodyne technique has been used to measure the output pulse duration. A FWHM of 1.0 ps has been recorded after propagating for 110 m in standard single mode fiber. The phase spectrum with a maximum of 2.5 radians variation within the 6 nm frequency comb has been obtained. This value agrees with the simulation output, which models the amplification and the absorption out of this two-section laser. Q-switched mode-locking behavior is observed from the time traces. The measurements of the q-switching dynamics reveal a stepped behavior in the relaxation oscillations as function of current injected into the semiconductor optical amplifier, with the presence of an exotic dynamical system with different periodicities at the transition currents, that cannot be predicted by the model. The fit of the relaxation oscillation with the Q-switching self-pulsation frequencies, reveals a differential gain that is in-line with the parameter used in the simulations.

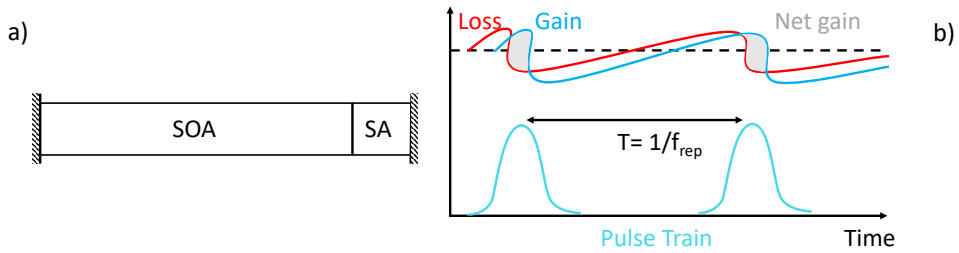


Figure 4.1 a) Schematics of two section laser characterized in this Chapter. Highlighted are the semiconductor optical amplifier (SOA), the saturable absorber (SA) and the reflective facet which create the Fabry-Perot laser cavity. b) Sketch of the pulse train in time, together with the gain and loss dynamics of a passively Mode-Locked laser with slow gain and absorption saturation. Figure b) has been taken from [117].

4.1 INTRODUCTION

A parametrized compact model to describe the SOA amplification and absorption is essential for analyzing the steady state and the dynamical laser behavior [105]. On the basis of such compact models it is possible to develop simulation tools for more complex laser systems that can be realized on active/passive integration platforms such as those on InP [29], [118]. A compact model of a new quantum well based amplifier at 1300 nm suitable for an active passive butt joint integration technology has been reported in the previous chapter. This model has now been used to describe a two-section passively mode-locked laser and in that way to test the parameters of the compact model. Mode-locked (ML) semiconductor lasers in the form of photonic integrated circuits (PIC) are best suited to accomplish compact devices for distance metrology sensing [119] and high-resolution optical spectroscopy [120], high-precision frequency clocks [121], and optical communication systems [122]. Passively ML lasers exploiting a saturable absorber are used to obtain ultra-short pulses due to the loss modulation inside the saturable absorber. Therefore, passive ML lasers are more simple and compact compared to actively driven laser devices [123]. The passively ML laser operates using a SOA and a saturable absorber (SA) inside a linear Fabry-Perot cavity (as shown in Figure 4.1 a). Figure 4.1 b) illustrates the operating principle: the optical pulse travels back and forth, saturating the absorber to create a steeper rising slope and higher peak pulse gain. At the end of the pulse, the SOA becomes saturated, causing a net loss. While the recovery times for the two saturations are longer than the pulse duration, combining their effects creates a short net gain window. Overall, this setup enables the passively ML laser to generate ultra-short optical pulses.

Monolithically integrated InP quantum well (QW) based ML lasers can be realized in a generic integration platform at 1300 nm. Such a platform offers the opportunity of decoupling the laser cavity length from the length of the amplifier. The passive section can e.g. be used to

include an intra-cavity tunable bandpass filter to adjust the central wavelength of the frequency comb as needed [85]. To be able to make designs of such lasers, parameters as presented here are needed.

The 1300 nm laser simulator model used here uses the parametrization of the gain and the absorption of the optical amplifier when it is under forward or reverse bias conditions. The devices studied are all-active two-section lasers with a 2 mm long Fabry-Perot cavity. A two-section passive mode-locked laser is chosen since its operation is highly sensitive to change in the amplification or absorption parameters. The characterization results obtained from the fully active stack InP based passively mode-locked lasers are compared with the simulation results to draw conclusions on their validity.

This chapter 4 is structured as follows. First the parametrization of the material and modal gain and loss as used in the travelling wave-based simulation is presented. Then the laser design and the components' characterization are presented including a more detailed investigation of the different laser dynamics regimes. This is followed by characterization results. Laser output time traces have been recorded as a function of injection current with a 50 GHz bandwidth photodetector and oscilloscope system to identify the different dynamic regimes. A stepped heterodyne method [124] is used to retrieve the optical pulse and the relative spectral phase of the optical modes inside the frequency comb when the laser is in a pure mode-locked operating regime. The pulse width is then compared with the output of the laser simulator [125]. The effect of the SOA current on the repetition rate in mode-locked operation is discussed and compared with the simulation prediction. The Q-switching dynamics of the laser are analyzed to extract the differential gain of the SOA which is compared to the one derived from the gain parametrization performed earlier. We end with drawing conclusions on the validity of the model and the parameters used.

4.2 SIMULATOR MODEL AND PARAMETERS

In this section the SOA gain and absorption parametrization are described and the conversion to parameters that can be used in the travelling wave simulator to predict the behavior of the laser dynamics [126]. Similarly as other travelling wave models like [127] and the FreeTWM software [128], this model in the simulator involves the use of rate equations for the photon densities in both directions, phases and carrier densities [129]. To solve the set of equations, the laser is meshed into several segments of equal length and multiple of wavelength. The differential rate equations include a description of non-linear effects such as non-linear gain compression due to two-photon absorption, carrier heating and spectral hole burning [130] as well as carrier concentration dependent optical and carrier losses including drift related losses. The SA is described as a short SOA that is reversely biased [131] with the same equations as the amplifier but without carrier injection and with a different

cross section σ [129] and carrier lifetime. Differently from [128], the simulator does not have a bandwidth limitation on the exchange of energy between the photon and the carrier inside the active region. However, a bandwidth limitation was introduced in the circuit by using an intra-cavity first order finite impulse response filter with a delay of one 63 fs time step. This makes that the transmission of the filter is zero at the edges of the full spectral range of the simulation. This model is also useful to describe the behavior of extended cavity lasers based on monolithic active passive integration because it includes two photon and free carrier absorption effects inside passive elements, together with non-linear refractive index. This model has been already used for the simulations of InP monolithically integrated continuous wave CW widely tunable lasers [118], as well as for extended cavity Fourier domain mode-locked laser [132]. The InP passive waveguides are modeled as lossy elements, while electro-refractive modulators can be included in the circuit and the phase change is arbitrarily applied from the user. It is worth noticing that the waveguide dispersion is not included in this simulator. In this work, each mesh segment is chosen to be 14 times the central wavelength $\lambda_0 = 1310 \text{ nm}$, which is equal to $5 \mu\text{m}$ in optical path length, and a discretization time $T_{seg} = 63 \text{ fs}$ is derived from a group index of $n_g = 3.62$. The other parameters for the simulator can be found in [133].

4.2.1 SOA GAIN PARAMETRIZATION

The SOA material gain is modeled with a well-known logarithmic material gain dependence approximation on the carrier density, as described in [130][97].

$$g_{mat}(\lambda) = \sigma(\lambda) \cdot N_0(\lambda) \cdot \ln\left(\frac{N + N_\epsilon}{N_0(\lambda)}\right) \quad (4.1)$$

where $\sigma(\lambda)$ is the wavelength dependent gain cross section and N and $N_0(\lambda)$ represent the carrier density and the carrier density at transparency at wavelength λ respectively. N_ϵ is included in the material gain to ensure that the logarithm is always a finite number and limits the negative gain values. The value of the parameters $\sigma(\lambda)$ and $N_0(\lambda)$ are determined by fitting equation (4.1) to a gain parametrization using a formula as described in [105] and repeated here:

$$g_m(f, N) = \chi \left[\text{atan}\left(\frac{f - f_0(N)}{\gamma}\right) - 2 \text{atan}\left(\frac{f - f_0(N)}{\gamma} - \frac{N}{N_{tr}}\right) - \frac{\pi}{2} \right] \quad (4.2)$$

where χ is the material susceptibility, γ the homogeneous linewidth, f_0 the bandgap frequency, and N_{tr} represents the transparency carrier density at the bandgap frequency. This expression has been experimentally validated on the active layer stack used in this laser design with the modal gain measurement described in [53]. The wavelength independent parameters in this model γ , χ and N_0 have been determined from fitting to modal gain measurements as well as the relation between the bandgap frequency f_0 and the carrier density N , as explained in detail in [39]. The modal gain is then calculated including a parametrization of the amplifier free carrier losses. These losses are modeled as a polynomial

quadratic function of the carrier density N , with coefficients that have been fitted from the measurements of the modal gain of section 3.5. The free carrier absorption losses are modeled for current densities between 1 and 8 kA/cm², where the parametrized relation between the current and the carrier density is verified from the solution of the carrier rate equation at steady state. From the agreement between equations (4.1) and (4.2), it is possible to extract the material transparency carrier density N_0 and the gain cross section σ at each wavelength. An example is presented in Figure 4.2. The curves from equation (4.1) (green curve) fits well to the curve from (4.2) (blue curve) for the wavelength at 1310 nm (the center of the O-band) for values of σ and N_0 listed in Table . The transparency carrier density N_0 and the gain cross section σ are then retrieved for the SOA, as function of the wavelength.

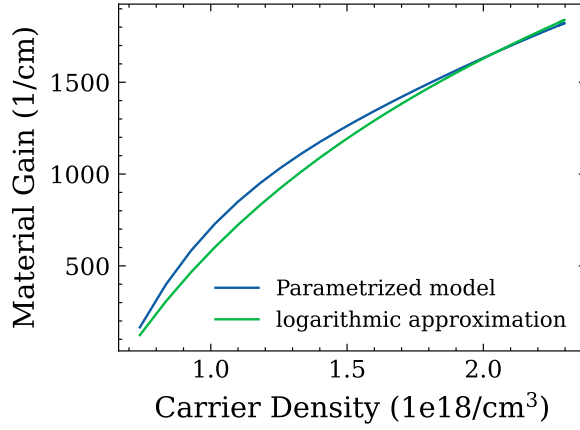


Figure 4.2 Material gain in cm⁻¹ derived from the parametrized gain as described in [53] (blue curve) and the logarithmic gain approximation fitted to it (green curve) with equation (1) and the parameters of Table 1. as function of carrier density at $\lambda = 1310$ nm.

4.2.2 ABSORPTION CHARACTERIZATION AND PARAMETRIZATION

The material absorption in the SA is modeled using the same logarithmic expression of (4.1) but with different parameters which are valid for carrier densities under transparency ($N < N_0$). To determine the value for the absorption cross section σ , the modal absorption spectra were measured for different reverse bias conditions. For this purpose, absorption measurements were performed on a two-section device that has both end facets anti-reflection (AR) coated which prevents the device from lasing. The 1.8 mm long SOA section was forward biased. The spectrum and intensity of the amplified spontaneous emission (ASE) from the SOA was measured from the facet at the SA section, after it had passed through a 100 μ m long SA. The SA is reversely biased, and the voltage is varied from -1 to -6 V. The ASE spectrum and intensity of the SOA is also measured directly from the other facet, and it is

assumed to be the same as that of the input light to the SA. Assuming the ASE attenuation of the absorber follows the exponential decay with the length, the absorption per unit length (1/cm) was calculated as function of wavelength. The results are presented in Figure 4.3 a) (solid lines). To align the measurement curves to the simulation results, an experimental coupling mismatch of 1 dB has been assumed at 1380 nm between the two different edges of the chip. The measured curves, however are quite different from simulations results for TE and TM material absorption (dashed lines) performed with the commercial software package HAROLD from Photon Design [134]. This is due to the fact that the ASE generated by the SOA does contain both TE and TM polarizations with a varying relative intensity over whole wavelength range [135]. The difference between the TE and TM simulated material absorption slopes is due to the compressive strain applied to the InP QWs, which removes the degeneracy of the heavy and light holes valence bands at the Γ point [113]. For this reason, the TE polarized light emission and absorption is the dominant mechanism between 1280 and 1340 nm. At λ lower than 1270 nm the TM absorption start to impact the overall measured absorption spectra. The absorption between 1280 and 1260 nm is affected by the mixing of TE/TM states in the ASE of the SOA. This leads to a dip in the measured absorption as mentioned in [135]. At this purpose in Figure 4.3 b) we repeated the measurements with a control on the polarization, selecting only TE modes. The absorption has been measured from the analysis of the photocurrent generated in the absorber (I_{abs}) and the SOA (I_{SOA}) when light from a tunable laser source is injected into the device. The reverse bias voltage has been kept constant to avoid any leaking current between the two sections. The absorption is calculated making two different assumptions. First that the light to current conversion efficiency is equal in the two sections. Second that the light is completely absorbed in the long SOA section. In this way the absorption becomes:

$$\alpha(\lambda) = \frac{1}{L_{abs}} \ln \left(\frac{\left(\frac{I_{SOA} - I_{abs}}{I_{SOA} + I_{abs}} + 1 \right)}{2} \right) \quad (4.3)$$

Where L_{abs} is the length of the absorber and the photocurrents are wavelength dependent. The TE polarization is ensured using a polarization maintaining lensed single mode fiber at the input facet of the die. The measured absorption spectra of Figure 4.3 b) have been smothered through a moving average method. The confidence interval represents the reflections at the fiber tip, which happened to be relatively higher for lower absorptions (1330-1360 nm). It is worth to notice that the model and the experimental results share the same trend, however, a discrepancy in the absolute values is present at lower wavelengths. We can address this to the uncertainties on the length, contact resistance, or to variations in the ridge waveguide width between different samples. We can further notice that an increase in the reverse bias voltage leads to a higher absorption at lower energies, as consequence of the quantum confined Stark effect [97]. It leads to a blue shift in the

absorption spectrum. Another remark is that the simulations have been carried out for an SOA bias of 0 V, due to the limitations of the Harold base model from Photon Design®. During the measurements, the use of a small reverse bias is needed to obtain an appreciable photocurrent. Anyway, the voltage dependent blue shift due to the reverse bias driven carrier depletion in the quantum wells is a rather small effect in such measurements. Therefore, the absorption of -1 V is used in this work for the absorber parametrization.

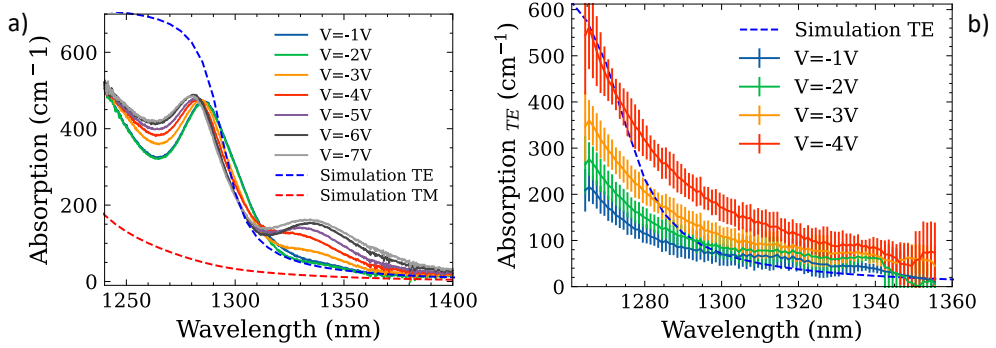


Figure 4.3 a) Absorption spectra measured for a 100 μm long device on chip, applying a current density of 1.5 kA/cm² to the SOA section, together with the simulated absorption for different light polarizations. A 1 dB coupling mismatch between the two facets has been accounted for. b) Absorption retrieved from the analysis of the photocurrent on the absorber for different voltages TE laser light polarization. The errorbar is resulting from the confidence interval. It reproduces the reflection between the fiber and the chip's facet.

From the measurements of the absorption at -1 V (blue curve in Figure 4.3 a) and b), it is possible to retrieve the necessary information on the SA. The material absorption is derived from the measured modal absorption (1/cm) using the following equation:

$$\alpha_{mat}(\lambda) = \frac{\alpha(\lambda)}{\Gamma} + Losses \quad (4.4)$$

where α is the measured absorption, Γ is the optical confinement in the QWs equal to 4% and the *Losses* term refers to the free carrier absorption within the active region. The free carrier absorption losses are modeled with the same parabolic approximation as function of the carrier density that is used for the SOA, but in the case of the SA the carrier lifetimes are much shorter, due to the reverse bias applied on the SA structure. The absorption cross section σ_{abs} is calculated from the fit with equation (4.1), where the transparency carrier density N_0 and the measured absorption at carrier density values of N_e ($1 \cdot 10^{22} \text{ m}^{-3}$) are considered, The N_e is used since it is considered to be the estimated number of carriers in the non-intentionally doped InP layers present in the active layer stack. From the fit of equation (4.1), it is possible to retrieve the absorption cross section σ_{abs} at different wavelengths λ . Table reports the gain and absorption cross section and the material transparency carrier density for three different wavelengths of $\lambda = 1270, 1310$ and

1344 nm. These three wavelengths have been reported in the table below since are the edges and the center of the gain bandwidth for this quantum well based 1300 nm amplifier.

Table 4.1 Material transparency carrier density N_0 and gain and absorption cross sections for different amplification/absorption wavelengths. These values have been obtained from the -1 V reverse bias curve of the measurements of Figure 4.3.

Wavelength	N_0 (m^{-3})	$\sigma_{\text{gain}}(\text{m}^2)$	$\sigma_{\text{abs}}(\text{m}^2)$
1270 nm	$1.26 \cdot 10^{24}$	$2.32 \cdot 10^{-19}$	$7.10 \cdot 10^{-19}$
1310 nm	$6.82 \cdot 10^{23}$	$2.22 \cdot 10^{-19}$	$3.85 \cdot 10^{-19}$
1344 nm	$6.48 \cdot 10^{23}$	$1.18 \cdot 10^{-19}$	$1.52 \cdot 10^{-19}$

4.3 DEVICE DESIGN AND FABRICATION

For this study, a two-section Fabry-Perot linear cavity laser has been designed and fabricated with a total length of 2 mm, which leads to 20.4 GHz spaced modes.

The ridge waveguides are $2 \mu\text{m}$ wide and are etched until 100 nm above the active waveguide. This leads to a rib-loaded waveguide, fundamental transversal mode with a $1.66 \mu\text{m}^2$ effective mode surface, which presents a $4\% \pm 0.1\%$ optical confinement for the four quantum wells. The electrical isolation between the two sections is created by removing $1 \mu\text{m}$ of highly doped p-InP from the top layers, to increase the electrical resistance between the two pin junctions. Two evaporated Ti/PT/Au metal pads contact the two sections ending into two separate electrodes. Au-plating increases the contact thickness to ensure uniform current injection and enhanced heat dissipation. The plating layer is not present at the FP cavity edges to avoid any metal folding over the waveguide's facet after the cleaving process. The two-section device is operated by forward biasing the longer gain section, which serves as semiconductor optical amplifier (SOA), and by reversely biasing the shorter section, which acts as saturable absorber (SA). The absorber section is $100 \mu\text{m}$ long in this laser design and a $20 \mu\text{m}$ long electrical isolation section is present between the SOA and the SA. The length of the isolation section has been chosen to ensure the lowest amount of carrier leakage, as their calculated diffusion length is $< 5 \mu\text{m}$. The resistance of the isolation section has been derived from the measurements of the photocurrent on both the electrodes as function of the reverse bias voltage applied in the range 0 to -20 V. The resistance varies with voltage between 6 and 40 k Ω .

4.4 LASER DEVICE CHARACTERIZATION

The light intensity characteristics and the laser dynamics are studied as function of the SOA current and the SA reverse bias voltage. The experimental setup schematics used to characterize the 2 mm laser is shown in Figure 4.4. A lensed fiber is used to collect the output

of the two-section laser and an optical isolator is included in the setup to avoid any back reflected light into the laser, which can affect its performance. The laser output has been investigated with an optical spectrum analyzer (AndoAQ6317C) with 1 GHz (10 pm) resolution and using a 50 GHz electrical spectrum analyzer ESA with a 50 GHz bandwidth photodiode (U2t XPDV 1020R 50 GHz photo detector). The different laser dynamics regimes such as Q-switching or passive Mode-Locking have been experimentally identified from measurements of the RF power. The results for the different regimes are each presented separately in the following subsections.

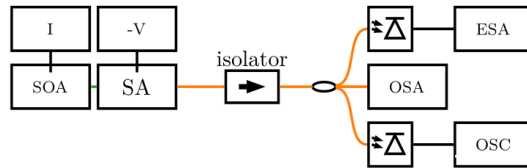


Figure 4.4: Experimental Setup used to test the two-section laser

The steady state light intensity curves of the laser have been measured as function of the reverse bias applied to the 100 μm long SA between 0 and -2.5 V. The measured threshold current varies from 45 to 50 mA, for the SA voltage varying between 0 and -2.5V. This agrees with the threshold current in the simulations (50 mA), which is an indication of the correctness of the parameters for the gain/absorption cross section and the free carrier passive loss parametrization. For a -1V of reverse bias on the SA the measured threshold current is equal to 48 mA, as depicted in Figure 4.5 a). The total power measured with an optical power meter (Agilent 81632A) reached 1.50 mW in fiber for an injection current of 150 mA on the SOA and -1 V reverse bias on the SA.

The step like behavior one can observe in the optical power as function of injected current indicates changes in the dynamics of the laser output. This is investigated further in the next sections of the paper. Figure 4.5 b) shows the RF spectrum of the photodetector measuring the laser output as recorded with the ESA, as a function of injected current on the SOA for a fixed reverse bias voltage of -1V on the SA. From this graph we can notice different behaviors of the laser dynamics and investigate some specific features. The threshold of the laser is at 50 mA, and as soon as it emits, the device behaves in a Q-switching regime. Observed are undamped relaxation oscillations up to 4 GHz. Compared to continuous-wave lasers without absorbers, the relaxation oscillation in the passively mode-locked lasers are damped more weakly, as the semiconductor SA introduces lower loss for higher pulse energies [136]. These lead to Q-switching dynamics, where the laser shows a periodicity in its output at frequencies that are lower than its repetition rate. Between 60 and 70 mA, the laser enters the Q-switched mode locking regime, as evidenced by the presence of the peak in the RF signal at 20.4 GHz, which is the mode separation frequency of the laser. Increasing further the injected

current above 70 mA, the laser returns to show Q-switching dynamics but with a repetition rate that is doubled with respect to the laser frequency at 50 mA. When the injected current is higher than 90 mA, the laser starts to operate in the mode-locked regime, with small modulation at around 500 MHz, which fades with increasing injection current. At higher current the only output frequency component corresponds to the longitudinal mode spacing of the Fabry Perot laser cavity of 20.4 GHz.

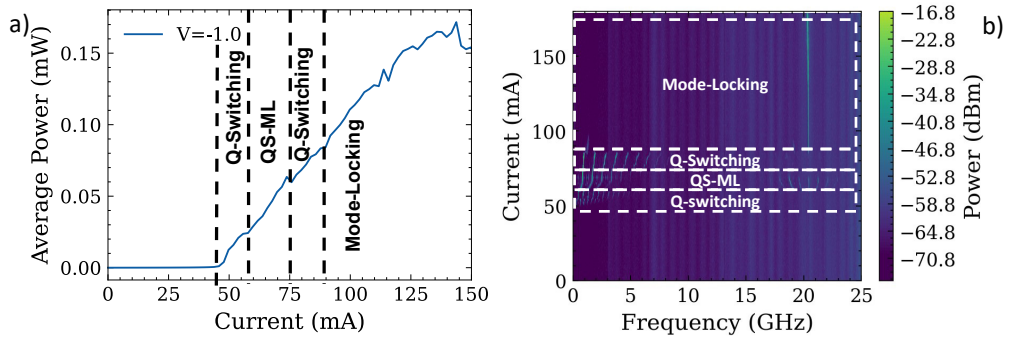


Figure 4.5: a) Light intensity curve of the laser at -1.0 V (reverse bias) voltage on the SA. b) RF power between 0 and 25 GHz as function of different SOA currents for a reverse bias voltage of -1V applied to the SA.

To characterize the behavior of optical pulses output from the device, firstly we measured them in a 50 GHz photodiode coupled to a 50 GHz bandwidth real time oscilloscope (Lecroy-LabMaster 10 Zi-A) which was in another lab room. For this reason, the pulses from the laser had to propagate over 110 m into a standard single mode optical fiber before reaching the oscilloscope. The time traces of the laser have been taken as a function of the current injected into the SOA. Figure 4.6 a) shows two different time traces, for 120 mA and 70 mA of injected current in the SOA.

The different dynamics that can be identified in Figure 4.5 b) are clearly visible from the output time traces read on the real time oscilloscope. The blue curve of Figure 4.6 a) for 120 mA shows a train of pulses which are separated from each other by 49 ps, corresponding to the 20.4 GHz repetition rate of the laser cavity. The green curve was recorded at 70 mA. This is an operating with a very particular dynamic. In this region there is a signal around 1 GHz and its harmonics as well as a weaker signal around 500 MHz and its harmonics. From the green curve in Figure 4.6 a) one can see a train of short pulses at 20 GHz that are amplitude modulated at 1 GHz with higher and lower maxima every other maximum, which is therefor a variation around 500 MHz. The difference in operating modes is also confirmed by the optical spectra, depicted in Figure 4.6 b). The spectrum recorded at 120 mA shows a for a mode locked semiconductor laser typical skewed gaussian-like shape.

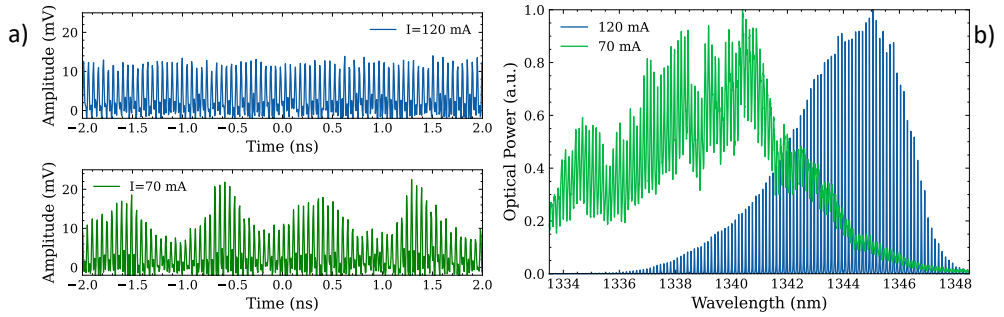


Figure 4.6: a) Time traces of the output laser pulse for Q-switching and mode-locking operating conditions recorded with a 50 GHz bandwidth real time oscilloscope with sampling rate of 160 GSa/s after the propagation over 110 m of single mode fiber. (b) Operating spectra for the two different currents to highlight the difference between the modal phase relations in the two cases. The optical spectrum analyzer was used at 10 pm (1 GHz) resolution.

The green spectrum recorded at 70 mA instead shows that the laser operates mostly at shorter wavelengths. The higher background of the green curve is determined by the measurement technique. The QS-ML dynamics involves a jittering of the spectral modes, which results in a wider optical linewidth. This leads to the difficult resolution of the single comb lines with a 10 s OSA snapshot with a 1 GHz (10 pm) optical resolution. This avoids the complete resolving of the comb lines, leading to a higher background noise in the measured spectrum. The presence of the optical frequency comb in the mode locked state at the edges of the gain and absorption spectra, can be explained by the long length (1.88 mm) of the SOA inside the cavity. Such a length leads to a significant amplification in the long wavelength side of the 1300 nm wavelength range at relatively low current densities; the lasing threshold is at 1.3 kA/cm^2 . The laser will want to operate near the minimum absorption of the SA which also pushes the laser to longer wavelength, leading to a ML laser output in the 1340-1350 nm range. The mode-locked optical frequency comb appears in the spectral region where the unsaturated absorption of the SA has its minimum value, as shown in Figure 4.3, rather than at the maximum of the SOA gain curve. This is visible from the shift of the optical spectra of Figure 4.6 b). Different dynamics leads to different peak intensities in the cavity, i. e. different carrier density levels inside the SOA, which, in turn, correspond to different gain spectra. For this reason, the ML and QS-ML laser dynamics present a difference center of their frequency comb. For the current level of 120 mA the frequency comb is at a slightly longer wavelength compared to the lasing wavelengths at 70mA, which is centered at 1335 nm instead of 1345 nm. The presence of the mode-locking frequency comb at 1335 nm can also explain the limited optical bandwidth of the frequency comb presented in Figure 4.6 b), as the gain curve presents a steep slope when approaching the bandgap frequency of 1360 nm [53].

4.5 PASSIVE MODE-LOCKING

4.5.1 PULSE DURATION AND RELATIVE PHASE MEASUREMENTS

In the ML operating region, the phase and the amplitude of the optical pulse have been measured with a stepped-heterodyne technique. This method is extensively described in [137] and a simplified schematics is shown in Figure 4.7.

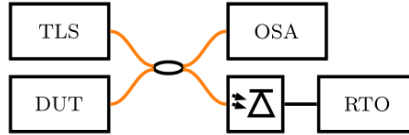


Figure 4.7: Setup schematics of a stepped heterodyne pulse measurement. The Tunable laser source (TLS) the Device under test (DUT) the Real time Oscilloscope (RTO) and the Optical Spectrum Analyzer (OSA) are the instruments involved.

This measurement has been applied earlier e.g. to characterize a 1550 nm InP based passively ML laser in [124]. The method allows for measuring the time domain amplitude and the phase of the pulse, without the need of filtering the comb or amplifying it with an external booster (which may lead to pulse deformation). It consists of the analysis of the beating frequencies between the integrated frequency comb and a local oscillator, which in this experiment is a tunable laser source (TLS) with 100 kHz linewidth (SantecTSL550). By stepwise tuning the TLS across the full optical comb and recording the beating with each tone it is possible to retrieve the frequency comb relative phase spectrum and reconstruct the temporal profile of the laser output. As shown in Figure 4.7, the TLS and the ML laser signal are beating on the photodetector, and the interference signal on the detector is recorded with a 50 GHz real time oscilloscope after traveling on a single mode fiber for approximately 110 m to cover the distance between the laser and the oscilloscope. Such a length of fiber leads to an amount of dispersion that will be noticeable even at 1340 nm which is close to the zero-dispersion wavelength at 1310 nm. The beating signal observed on the oscilloscope includes the oscillations of the modes of the comb and the beating of the TLS output with the two adjacent tones. The method consists of three steps: (i) a digital filtering of the signal to isolate the three frequency components, (ii) the back-transformation of the components to get to the corresponding beatings in the time domain, and (iii) phase differences analysis to extract the phase relation between the comb modes. More details are given in [137]. By tuning the TLS across the full comb, it is possible to retrieve the relative phase of all the modes and a complete temporal pulse is then achieved. Figure 4.8 a) shows the overlap of the retrieved spectral phase and the optical comb (with SOA current of 120 mA and reverse bias voltage of -1V on the SA). In Figure 4.8 b), a pulse duration of 1.0 ps and a frequency chirp of 500 GHz were observed. This result is significantly narrower than what is predicted

from the model which is represented with a dashed line. The reason for the difference of the pulse widths between the simulation and the measurements are due to a slight pulse compression due to the fiber transmission, which is possible due the near linear chirp present in the central part of the pulse.

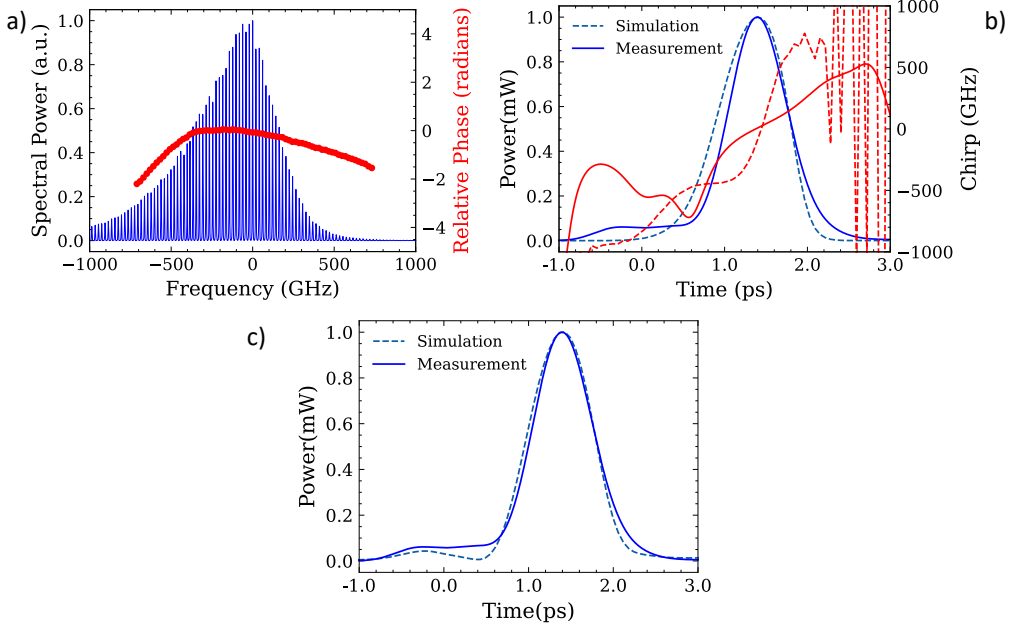


Figure 4.8: a) The spectral phase (red) and optical frequency comb spectrum at a SOA current of 120 mA and a reverse bias voltage to the SA of -1V. b) Temporal pulse power and frequency chirp measured with the stepped-heterodyne technique (solid lines) and simulation results (dashed lines) c) simulated pulse after traveling over 110 m of linear dispersive fiber.

To calculate the effect of the fiber dispersion we propagate the output of the laser simulator into a lossless linear fiber.

In this way it is possible to calculate the electric field at a distance L as:

$$A(L, \omega) = A(0, \omega) \exp \left[\frac{i}{2} \beta_2 \omega^2 L \right] \quad (4.5)$$

where $\beta_2 = -D\lambda^2/2\pi c$, with D considered to be the fiber dispersion of 0.4 ps/nm [138]. The result of $|A(L, \omega)|^2$ is plotted together with the measured pulse in Figure 4.8 c). The fiber thus induces a pulse compression which brings the simulation result in agreement with the measurement.

4.5.2 LASER REPETITION RATE

The repetition rate of the laser when it is mode locked is studied by recording the RF spectrum in detail around the repetition rate as a function of SOA current. The results are

presented in Figure 4.9. The repetition frequency is decreasing throughout the current range. This is due to the SOA and SA gain/saturation mechanisms as explained in [139]. The white dashed line in the plot of Figure 4.9 shows the expected frequency decrease of the repetition rate, which has been simulated with the parametrized laser model described in section 4.2 for every 10 mA between 100 and 200 mA. The shift is simulated to be 50 MHz within 70 mA, which corresponds to 0.25% of the round-trip frequency. Since the repetition frequency is decreasing, we assume that the detuning is due to the absorber saturation while the amplifier remains almost entirely saturated, and the carrier density inside the SOA is almost equal to the carrier density at threshold, as reported in [139]. Moreover, from Figure 4.9 one can see the electrical linewidth increase with the SOA current, which can be attributed to the increase of technical noise with the current.

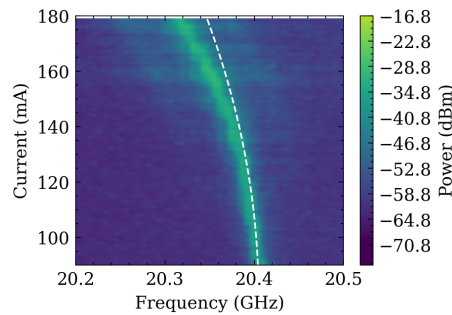


Figure 4.9: 2D map of the RF frequency spectrum of the signal from the photodetector covering SOA currents between 90 and 170 mA when the laser is in mode locked operation to observe the repetition rate shift between 20.4 and 20.3 GHz, together with the repetition rate predicted by the laser simulations (dashed white line).

4.6 Q-SWITCHING

The Q-switching behavior of the laser is difficult to be predicted by the simulation software for two main reasons. The first is that a very long simulation time is needed for the simulation to settle down to a stable dynamic mode where this behavior can be observed. The second issue is that there are differences in the output spectrum in the different operating modes. This is due to the larger changes in carrier density that can occur in Q-switching operation. The change in spectral properties of the SOA that occur due to the carrier density changes are not included in the modelling. The gain spectrum in simulation is controlled using a fixed spectral filter. Therefore, one cannot expect correct simulations for both the Q-switching and mode locked regime. However, the analysis of the q-switching dynamics can be used to confirm some parameters for the SOA, such as the differential gain. Figure 4.10 shows the measured RF spectra as of the laser intensity variations at lower frequencies where the laser is in a Q-switching operating regime. These intensity variation are induced by low frequency self-modulation of the cavity losses [130]. The Q-switching dynamics is varying as function of

the SOA current. The frequencies of these oscillations are expected to be close to the relaxation oscillations. Therefore we expect the repetition rate to be proportional to the square root of the current above threshold as stated in [97] with the equation:

$$\omega_r = \sqrt{\frac{\Gamma v_g a}{qV}} \eta_i (I - I_{th}) \quad (4.6)$$

where Γ is the optical confinement in the active region, v_g is the group velocity, $a = dg/dN$ is the differential gain, q is the electron charge, V is the volume of the active region and η_i is the injection efficiency. The measurements of the Q-switching dynamics of Figure 4.10 were first fitted with equation (4.6), as you can see in the yellow dashed line. The equation is fitted using the injection efficiency $\eta_i = 0.66$ and the confinement factor $\Gamma = 0.04$, already analyzed in [39] for a 1300 nm quantum well based amplifier. In this way it is possible to obtain the differential gain, which is $a = 0.45 \cdot 10^{-16} \text{ cm}^2$. Using the SOA and SA parameter values of the simulator in eq. (6), and a value of the differential gain derived from eq. (1) of $a = 0.41 \cdot 10^{-16} \text{ cm}^2$, the white dashed line is plotted. The differential gain derived from equation (4.1) is calculated using the carrier density at the laser threshold and the transparency carrier density N_0 for $\lambda = 1340 \text{ nm}$. Putting this differential gain value in equation (4.6) results in the white dashed curve which is close to the one fitted to the experimental data. It is clear from Figure 4.10 that the measured relaxation oscillation frequencies are not a continuous function of the injected current.

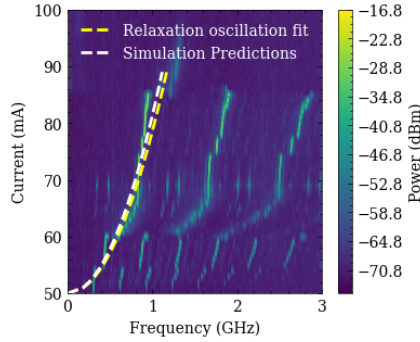


Figure 4.10: 2-Dimensional contour plot of the ESA measured power as function of SOA current and frequency for a reverse bias voltage of -1V on the SA. The yellow dashed line shows the result of fitting eq. 4 to the experimental results with equation 4, to obtain the differential gain $a = dg/dN$, and the white dashed line predicts the output of equation (4) with the differential gain obtained from the SOA parametrization at the operating wavelength.

The RF power presents discrete frequency steps at specific currents. For this purpose, the points where kinks appear in the light intensity curves of Figure 4.5 a) were studied in detail. They demonstrate a sudden change in the laser dynamics [140]. Figure 4.11 a) and b) highlight the low frequency part of the ESA spectrum and the time traces from the real-time oscilloscope at the discontinuity point for a reverse bias of -1 V and an SOA current of 80 mA, respectively. In this range we can clearly observe the simultaneous presence of different

relaxation oscillations with different rates. We can identify the presence of the dynamics in Figure 4.11 a) and b) as a dynamical system with period-6 [141], where the 900 MHz component is the fundamental self-pulsation frequency of the un-damped relaxation oscillation of the laser system, in line with the differential gain parameter.

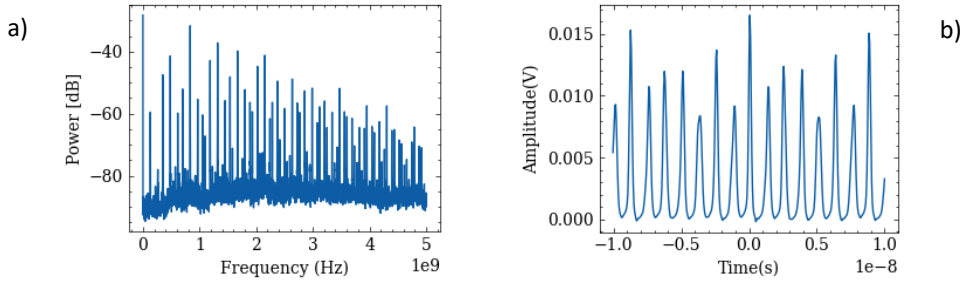


Figure 4.11: a) Electrical spectrum and b) time trace for a $V=-2V$ and $I=80$ mA. A mixing of dynamics of the electrical spectrum is confirmed by the time trace acquired with a 6GHz real time oscilloscope.

4.7 CONCLUSIONS

We presented measurements of a passively two-section mode locked laser based on a multi quantum well layer stack on InP n-doped substrate. The measurements are compared with the output from a laser simulator which has been built from the gain and absorption parametrization of an amplifier compatible with an active passive integration technology at 1300 nm. This new amplifier together with a laser simulator are needed to realize and model the dynamics of complex laser circuits, with intra-cavity optical filters realized through active/passive integration. The absorption cross section and the transparency carrier density are obtained from the parametrization of the absorption measurements of 50 and 100 μm long absorbers, which are used as saturable absorber inside two-section passively mode-locked lasers. These parameters are used to predict the mode-locked laser behavior in terms of optical pulse duration and change of repetition rate with SOA amplification. The measurements of the Q-switching dynamics of the laser are fitted to evaluate the correctness of the differential gain used in the simulator. The mode-locked laser presents a 5 nm wide frequency comb together with a 1 ps pulse train and a 500 GHz frequency chirp after the propagation of more than 100 m in fiber, in accordance with the simulations' prediction.

5. ACTIVE/PASSIVE INTEGRATION TECHNOLOGY ON INP AT 1300 NM

In this chapter, a new monolithically integrated widely tunable laser system on InP at 1300 nm is realized and demonstrated. From our knowledge, this is the first 1300 nm extended cavity tunable laser system realized on an active/passive integration technology platform monolithically grown on InP substrate. First, the voltage-controlled phase modulator is described as a functional building block of this 1300 nm platform. Its physical modeling is compared with a phenomenological description based on the fitting of Mach-Zehnder modulator (MZM) measurements. An efficiency around 20°/V mm has been measured together with a voltage dependent optical loss as low as 1.5 dB/cm at -10 V and 1300 nm. Then the use of the phase modulator inside tunable optical bandpass filters is discussed and analyzed. Ring resonators with Q-factor of 1700 have been realized and tested. The compact description of these functional building blocks and the optical amplifier is then used in a spectral steady state model to predict the behavior of tunable laser systems at 1300 nm. A 25 nm tuning range is measured from a widely tunable laser system with Vernier tuning of two ring filters and one asymmetric Mach-Zehnder interferometer (AMZI). The results highlighted in this chapter revealed the successful development of a 1300 nm active passive integration platform on InP for generic application purposes.

5.1 INTRODUCTION

The use of InP in photonic integration platforms is crucial for the development of circuits that require active/passive integration capabilities such as tunable laser systems or large capacity optical switches. In particular, a 1300 nm integration platform enables photonic integrated circuits for medical imaging techniques such as optical coherence tomography [26]. To obtain OCT imaging with high axial resolution a wide operating range of the tunable laser and associated optical components is required. Different approaches to realize a 1300 nm integration platform, such as heterogeneous or monolithic heteroepitaxial integration of III-V on Si have been reported [2]. These techniques require tailored processes with high precision alignment and high control over the formation of defects at the interfaces between different material compounds [91]. In this chapter, a new monolithic InP based active/passive 1300 nm photonic integration platform is presented. In this platform the passive and active components described in chapter 2 and chapter 3 are combined to realize photonic circuits with high complexity. This platform has the advantage of having fast electro-optics phase modulators and utilizes existing fabrication schemes like those of the 1550 nm InP based

monolithic platforms [3]. The butt-joint active/passive integration scheme (Figure 5.1) is optimized to maximize the mode overlap between the two regions and minimize the reflections at the interface between the amplifier and the passive waveguide. The interface is also tilted to avoid any in plane back-scattered light. To demonstrate the capabilities of such 1300 nm platform we have realized extended cavity widely tunable laser systems. Widely tunable lasers have been designed using the functional building blocks described in the previous chapters such as passive waveguides, multimode interference (MMI) couplers and semiconductor optical amplifiers (SOAs) [39]. The goal of the present chapter is to investigate the performance and the limitations of widely tunable laser systems realized on the 1300 nm active passive integration platform, grown monolithically on an InP substrate. In this InP platform, a contacted passive waveguide is used as electro-refractive phase modulator (ERM) controlled through a reverse bias voltage. The phase efficiency and the residual absorption of the ERM are evaluated as the fundamental property of this functional building block. The phase efficiency and the absorption measurement are compared with the output of a detailed physical simulation of an ERM under reverse bias voltage. The use of ERMs inside optical bandpass filters and tunable laser systems is then studied. A compact model to describe the phase change and the losses of ERMs is used inside a transfer matrix simulator, together with the amplifier and the passive components, to predict the steady state behavior of extended cavity widely tunable laser systems when they are tuned in the 1300 nm wavelength range. The results obtained on the tuning of 1300 nm extended cavity widely tunable lasers are then compared to the simulator predictions.

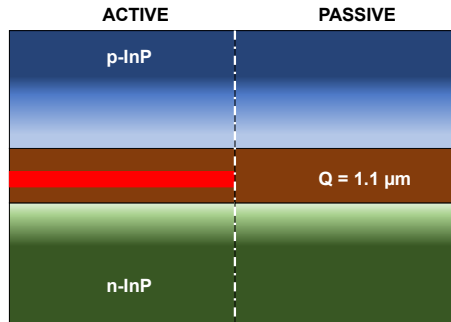


Figure 5.1 Schematics of the active/passive butt-joint coupling scheme used in the 1300 nm monolithic integration platform. The gradient fill reflects the doping concentrations over the layer stack. The details on the doping levels and dimensions of the layers are listed in Table 2.1 of Chapter 1 (passive layer stack) and in section 3.2 (active layers).

5.2 ELECTRO REFRACTIVE PHASE MODULATORS

The ERM is designed with the same guiding layer material as the passive waveguide, but with an additional contact layer made of InGaAs. The presence of a 300 nm thick InGaAs contact

layer leads to the possibility of applying reverse bias voltage to the structure, that creates an electric field which changes the optical phase in the ERM. In this section we will investigate the phase and the amplitude change over a designed ERM with the passive waveguide layer stack. The physical mechanisms involved due to the applied field and the change in free carrier concentration are explained. Further, the ERM efficiency and residual absorption are extracted from the measurements of Mach Zehnder modulators (MZM).

5.2.1 THEORY AND SIMULATIONS

To evaluate the voltage dependent phase shift and losses of the ERM, we have built a cross-sectional steady state 2D simulation model with the commercial software Device and Mode by Lumerical Ansys®, for electrical and optical simulations respectively. In Figure 5.2 a) the main layers and dimensions of the ERM cross section are presented. The layer thicknesses, compositions and the doping levels are identical to the passive layer stack as presented in table 2.1. The deep etched waveguide cross-section, i.e. a ridge width of 1.5 μm and a completely etched waveguiding core layer, is chosen for the design of ERMs. First the electric field and the carrier concentration are calculated over the cross-section for different reverse bias voltages between 0 and -10 V. The electric field and the change in carrier concentration induce a change in the real and imaginary part of the effective refractive index. This will in turn leads to a voltage dependent phase shift and propagation losses respectively. There are four mechanisms contributing to the change of the real part of the refractive index. These can be divided into two different categories. The Pockels and the Kerr effect, are caused directly by the applied field, and we will be referring to them as field effects [142]. On the other hand, the plasma and the band filling effect are caused by the change in the carrier density inside the PIN junction, and are considered as carrier effects [8, 9].

The change in the imaginary part of the effective refractive index is strictly linked to a change in the propagation loss of the ERM. It is modeled considering two main different mechanisms. The electro-absorption and the change in the carrier concentration. The reverse bias applied across the PIN junction causes carrier concentration to reduce through carrier depletion. As explained in section 2.2, the presence of free carriers, especially in the p doped InP region, is the main cause of optical propagation loss of defect free waveguides. This free carrier depletion, in turn leads to lower propagation losses compared to when no reverse bias voltage is applied. Additionally to the loss change due to carrier concentration, it is important to consider the electro-absorption or Franz-Keldysh effect [145]. This effect depends on the energy difference between the quaternary bandgap and the photon energy and on the electron's effective mass. The wavelength dependent electro-absorption increases for higher photon energies, i. e. lower wavelengths.

In the simulations, the 2-dimensional cross section is discretized and once the electric field and the charge densities are calculated at each discretized grid by solving the drift-diffusion

equations for the carriers (both electrons and holes) [146], then the real and imaginary index change are calculated considering the effects mentioned above. The effect on the optical modes at different wavelengths are then simulated, with the same approach used in [147] for 1550 nm InP modulators. The optical modes supported by the waveguides are simulated with finite difference element simulation of the 2-dimensional cross section for the different electric field and charge distributions. It is possible to see in Figure 5.2 a) the schematics of the 2-D cross section of an ERM and in Figure 5.2 b) the distribution of the electric field over the structure for a -10 V reverse bias voltage applied to the contact layer. The new effective indices of the optical modes are extracted with their amount of propagation losses in dB/cm.

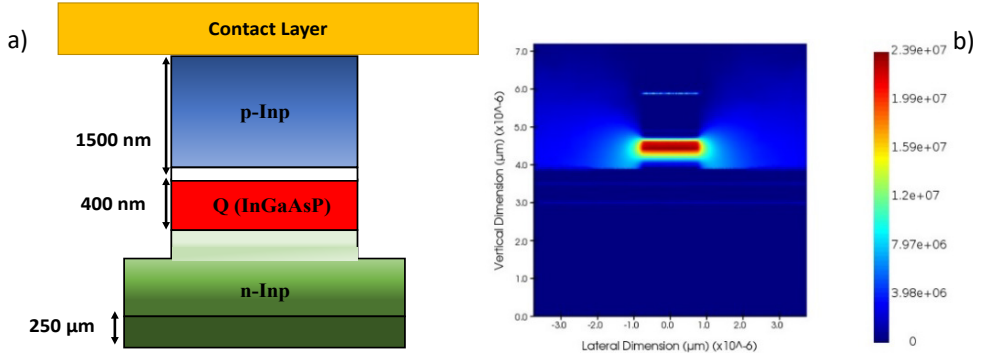


Figure 5.2 a) Schematics of the cross section of the deeply etched ERM highlighting the different doping types. The shaded color refers to less doping concentration. b) Electric field distribution over the deep etched waveguide cross section as function of -10 V of reverse bias voltage.

5.2.2 MEASUREMENTS AND ANALYSIS

The efficiency and the voltage dependent loss of the ERMs have been measured from the voltage dependent transmission of a Mach-Zehnder modulator (MZM). A MZM is shown in the schematics of Figure 5.3 a) and briefly described here. The MZM consists of two 1x2 MMI couplers which connect two ERMs. The reverse bias voltage applied to one of the two arms of the MZM, lead to an optical path difference between the two arms, through a change in the effective index of the optical modes. The phase difference between the light at the input waveguides to the right side MMI, results in a coupling difference at the output. The transmission of the MZM presents a sinusoidal behavior with the reverse bias voltage applied to one of the ERMs. The output power, as function of the input power on one port is calculated from [38], to be:

$$P_{out}(V) = P_{in} \left(\frac{1}{4} + \frac{1}{4} e^{-\alpha(V)} + \frac{1}{2} \cos(\Delta\phi(V)) \cdot e^{-\frac{1}{2}\alpha(V)} \right) \quad (5.1)$$

where $\Delta\phi$ refers to the phase change induced by the field applied on one arm of the MZM, and α refers to the voltage dependent amplitude modulation. The phase change $\Delta\phi$ is assumed linear with the voltage with a dependency of the type: $\Delta\phi = \frac{2\pi}{\lambda} \Delta L A n_g$ [148]. A is

calculated applying the boundary condition of having a π phase change ($\Delta\phi = \pi$) when $V = V_\pi$. V_π is identified in the measurement of the transmission of the MZM (P_{out}) as the voltage difference between the maximum and the minimum when varying the voltage of one ERM. For the residual absorption we use a parabolic polynomial function of reverse bias voltage $\alpha(\lambda, V) = p_0(\lambda) + p_1(\lambda)V + p_2(\lambda)V^2$, with fitting parameters p_0 , p_1 and p_2 that depends on the wavelength. p_0 refers to the passive waveguide propagation loss while p_1 and p_2 are voltage dependent. Evaluating equation (5.1) at different wavelengths, it is possible to obtain the variations of the phase change and the propagation loss in the 1300 nm range of the ERMs. The light from a tunable laser system (Santec TSL-520A) enters the MZM on-chip structure from the coupling of a lensed fiber to the waveguide. The output power as a function of voltage applied to the top arm of the MZM is recorded with a photodetector (Agilent 8315B).

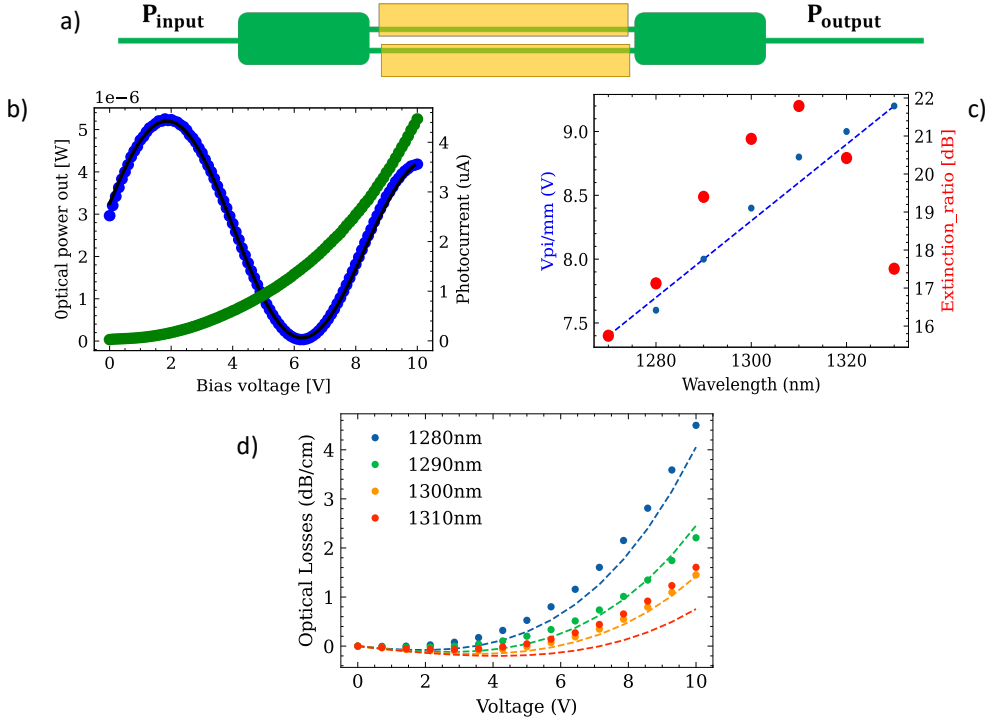


Figure 5.3: a) Mach-Zehnder modulator (MZM) schematics with two 1x2 3-dB MMI coupler and ERMs in the top and bottom arms. b) Transmitted optical power at 1300 nm of a MZM as function of reverse bias voltage on top ERM (blue curve). Measured photocurrent through the ERM as function of the reverse bias voltage (green curve). Fit of the transmission function (black curve) of the MZM with equation (5.1). c) Fitted efficiency V_{π} (V-mm) and extinction ratio (dB) as function of wavelength, together with the simulation for the V_{π} values from the physical 2-D model (solid blue line). d) Voltage dependent loss for different wavelength fitted with p_0 , p_1 and p_2 (dots), compared with the simulations of the physical model described in 5.2.1.

In Figure 5.3 b) one can see the output power for a wavelength of 1300 nm (blue curve) when changing the top arm reverse bias voltage. The tunable laser input power is set at 0 dBm (1 mW). The fit of the measurement with equation (5.1) (black curve) is used to extract the ERM efficiency and the voltage dependent absorption. Changing the input wavelength of the tunable laser system, it is possible to observe the different MZM transmission curves as function of wavelength. Figure 5.3 c) plots the efficiency and the extinction ratio calculated from the measurements, together with the V_π simulation results as function of wavelengths between 1270 and 1330 nm. The electro-optic efficiency was measured to be between $23^\circ/\text{V}$ mm at 1280 nm and 17° at 1330 nm, showing a near linear dependency on the input wavelength. The extinction ratio is calculated as the difference in dB between the maximum and the minimum power level of the MZM transmission. The evaluation of the extinction ratio is between 16 and 22 dB over the wavelength range. The maximum is at 1310 nm which corresponds to the wavelength where the MMI is optimized for lowest imbalance in the splitting ratio. The lower 16 dB extinction ratio can be due to the difference in losses between the two branches of the MZM or due to splitting imbalance in the MMI couplers. The use of an actively tunable MMI can lead to a constant splitting imbalance in the whole wavelength range [149]. The absorption dependent losses are plotted in Figure 5.3 d). We can see how the matching between the measurements fit and the physical simulation output around 30 nm centered at 1300 nm is ensured, with propagation losses ranging from 1 to 4 dB/cm at 10 V. The ERMs parametrization with the experimental data is aimed to be used in a steady state spectral laser simulator to model the effect of the ERM in the laser tuning, where the polynomial coefficients p_0 , p_1 and p_2 are wavelength dependent.

5.3 OPTICAL TUNABLE BANDPASS FILTERS

In this section the two types of optical filters are described that are used inside a laser cavity that will be presented in the next section. Different filter interferometric geometries lead to different wavelength dependent transfer functions. The use of such tunable bandpass filters inside a laser cavity has two goals. They limit the broad emission of the intra-cavity amplifier and one can obtain single mode laser emission. At the same time, due to the presence of intra-filter ERMs, they are responsible for the laser tuning.

5.3.1 ASYMMETRIC MACH ZEHNDER INTERFEROMETERS

The first class of optical filters is the one made of MZM with a small geometric length mismatch between the two arms, which leads them to behave as asymmetric Mach-Zehnder interferometers (AMZI). The filter transfer function becomes a sinusoidal function with optical frequency. The transmission periodicity characteristic of each AMZI is given by its free spectral range (FSR) which is determined by the length mismatch between the two arms ΔL :

$$FSR = \frac{c}{n_g \Delta L} \quad (5.2)$$

where n_g is the waveguide group index, and c is the speed of light in vacuum. Over a wide wavelength range the FSR depends on the wavelength through the group index dispersion. In Figure 5.4 b) the sinusoidal transfer function of an AMZI with 1.7 mm of ΔL is plotted as function of wavelength between 1300.5 and 1301.5 nm. For this AMZI, the FSR is calculated to be 0.27 nm (48 GHz) which is in line with the measured value. The extinction ratio of the measurements is between 10 and 12 dB, which is around 10 dB lower than what has been measured from the MZM voltage dependent transmission. This can be interpreted because of differences in optical losses in the two arms in the AMZI due to their length difference, but this leads to unrealistically high loss numbers (>20 dB/cm). Therefore, the difference in the extinction ratio can be attributed to small deviations in the MMI splitting ratio. The efficiency of the ERM measured from the AMZI transmission spectra is around 20°/Vmm which agrees with the efficiency of MZMs at 1300 nm.

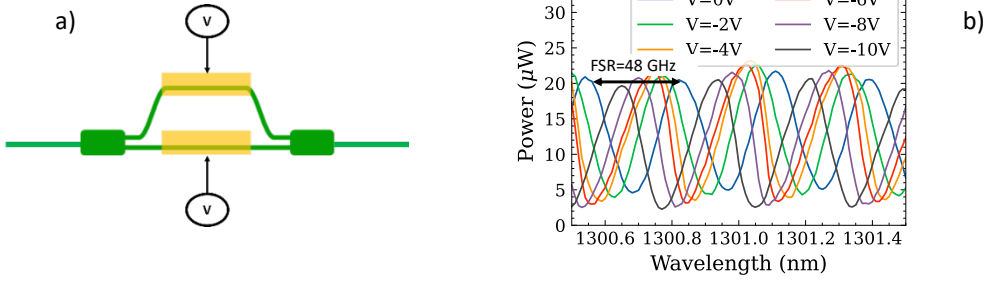


Figure 5.4 a) Schematics of an Asymmetric Mach-Zehnder interferometer (AMZI). Two 2x2 MMI couplers and a length mismatch between two arms are visible. The electrical contacts provide the reverse bias voltage to account for a phase shift and a frequency tuning. b) Examples of the transmission function of the AMZI for different reverse bias voltage applied to the ERM in the top arm of the schematics in a).

5.3.2 TUNABLE MICRO-RING RESONATORS

A different wavelength dependent transfer function can be created using an optical micro ring resonator. In the transmission spectrum of a ring resonator a sharper transmission peak close to its resonance wavelength is present [150], [151]. In this 1300 nm integration technology, micro ring resonators have been designed and realized using two 2x2 MMI couplers connected by arc waveguides (see Figure 5.5 a). The two-arc waveguide section are contacted to be biased and used as ERMs. The two contacts are connected to ensure that the same reverse bias voltage is applied to the full ring except for the MMIs. The MMIs couplers are used to couple light in and out of the ring resonator. The power splitting ratio is 50% and their expected insertion loss from the design is between 0.3 and 1 dB over 100 nm, as has been reported in section 2.4.3. The MMIs are not contacted to avoid any voltage dependent

interference change with respect to the 3-dB coupling. In the ring resonator, the FSR is inversely proportional on the radius of the ring. The wavelength FSR of an individual micro-ring resonator is given by:

$$\Delta\lambda_{FSR} = \frac{\lambda^2}{n_g L} \quad (\Delta f_{FSR} = \frac{c}{n_g L}) \quad (5.3)$$

where L is the circumference of the ring, n_g is the group index, and λ is the wavelength. Smaller rings will lead to higher FSR and vice versa. However, the radius of the ring is clearly directly linked to the length of the phase modulator. Smaller radii lead to shorter ERMs and smaller ERM phase change per volt. Figure 5.5 b) depicts the transmission of a tunable ring resonator with $R=150 \mu\text{m}$ and two MMIs with length of $200 \mu\text{m}$ each. The transmission is measured through the bar port as shown in the schematics of Figure 5.5 a). The radius is chosen to be bigger than $100 \mu\text{m}$ to ensure bending loss smaller than $0.1 \text{ dB}/90^\circ$ which makes the additional loss due to the bend negligible compared to the MMI losses inside the rings. The total ERM length is chosen to be of around 1 mm , to obtain a phase change bigger than π between 0 and -10 V . Please note that the total length of the ring resonator needs to include the length of the two MMI couplers present in the cavity, i.e. 2 times $212 \mu\text{m}$. The tuning over π of the micro-ring is sufficient since inside laser configurations, which exploit Vernier effect between two micro-ring resonators, the remaining FSR will be covered with the tuning of the other tuning element. The ring resonator transmission is recorded for three different voltage configurations of the ERM of 0 , -2 and -4 V (see Figure 5.5 b).

The FSR of the filter around 1300 nm is measured to be 46 GHz as the frequency distance between two adjacent transmission minima. The full width at half maximum (FWHM) is measured to be 14 GHz . From these two parameters, it is possible to calculate the quality factor and the finesse of the micro ring resonator. The ring resonator showed a quality factor $Q = \omega/2\pi\text{FWHM}$ of about 17000 and a finesse $F = \text{FSR}/\text{FWHM}$ of 3.3 . These values are lower than what has been measured for a $80 \mu\text{m}$ radius ring resonator on InP platform at 1550 nm [118]. This reduction can be attributed partly to the higher amount of insertion loss in the ring as explained in [152]. The higher loss can be due to the higher passive loss in the 1300 nm integration platform, or due to the larger radius of curvature, which leads to a smaller FSR. The insertion losses of the 3-dB MMI coupler also deteriorates the performance of ring resonator, widening the FWHM of the transmission function.

Two different approaches can be realized to improve the quality factor of this micro-ring resonator. It is possible to replace the MMI couplers with directional couplers in such 1300 nm platform. This can reduce the losses and therefore increase the Q-factor and the effective length. On the other hand, the splitting ratio of the MMI can be changed with respect to 3-dB or 50-50 splitting. Changing to 85-15 or 90-10 splitting ratio, would keep more optical power at the resonant frequency into the ring. This would narrow the FWHM, increasing in this way the finesse and the Q-factor of the ring for the same bending radius. Changing the

ratio of the MMI splitting has a double effect on the ring transmission. It can improve the sharpness of the transmission function, but at the same time decreases the transmission due to the higher losses. This happens since the light travels for multiple roundtrip inside the micro-ring before being coupled out, and it results in more effective losses due to the MMI present in the resonator [153].

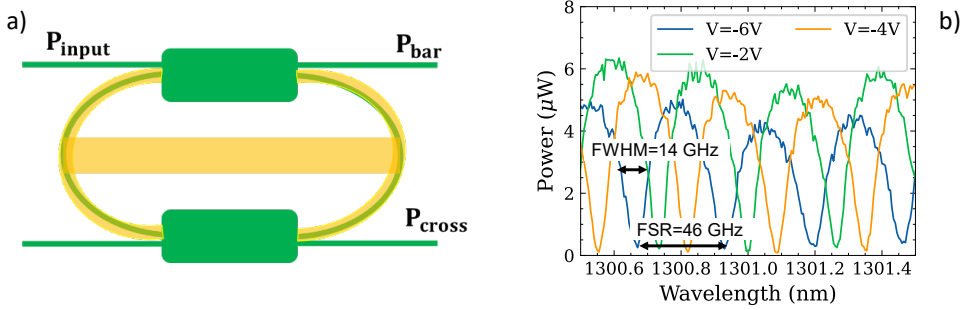


Figure 5.5 a) Schematics of a micro-ring resonator bandpass tunable filter. b) Bar port transmission between 1300.5 and 1301.5 nm of a micro-ring resonator with $R=150 \mu m$ at 0 (blue) -2 (green) and -4 (yellow) V. Highlighted in the graph are the Free spectral range (FSR) and the full width at half maximum (FWHM) of the power transmission curve.

5.4 TUNABLE LASER SYSTEMS AT 1300 NM

In this section we describe and test the realized widely tunable laser system at 1300 nm. The bandpass tunable filters explained in section 5.3, will here be used to tune the laser emission wavelength. To describe the laser and interpret the results, a steady state spectral model is developed and is first introduced and explained. The basis of this model lies in the parametrization of the loss and the phase change of different photonic functional building blocks contained in the 1300 nm library. Such a model is validated with the measurements of a widely tunable laser system at 1300 nm exploiting the Vernier effect between two micro-ring resonators of different radii. The choice of this laser arises from the fact that for this new platform the use of high suppression from the rings would lead to single mode laser emission. The total tuning range of the laser and the limitations to its side mode suppression ratio (SMSR) will be investigated. A wavelength look-up table (LUT) within 13 nm is experimentally obtained through the sweep of the control settings on the intra-cavity filters, as a step towards the use of 1300 nm laser sources in SS-OCT measurement systems.

5.4.1 STEADY STATE SPECTRAL MODEL

In this section we introduce the simulator used to describe widely tunable laser system for the 1300 nm wavelength range. A phenomenological steady state spectral model [154] is

developed to estimate the output spectrum of widely tunable laser at threshold. Every functional building block of the tunable laser circuit is described in a compact way but with sufficient detail, including the parametrization of its gain, absorption, or phase modulation. The model is based on a transfer matrix (T-matrix) formulation [97]. The electric field amplitude and phase transmission of every functional building block present in the laser circuit is described by a wavelength dependent T-matrix. For example, an ERM can be described as:

$$T_{ERM} = \begin{pmatrix} e^{-j\Delta\phi} * e^{\alpha L} & 0 \\ 0 & e^{j\Delta\phi} * e^{-\alpha L} \end{pmatrix} \quad (5.2)$$

where $\Delta\phi$ and α are represented by the wavelength function extracted from the measurements of section 5.2.2, and L is the length of the ERM. Please note that the off-diagonal elements are set to 0, since we assume to have negligible spurious reflections or back scattered light from the building blocks. Differently than in [154], we adapted the parameters of the amplifier (SOA) and the passive waveguide to the gain losses and phase change for the 1300 nm integration platform on InP. Moreover, in this modeling, the novelty lies on the fact that we include the compact description of the voltage dependent absorption losses of the ERMs at 1300 nm. The MMI is modeled as a transfer matrix of a 3-dB coupler with a fix value for insertion loss (1 dB). The wavelength dependence of the MMI can be included in the steady state spectral model, to obtain better predictions on the behavior of AMZI or ring resonator bandpass tunable filters. This can be done by including the measurement of the imbalances and the optical losses of 2x2 3-dB MMI couplers described in Chapter 2. In the work here this was however not included, since those active/passive 1300 nm run are experimental and can lead to high fabrication tolerances.

By multiplication of the T-matrices of the different elements inside the cavity, and adding the amplified spontaneous emission (ASE), a linear laser system is described by the following equation system.

$$A_1 = A_2 T_{11} + B_2 T_{12} + ASE \quad (5.3)$$

$$B_1 = A_2 T_{21} + B_2 T_{22} \quad (5.4)$$

Where $T_{11}, T_{12}, T_{21}, T_{22}$ are the elements of the total T-matrix describing all the elements present in the cavity. $A_{1,2}$ and $B_{1,2}$ refers to the intensity level of the light at the front and the back reflectors of the laser cavity, for the two different light propagation directions as shown in the schematics of Figure 5.6.

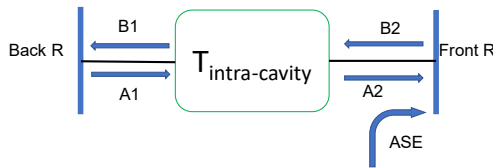


Figure 5.6: Schematics of the steady state spectral model operating principle.

Imposing the proper boundary conditions, that depend on the laser cavity geometry, it is possible to calculate the relative steady state optical field amplitude. The field amplitude is calculated for an arbitrarily set range of optical wavelengths for a specific SOA modal gain. The SOA current is then gradually increased until the roundtrip gain plus the ASE reaches unity at some specific wavelength inside the range. At this point the laser is reaching threshold and starts to operate in a coherent way.

5.4.2 LINEAR LASER DESIGN WITH LOOP MIRROR INCLUDING MICRO-RINGS

The 1300 nm laser, realized on the active/passive integration platform, consists of a linear cavity with ring resonators and AMZI based tunable bandpass filters. The laser design is schematically shown in Figure 5.8, together with a picture of the realized laser on-chip. The laser consists of a linear cavity which includes a 1 mm long SOA, where the two ring resonators and the AMZI filter form a wavelength selective loop mirror. The choice for putting the amplifier in a linear cavity has the advantage that a shorter amplifier can be used to get to threshold. The laser is tuned using the Vernier effect [155] of the two rings which have a slightly different circumference (Figure 5.7 a). The enhanced FSR of the two rings in sequence can be calculated from the Vernier effect works as follows:

$$\Delta\lambda_{\text{tuning,Vernier}} = \frac{\Delta\lambda_{FSR1}\Delta\lambda_{FSR2}}{\Delta\lambda_{FSR1}-\Delta\lambda_{FSR2}} \quad (5.5)$$

where $\Delta\lambda_{FSRi}$ are the FSR of the two rings respectively. During the design of this laser, there are trade-offs to be made. The size of the rings and the difference between their circumferences are key considerations for a single mode widely tunable laser system. First, it is important to note that the size of the ring is constrained by the length of the ERM which must be around 1 mm to achieve at least a π phase shift for -10 V of reverse bias voltage. Then, a smaller difference between the radii of the micro-rings increases the Vernier FSR, but the limited Q-factor of the rings in this 1300 nm active/passive integration technology and the long extended linear cavity of the laser means that too small radius difference results in a smaller SMSR in the laser spectrum. The introduction of a directional coupler in this 1300 nm monolithic platform could improve the Q-factor of the ring and enable a smaller geometrical length without affecting the beam quality of the laser. The difference in the radii between the two rings is 3 μm ($R_1 = 150 \mu\text{m}$, $R_2 = 153 \mu\text{m}$), which leads to a total difference of 18.85 μm in the circumference. This value was taken from similar laser design exploiting Vernier effect at 1550 nm [153]. The $\Delta\lambda_{\text{tuning,Vernier}}$ results to be 25 nm centered at 1310 nm, which is narrower than the SOA gain bandwidth for threshold current densities between 5 and 6 kA/cm^2 . To increase the laser tuning range beyond the Vernier FSR, we introduced an AMZI filter in the cavity (Figure 5.7 b). The AMZI presents two 1 mm long phase modulators, and a length imbalance of 9 μm , which leads to a desired FSR of 50 nm.

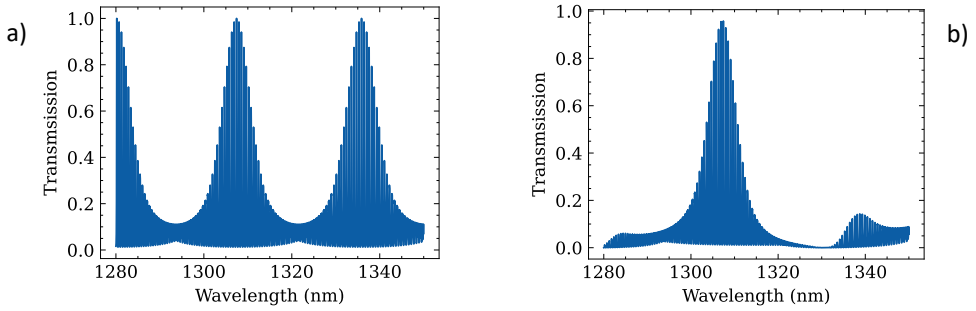


Figure 5.7 a) Sketch of the Vernier filtering effect between two micro-ring resonators of radii $R_1 = 150 \mu\text{m}$ and $R_2 = 153 \mu\text{m}$. b) Total transfer function of the cavity, combining the Vernier filter with the AMZI (FSR=50 nm) used to increase the tuning range.

The overall cavity length is 9 mm corresponding to a cavity mode FSR of 4.5 GHz in a linear cavity laser. The laser is fabricated with the 1300 nm active/passive integration run through the integration of several functional building blocks. The chip's facet is AR coated and the output waveguide from a single mode ridge width of $1.5 \mu\text{m}$, is adiabatically tapered to a width of $3 \mu\text{m}$ at the edge of the chip to increase the fiber to chip output coupling. The waveguide is also tilted by 7° to avoid any external spurious reflection, which can compromise the laser performance.

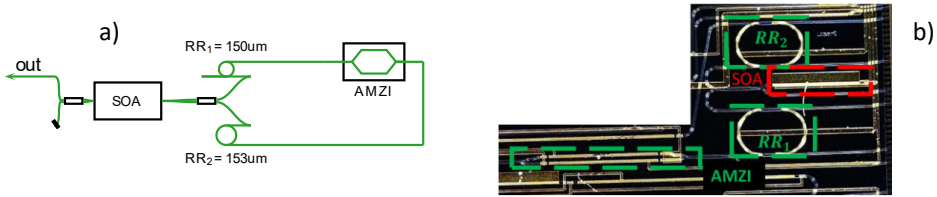


Figure 5.8 Left: Schematics of the laser design. The optical bandpass filters are the two micro-ring resonators RR_1 and RR_2 and the asymmetric Mach-Zehnder interferometer (AMZI). The semiconductor optical amplifier (SOA) is the gain medium. Two MMI splitter are also present in the drawing. Right: Photography of a realized photonic chip with the laser circuit described in the setup schematics.

5.4.3 TUNABLE LASER SIMULATION

The laser system is simulated using the steady state spectral model described in section 5.4.1. This simulation are aimed to obtain the tuning range and the laser quality in terms of side mode suppression ratio (SMSR), for different control settings of the tunable filters inside the laser cavity. In particular the tuning of one micro-ring resonator will be then compared with the laser tuning measurements. The linear cavity design is modeled with three concatenated T-matrices. The first refers to the outcoupler. The output coupler is assumed to couple out 40% of the light entering. This is the combination of a 50% coupling and a 1 dB insertion loss of the MMI coupler [69]. The SOA gain is modeled with the compact model presented in

chapter 3. The third matrix describes the combination of the three different wavelength selective filters. The light is assumed to travel through the first ring resonator (RR_1) then the AMZI and then the RR_2 . In the simulation, it is assumed that the light is traveling unidirectionally through the three filters. This description is correct since the mixing of the two different directions of the light in a real device would have a negligible effect on the steady state spectral features of the laser. A different situation would occur for a description of time dependent behaviour of the laser dynamics with high peak power intensities. Then the two possible light paths in the cavity need to be taken into account. Please note that during these simulations, the electro-absorption losses in the ERMs are function of voltage only. The wavelength dependence is neglected and for the parabolic curve describing the voltage dependence of the loss values have been taken for $\lambda = 1300 \text{ nm}$. This approximation is considered valid since the ERMs inside the filter are relatively short ($\leq 1 \text{ mm}$), which leads to a small contribution to loss variation smaller than $<0.4 \text{ dB}$ for -10 V of reverse bias applied at 1280 nm . This leads to negligible contribution of the higher electro-absorption losses at lower wavelengths.

The tuning of the laser is simulated by sweeping the voltage on the RR_1 and on the AMZI between 0 and -10 V with 1 V steps. A voltage of -10 V is needed to obtain a full π phase shift in the micro-ring tunable filters. The ring resonator circumference is slightly smaller than 1 mm (0.942 mm for RR_1). Since V_π has been measured to be between 7.4 and 9.2 V/mm over the whole band, a voltage of -10 V is needed. Figure 5.9 a) presents a number of simulated laser threshold spectra when sweeping the RR_1 between 0 and -10 V . From these results, the calculated tuning results to be equal to 12.5 nm , which is exactly half of the Vernier FSR, since the tuning is over half the ring FSR. The laser is single mode in all the calculated spectra shown here with an SMSR over 30 dB . The mode spacing is around 5 GHz , as one can see in Figure 5.9 b), which is close to the calculated linear cavity FSR of the laser. The Vernier effect makes that the wavelengths for identical voltage intervals are not equally spaced. In Figure 5.9 c) the threshold current density of the laser as function of the lasing wavelength when tuning the RR_1 is presented. This threshold is changing due to the change in the optical loss of the circuit. This is caused by losses in the ERMs that are voltage dependent within this 10 nm tuning range. The steady state spectral model simulations revealed three important properties of the laser and the model. Firstly, the high SMSR ratio ($>30 \text{ dB}$) of the laser at threshold is attributed to the use of micro-ring intra-cavity filters which present a sharper wavelength dependent transmission function. Secondly, the Vernier effect causes mode hopping between different longitudinal cavity modes, leading to non-equally spaced lasing wavelengths with the voltage control settings on the ERMs in the rings. Finally, the analysis of the threshold current change with the ring tuning shows the parabolic voltage dependent loss function that has been extracted from the ERM parametrized model. The simulation

results obtained with such a model will be used to explain the laser behavior during the tuning measurements.

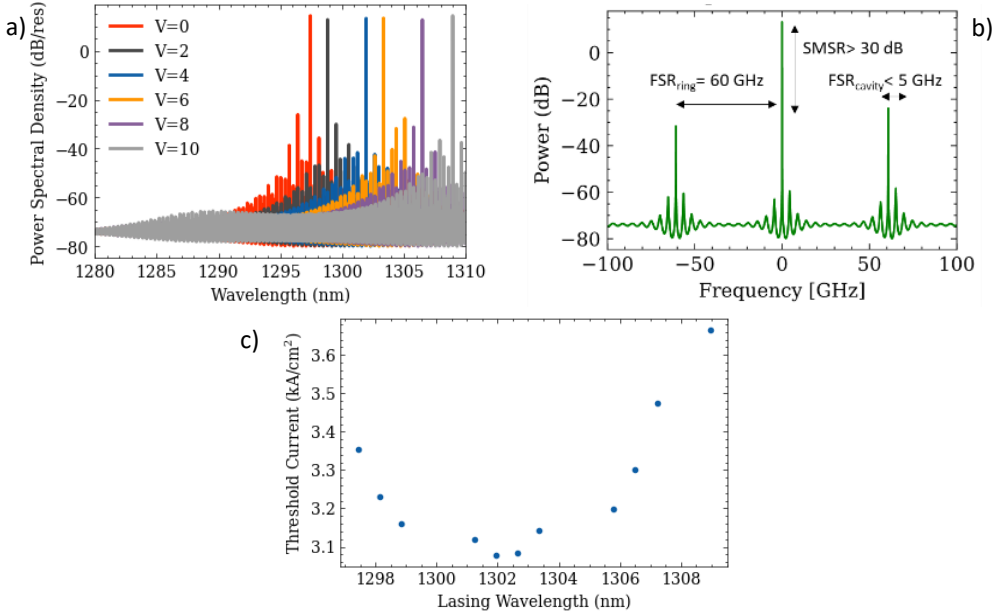


Figure 5.9 Simulations of a) the lasing spectra at threshold for different RR_1 reverse bias voltage settings. b) Laser spectrum at threshold as function of optical frequencies (GHz). This graph is shown to highlight the SMSR (>30 dB), the longitudinal cavity modes spacing (≈ 5 GHz), and the FSR of the ring resonator (≈ 60 GHz). c) threshold currents of the tunable laser system as function of the output calculated lasing wavelength at threshold, while tuning the micro-ring resonator (RR_1). The 10 points correspond to the tuning of RR_1 from 0 to -10 with 1 V steps sequentially.

5.4.4 LASER TUNING MEASUREMENTS

The laser design presented in section 5.4.2 was fabricated and its tuning range and its side mode suppression ratio (SMSR) were evaluated. The light intensity characteristic of this laser is measured to obtain its threshold current and the highest achievable output power. The output optical power is measured as function of the current supplied to the SOA. The SOA current is supplied through a laser diode controller (Thorlabs Pro8000). The output power in fiber after passing through an optical isolator, is measured with a power meter (Agilent 81635A). The substrate of the chip is kept at 18°C during the measurements. It is important to note that 0 V reverse bias is supplied to the filters during this light characteristics' measurements. We can observe from Figure 5.10 a), that the threshold current for this laser is around 90 mA at 1296 nm. This corresponds to a current density $J = 5.625 \text{ kA/cm}^2$, which is higher compared to the simulated threshold current density equal to ($J = 3.4 \text{ kA/cm}^2$). This difference can be attributed to a higher passive loss in the realized laser cavity and a

different filter tuning than used in the simulation. The maximum optical power of 300 μW in fiber is obtained at 190 mA of injection current. The output power of the laser can be increased with a different design, choosing a preferable position for the output coupler. The kinks in the LIV curve originate from the mode hopping of the laser between different wavelengths as function of current. This is due to changing of tuning of the filters by the increasing heat generated in the SOA. The laser tuning is measured by recording the optical spectra for different reverse bias control voltages applied to the optical filters. The control settings are applied using source measurement units (SMU) (Keithley 2620B), and the optical spectra recorded with an optical spectrum analyzer (OSA). The OSA (Ando AQ6315A) has a resolution of 0.01 nm (1 GHz). The laser tuning is done by biasing individually all the three wavelength selective elements between 0 and -10 V, with the SMU. The tuning of the RR_1 between 0 and -10 V is observed in Figure 5.10 b). A laser tuning of 17 nm has been measured. This is a wider tuning range than was predicted by the simulation. This wider tuning range can be linked to the ERM efficiency, which increases for lower wavelengths, as shown in Figure 5.2 c). At 1290 nm, a reverse bias of 10 V results in a 1.25π phase shift in the ERM and 16 nm of tuning range from the Vernier effect.

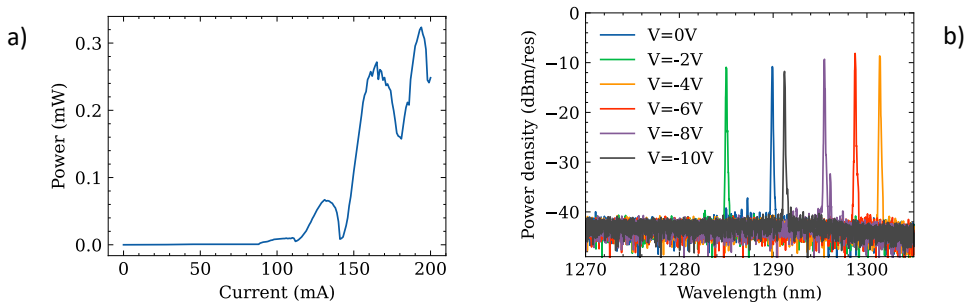


Figure 5.10 a) Light intensity curve of such a laser design between 0 and 200 mA. It is possible to see that the threshold current is around 90 mA. b) Example of Vernier effect tuning when the RR_1 voltage is swept between 0 and 8 V. Less than half of the Vernier FSR is covered due to the circumference of the ring which is less than 1 mm.

Unfortunately, the laser is not emitting single mode output for all the voltage control settings of the three filters. As an example, two different filter configurations leading to very different laser states are shown in Figure 5.11. The tuning of the emission wavelength can degrade the SMSR with respect to more than 30 dB (blue curve). Due to the small detuning between the two RRs circumferences ($<19\ \mu\text{m}$) with respect to their radii ($150\ \mu\text{m}$), the neighboring cavity modes are not suppressed enough when the transmission maximum of the two rings is not sufficiently near to a single longitudinal cavity mode. Then the laser tends to operate in a multimode configuration for such control voltage settings (green curve). The distance between the two modes is around 50 GHz, which corresponds to the FSR of a ring resonator in the laser cavity, as shown for the simulations of Figure 5.9 b). In this case the poor

suppression of the cavity modes, due to the wide FWHM wavelength dependent transmission, leads to a dual mode laser configuration. To overcome this limitation, the introduction of a single ERM inside the cavity is required to independently tune the longitudinal laser modes. In such a way, it is possible to align a single cavity mode to the resonance of a Vernier FSR.

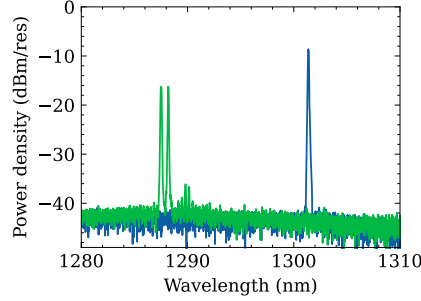


Figure 5.11 Examples of different laser configurations. The laser is single mode with more than 30 dB of SMSR (blue curve). The setting applied to obtain this curve are $V_{AMZI} = -3\text{ V}$, $V_{RR_1} = 0\text{ V}$, $V_{RR_2} = -4\text{ V}$. The green curve shows a situation where the Vernier effect is not sufficiently narrow to separate only a single cavity mode. The setting applied to obtain this curve are $V_{AMZI} = -2\text{ V}$, $V_{RR_1} = -9\text{ V}$, $V_{RR_2} = -9\text{ V}$. To overcome this situation an efficient way to tune the longitudinal cavity modes is required.

The total tuning range is obtained by tuning all the intracavity filters from 0 to -10 V. Single mode lasing spectra observed between 1282 and 1307 nm are reported in Figure 5.12 for an SOA current of 150 mA. SMSR values of over 30 dB have been observed. The tuning range is limited to 25 nm even for the AMZI FSR of 50 nm implemented. The losses from the passive components, such as passive waveguides or MMI couplers, appear to limit the laser tuning range. This hypothesis is also confirmed from the fact that the laser emits at wavelengths lower than the center of the photoluminescence curve ($\lambda_c = 1310\text{ nm}$). High losses lead to higher threshold currents, which lead to a blue shift in the modal gain of the SOA. The main suspect is the high losses of the passive waveguides. This is also indicated from a link between the emission wavelength and the cavity length observed in several other laser designs not reported here. Longer cavity lengths lead to a blue shift in the emission and higher threshold currents. Note that the wavelengths are non-uniformly distributed over its tuning range indicating possible unwanted reflections inside the cavity. To be used as an OCT source, a tunable laser needs to have uniformly distributed optical frequencies over a certain range. Some effort has been spent to train this laser design to be used as an OCT source. The goal was to obtain a LUT over a certain range of nanometer with equally spaced optical frequencies. A search optimization on the reverse bias control settings of the filters, based on a Nelder-Mead method [156] helps for this purpose. The setup and the optimization mechanism will be extensively covered in the next chapter. The aim is to obtain the best

reverse bias configuration settings for the laser to emit at a specific wavelength. To do so, the output power in fiber from the laser is passing through a tunable bandpass filter (EXFO XTA, Bandwidth=0.2 nm), and collected from a photodetector. The maximization of the transmission from this external filter, led to the best possible laser configuration for that wavelength. Figure 5.13 presents laser output spectra in the 1280-1300nm range as a function of the setting points. It shows how it is possible to obtain equally spaced wavelengths over more than 10 nm between 1285 and 1296 nm. The SMSR is also kept above 20 dB.

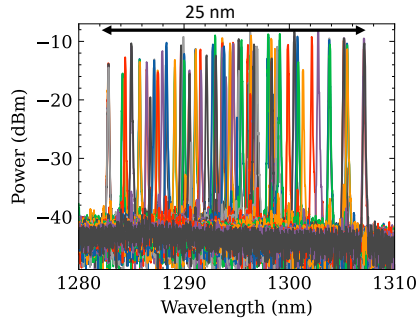


Figure 5.12 Tuning range measurement of the tunable laser system. Here a 25 nm tuning range between 1282 and 1307 nm has been obtained. All the configurations with SMSR higher than 25 dB have been reported here. The high background level can be due to the high losses of the cavity, which lead to higher-than-expected level of threshold currents ($J_{th} > 5 \text{ kA/cm}^2$).

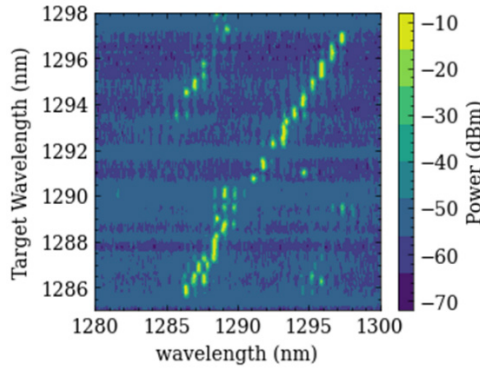


Figure 5.13 A linear wavelength map optimized with a Nelder-Mead search algorithm between 1285 and 1298 nm.

5.5 CONCLUSIONS

In this chapter, the realization of a first InP monolithic active/passive integration technology at 1300 nm is demonstrated. The use of passive waveguide as an ERM when contacted has been experimentally evaluated. A 20°/mm of phase efficiency and low amount of residual

absorption losses (< 1.5 dB @ 1300 nm) have been achieved. The measurement results show good agreement with the calculation output of a physical model of reverse bias driven pin junction, used to design the ERM. The use of the ERMs inside a 1300 nm active-passive platform is tested with the realization of tunable laser systems. The development of a steady state laser spectral model based on compact model of different components such as passive waveguides, ERM and SOA has been described. In this way it is possible to obtain predictions on the behavior of multiple laser designs using this platform. The evaluation of this transfer matrix model is done with the comparison of its prediction with the tuning range measurements of a tunable laser cavity design at 1300 nm. A tuning range as wide as 25 nm has been observed for a tunable Vernier laser. Due to the insertion loss of 0.5-1 dB/MMI coupler and the straight waveguide propagation loss of 2.5-3 dB/cm, the tuning range of monolithic lasers realized on such 1300 nm integration is measured as 30 nm. A detailed analysis of the wavelength dependent losses of the passive components can help to identify the causes of such reduced tuning range in the measurements. As a future direction, it is possible to test the influence of the passive cavity length or the length of the intra-cavity SOA to the laser tuning range. The amplifier length of the laser can in principle be tailored to obtain 80 nm of tuning range, which equals the gain bandwidth (FWHM) at an injection current density of 7 kA/cm^2 . A preliminary study of the laser tuning capabilities in relation to OCT has been performed. This is done with the creation of a look up table to link the lasing wavelengths to the control settings in a sequential way.

6. CONTROL SETTINGS OPTIMIZATION AND STEP-WISE WAVELENGTH SCANNING OF AN INP MONOLITHICALLY INTEGRATED TUNABLE LASER AT 1550 NM

An InP integrated widely tunable laser at 1550 nm is investigated in a fast stepwise scan configuration as a step towards its use as a swept source in optical coherence tomography (OCT) applications. The laser is realized on a generic integration technology platform. It consists of a gain medium and a bandpass filter with 3 cascaded asymmetric Mach-Zehnder (AMZI) interferometers. In this chapter, we show the steps to obtain a linear stepwise fast wavelength scan of this widely tunable laser source over 50 nm. The tuning of the laser wavelength is first addressed by understanding its behavior through the analysis of the three AMZI filters separately. Then the tuning reproducibility is addressed. An optimized control strategy based on the a-priori knowledge of the coarse and the medium filter tuning is followed by the application of a search optimization algorithm using the Nedler-Mead method to determine the precise settings for each required laser wavelength. The laser is scanned over 1000 different wavelengths with 10 GHz frequency step and sub-GHz accuracy. A fast wavelength monitoring system with sampling rate of 10 kHz has then been introduced in the system. In this way it is possible to compensate for short-term wavelength drift of the emission wavelength of the laser. Through the real-time wavelength measurements 1 kHz scan speed over 50 nm can be realized. The scan speed is currently limited by the speed of the control electronics used to address the Mach-Zehnder interferometers and by the electronic bandwidth of the photodetectors used to measure the laser power. At the end of the chapter a possible solution to increase the wavelength tuning range to 90 nm and beyond is proposed.

6.1 INTRODUCTION

Tunable laser systems are extensively used for sensing and biomedical imaging applications such as optical coherence tomography (OCT) [1, 2]. OCT is a noninvasive medical imaging technique that reveals tissue information down to millimeter depth and with micrometer

resolution. This technique is employed for diagnostic purposes in ophthalmology [3], and bladder [4] and skin cancer detection [5], using frequency swept lasers which have enabled imaging speed of several thousands of 2-D OCT image scans per second [1]. Photonic integrated circuits (PICs) have the potential to satisfy the need of miniaturization e.g., by combining the light source with interferometer optics. Such miniaturization is increasingly of interest in OCT technology to perform diagnostics of internal organs in a minimally invasive way. In addition, an OCT system on a chip would not suffer from misalignment and optical path instability such as free-space and fiber-optics based OCT systems. Efforts to integrate parts of an OCT system on a photonic integrated circuit (PIC) have resulted in the integration of widely tunable light sources on an InP chip [6], [7]. A 74 nm integrated widely tunable laser system [8] has already been demonstrated on this generic integration platform on InP. However, the use of integrated InP tunable laser systems as swept sources for OCT systems needs to address strict requirements of having OCT signal samples at 10 GHz closely spaced wavelengths over a 100 nm wide tuning range, with uniform output power. This metric is needed to perform OCT imaging at 1550 nm with 30 μm axial resolution and 1 mm of penetration depth inside biological tissues. In this chapter a tunable laser system on InP in which reverse biased electro optic phase modulators are used [9], is studied to achieve stepwise tuning with a scan speed of several kHz. A 1550 nm tunable laser design is here investigated; however, the results of this study can be applied to 1300 nm tunable lasers with similar designs. Ideally one would like to obtain a uniform frequency grid over 100 nm of at least 1000 points with 10 GHz equally spaced optical frequencies. Such a regular grid can be used for optical sampling for a fast Fourier transform (FFT) of an interferometric signal coming from an OCT measurement setup. A robust control mechanism for the laser is also developed to achieve near equally spaced stepwise laser tuning over 50 nm. A real-time wavelength meter that monitors the laser output with a fast (10 kHz) read out helps us to obtain the actual sampled optical frequencies. These can then be used for a non-uniform discrete Fourier Transform of the recorded OCT signal. The laser scan is tested by analyzing the transmission of the laser system through an external bandpass tunable filter. In section 6.2 the specific laser design chosen for this study is discussed. Measurements of the laser tuning are compared with a steady state spectral model of lasers [154], in section 6.3. The highest tuning resolution is then measured with a sub-pm resolution spectrum analyzer, while linearly tuning the longitudinal cavity modes of the laser. The reproducibility of the filter tuning is addressed, and the potential causes of the poor tuning reproducibility are then highlighted and studied. The results suggested the need of a real-time wavelength monitoring unit to be to measure quickly and regularly the short-term drift of this laser calibration. The wavelength monitoring unit helps to the reorganizing of the output laser signal in time whenever the laser frequencies become not sequential. The results reveal the proper reconstruction of the bandpass filter transmission through the analysis of the laser

sweeps. A scan speed of 1 kHz for 1000 different wavelengths is obtained. The scan speed of the laser is currently limited by the output sample rate used with the control electronics (3 MHz) and by the photodetector bandwidth (1 MHz). In principle scanning up to 20 kHz with a 1000 scan steps can be achieved. The optical switching time between two wavelengths determines the fundamental limit to the speed which can be as high as 50 ns [36]. The use of this tunable laser in a fast scan configuration is a milestone towards its use as a swept source for OCT imaging technique.

6.2 TUNABLE LASER DESIGN

The laser circuit is composed of several building blocks available in a 1500 nm generic integration technology platform on InP [31]. Figure 6.1 a) depicts the schematics of such a laser as described in [29]. A semiconductor optical amplifier (SOA) 1 mm long is used as the gain medium of the laser cavity [103]. The laser cavity consists of a ring resonator with the wavelength selection mechanism achieved by three cascaded Asymmetric Mach-Zehnder interferometers (AMZI), present in the ring resonator and used as spectral filters. Three AMZI stages with different periodicity of the sinusoidal transmission profile are needed to ensure wide tuning range while maintaining single mode lasing operation with high side mode suppression ratio (SMSR), as previously demonstrated by Latkowski et al. [29]. This laser, without the use of Vernier effect, can lead to smoother quasi continuous tuning between adjacent cavity modes, due to the sinusoidal profile of the AMZI. The periodicity of the transmission of an individual AMZI, denoted with its free spectral range (FSR), is determined by the physical length mismatch ΔL_i between the two arms of the AMZI as described in section 5.3.1. In this design, the three AMZIs present FSRs of 66 GHz, 0.9 THz and 9 THz respectively. The multiplication of different sinusoidal transmission profile with wavelength with different periodicities, leads to the selection of a single longitudinal cavity mode in the laser (Figure 6.1 b). The introduction of reverse bias-controlled phase modulators (ERM) is needed to move the peak of the wavelength dependent transfer function which tunes the laser emission wavelength. From the smallest to the highest free spectral range, they are responsible for the fine, the medium and the coarse tuning of the lasing wavelength. The overall cavity length is 1.6 cm, leading to a longitudinal mode spacing of 5.4 GHz (0.05 nm). The introduction of a phase modulator in the cavity is needed to be able to align the longitudinal cavity modes to the maxima of the intra-cavity filters. The wavelength tuning is done through reverse bias voltage-controlled electro refractive modulators (ERMs) that have lengths of 2 mm. These ERMs have an approximately linear phase change of $15^\circ/\text{V}\cdot\text{mm}$ [27]. Their voltage dependent absorption has measured to be as low as 1 cm^{-1} for a reverse bias voltage equal to 10 V at 1550 nm [147]. The filters can then be tuned over the full FSR by biasing the ERM in each interferometer arm separately from 0 to -8 V. One arm tunes the

filter one way, the other arm tunes in the opposite direction. This leads us to the use of seven different voltage control settings to tune the emission wavelength of the laser system. During the tuning of the ERMs present on every AMZI filter, the SOA current and the substrate temperature are kept constant. This was done to avoid as much as possible variations in power dissipation in the laser that can lead to temperature variations affecting the laser tuning. The chip (Figure 6.1 c) is packaged together with a thermistor as a temperature sensor and a Peltier element to actively control the temperature of the substrate (Figure 6.1 d). A polarization maintaining fiber is glued to the laser output to maintain the waveguide to fiber coupling over time.

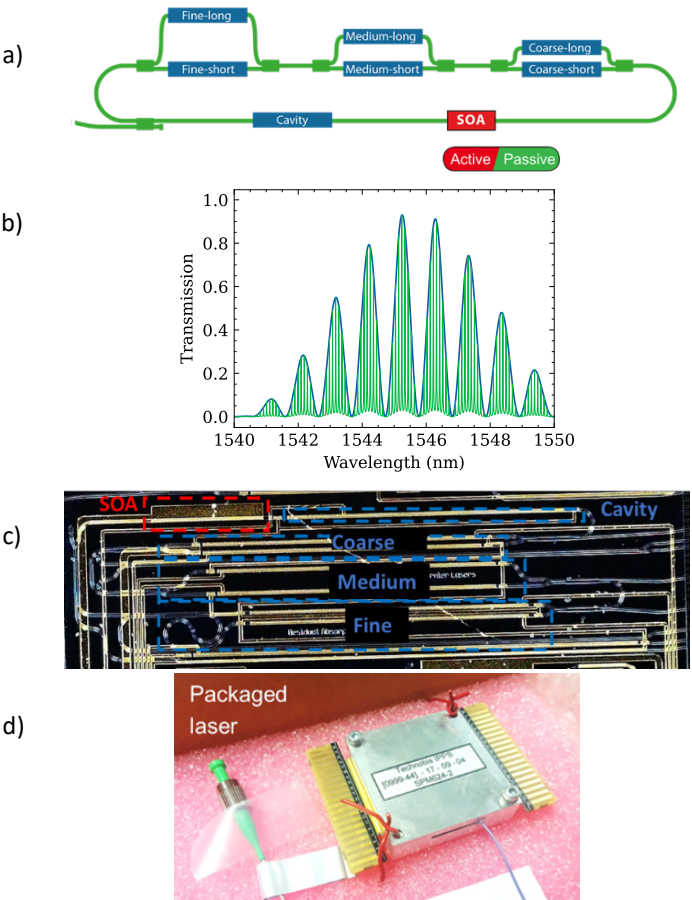


Figure 6.1: a) Schematic of the extended cavity ring laser with three intra-cavity wavelength filters. b) Sketch of the wavelength selection mechanism of the laser, highlighting the intra-cavity filter functions (blue) and the longitudinal cavity modes from the laser ring cavity (green). c) Picture of a chip with a realized tunable laser highlighting the SOA and the filters. d) Packaged laser with the electric pins and the output fiber from Photon First®. For more details on this laser configuration please refer to [29].

6.3 LASER TUNING

6.3.1 INTRA-CAVITY FILTERS TUNING

The effect of the filter tuning on the lasing output wavelength is addressed in this section. The measurement of the filter tuning is done sequentially from coarser to finer tuning elements. In this way, the effects of different filters to the lasing wavelength can be evaluated. The tuning of the filter is compared with the simulation predictions of a steady state laser model as described and used in chapter 5. Please note that in the model used here the phase modulator do not have any residual absorption loss and the MMI coupler properties are assumed wavelength independent. The losses in the cavity in the simulation originate from the passive elements only (waveguides and MMI). The measurements of the laser tuning resolution are performed sweeping the phase cavity section control voltage, which tunes the longitudinal cavity mode positions. The maximum voltage applied on the phase modulators is limited to 8 V in these measurements, corresponding to a phase variation on a single ERM of approximately $8 \text{ V} \cdot 2 \text{ mm} \cdot 15 \text{ deg/V} \cdot \text{mm} = 240 \text{ degrees}$. The maximum voltage is chosen to limit the effects of the residual amplitude modulation (RAM) and the phase modulator non-linearity. The RAM arises from the phase modulator electro-absorption, which is highly wavelength dependent, ranging from 1 dB/cm to 9 dB/cm between 1580 and 1480 nm at 12 V [15]. It is possible to limit the wavelength dependence on the ERM amplitude modulation by limiting the maximum reverse bias voltage to -8 V, which leads to at most 1 dB loss (at 1500 nm) for 2 mm long ERMs. Because of this limitation we can neglect the voltage dependence of the ERM absorption in the simulations. The step-size in the voltage sweeps on the ERMs are chosen differently for the different filters. The coarse and the medium filter are tuned with 0.5 V steps, on both the ERMs in the arms of the filters. These big voltage steps are justified because of the relatively flat spectral profile of the sine shaped wavelength dependence around the transmission maximum. For the fine filter the step-size is halved, due to the steeper spectral profile.

The reverse bias voltages are supplied by a programmable arrayed waveform generator (AWG) card (Spectrum Instrumentation M2P.6566-X4) inside the computer, which is specified to be capable of an output rate of 125 MS/s at 70 MHz bandwidth. The laser calibration starts from forming a tuning map consisting of 1024 coarse and medium filter setting combinations covering the full tuning range of the laser. These setting combinations are determined using the results of the voltage sweeps. During the laser tuning calibration, the SOA current is kept at 150 mA, which corresponds to a current density of 10 kA/cm^2 , and the temperature is fixed to 18°C. Figure 6.2 (a) shows all observed lasing wavelengths for all coarse and medium filter settings, as a function of the coarse (blue crosses) and Figure 6.2 b) as a function of the medium (blue crosses) filters voltage control settings. Note that in the

figure the negative voltage indicates the voltage on one of the two ERMs in the AMZI while keeping the other ERM at 0 volt. The positive voltage indicates a configuration where this situation is reversed. The result is that going from the negative voltage to the positive voltage the filter is scanned continuously over its full range. The tuning results of the coarse and the medium filters are compared with the steady state spectral model simulation results in Figure 6.2 (red dots). Please note that the red dot data have been shifted down with respect to the scale by 10 nm, so dots and crosses do not overlap in the figure. Moreover, the tuning results can be fitted with continuous polynomial functions. The idea behind the fitting is that the effects of the other filters are averaged out and we retrieve the tuning curve of the individual AMZI. The wavelength of the highest peak in the laser spectrum as function of the coarse filter settings can be fitted with a second order polynomial. The medium filter results can be fitted with concatenated independent linear fit, which corresponds to different coarse filter settings. In this way it is possible to obtain some predictive continuous function to relate the control settings to the output laser wavelengths [157].

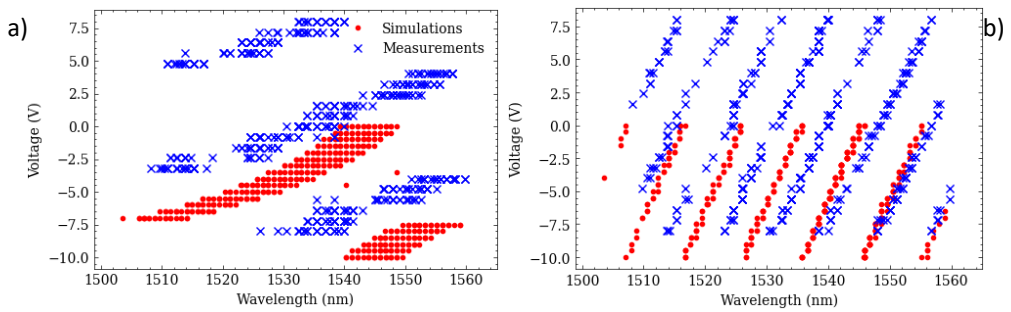


Figure 6.2: Tuning of the Coarse (a) and the Medium (b) filter control settings measured (blue x) and simulated with the steady state spectral model (red dots) Please note that the positive voltage refers to the tuning of the bottom ERM present in the asymmetric Mach-Zehnder interferometer.

To address the gaps between two consecutive wavelengths of the medium filter, the fine filter is tuned over its FSR. A smaller step in the fine filter step is chosen to investigate its behavior as a longitudinal mode selector. Please note that the cavity modes are also tuned due to the phase change induced by tuning one arm of the fine filter. The voltages on the fine filter arms are tuned with 0.25 V steps (approximately 1.4 GHz steps). The lasing wavelength map as function of the control settings is plotted in Figure 6.3 (left y-axis) together with the SMSR values obtained (right y-axis). From the analysis of the laser simulations (Figure 6.3 a), the fine filter acts like a cavity mode selector, where different cavity modes are selected one after the other. In Figure 6.3 a) we can see the simulation results of tuning the output wavelength as function of the fine filter control settings. Similar behavior to that predicted by the simulation is clearly visible in the measurements (Figure 6.3 b). When the SMSR is at the minimum, the two lasing wavelengths are simultaneously

present in the spectrum. Unfortunately, in the measurements it is not always possible to select the longitudinal modes sequentially as predicted by the simulations; we observe different wavelength changes as function of the settings.

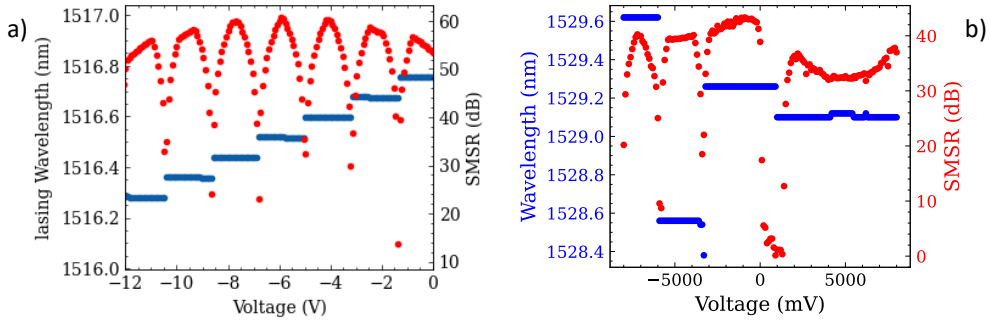


Figure 6.3 a) Simulation and b) measurements of the tuning of the Fine filter settings where the single mode lasing wavelength (blue) is plotted with the SMSR (red) values. The parabolic behavior of the side mode suppression ratio (SMSR) as function of the control settings, shows how the fine filter acts as a longitudinal cavity mode selection mechanism.

As a final step, the tuning of the longitudinal cavity modes of the laser is investigated. This is done by applying reverse bias voltage on the ERM indicated as cavity in Figure 6.1 which controls only the optical cavity length. The laser spectra for different cavity control ERM settings are measured using an optical spectrum analyzer (OSA) with a resolution (Apex AP268x-A) of 100 MHz (0.8 pm). Figure 6.4 a) shows the linear tuning of the lasing wavelength between 1532.155 and 1532.175 (blue dots) keeping the SMSR (red dots) higher than 35 dB for all the five lasing wavelengths. From the graph, it is possible to observe how a single longitudinal cavity mode is tuned over 35 pm. The laser peak keeps a high SMSR, which is a clear indication of single mode laser emission. On Figure 6.4 b) it is possible to evaluate the tuning resolution of this laser. A distance of 3 pm, between two different laser peaks which do not overlap their linewidths can be achieved. It is crucial to understand the influence of the tuning of the individual filters and the phase section on the laser output wavelength. We found that the coarse and the medium filter tuning can be predicted from cold cavity simulations. This is illustrated by the simulation results in Figure 6.2 a) and b), where the red dots show the simulation results. The gaps between two adjacent wavelengths of the medium filter can be addressed by tuning the fine filter. The fine filter acts as a longitudinal mode selector, as can be evidenced from the SMSR function with voltage. Unfortunately, the tuning of the fine filter results in jump between different fine filter maxima and not always between adjacent longitudinal cavity modes. This leads to the necessity of adjusting the coarser filters when a finer tuning element is addressed. Moreover, the control setting resolution influence the wavelength tuning differently for different emission wavelengths. A high-resolution uniform wavelength or frequency grid needs to be created by addressing all

the possible combinations of all the filters. The main reason for the differences between the simulation results and observations are a few points neglected in the simulations and unknowns. The wavelength dependent behavior of the MMI in transmission and phase is neglected in the simulation and reflections inside the laser cavity are possible at e.g., active/passive interfaces but their position and amount of reflectivity are unknown.

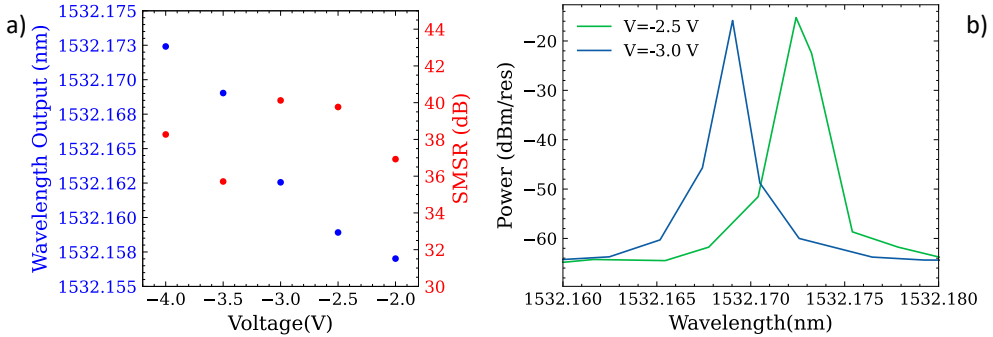


Figure 6.4 Spectra b) and Tuning Figure a) of the laser system for different inline phase modulator (cavity) voltage settings.

6.3.2 LASER STABILITY OVER TIME

To create a look-up table (LUT) for the laser by addressing all the filter simultaneously, the total number of control settings combinations required scales exponentially with the voltage resolution and the number of controls. This will in turn lead to a quite long wavelength calibration time of several days, considering that every laser spectrum acquisition takes a few seconds at the fastest settings of a typical OSA. Unfortunately, the laser is not sufficiently stable even over the time that kind of calibration takes. We have observed that in continuous operation the lasing wavelength drifts substantially. Figure 6.5 shows how using the same control settings over 2 days, the laser shows significant wavelength drifts. The lasing wavelength drift observed is around 10 pm (1.3 GHz) every 3 hours. Sometimes larger drifts can be observed due to the misalignment of the filters that start occurring with respect to the longitudinal cavity modes, as can be seen in Figure 6.5 a) after more than 1000 minutes. This leads us to investigate the origins of this wavelength drift over time. According to our evaluation, the main reason is related to small changes in temperature over time. Attempts to get back to the original wavelength at the start of the measurement by only changing the temperature of the chip were not successful. A small change in temperature distribution over the chip can also lead to different changes in relative optical path lengths which will affect the tuning of the laser. When intracavity reflections are involved, the relative positions will change and there will be an effect on tuning of the laser wavelength as well. The time dependent variations of power dissipation in the SOA in combination with properties of the

non-hermitically sealed laser packaging can in principle cause non-uniform temperature variations inside the laser cavity. An additional measurement was done to study the effect of a uniform temperature change, by varying the substrate temperature. When the temperature is uniform in the laser circuit, the lasing wavelength increases linearly with the increase in temperature. The linear slope of $130 \text{ pm}/^{\circ}\text{C}$ between lasing wavelength and temperature agrees with [19], which indicates a $120 \text{ pm}/^{\circ}\text{C}$ thermal tuning in the ERM due to temperature induced effective index change. In this way we can notice how local temperature changes smaller than 10 mK can lead to 12 pm wavelength drifts in the output laser wavelength.

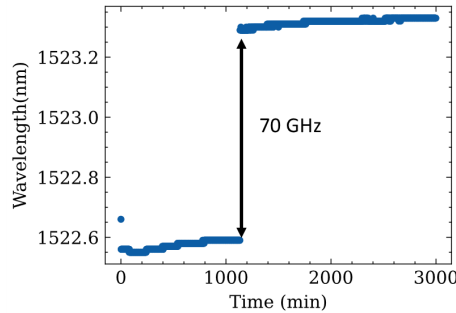


Figure 6.5 Lasing wavelength as function of operation time applying the same control settings.

As well as temperature, the humidity of the air can act as external factor to the laser tuning. The vapor present in the air increase the stress between the polyamide and the quaternary waveguiding material [20], which can induce differences in the refractive index and optical path lengths in the filters thus leading to a change in the emission wavelength. Controlling the temperature and the humidity variations within the chip is very difficult in practice in our packaged chip. Mounting an active cooling system on top of the device is currently not feasible without damaging the device and the wire bonded connections to the PCB. For these reasons, real-time wavelength monitoring of the laser is necessary to keep a track on the drift of the calibration and find ways to compensate for this effect.

6.4 CALIBRATION STRATEGY FOR THE LASER SWEEP

In this section we present a new calibration approach for an InP widely tunable laser sweep over 50 nm , from 1515 to 1565 nm . The first step is the development of a look up table (LUT) for the control settings of the laser for a set of emission wavelengths. The method for finding the setting uses an optimization (direct search) algorithm for finding these setting accurately and fast [30]. This LUT is then used, and the laser performance is monitored with a high resolution (1 pm) wavelength monitoring unit that is based on a fiber Bragg grating

interrogator and that is capable of sending out a wavelength reading up to 19 kHz. Due to the lack of reproducibility of the laser calibration, the wavelength monitoring is a crucial step. In this way it is possible to use such a laser in a scan configuration knowing its wavelength at each step in the sequence of the scan. And using this fast readout monitor one can measure 1000 wavelength settings within 0.1 s. This can therefore easily be done frequently, e.g., every minute of imaging where the laser needs to scan at full speed (e.g., at 20 kHz scan repetition rate). Scanning the laser in these ways is tested by measuring the transmission of a tunable bandpass filter. By tuning the filter over the laser wavelength range the quality of the complete scan can be investigated. Due to the lack of reproducibility of the laser, a uniformly distributed frequency grid is hard to achieve over a laser scan. The wavelength tracking of the laser will therefore require the use of the nonuniform discrete Fourier transform and leads to the possibility of applying e.g., sparse sampling Fourier transform technique to obtain OCT signal images.

6.4.1 EQUALLY SPACED WAVELENGTHS LOOK-UP TABLE

In this sub-section we describe the way the lasing wavelengths are linked to the voltage control settings on the filters in a sufficiently fast way to keep the calibration up to date [30]. First a LUT is developed to obtain settings for 1000 different wavelengths between 1515 and 1565 nm. This takes approximately 8 hours. For this LUT an optical bandpass filter (BPF_1) is used to get the output power of the laser at a specific wavelength. The filters and the cavity phase modulator settings are changed to maximize the output power from the bandpass filter as in [158]. To accelerate the speed of this calibration, a search optimization algorithm is used to search the appropriate control settings. The optimization search algorithm used is the Nelder-Mead method [159]. It is a direct search method for optimizing a target function. In our case we aim at maximizing the output power transmitted from the bandpass filter. This function has a 7-dimensions domain as the numbers of ERMs to be driven. To pursue the optimization, the target function is evaluated in 8 points of the search domain, describing the vertices of a polytope. Depending on the interrelationships between the values acquired by the target function, the polytope can go through reflections, expansions, contraction or shrink to improve the output power at least in one vertex, as shown in Figure 6.6 b). The algorithm converges when the vertices degenerate, within a certain tolerance. In our case, as starting vertices for the optimization, we chose the coarse and the medium filter configuration already measured in section 6.3 which present a single mode lasing condition with wavelength distance smaller than 0.5 nm from the target wavelength. Please note that if more than 8 coarse and medium filter configurations satisfy the requirements stated above, the first 8 configuration with the highest SMSR are chosen as the polytope vertices for the initial condition.

The experimental setup schematics is shown in Figure 6.6 a) and is described here briefly. The laser output is split with the use of a 90/10 optical coupler. The 90% of the output power is transmitted through a commercial (JDS TB9 optical grating filter) tunable bandpass filter (BPF_1). The BPF_1 has a gaussian shape with a 3-dB bandwidth of 0.3 nm and its center wavelength can be tuned with 10 pm steps. The transmitted output power is measured with a power sensor (Agilent 8163B). After the optimization is done the laser spectrum is recorded with the OSA to measure the exact lasing wavelength with 10 pm resolution and the SMSR. The BPF_1 is then moved to the next wavelength and the optimization is repeated to obtain the subsequent configurations.

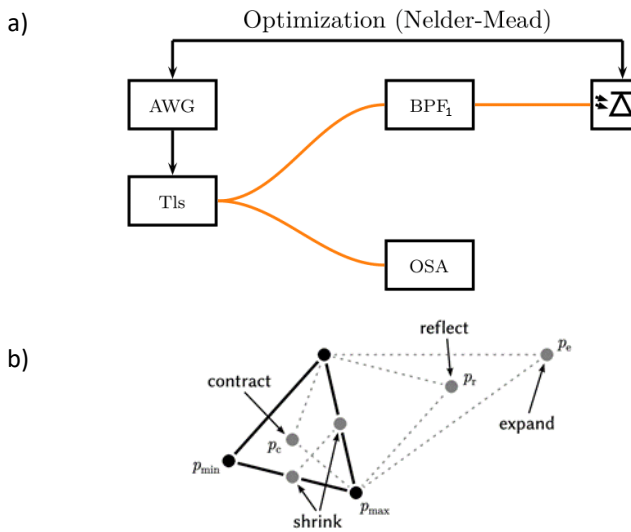


Figure 6.6 a) Schematics of the control strategy setup. The laser (Tls) output power is split in two. Part is going through a bandpass tunable filter (BPF_1) at a specific wavelength and then on a photodetector. The optimization is finalized to obtain the combinations on an arrayed wave generator (AWG), which maximizes the power reading on the photodetector. For the optimized condition an optical spectrum (OSA) is recorded as a confirmation. b) Example of the possible configuration changes on a 2-Dimensional search domain. Note that the initial conditions, which are the vertices of the polytope, are taken as the coarse and medium filter configurations which give a wavelength as close as 0.5 nm with respect to the target wavelength which is set on the external bandpass filter.

Figure 6.7 (a) shows a two-dimensional map of the laser spectra obtained with this control strategy, as function of the wavelength set on BPF_1 (y-axis). It is possible to see how the wavelengths lie on a linear function. There is a presence of a small gap around 1519 nm, where the optimization algorithm does not find any lasing peak. This can be due to the presence of spurious reflections which lead to some forbidden lasing conditions. The SMSR is not always higher than 30 dB, as can be seen from the presence of lower power at exactly

one medium FSR from the main laser mode of operation. An example of this multimode behavior in the LUT is shown in Figure 6.7 b) for the blue curve. It is possible to see the presence of 10 dB difference between the lasing power at two adjacent medium filter maxima (8 nm far apart). This multimode behavior will cause uncertainty with the fast wavelength monitor which currently assumes single frequency input. If we can keep the environmental conditions fixed, it should be possible to overcome the multimode operation situation by using multiple probabilistic restarts to find different voltage configuration to obtain a global maximum of the laser power at the target wavelength [160]. Moreover, it is important to mention that the bandwidth of the BPF_1 is a strong requirement in the calibration [30]. When the 3-dB bandwidth of BPF_1 is bigger than twice the longitudinal mode spacing in the laser cavity, i.e., $2 \cdot 0.05 \text{ nm} = 0.1 \text{ nm}$, the optimization algorithm might find a maximized power for dual mode lasing operation, where the lasing wavelengths are closer than the filter bandwidth.

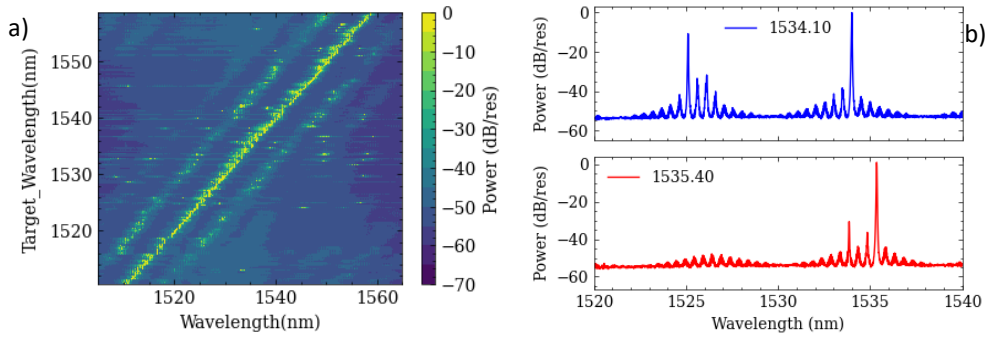


Figure 6.7 (a) Recorded laser spectra as function of the target wavelength presented as a 2D map and (b) an example of laser spectra with a multimode behavior (blue) to be compared to (c) a single mode behavior example (red). The label of the plots is the target lasing wavelength, the center of the passband filter BPF_1 . It is visible how two adjacent maxima of the medium filter transfer function are suppressed in one case and not entirely in the other, leading to partial multimode lasing conditions.

6.4.2 WAVELENGTH MEASUREMENTS WITH A FAST READ-OUT UNIT

The stability of the LUT, which correlates the lasing wavelength to the control settings is tested in this sub-section. A fast (10 kHz sampling speed) fiber bragg grating interrogator (Gator Photon First®) is used to measure in real time any possible drift of the wavelength calibration. This Gator unit can measure the lasing wavelength with a 1 pm resolution over 70 nm between 1500 and 1570 nm. Its use allows for a real time detection during a laser scan of 10 Hz (10 kHz sampling for 1000 points). Inside the Gator, the wavelength is calculated from the power measurement of an array of photodetectors at the output of an integrated multichannel spectral filter system. The algorithm calculates the wavelength from the current levels on several detectors (48 detectors divided in 8 channels). This real-time

measurement is beneficial to perform a laser sweep to detect any possible calibration drift. This allows to reorganize the intensity data recorded in the laser scan as function of time into intensity data as function of wavelength. The experimental setup shown in Figure 6.8, is used to perform laser sweeps. The output of the laser is split in three different parts. The 10% of the output power is collected by the Gator and is used to measure the lasing wavelength. The 90% of the power is split in two parts and is measured with two different photodiodes (Thorlabs PDB450C) and recorded with a real time oscilloscope (RTO). One photodiode measures the total output power of the laser, while the other channel collects the transmission through an external bandpass tunable filter (BPF₂). The BPF₂ has a 1 nm FWHM and can be tuned between 1520 and 1570 nm. To correct for variations in laser power with each wavelength, the recorded transmission of the filter is normalized with the laser output power at each scan step.

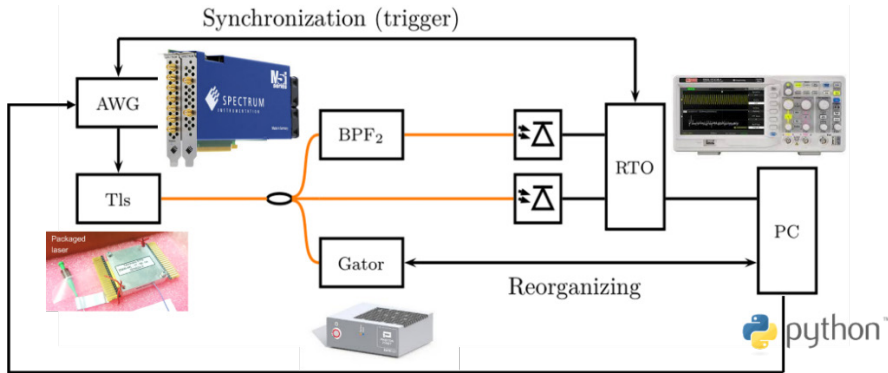


Figure 6.8 Experimental Setup for the measurement of a fast scan of the integrated tunable laser system. The light from the Tunable laser (Tls) that is controlled by the multichannel arbitrary waveform generator (AWG), is split into three different fibers. The Gator measures the wavelength of the lasing light. The laser scan is tested with the transmission over a bandpass filter (BPF₂). The signal in time recorded by the real Time oscilloscope (RTO) is reorganized with the reading of the Wavelength Read-Out unit (Gator). Thus, the signal in time is converted into signal as function of lasing wavelength and the BPF₂ can be characterized.

The wavelength reading on the Gator unit depends on a threshold setting for the signal strength on its detectors. Obviously if the setting is too high no wavelength value is reported. If it is set to a low value, too many spurious signals from the detectors make that the Gator software does not respond with the correct wavelength. Please note that the output power of the integrated tunable laser system under test strongly depends on the emission wavelength. The main practical issue that arises from the fact that the threshold cannot be set dynamically sufficiently fast in the current firmware of the Gator. The optimal threshold setting arises from a trade-off between obtaining the maximum number of single mode points and at the same time the minimum number of multimode laser configurations which give rise to above threshold signals on multiple sensors which cannot be interpreted by the

current firmware. The laser output generated by the 1000 configurations in the LUT of section 6.4.1 are fed into the Gator unit to measure the wavelength in real time. The clock of the AWG for the scan step rate is chosen to be 10 kHz to match the sampling speed of the Gator. The scan step rate can influence the real-time monitoring of the Gator for two reasons. First having the same measurement time as the scan step means that the read-out is influenced by the output of the laser while it is switching. This effect is negligible due to the faster scale of the wavelength switching time (50 ns), with respect to the Gator sampling time (100 μ s). Secondly, the absence of the trigger leads to the absence of perfect synchronization between the change in the control setting and the wavelength reading. This can lead to variations in the measurements from the expected lasing wavelength. Figure 6.9 shows the Gator wavelength measurements and the detuning with respect to the wavelength in the LUT. The detuning is smaller than 1 nm for more than 80% of the lasing wavelengths and can be attributed to environmental conditions changes during the scan. However, the Gator reading can present deviations as big as 8 nm, as observed from the red dots. This is due to some mode hopping between different maxima of the medium filter, as evidenced already in section 6.4.1. Moreover, the wavelengths are not evenly distributed over the whole wavelength range. This can be attributed to small time-dependent reflections inside the laser which lead to more stable wavelength configurations, as was investigated in [157]. This measurement represents clear evidence of the need of a real time wavelength read-out system to compensate for any drift over the lasing output wavelengths.

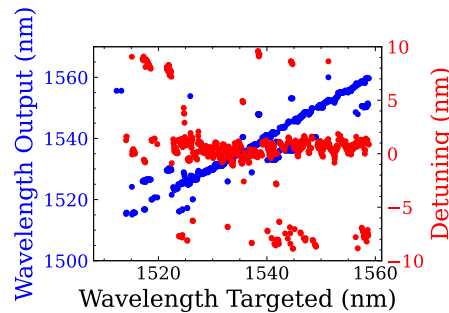


Figure 6.9 Recorded wavelength output as function of the target wavelength of the look up table (blue). The deviation of the measured wavelength (red dots) in real time with respect to the measured single mode lasing wavelength with the search optimization method.

6.4.3 TUNABLE LASER SCAN

The performance of this system is evaluated through scanning the laser and measuring the optical power spectrum at the output of the BPF₂. Please note that the Gator does not have the option for any input trigger. This limits the accuracy of the simultaneous reading to 100 μ s. Since the laser control settings are driven in reverse bias mode, the tuning speed is much

higher (MHz), then the wavelength sweeps allowed by the Gator (20 kHz). The wavelength reading cannot be simultaneous with scanning rates higher than 20 kHz. The transmitted optical power after BPF1 is recorded on a 1 MHz bandwidth photodiode and a RTO. A trigger signal is sent from the control setting laser driver to the RTO at the beginning of the sweep to start the acquisition (orange curve in Figure 6.10 a). The BPF₂ transmission is shown in the blue solid curve, where it's clear that the laser does not always emit consecutive wavelengths in time during the scans. The total output power (green curve) of the laser is also recorded during the laser scan. Figure 6.10 b) highlights the output spectrum for a single BPF₂ position along the laser scanning range. Combining the time traces of the oscilloscope and the read-out of the Gator (wavelength meter) it is then possible to reconstruct the time signal into an intensity signal as function of wavelength. Figure 6.10 c) shows the reconstructed signal as function of wavelength together with the gaussian shape of the filter transmission. The gaussian curve is assumed to be centered at the maximum transmission, as BPF₂ can be tuned only manually. The presence of some points outside the gaussian shape of the filter in Figure 6.10 c), can be due to the lack of simultaneous acquisition of the RTO and the Gator. It's worth to notice that these issues can be solved if a common trigger was shared by the RTO and the Gator. When not recording the wavelength the scan speed can be increased. Here we have used the scan rate of 1 kHz, which means a waveform sample output rate (clock speed) of 1 MHz in the laser control setting driver is used. The clock speed that can be used is currently limited by the bandwidth of the photodetector (1 MHz) used in the output power measurements. The optical wavelength switching time has not been addressed here, since it has been verified to be much faster (10-50 ns) than the electronics sampling (1 μ s) time, in previous measurements of the same laser cavity design [12]. In Figure 6.11 it is possible to see the evaluation of the laser scan at 1 MHz for three different bandpass wavelength transmissions of the filter. The different behavior in the laser stability over the scan can be evaluated. Since the wavelength reading is assumed the same as the one of several minutes before, the behavior of the laser scan can be studied by moving the bandpass filter in different regions. When the filter is centered at 1525 nm (Figure 6.11 a), it is clear how during the sweep of the control settings, the laser is not emitting light at wavelengths around 1519 and 1522 nm. In Figure 6.11 b), the filter is centered at 1533 nm. In this stable region the wavelength is not drifting over minutes and the Gator reading is experimentally verified to not drift significantly, when calibrated with an external commercial laser (Agilent 8613A). It is possible to fully reconstruct the filter gaussian shape. In Figure 6.11 c), we can notice the presence of multimode behavior, or unstable laser operation. We can notice the presence of a second peak 8 nm smaller than the filter center of 1555 nm. This can be since the laser presents poor SMSR at those wavelengths and small changes in the environment can lead to the lasing emission at the adjacent medium filter maximum transmission. The presence of outliers and spurious points out of the BPF₂ bandwidth can be due to the low photodiode

bandwidth (1 MHz), with respect to the AWG sampling rate (1MHz). This can lead to measurement errors when the laser makes large wavelength jump from scan step to scan step. By using this system, we can reorganize the optical wavelengths and maintain the laser's stability over time. This can be done with scan speeds up to 1 kHz in a stepwise tunable laser system. We have tested our 1 kHz laser scan with a range of 50 nm and 1000 laser points, taking us one step closer to using this laser in OCT measurements.

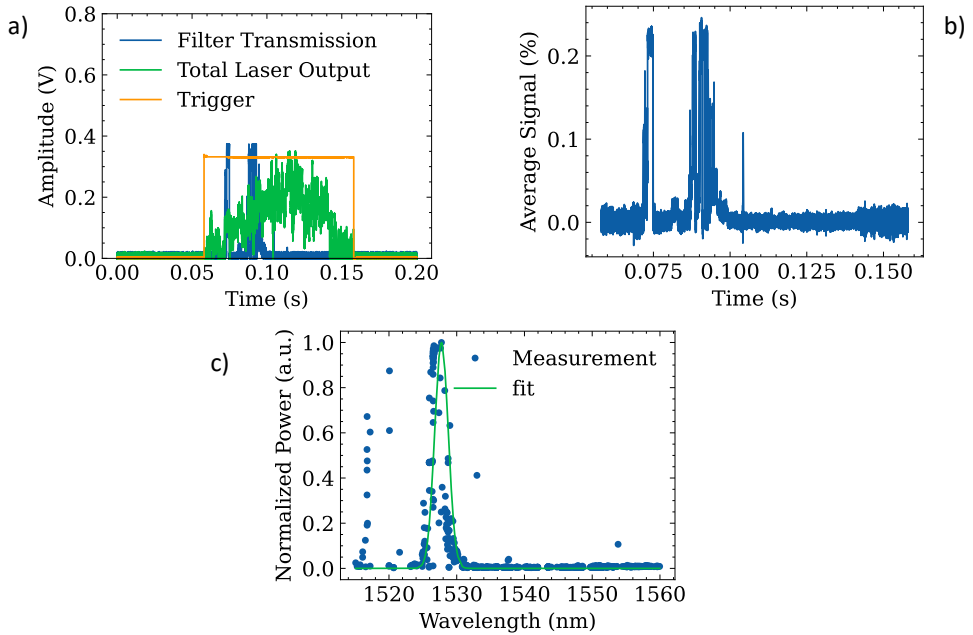


Figure 6.10 a) Time dependent signals for the wavelength scan. It is possible to see how at the start of the trigger (orange signal) the total laser power (green) increases and the transmitted power at the output of the filter (blue) is present only for certain amount of time. Please note that the total power has been offset down to better visualization of all the three signals. The measurement of the spectrum is done within 100 ms (10 Hz) since the waveform sampling is maintained as the same readout sampling rate of the Gator. b) The relative amplitude transmitted through the filter is referenced with respect to the power of the laser. c) Filter function reconstruction through the analysis of the relative time trace in Figure 6.10b) and the wavelength readout of Figure 6.9.

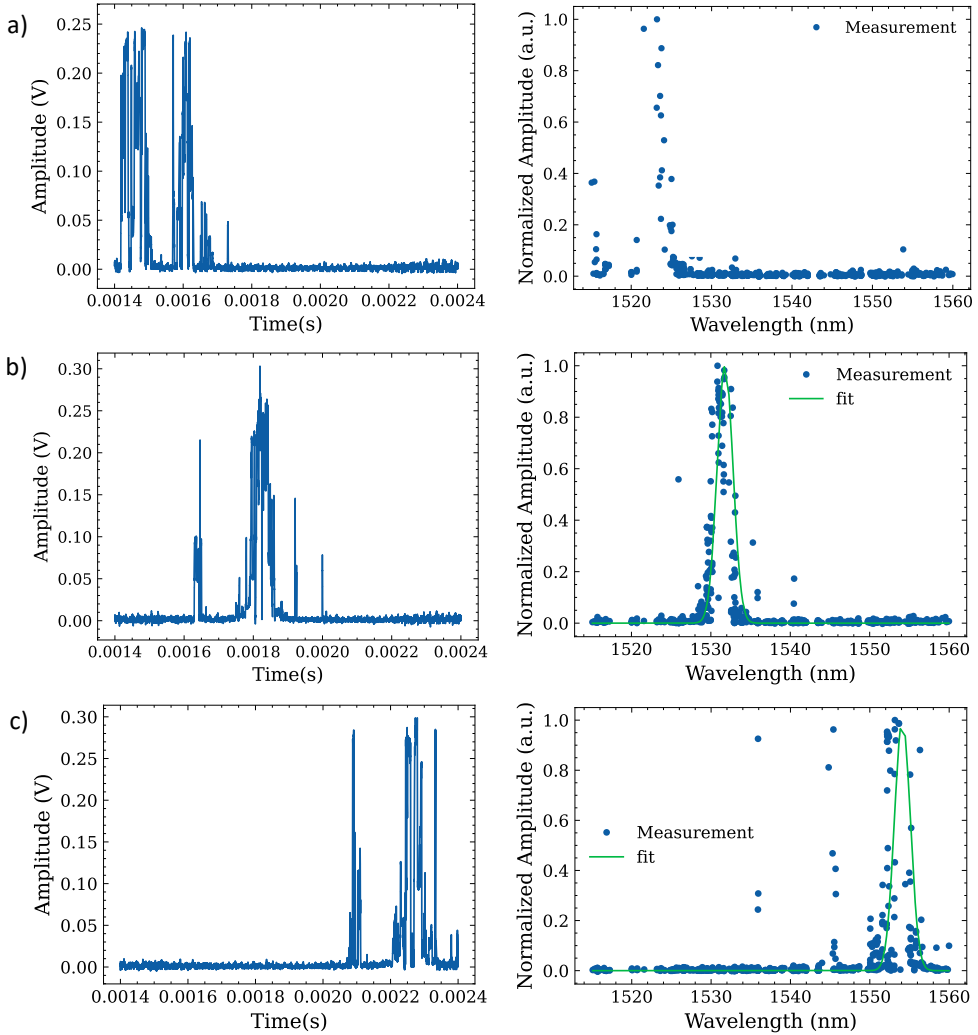


Figure 6.11 a), b), c) Examples of transmission measurements using the tunable of the tunable band-pass filter positioned at three different wavelengths with respect to the laser tuning range. It is possible to observe three very different situations. a) The absence of wavelengths measured by the Gator unit at the filtering wavelength. b) A stable wavelength region which is not affected by big calibration drifts over minutes. c) A highly multimode region which leads to big drift in the actual laser output wavelength with respect to the Gator read-out a few minutes earlier.

6.5 CONCLUSIONS

In this chapter, we have presented and investigated the use of an integrated InP based tunable laser system for a scan speed of 1 kHz over 50 nm in the 1500 nm wavelength region.

The first step was the development of a control strategy for the wavelength calibration of a tunable ring laser system containing asymmetric Mach-Zehnder modulators as tunable filters. A calibration method with 0.1 nm evenly spaced optical frequency over more than 50 nm, was demonstrated on an integrated laser with 2 mm ERMs. The calibrated wavelengths are then tested with a fast wavelength read-out unit (10 kSa/s) to compensate for any short-term calibration drift. It is possible to integrate the wavelength monitoring unit on the same chip as the laser using an approach like what has been done in [25] for Si based and in [26] for InP based wavemeters. It can be beneficial since the laser and the wavemeter can share the same heat sink. Higher scan rate will also be achieved with the use of photodetectors with bandwidth of several GHz. Laser scan with different scan speeds (10 Hz-1kHz) have been investigated through the analysis of the transmission of a bandpass manually tunable filter at the output of the laser. The suitability for OCT still must be proven in future measurements, due to the presence of several gaps in the laser tuning and imperfect reading of the wavelengths in the Gator due to multimode operation and power fluctuations. This can be improved by multiple real-time wavelength readings with slower calibrations stepwise scan (1 – 5 Hz), and by reducing the spurious reflections coming from the passive components in the laser circuit during the design phase of the functional photonics building blocks. The use of electronic synchronization between the Gator and the oscilloscope can help neglecting measurements artifacts. Moreover, as a future development, a different wavelength monitoring unit design can be implemented to discriminate between multimode configurations with 8 nm or closer lasing wavelengths. With the current system, the use of non-uniform FFT or digital signal processing techniques are needed to use this laser as a swept source in OCT measurements.

6.6 DESIGN IMPROVEMENTS TO INCREASE THE LASER TUNING RANGE

6.6.1 LASER DESIGN

As an outlook, a new laser cavity design has been realized to improve the tuning range of the laser, and to reduce the build-up time of the laser to achieve higher limit for scan speeds compared to the design in Figure 6.1. The schematic of the design is presented in Figure 6.12 a) and a photograph of the realized and package mounted chip is in Figure 6.12 b). The key feature of this laser cavity is the presence of a variable output coupler that functions as an independent threshold control mechanism, as previously explained in [161]. The principle is that the threshold carrier density can be controlled accurately to have the widest gain spectrum in the SOA possible. A semiconductor optical amplifier (SOA) 800 μm long is used

6.6 Design improvements to increase the laser tuning range

as the gain medium of the laser cavity [103]. The laser cavity consists of a ring resonator with a balanced Mach-Zehnder modulator (MZM) as output coupler. The MZM uses two-by-two port multimode interference couplers (MMI) and the interferometer is controlled by a voltage-controlled phase modulator in each arm. The overall cavity length is 7.47 mm, leading to a longitudinal mode spacing of 11 GHz (0.09 nm). This cavity design implies a reduction of 9 mm in the overall cavity length with respect to the laser design discussed in the section before [14]. The reduction in length was mainly achieved by using 1x2 MMIs in the AMZIs and reducing the length of the ERMs as well as using curved ERMs. With this increase in cavity mode spacing, the filter transfer functions could be designed to achieve at least a 10% of power loss between two adjacent longitudinal cavity modes, or adjacent AMZI transmission maximum. This increase in selectivity between the modes not only improves SMSR values but it also makes the switching between wavelengths faster. The price to pay is the need for higher voltages on the ERM for tuning with increasing losses.

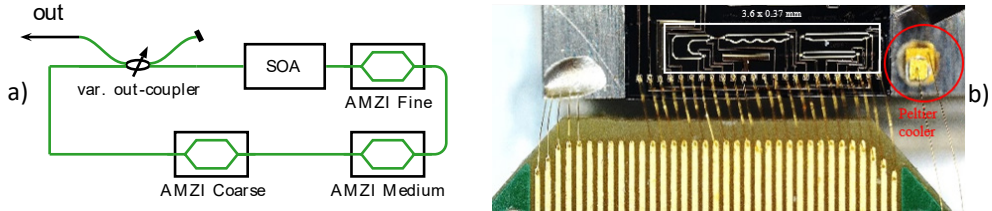


Figure 6.12: a) Schematics of the tunable laser ring cavity. (b) Picture under the microscope of the package laser system from Photon First ®.

6.6.2 OUTPUT COUPLER CHARACTERIZATION

The behavior of the MZM used as output coupler is characterized before analyzing the laser tuning range. To measure the voltage dependent out-coupling fraction as function of the reverse bias applied to both arms, the photocurrent on the SOA is recorded for different reverse bias settings on the MZM arms, when an external laser light at 1550 nm is sent into the laser system via the output waveguide. The result is presented in Figure 6.13 a). It is important to mention that the voltage applied is always negative and the sign in the x-axis refers to the reverse bias tuning of the top (+) or the bottom (-) arm of the MZM respectively. From the normalized out coupling fraction, it is possible to see that a 9 dB difference in the out-coupling fraction can be achieved by tuning the ERMs inside the MZM. Since different MZM voltage settings led to different effective loss inside the ring cavity, the out-coupling fraction impacts the threshold current density of the laser and the threshold 3-dB gain bandwidth. Higher cavity loss will result in higher threshold current densities which lead to wider gain bandwidth and an extended laser tuning range. For the same voltage setting on the out coupler, it is possible to maximize the tuning range and the output power in fiber simultaneously. Measuring the laser sub-threshold spectra, it is possible to verify the spectral

behavior of the MZM as a function of its settings. Figure 6.13 b) shows the sub-threshold laser spectra as function of the MZM voltage for a fixed amount of injected current density in the SOA ($J=3.125 \text{ kA/cm}^2$). The ring cavity spectral feature is more visible when the outcoupling normalized fraction is smaller, which means that a bigger fraction of the light generated in the SOA is travelling inside the ring laser cavity before being coupled out. The introduction of the output coupler can in principle also be beneficial to tune the laser output power to be uniform within the tuning range. However, this is not independent on the tuning of the laser. Analyzing the 2 V sub-threshold spectrum (purple curve), it is possible to notice a small dip around 1520 nm, which is currently attributed to reflections inside the two 2x2 3-dB MMI coupler present in the balanced MZM. Although such a dip looks small, it is 1 dB and will have a significant influence on the tuning of the laser since it is larger than the loss differences of the different cavity modes due to the AMZI filters. Moreover, it is possible to notice how gaps in the tuning range can vary with the control settings applied to the ERMs in the output coupler.

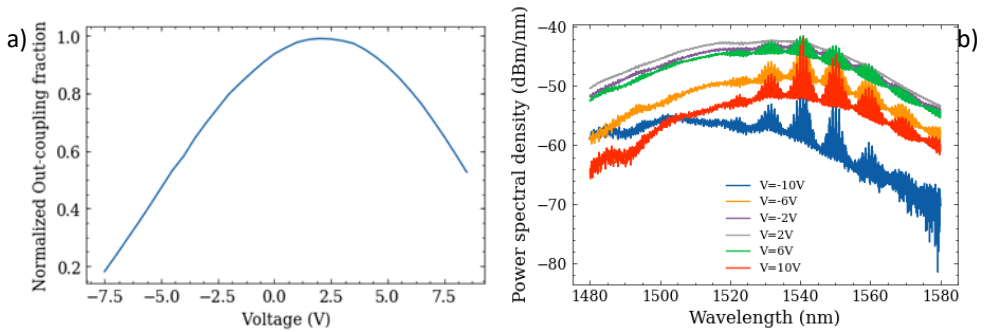


Figure 6.13: a) Normalized outcoupling fraction as function of Voltage in the MZM arms. b) Subthreshold laser spectra as function of the out-coupler voltage.

When the laser is running above threshold ($I=160 \text{ mA}$, $J=10 \text{ kA/cm}^2$), it is possible to investigate the effect of the out-coupler on the laser tuning range. Higher output coupling fractions lead to increased tuning range. We can see how for an out-coupling fraction of 55%, the laser tuning range is limited to less than 60 nm tuning range (Figure 6.14 a), while for a 99% of out-coupling fraction the tuning range is extended to more than 85 nm (Figure 6.14 b). Moreover, higher out-coupling fractions present lower lasing wavelengths. This agrees with the blue shift of the gain spectra with higher threshold current densities [14]. The presence of tuning gaps in the wavelength maps is depending on the out-coupling fraction. This leads us to think that the out-coupler is acting as a fourth frequency filter inside the laser cavity, due to some fabrication imperfections in the 3-dB MMI couplers.

6.6 Design improvements to increase the laser tuning range

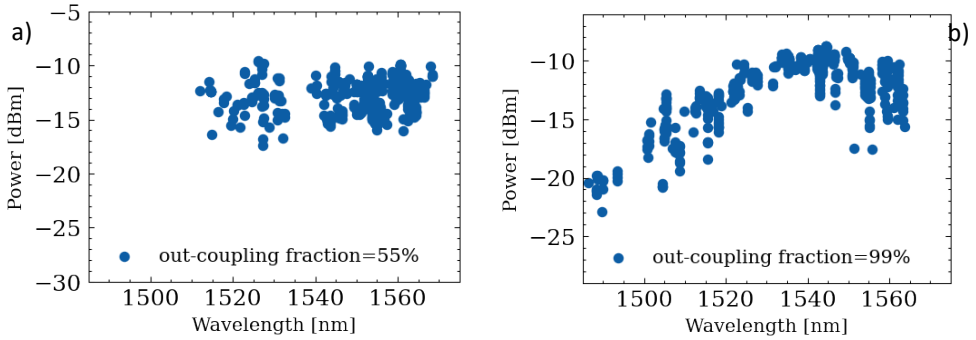


Figure 6.14: a) Laser peak wavelengths and power as function of the Out-coupling fraction. It is possible to see how higher intra-cavity loss increase the tuning range from 60 to more than 85 nm tuning range, but it also reveals a blue shift in the tuning gap from 1520 to 1500 nm.

The goal of the following analysis of the variable output coupler is to investigate whether its presence leads to a de-facto introduction of an additional spectral filter inside laser cavity. Such a wavelength dependent transmission can occur due to a wavelength dependent coupling and phase relation between the two ports on one side of the MMIs in the balanced MZM. This can also lead to a difference in wavelength response between using the phase control setting on one of the two arms.

To establish these effects, we measure the response of the variable out coupler by isolating this element from the rest of the cavity. An external input laser light at 1550 nm is injected in the laser circuit via the output waveguide. This is transmitted through the variable output coupler. One MMI port connects to the SOA and the light is completely absorbed by the optical amplifier which is now reversely biased. This also makes that no resonances are visible from the laser cavity. The other port from the MMI near the SOA is connected to an MMI mirror which sends the light back through the MZM and the output waveguide. The output coupler behavior can thus be studied by analyzing, with a circulator, the reflected light from the circuit which is passing twice in the MZM (Figure 6.15 a). Figure 6.15 b) shows the reflected power, when 12 dBm are injected, as function of the reverse bias voltage applied to the out-coupler arms. It is possible to see how the lasing power follows a sinusoidal curve as function of the voltage control settings in each MZM arm. The extinction ratio is 25 dB for a double pass of the light in the MZM out coupler. From Figure 6.15 b), it is possible to notice how between 0 and 5 V the reflected power is at its minimum value, which identifies the maximum out-coupling fraction in that region. The minimum of the voltage dependent reflected power in Figure 6.15 b) at 2 V coincides with the highest normalized out-coupling fraction. Different voltage control settings give equal 1550 nm lasing output power because of the same phase interference between the two arms. To extend the analysis over the full wavelength range, we measure the reflected spectrum with an optical spectrum analyzer

(OSA), when light from a broadband source (spontaneous emission from an Erbium doped Amplifier) is sent into the circuit. Figure 6.15 c) shows the spectral response of the MZM, with an input broadband source with constant power between 1530 and 1580 nm, for two voltage settings conditions which give same lasing power output at 1550 nm.

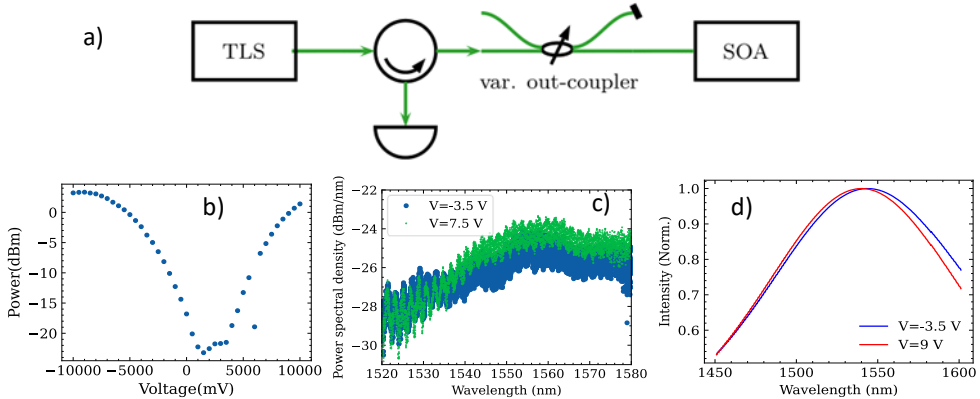


Figure 6.15: a) Setup schematics used to characterize the variable output coupler as a MZM. b) Transmitted power to two times the output coupler for 12 dBm of input laser light at 1550 nm. c) Output power spectral density for $V = -5$ V (blue) and $V = 9$ V (green) out-coupler control settings of Figure 6.15 b) and 50 mA of EDFA current. d) Simulations of a balanced MZM transmission with same interference phase condition for 1550 nm, with a small fabrication error in the 2x2 MMI coupler widths.

The spectral response for a voltage of -5V applied to the top arm and for a voltage of -9 V applied to the bottom arm are plotted in Figure 6.15 c). The two curves are expected to give an identical phase response over the whole wavelength range as they are showing for input light at 1550 nm. The two spectra are however showing different wavelength behavior which lead us to think to a possible tuning mechanism given by a phase dependent response in the MMI. From the simulations of a passive circuit with MMIs with small deviations on the output waveguide ridge widths from the design specifications, due to imperfections on critical dimensions control, we can observe how the behavior of the calculated output wavelength response of Figure 6.15 d) agrees with the measurements between 1530 and 1580 nm. This suggests that some fabrication imperfections in the 2x2 MMI couplers, can lead to some forbidden lasing wavelengths which are voltage dependent.

6.6.3 TUNING RANGE MEASUREMENTS

The maximum achievable tuning range of the laser system is then measured. The tuning range of the laser was measured by recording spectra for a wide range of different reverse bias settings applied to the different phase modulators between 0 and -8V with 1 V steps for the medium and the coarse filter. For the variable out-coupler a voltage step of 0.5 V is

6.6 Design improvements to increase the laser tuning range

chosen. The fine filter is swept with 4 V steps since the fine tuning of the laser output wavelength was outside of the scope of the tuning range measurements. A total number of more than 32000 spectra were recorded with an optical spectrum analyzer (OSA) with a resolution of 0.1 nm (Ando AQ8163 A).

As shown in Figure 6.16 a tuning range of 90.9 nm has been measured between 1480 and 1570 nm with a maximum output power in fiber of 200 μ W. To our best knowledge, this is the widest tuning range reported for monolithically integrated tunable laser systems. This wide tuning range enables axial resolution of 11.4 μ m in an OCT system in vacuum. To further increase the tuning range, we must induce a greater phase variation on every ERM to achieve more than 240° ($15^\circ \cdot \pm 8 V \cdot 1 mm$). One option would be to increase the length of the ERMs in the filters. However, this will increase the length of the laser cavity which leads to narrower longitudinal mode spacing which makes that the filter design will have to be adapted to smaller FSR values which makes it more difficult to achieve the large tuning range. The alternative way would be to change the technology and make multi quantum well based modulators, which present much higher phase efficiency due to quantum confined stark effect and can be tuned over the full FSR, with reverse bias voltage limited to 8V [161]. A maximum tuning range of 110 nm has been predicted by a model developed within the photonic integration group, which considers the amplifier length, the FSR of the coarse filter and the amount of passive losses in the laser ring cavity [162].

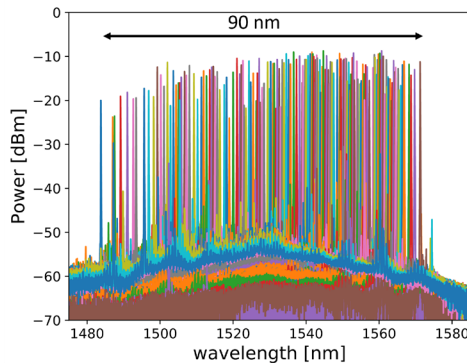


Figure 6.16: Laser spectra for different control settings to the AMZI filters to highlight the maximum tuning range of the laser.

7. FOURIER-DOMAIN MODE-LOCKED SEMICONDUCTOR LASER FOR OPTICAL COHERENCE TOMOGRAPHY

As alternative laser source for swept source OCT (SS-OCT), in this chapter, an integrated semiconductor Fourier-Domain Mode-Locked Laser (FD-MLL) at 1552 nm is modeled and designed. The focus of the chapter is to describe the dynamics of an integrated 2.5 GHz linear cavity FD-MLL with an Asymmetric Mach-Zehnder (AMZI) as a bandpass tunable filter. The influence of parameters such as the high modulation frequency, the modulation depth, and the amplifier current on the FDMML operation is studied. A detailed simulation revealed that a radio frequency tuning accuracy better than 1 MHz is required to achieve FD-MLL operation. The amplifier current and the modulation depth of the tunable intracavity filter are linked and they reveal the presence of a FDMML current region as function of the modulation depth of the filter. The simulated FD-MLL shows a comb width of 21 nm and a spectral linewidth of 10 MHz which result in a coherence length of 29.7 mm in a simulated swept-source OCT setup. The use of an integrated AMZI on InP substrate in a fiber based FDMML with lower repetition rate (12 MHz) is characterized as possible source for SS-OCT setup schemes. Optical and electrical measurements reveal a FD-MLL operation with 3 nm comb width, and highly chirped 83.3 ns optical pulses. Moreover, the use of AMZI filter raises the opportunity of sending electronics driving which are different than the sinusoidal driving waveform. This leads to the opportunity of having gaussian-like spectra which increase the signal to noise ratio (SNR) of the OCT images.

7.1 INTRODUCTION

Fourier domain mode-locked (FDML) lasers are among the fastest wavelength-swept light sources. They are used in many applications, like optical coherence tomography (OCT) [163] and Raman or two photon microscopy [164]. A FDML (Frequency Domain Mode Locked) laser is a ring laser structure that comprises an optical amplifier and a tunable filter. It overcomes the physical limitations of cavity build-up dynamics by matching the optical roundtrip time of the light circulating in the laser cavity with the bandpass filter sweep period [165]. This ensures that lasing modes do not have to build up from a spontaneous emission background but are already present from the last wavelength sweep of the filter. This is enabled by the very long optical delay line present in such laser cavities (Figure 7.1 a). From a viewpoint of physics, the FDML lasers are very different from other tunable lasers, such as

swept sources or passively mode locked lasers described in this thesis in chapter 6 and chapter 4 respectively. A comparison between these three types of lasers is sketched in Figure 7.1 b), where we can observe the electric field and the output spectra of such laser configurations. The FDML laser present an almost constant output power (like a cw-laser), however the output spectrum is broad and has a comb like structure (i.e., the one of a passively mode-locked laser). This can be understood since the FDML presents a fixed phase relationship between the longitudinal cavity modes and a highly chirped optical pulse [166]. This results in a quasi-Continuous Wave (CW) operation and a frequency comb with equal mode spacing. Current FDMLLs consist of long ring fiber cavities (10-100 km) with tunable Fabry-Perot bandpass filters (FFPs) that operate at 10 kHz-100 kHz for the scan repetition rate. Such long ring cavities are needed to match the relatively low tuning speed capabilities of the Fabry-Perot etalons which are used as bandpass filter. The transmission wavelength of the mechanically tunable FFPs is modulated sinusoidally with a repetition period equal to the fundamental cavity round trip time. In this way, these lasers allow for sweeps up to 290 kHz [167]. There are two limitations of such mechanically tunable FFPs apart from mechanical stability issues. The first is the limit on the tuning speed due to the limit on piezo actuators which affects the length of the laser cavity. The second is the that the scan speed also varies sinusoidally in time leading to a large variation in average power over the wavelength scan. A possible approach for the realization of a FDMLL source with increased tuning speed is the use of an electro-optically controlled bandpass filter on a photonic integrated circuit (PIC). A tunable filter tuned using electro-optic phase modulators with electrical control bandwidths of well into the GHz range allows for much faster scanning speeds and/or linear scans of the optical frequency as a function of time. The high speeds allow for a shorter laser cavity that can be integrated onto a single PIC. Such PICs offer some major advantages over bulky fiber optic systems such as small footprint, lower power consumption compared to that of the fast piezo actuators and robustness towards misalignments in case the complete laser is integrated. FDML laser with GHz repetition rate can be used as future comb sources for ultra-fast wavelength division multiplexing (WDM) interconnects. Their use as laser sources in SS-OCT can be hampered by the rather slow data acquisition, since the fastest SS-OCT measurements has been obtained with 400 MHz sweep rates [15]. However, they can be used as comb sources for spectral domain OCT (SD-OCT) where the analog acquisition through spectrometers allows for higher sweep rates. The use of an electro-optic tunable filter in an FDMLL has been reported in literature. A lithium-niobate Mach-Zehnder interferometers [168] was used as a wavelength-tunable comb filter in a fiber based FDML ring laser. In this chapter we investigate the use of the available 1550 nm generic integration technology on InP [27], [31] to develop a FDMLL suitable for OCT imaging. Recently demonstrated high speed phase modulators on this platform [38] can be used to make tunable filters that can tune at GHz scan rates. This will enable the realization

of monolithically integrated FDMLLs with much shorter cavities in mm as described by Heck et al [169] that can be suitable for real-time in vivo SD-OCT application. The integrated high speed phase modulators also enable the realization of a tunable filter and optical amplifiers for a lower repetition rate laser for SS-OCT. In this chapter we first present the design, modelling, and simulation results of a 2.5 GHz InP monolithically integrated FDMLL using an asymmetric Mach-Zehnder interferometer (AMZI) as intra cavity electro-optical tunable filter [132]. A time domain model description of integrated semiconductor lasers [133] is used to simulate the influence of several parameters, e.g. the applied scanning frequency of the tunable filter, on the laser dynamics. Then a swept source OCT setup simulation was done to investigate the suitability of the designed laser for application in OCT.

As a first step towards the realization of a fully integrated InP FDMLL, we present preliminary measurements on a fiber based FDMLL that have been performed. An AMZI bandpass tunable filter integrated on an InP based PIC is used to tune a ring based FDMLL in fiber at a 12 MHz repetition rate. The AMZI is tuned through reverse bias voltage applied to electro optical refractive index modulators (ERMs) [147]. Optical and electrical spectra, and output pulse duration have been measured for FDMML operation. These results can be considered as a milestone for the monolithic integration of FDMML laser on InP, to achieve GHz scan speeds.

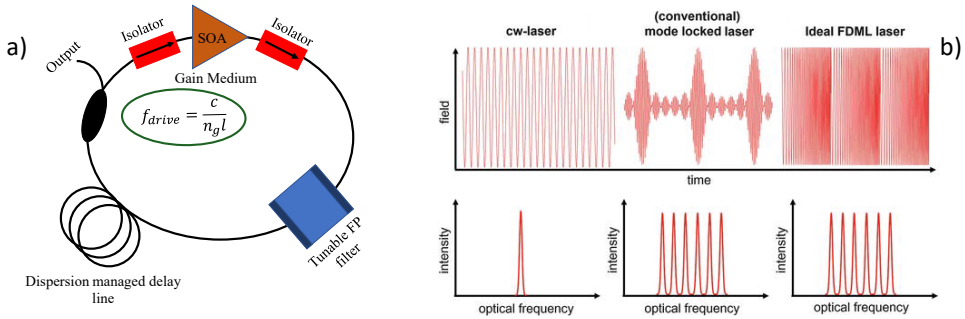


Figure 7.1 a) Schematics of a fiber-based Fourier Domain Mode-Locked laser system in fiber, where a tunable Fabry-Perot (FP) filter is tuned within the same roundtrip time of the laser cavity. b) Sketched comparisons of the time-dependent field and the laser spectra between a single mode CW-laser, a passively mode-locked laser and a FDMML laser. (After [170])

7.2 FOURIER-DOMAIN MODE-LOCKED LASER DESIGN

In this section, a bi-directional time domain simulator, based on the optical amplifier described in detail in the Appendix A and a gain parametrization described extensively in Chapter 3 and Chapter 4 for similar quantum well amplifiers at 1300 nm, is used to simulate the behavior of an integrated FDMML laser design on InP. The model is used to study the dynamics of FD-MLL with a Fabry-Perot linear cavity. The laser design follows from a FDMML design already published in [169], with a few improvements. First the laser cavity is longer to

decrease the repetition rate to lower frequencies (2.5 GHz instead of 20 GHz). This will allow the testing the laser without the use of high-frequency electronics. Secondly, despite the possibility of breaking the roundtrip periodicity of the light filtering, which results to be negligible from the simulation results, this approach offers an advantage in terms of stronger filtering effect since the light passes twice through the AMZI within a single roundtrip. Moreover, in this configuration, through the tuning of one phase modulator (ERM) in the AMZI filter, we can achieve time-domain modulation and wavelength sweep simultaneously. Five different optical components are used in the laser design as standard building blocks for the simulator: Multiple Quantum Well (MQW) based SOA, passive waveguides, Electro-Refractive Modulators (ERM), couplers and mirrors.

The design is presented schematically in Figure 7.2. The total laser cavity length is 1.644 cm which corresponds to a longitudinal mode spacing of 2.5 GHz in a linear cavity. This cavity length is chosen because such laser cavity lengths have been realized successfully before on InP [124]. In the simulator, the laser is discretized into 8.6 μm long segments corresponding to 103.4 fs time steps. This means that in the design all components have lengths that are an integer multiple of this segment length. The tunable bandpass filter (marked by the dashed bigger circle) is realized as an Asymmetric Mach-Zehnder Interferometer (AMZI) consisting of two Multimode Interference (MMI) couplers with 50:50 splitting ratio and two ERMs. The arm difference δL between the two arms is defining the filter free spectral range (FSR). As explained in chapter 5, the bandpass filter transfer function presents a sinusoidal wavelength dependence which is linked to the optical path mismatch. The AMZI filter is designed with a length imbalance of 34.4 μm (4 segments) to achieve a 2.4 THz FSR (21.2 nm around 1552 nm). The phase change is applied to the 2mm long PMs where a relative phase change of 2π between the two arms will tune the filter over its full FSR.

Since in the simulator, the amplifier gain is assumed to be constant as function of wavelength, the laser design in the simulation also includes another bandpass filter which limits the gain bandwidth. In this design, the gain bandwidth filter (indicated by the dashed smaller circle in Figure 7.2) is an AMZI bandpass filter with a length mismatch of 8.6 μm (1 optical segment). This results in a bandwidth limitation of the positive gain to 9.6 THz (80 nm around 1552nm) which is a reasonable approximation of the SOA gain bandwidth at high current densities (6-7 kA/cm^2). The length of the SOA is 800 μm to ensure a threshold current density higher than 5 kA/cm^2 .

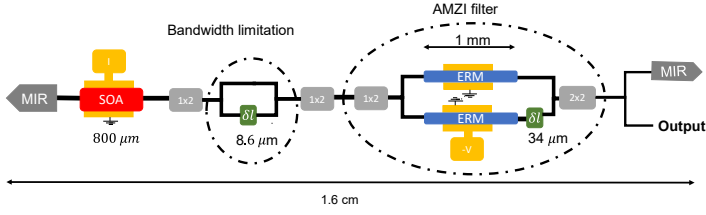


Figure 7.2: A schematic of the FD-MLL design studied. The dashed circle indicates a filter used to limit the gain bandwidth to 80 nm. The filter arm imbalance is $\delta l_1 = 8.6 \mu\text{m}$. The tunable AMZI filter is sinusoidally swept to achieve FDML operation. The arm imbalance is $\delta l_2 = 34.4 \mu\text{m}$. The 1x2 coupler has 0.5 coupling ratio. RHS and LHS mirrors are assumed to have reflectivity of 0.99 and 0.3 respectively. The total FP cavity length is 1.644 cm

The output optical power as function of time is measured from the right-hand side (RHS) semi-transparent mirror which presents a reflectivity of 33%, to simulate the effect of the out-coupler. The LHS mirror has a reflectivity of 99%. During the device modelling all the multi-mode interference (MMI) couplers and mirrors are assumed to be lossless, while the passive waveguides present a propagation loss of 1.5 dB/cm. This means that the output power and the threshold current of the laser in the simulation will be overestimated, but the influence on the conclusions of the laser dynamics will be negligible. An important limitation of the simulator used is that dispersion in the passive waveguide sections is not included in the underlying model.

7.3 LASER SIMULATIONS

The goal of the simulations of the FD-MLL cavity design are first to demonstrate that the FDML state can be achieved and to investigate how the operating regime depends on the control parameters of the laser. The simulations mainly focused on investigating the changes in the optical spectrum, the output optical power, and the frequency chirp as function of several parameters. The parameters that are varied during the simulations are the modulation frequency, the modulation depth, and the SOA injection current. Then the suitability of the FD-MLL output for OCT is investigated. This is done by using the simulated laser output time traces inside a Michelson interferometer to determine the achievable imaging depth in vacuum and the laser coherence length.

7.3.1 OPTICAL SIMULATIONS

In the simulations of FDML, the AMZI bandpass filter is tuned by directly applying a sinusoidal time varying phase shift to the longer arm. The RF frequency of the driving signal applied to the ERM in the AMZI is the first parameter addressed in the study of the laser dynamics. Note that during the simulations the ERMs are assumed to not have any bandwidth limitation. As explained in the introduction, to achieve FDML operation, the optical bandpass filter needs

to be tuned with the same repetition rate of the laser cavity. However, due to the carrier-photon density dynamics, pulsed behavior on the time scale of a single or multiple round trips may occur, e.g., in regular mode-locking the pulse shape will be distorted due to self-modulation effect. This causes the repetition rate to vary as function of current as described in [139]. The analysis of the effect of varying the driving signal frequency can lead us to find the operating point for FDMLL operation. In the simulations the drive frequency is scanned for 40 MHz around the fundamental frequency (2.513 GHz) of the laser cavity with a frequency resolution of 1 MHz (0.04% of repetition rate). The resolution was determined as the smallest frequency step that gave rise to noticeable changes in the laser operation. The peak-to-peak modulation depth on the phase modulator was set to π which is half the free spectral range of the AMZI. This represents the phase difference of the sinusoidal driving between the maximum and the minimum over a single period. The current in the SOA was set at 120 mA. Simulations results for other SOA current levels and modulation depths are discussed later in this section. The optimal modulation frequency is found to be 2.523 GHz. Figure 7.3 (a) shows the laser output power as function of time for three drive signal frequencies. For a modulation frequency of 2.523 GHz, the average optical power is around 13.3 mW with a variation of $\pm 5 \text{ mW}$. This value is close to the average power at steady state operation of the laser without driving the phase modulator which is 13.9 mW. In Figure 7.3 b) the instantaneous frequency is presented for the same three driving frequencies. For a driving signal frequency of 2.523 GHz, the frequency chirp presents a sinusoidal profile. The frequency chirp ranges between $\pm 625 \text{ GHz}$ centered at -185 GHz for a modulation depth of π . This equals the half of the FSR of the AMZI filter. We can therefore conclude that the laser is in a FDMML state at this driving frequency. A detuning of $\pm 1 \text{ MHz}$ from the optimum frequency, will result in a lower average power around 12.7 mW. From Figure 7.3 (a), the output power varies between 200 nW and 40 mW in the top and bottom time traces. Moreover, this pulsed-like operation results in more random phase relation variations between the modes leading to a noisier frequency chirp as can be seen from the top and bottom graphs of Figure 7.3 (b). In Figure 7.3 (c) the output spectra, calculated over 60 ns, are recorded for the same three different modulation frequencies. At the optimal frequency, the average optical power is highest. One can notice how the highest spectral power is concentrated at the edges of the optical spectrum. This is a consequence of the sinusoidal driving signal applied to the ERM of the AMZI filter. It is observed that detuning the modulation frequency results in lower output power within the tuning range. This happens since a detune of the sweeping speed of the filter will introduce a mismatch between the maximum transmission of the bandpass filter and light at a specific wavelength travelling in the cavity. This will lead to an extra loss on the spectral modes and to a higher fraction of Amplified Spontaneous Emission (ASE), which are transmitted by the filter for each round-trip time [171]. The spectral power for detuning of -1 MHz and +1 MHz are 1.2 dB and 1.9 dB

lower on average. It should be noted that FDMML operation could not be achieved by operating the AMZI filter in a push-pull configuration where one phase modulator in one arm is driven opposite to the phase modulator in the other arm. In such a configuration there is, in the ideal case, no phase modulation on the transmitted light.

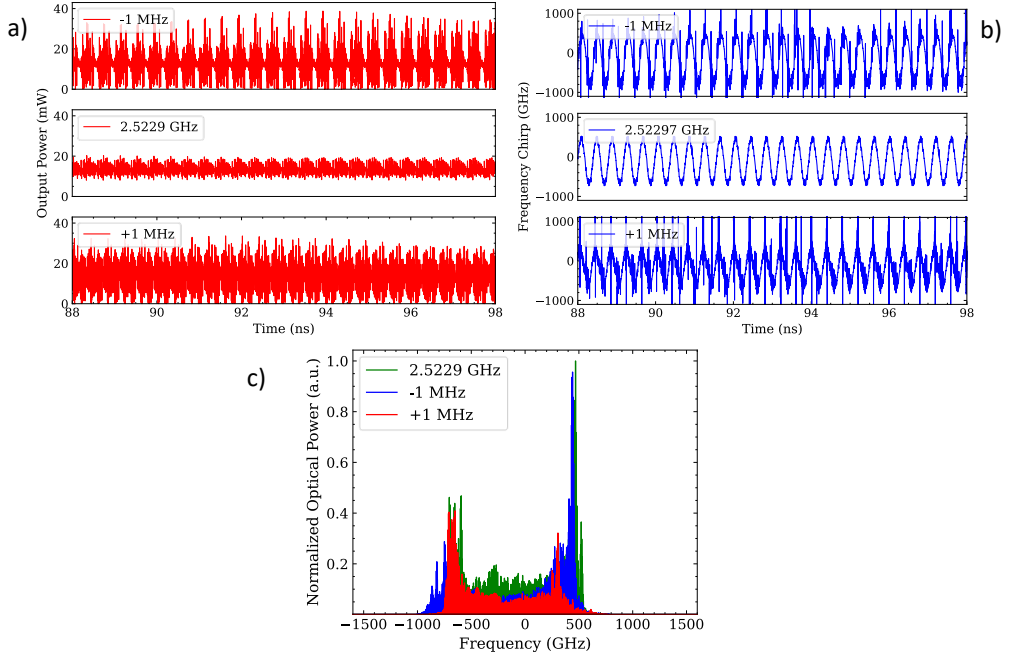


Figure 7.3: (a) Output power and (b) frequency chirp (Instantaneous frequency) as a function of time, and (c) the optical output spectra at the optimal modulation frequency of 2.5229 GHz and detuning of ± 1 MHz for π modulation depth and $I_{SOA}=125$ mA.

The FDMML operation is investigated for SOA currents ranging between 90 mA and 180 mA and for different modulation depth values between 0.5π and 2π . The driving frequency was kept constant at 2.523 GHz. The output power is analyzed for a 30 ns time trace to evaluate the stability of the FD-MLL operation. Figure 7.4 (a) shows multimode operation with power fluctuations between 0 and 30 mW for a SOA current of 90 mA and modulation depth of π . The power variation is due to beatings between the modes which are varying over time due to changes in phase relation between the modes, i.e. clearly a non-modelocked state. Increasing the current up to 120 mA, the output power is stable, and the power variation is reduced to ± 7.5 mW around an average power of 12.6 mW. This indicates that there is a certain current range that ensures a stable FD-MLL operation at 2.523 GHz. This range of currents depends on the modulation depth. We also see that increasing the current, it can result in power instability. Figure 7.4 (b) illustrates (green) the range of FDMML operation with the current at different modulation depths. We observe that the minimum current to

observe FDML operation increases for higher modulation depth of the sinusoidal driving function. This happens since the larger the modulation depth, the shorter is the fraction of time the laser is operating at one of the cavity modes. This leads to the need of higher light amplification to reach the same FDML operation.

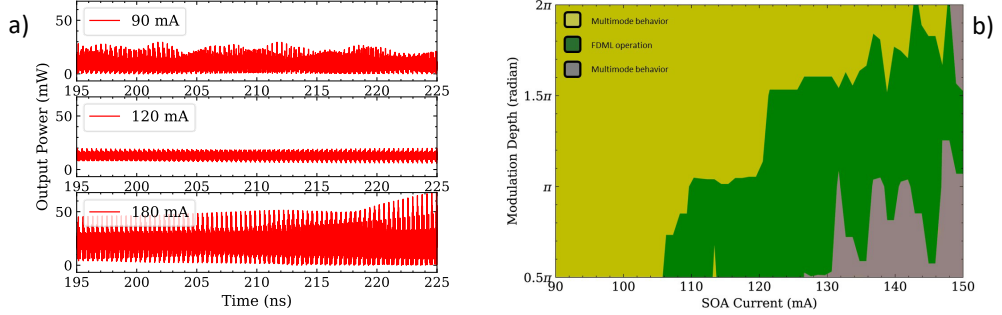


Figure 7.4: (a) Output power for different SOA injection current at a fixed modulation depth of π . (b) different operations of the simulated FD-MLL for different SOA current and modulation depth. The modulation frequency is set at 2.523 GHz for all the different currents and modulation depths.

Furthermore, we investigate the comb spectral width as a function of the modulation depth of the RF drive signal at 125 mA injection current. Figure 7.5 a) shows the output spectra of driving the AMZI filter with modulation depth $0.5\pi, \pi, 2\pi$ respectively. The optical bandwidth of the FD-MLL increases with increasing the modulation depth. The 20 dB laser spectral widths are calculated to be 640 GHz, 1.25 THz, and 2.42 THz respectively, which is in line with the tuning of the AMZI. The 2π modulation does not correspond to a FDML operation, as can be seen by the absence of any power concentration at the spectrum edges. This is in line with what expected from Figure 7.4 b). Moreover, all the three spectra are not flat and show modulation dips of 6.4 dB, 8.9 dB and 10 dB respectively. The dips obtained on the spectrum are related to the phase modulation applied on the laser. This has been analyzed in detail with separate phase modulation simulations. The effect has also been extensively studied in [172]. As a result of the strong phase modulation applied to the laser light, during the laser operation the cavity spectral modes are not only tuned but the light passing through is also strongly phase modulated during the frequency up-sweep and down-sweep. As mentioned before, it is important to mention that to achieve FD-MLL operation in the proposed design, it is essential that the modulation is applied only on one arm of the AMZI to exploit both the effects of wavelength filtering and phase modulation. In this way it is possible to obtain a fixed phase relation between adjacent modes. In Figure 7.5 b), an average FWHM linewidth (over 300 spectral modes) is calculated to be 10 MHz (0.08 pm). We note that the accuracy of the linewidth calculation is limited by 3 MHz resolution of the spectrum which is a limitation of a simulation window of 200 ns in time.

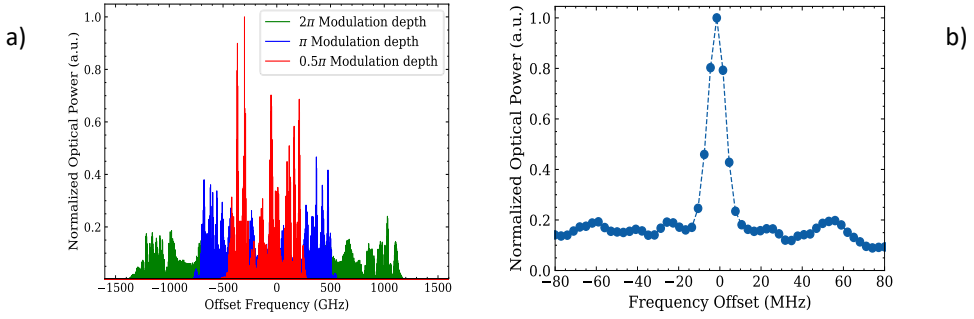


Figure 7.5: (a) Normalized optical spectrum for different modulation depth of the drive signal. Modulation frequency 2.5229 GHz. ISOA=126 mA. The zero frequency $f_0 = 193.3 \text{ THz}$ ($\lambda_0=1552 \text{ nm}$). (b) simulated optical linewidth averaged over 300 spectral modes obtained from the simulated FD-MLL. The spectral resolution is limited to 3 MHz.

7.3.2 SS-OCT SIMULATION

The proposed FD-MLL design is investigated as a source in a SS-OCT measurement. The simulated swept-source SS-OCT setup is a free space Mach-Zehnder interferometer ($n_g = 1$) [6]. The laser input power is equally split into two optical paths. The two optical paths have a variable optical path length mismatch which lead to an interference signal. The optical path is doubled in the calculation, to address the behavior of a Michelson interferometer with the use of a Mach-Zehnder interferometer in the simulations of an OCT setup configuration. The time dependent interference signal is measured with a photodetector. We assume no additional losses between the two arms. The photodetector is just the output power, so it is modeled as a detector with an electrical bandwidth determined by the step size in the time input trace of 106 fs, which is approximately 5 THz. In this SS-OCT model, a time trace of the output of the simulated FD-MLL with 2.4 THz (21 nm) tuning range, 2.522 GHz mode-spacing and 14.4 mW output average power is used as the laser input to the interferometer. To obtain one-dimensional depth profile, an Inverse Fast Fourier Transform (IFFT) is performed on the output interference spectrum. The IFFT is performed with a sampled acquisition of 1000 points over the sweep range of the FD-MLL. Zero-padding was also applied to improve the smoothness of the depth profile.

The axial resolution of an OCT image δL is determined by the scan range $\Delta\lambda_{\text{span}}=21\text{nm}$ of the laser. For a Gaussian intensity distribution over the full scan the resolution is given by equation (1.1), where $\lambda_0=1552\text{nm}$ is the central wavelength of the FDML frequency comb. The theoretical axial resolution achieved by this laser in an OCT system is $50 \mu\text{m}$ in vacuum. In the simulation, the axial resolution is calculated from FWHM of the reflection peak intensity as shown in Figure 7.6 (a) The obtained value is $70 \mu\text{m}$. The axial resolution value determined in the simulation is 40% higher than the theoretical one. The reason is that the

theoretical value is calculated assuming a laser source with a Gaussian shape of the intensity distribution over the wavelength scan range. However, in our case, the simulated FD-MLL spectrum presents a shape that is very different. It has the highest intensity at the edges of the spectral range covered. The coherence length of the laser over the complete wavelength tuning range can be calculated using the same interferometer setup. In practice, this is done by moving the reference mirror over a certain range and recording the reflected peak intensity at each position. The intensity decay (R) as a function of imaging depth (z) can be described as [20]:

$$R(z) = \exp \left[-\frac{\pi^2 \omega^2}{8 \ln 2} \left(\frac{z}{d} \right)^2 \right] \quad (7.1)$$

Where d is the maximum scan depth, $d = \lambda^2 / (4\Delta\lambda)$ in which $\Delta\lambda$ is the wavelength sampling interval, and ω is the ratio of the laser spectral linewidth (FWHM) $\delta\lambda$ to the wavelength sampling interval $\omega = \delta\lambda / \Delta\lambda$.

SS-OCT simulations were done for different optical path mismatch values ranging from 0.9 mm to 29 mm with 0.9 mm step and the depth profile was calculated as shown in Figure 7.6 (b). From the figure we can see that the reflected power intensity is almost constant over the full imaging depth range of 29.7 mm. The main reason behind that is that the spectral modes in the simulated FD-MLL show a very narrow FWHM of 10 MHz compared to the wavelength sampling interval of 2.522 GHz. This results in an almost flat intensity decay profile according to (7.1) which describes the long coherence length achieved by this simulated laser. In previous simulations, the bandwidth of the photodetector was determined by the time step in the laser output simulation data. However, the limited photodetector bandwidth can result in an intensity decay which limits the maximum imaging depth obtained. To not affect the imaging depth of the system, the photodetector bandwidth should be larger than the maximum frequency of the detected signal $f_{max} = \frac{c}{d_{max}}$, where d_{max} is the maximum scan depth described in (7.1). The maximum frequency is calculated to be 10 GHz. Figure 7.6 (c) shows a depth profile for different simulated photodetector bandwidths. The bandwidth limitation was simulated by Butterworth low-pass filter with cutoff frequency [173]. These simulations reveal the integrated FDMLL to be a good laser source for SS-OCT. Monolithic integrated FD-MLL lasers on InP will have high repetition rates that may be brought down to 1GHz or even 500 MHz, but those are still too high scan rates for ADCs needed to record the OCT signal in SS-OCT. InP integration can still be used however for realizing the tunable filter, possibly combined with an SOA in a fiber cavity. Using optical fiber, the cavity can be made sufficiently long to reduce the scan repetition rate to levels useful for an SS-OCT set-up. It is therefore useful to evaluate the suitability of an integrated AMZI as a tunable bandpass filter in a FDM laser.

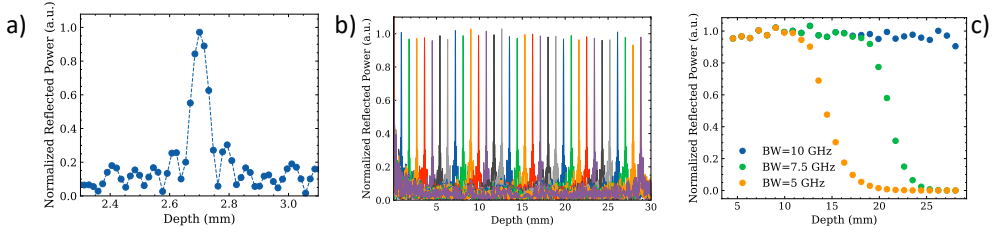


Figure 7.6: (a) Calculated axial resolution profile for a path length mismatch of 2.7mm (b) calculated depth profile of series of path length mismatches ranging between 0.9-29mm (0.9mm step) assuming no photodetector bandwidth limitation (c) calculated depth profile including photodetector bandwidth limitation.

7.4 FIBER-BASED FOURIER-DOMAIN MODE-LOCKED LASER WITH AN INP INTEGRATED FILTER

In this section, we present measurements on a fiber-based ring cavity FD-MLL operating around 1530nm with an integrated AMZI as a tunable filter. The filter has been fabricated on a multi project Wafer Run (MPW SP24) on an InP generic integration technology [27], fabricated by Smart Photonics. The AMZI voltage dependent transmission is investigated at different wavelengths. The CW laser performance as a function of the AMZI tuning is evaluated first. This is done to understand the threshold current, the maximum output power and the operating wavelength of such laser. For the FDML operation of the laser, the measurements are focused on investigating the changes in the optical spectrum, the output power, and the frequency chirp as function of the modulation frequency and the modulation depth. The results obtained can be later applied in the 1300 nm range to obtain hyperspectral OCT images with laser scans at different wavelengths.

7.4.1 ASYMMETRIC MACH-ZEHNDER INTERFEROMETER TUNABLE FILTER

An AMZI tunable filter is used in a FDML laser cavity. The chip is wire-bonded to a distribution printed circuit board (PCB) to have easier access to the electro-optic modulators from the voltage source. The FSR of the AMZI is determined by the physical length mismatch ΔL between the two arms and it is 6 nm. The AMZI was not specifically designed for this application which is why the FSR is relatively small. The wavelength tuning of the AMZI is done by applying a reverse bias voltage to one of the ERMs. First, we investigated the efficiency of the AMZI filter used in the laser cavity by measuring the half-wave voltage V_{π} of the ERM. Light from tunable laser source (Agilent 8163B-channel A) is coupled to the AMZI using a single mode lensed fiber. The output light is then detected with a photodetector (Agilent 8163B-channel B) as the reverse bias voltage source (Keithley 2401) applied to the ERM is swept between 0 V and -9 V with 0.18 V step. The laser source power is fixed at 10

dBm and the input wavelength is swept between 1520 nm and 1530 nm with 2 nm step. The optical alignment is automated [68], to optimize the fiber to chip coupling. For each voltage step, the output power was averaged over 20 scan (100 ms for each scan) to average out any possible misalignment during the measurements. Figure 7.7 shows the transmission of the AMZI for different voltage bias values and different wavelength of the input laser source. The average V_π value measured over the mentioned wavelength range is 5 V, varying of around 0.5 V with wavelength between 1520 and 1530 nm. The maximum measured Extinction Ratio (ER) is 25 ± 5 dB. This value is obtained when the wavelength of the tunable laser is aligned with the maximum transmission of the AMZI filter as can be seen for the curve of 1524 nm. As the laser source is tuned to higher wavelengths, we see that the ER is decreasing gradually to 20 dB. This indicates that the AMZI is tuning towards higher wavelengths with increasing the reverse bias on the ERM.

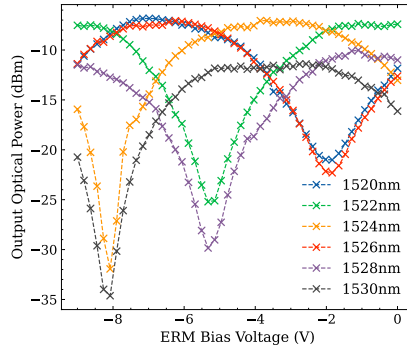


Figure 7.7: AMZI optical power transmission as a function of the reverse bias voltage applied to the AMZI filter for different wavelengths. The input laser source power is set at 10 dBm.

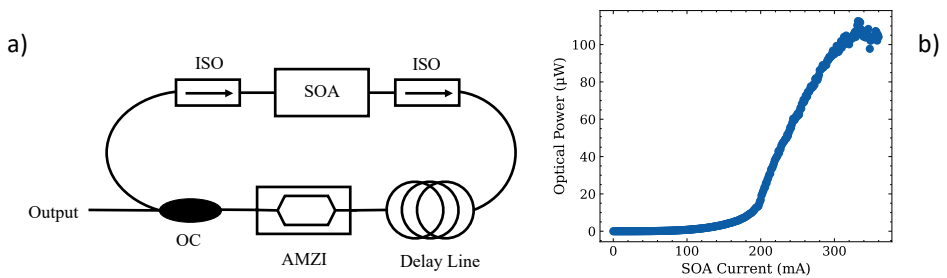


Figure 7.8: (a) Schematic diagram of the fiber-based FD-MLL with an integrated AMZI as a tunable filter. (b) measured LI characteristics of the laser cavity. The temperature of the SOA is fixed at 20°C and the reverse bias voltage of the filter is set at 0V. (b) laser optical spectrum for different DC bias voltages applied to the AMZI filter.

7.4.2 LASER DESIGN AND DC OPERATION

The laser design, depicted in Figure 7.8 a), consists of a ring cavity with the AMZI characterized in Section 7.4.1 as tunable bandpass filter. The amplification inside the cavity is provided by a packaged SOA (JDS Uniphase) where the temperature is controlled using a Peltier element and a water cooler element to extract any additional heat generated by the Peltier. Two optical isolators are included to ensure the uni-directionality of the light inside the cavity. The output of the AMZI is connected to a 2x2 output coupler where 90% of the optical power is fed back to the laser cavity and 10% is extracted as the output signal. A single mode fiber (SMF) delay line is added to the ring cavity to reach a total cavity length of 16.071 m which leads to an expected longitudinal mode spacing of around 12.038 MHz. The light intensity characteristics of the laser is measured to determine the operating threshold current of the laser. The output power is measured as function of SOA current between 0-360 mA with 1 mA step. During the measurement of the laser output power, the bias voltage applied to the AMZI is constant at 0 V and the temperature of the SOA is stabilized to 20°C. Figure 7.8 b) shows the LI characteristics of this laser. The laser threshold current is 200 mA, and the obtained optical power has a maximum of 110 μW at 320 mA. This low output power is mainly due to the coupling loss between InP chip and the fiber, and the fact that the power is measured at the output of the AMZI filter where the highest cavity loss occurs. We choose to operate at 318 mA to obtain the highest output power, before thermal roll-over occurs. The CW laser tuning range is investigated applying a DC bias voltage to one arm of the AMZI filter. The filter bias voltage is swept between 0 V and -7 V with 1 V step. We observed that increasing the bias voltage results in the tuning of the AMZI filter towards higher wavelengths in agreement with the filter characterization. The measurements indicate a V_π of 5.2 V for a 2 mm long phase shifter. From the wavelength tuning we observe that lasing modes are hopping between the different filter maxima separated by 6 nm. This is since the lasing wavelength occurs where the minimum loss is present and small variations in loss for the different filter transmission maxima occur during tuning. This behavior is a limitation to the FDML operation, since the laser hopping between different wavelengths will occur then as well. The variation in the laser output power observed with tuning is related to the residual amplitude modulation (RAM) of the ERM present in the AMZI. RAM rises from the electro-absorption effect of the ERMs which depend on both the wavelength and the applied voltage as discussed in [21].

7.4.3 FOURIER DOMAIN MODE-LOCKING OPERATION

The mode-locking operation of the laser is investigated tuning the AMZI filter with a sinusoidal drive signal with the same frequency as the fundamental frequency of the laser cavity. To confirm the FDML operation of our laser system, both electrical and optical spectra

have been recorded, together with time trace measurements of the intensity. The frequency tuning resolution of the driving signal used to tune the AMZI was 5 kHz. This resolution (1:2500) is determined with the simulations of the FDML operation in section 7.3. Once the FDML driving frequency has been established, the effect of the modulation depth on the frequency comb width is investigated. Finally, the time dependent output is measured and an indication on the pulse chirp is obtained.

Electrical spectra from a 12.5 GHz photodetector registering the laser output, are recorded for different modulation frequency of the AMZI tunable filter. The AMZI filter is tuned by applying a sinusoidal drive signal with a voltage offset $V_{Offset} = -2.5 \text{ V}$ and a Peak-to-Peak voltage $V_{PP} = 5 \text{ V}$. A frequency sweep of the filter drive signal over a 200 kHz interval with a step of 5 kHz around the laser fundamental frequency (12.038 MHz) is implemented. The electrical RF spectrum from the photodetector is recorded using an Electrical Spectrum Analyzer (ESA-50 GHz E4448A). In this way it is possible to judge the optimal driving RF frequency from the analysis of the RF electrical power. The optimal frequency was found to be 11.975 MHz, for an SOA current of 318 mA.

Figure 7.9 a) shows the measured RF spectra for a 15 MHz span with resolution bandwidth (RBW) of 100 Hz. The blue curve shows the electrical spectrum when a modulation frequency of 11.975 MHz is applied to the AMZI. RF power at the cavity repetition rate is measured to be -15.7 dBm, which is 85 dB higher than the noise floor (-100 dB/100Hz). As we detune the modulation frequency by 8.5%, the RF power at the driving frequency becomes -37 dBm (red curve in Figure 7.9 a). The remaining RF power is still present at the fundamental frequency of 11.975 MHz. Beating frequencies between the laser fundamental frequency and the electronic modulation frequency, are also clearly visible at 1 and 13 MHz. A high-resolution measurement reveals the effect of smaller detuning on the RF power. A high-resolution scan (1 Hz RBW-1 MHz span) is recorded for different driving frequencies in Figure 7.9 b). We see that a detune of 5 kHz, 15 kHz and 60 kHz results in 1 dB, 3 dB and 5 dB of RF power drop respectively. From the observation of the two different figures, it is possible to understand that the higher is the detuning between the RF and the laser fundamental frequency the lower is the RF power measured by the ESA at the driving frequency. This happens since part of the RF power is concentrated at the beating frequencies. According to this, the FDML laser frequency is obtained at 11.975 MHz, where the ESA detects the highest peak power. The same frequency detuning is investigated on the optical spectra. The first thing to notice is that the laser produces output at two different transmission maxima of the AMZI. There are two groups of modes separated by 6 nm, which refers to the FSR of the AMZI. We measured that a detuning of +5 KHz with respect to 11.975 MHz (0.04%) results in a 3-4 dB drop of the peak spectral power. The power further decreases for a +10 kHz detuning (Figure 7.10 a). This behavior is explained by the extra optical losses induced by the mismatch between the maximum transmission of the filter and the longitudinal modes spacing as function of time.

7.4 Fiber-based Fourier-Domain Mode-locked laser with an InP integrated filter

It is also linked to the lower peak signals in the RF spectra of Figure 7.9 b), as a confirmation of FDML operation of the laser.

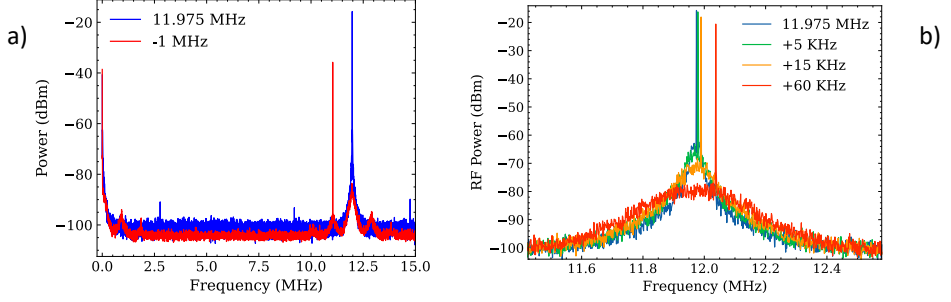


Figure 7.9: Measured RF spectra of the laser corresponding to different modulation frequencies (a) 15 MHz span with 100 Hz RBW and (b) 1 MHz span with 1 Hz RBW. ($I_{SOA}=318$ mA, $V_{PP}=5$ V, $V_{Offset}=-2.5$ V)

The spectra present the highest power peaks at the edge of the frequency comb generated by the filter sweep. This is a characteristic result for a sinusoidal drive signal applied to the AMZI filter as we predicted from optical simulations [132]. The asymmetric shape of the comb with respect to the center is related to dependency of the AMZI absorption on the applied voltage and wavelength.

The effect of the modulation depth on the spectral width of the laser frequency comb is investigated. The V_{pp} of the drive signal at the optimal frequency (11.975 MHz) is swept between 1 V and 5 V with 1 V step. In Fig. 7.10, we observe an increase in the spectral width of the combs by increasing V_{pp} of the drive signal. We can notice how a change of 5 V corresponds to half of the FSR of the AMZI filter (2.2-2.4 nm). This result is close to what is expected from the AMZI characterization of section 7.4.1. (≈ 2.5 nm).

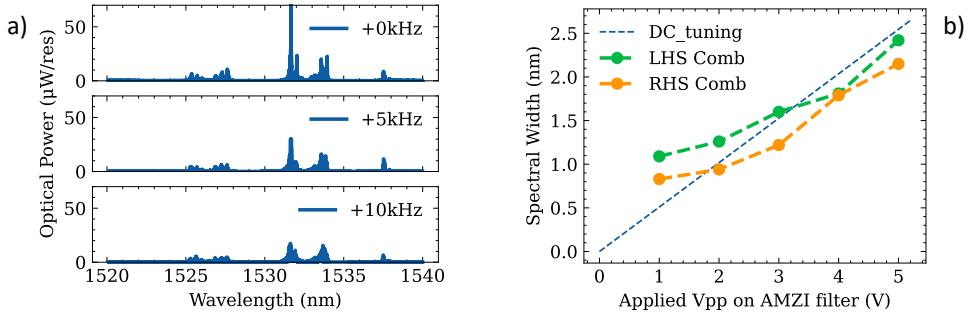


Figure 7.10: a) Optical spectral power for +5 kHz and +10 kHz detuning with respect to the 11.975 MHz (FDML frequency). b) Left hand side (LHS) and right hand side (RHS) optical spectral widths as a function of V_{pp} , for a sinusoidal modulation frequency of 11.975 MHz. ($I_{SOA}=318$ mA., $V_{Offset}=-2.5$ V), together with the DC tuning prediction from Figure 7.7.

The time dependency of the output from the laser system, was recorded with a real time oscilloscope (WaveMASTER 8600A-6 GHz bandwidth). The RF signal applied to the AMZI filter is used to trigger the oscilloscope acquisition and the time traces are averaged over 600 sweeps. The output signal from the laser needed to be amplified using an erbium-doped fiber amplifier (EDFA) to have sufficient signal strength from the 12.5 GHz bandwidth photodiode used. The EDFA did bring a problem, due to the fact the laser operates right at the short wavelength edge of the EDFA gain spectrum at 1530 nm. The spectral shape and what is observed in time of the laser is thus strongly affected by the amplification bandwidth of the EDFA. Figure 7.11 a) shows 500 ns long time traces of the amplified optical signal. The output time traces of FDML lasers are expected to be highly chirped long pulses where the output power is distributed over the whole pulse period of 83.3 ns (11.975 MHz repetition rate), which is an indication of FDML operation. During up and down sweep of the sinusoidal filter we would expect the highest output power to occur at the maxima and minima of the drive signal which corresponds to the two peaks at the borders of the comb. The presence of a drop in output power occurring at the maximum drive voltage of -5V can be related to the fact that the laser tuning is not continuous due to mode-hopping between different maxima of the periodic filter function. In this case, the wavelength corresponding to the maximum of the drive signal might have occurred in the left hand side comb between 1522-1525 nm where -40 dBm optical power is present. To evaluate the phase relation between different spectral modes in the obtained combs, an approach based on the experimental demonstration of [174] is adopted. The frequency comb is filtered with a bandpass filter with bandwidth of 0.25 nm. The filter is then tuned over the full output comb and time traces are recorded. These traces are then analyzed to determine the relative time delay of different spectral components. A chirp evaluation over the full obtained combs was not feasible due to the limitation of the used measurement system associated with EDFA amplification bandwidth.

Instead, the 0.25 nm bandpass filter is used at one fixed wavelength where a strong signal is observed. Because of the up and down wavelength sweep of FD-MLL, we expect to observe two pulses at a specific filtered wavelength within the sweep range of the laser. The time delay between the two pulses δt can be linked to the filtered wavelength λ_{filter} by: $\delta t = \frac{\lambda_0 - \lambda_{filter}}{\lambda_1 - \lambda_0} \cdot T_{period}$ where $\lambda_0 = 1528.3 \text{ nm}$ and $\lambda_1 = 1531.40 \text{ nm}$ which are the wavelengths at the edge of the sweep range of the obtained frequency comb. T_{period} is the round-trip time. Figure 7.11 b) shows 500 ns output time trace corresponding to filtered output spectrum at 1531.40 nm. We observe the existence of two pulses in the round-trip time of 83.3 ns and the time delay between them is found to be 56 ns which agrees with expected the time delay between the two pulses at 1531.40 nm. This result from the

investigation of the time traces of the laser signal, is the confirmation that the laser operates in a FDML operating regime.

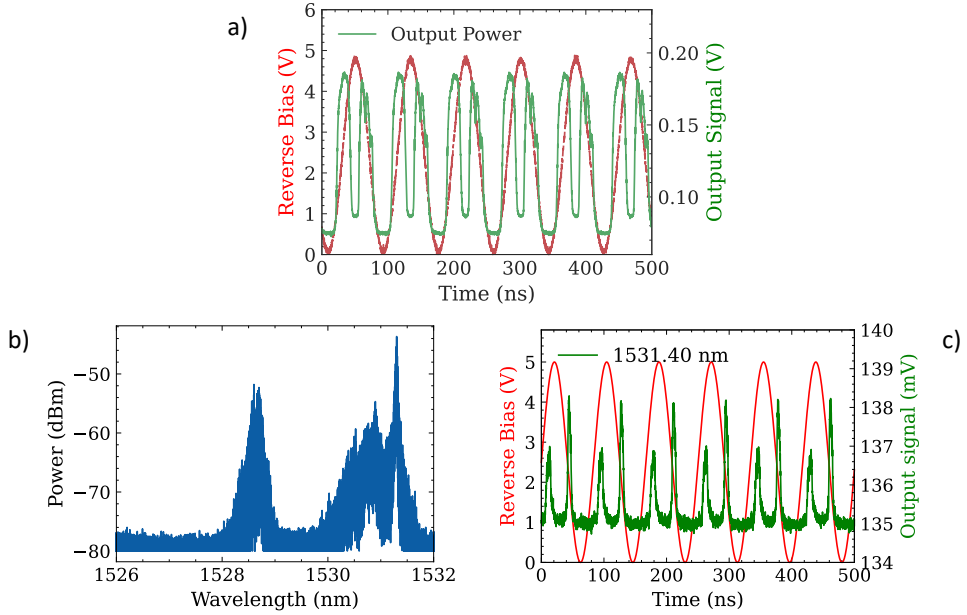


Figure 7.11: Output optical spectrum a) 500 ns recorded signal time traces (green) overlapped with the drive signal applied to the AMZI.(red) b) Optical spectrum where the time traces are extracted, and a highlight of the portion filtered with the optical bandpass filter. c) 500 ns recorded signal time traces corresponding to the filtered spectrum at 1530.4 nm (green) and the noise floor contributed to the EDFA (red) ($I_{SOA}=318$ mA, $F_{Modulation}=11.975$ MHz, $V_{pp}=5$, $V_{Offset}=-2.5$ V, $G_{EDFA}=11$ dB)

7.4.4 USE OF MULTIPLE DRIVING WAVEFORMS

The use of InP integrated AMZI as bandpass frequency raises the opportunity of sending electronics driving which are different than the sinusoidal driving waveform. This is a clear advantage of integration with respect to mechanically moved mirrors, which are used as Fabry-Perot tunable filter in current FDML lasers. The optical spectrum is changing when we apply a sawtooth signal with respect to a sinusoid, as depicted in Figure 7.12. We can observe how the highest spectral power is at the center of the comb, rather than at the edges. With a triangular electronic driving waveform we expect to obtain uniformly distributed power over the full width of the FDML frequency comb (3 nm) for a π phase modulation. This is a major advantage for the use of integrated filters into FDML lasers as OCT sources. Waveforms that give a Gaussian power spectral distribution over the tuning range of the laser, lead to a better signal to noise ratio (SNR) during the OCT imaging.

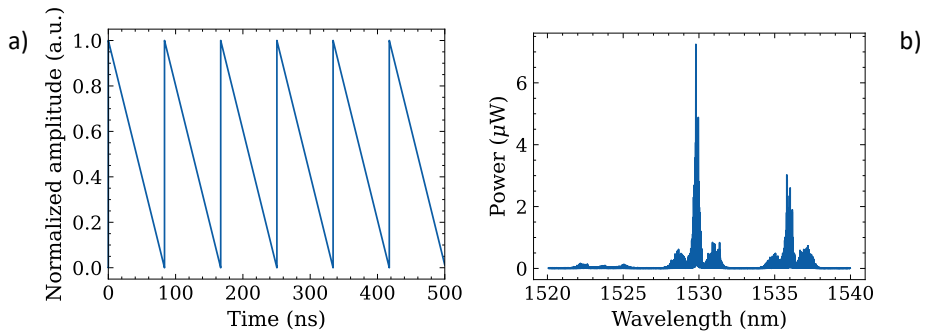


Figure 7.12: a) Electronic signal and b) resulting optical power spectrum of the FDML laser for a sawtooth electronic driving waveform.

7.5 CONCLUSIONS

Time domain model simulations for an integrated FD-MLL has been presented. The model was used to simulate an InP integrated 2.5 GHz linear cavity FD-MLL with AMZI tunable bandpass filter at 1552 nm.

Simulations demonstrated FD-ML operation can be achieved. Then studies were performed into the influence of different parameters such as modulation frequency, modulation depth and amplifier current on the laser behavior. Simulation results show that tuning accuracy less than 1 MHz is necessary to achieve FD-MLL operation in a 1.6 cm long cavity design. The amplifier current and modulation depth are related, and they show a threshold current to obtain a stable FD-MLL operation. The simulated FD-MLL has a sinusoidal chirp profile due to the sinusoidal drive signal applied to the AMZI filter. This results in a non-flat comb where the spectral power is concentrated at the edge of the comb as in a harmonic oscillator. The simulated FD-MLL show a comb width of 2.4 THz (21 nm) around 1552 nm and the laser linewidth is calculated to be 10 MHz. The use of the designed FD-MLL as a light source in a simulated SS-OCT was investigated and reveals a maximum imaging depth of 29.7 mm and axial resolution of 70 μm . The axial resolution can in principle be further enhanced by increasing the scan range of the laser which can be done by increasing the FSR of the AMZI tunable filter. As a drawback, for wider combs the model must account for waveguide dispersion since the dispersion has a high contribution over 50 nm on InP waveguides, as shown in Chapter 2. Overall, simulation results reveal that the FDML laser operation can be achieved on a monolithically InP integrated laser cavity design longer than 1 cm. The designed integrated FD-MLL is a promising light source for real time in vivo OCT, but one will have to use spectral OCT due to the very high repetition rate. The design can be scaled and transferred to other integration technologies at different wavelengths such as 1300 nm InP active/passive integration technology [15]. The use of voltage controlled ERMs as tuning

elements has the advantages of high tuning speed and the ability of applying different driving waveforms rather than sinusoidal which can lead to a flatter power distribution over the frequency comb.

The attempt to use an integrated tunable AMZI as a bandpass filter in a fiber-based cavity design is then discussed. We have demonstrated FDML operation in a 12 MHz fiber ring cavity configuration. The output pulses are long and highly chirped with 83.3 ns period. These results show the suitability of integrated AMZI as a tunable filter in FD-MLLs. For OCT application, this hybrid laser design has the potential to increase the scan rate (in several MHz) and scale down the dimensions (down to few meters) of current state-of-art FD-MLLs. More importantly, we discovered that a sawtooth electronic driving can be applied to the filter, to obtain a flat laser power distribution over wavelength, which is a crucial requirement in OCT imaging.

8. CONCLUSIONS AND OUTLOOK

The results presented in this dissertation represent significant progress towards the realization of a monolithically integrated tunable laser system emitting in the 1300 nm wavelength range that is to be used as a swept source in an Optical Coherence Tomography (OCT) system. The conclusions together with some recommendations for future research are divided over two sections following the two main questions that have been addressed in this thesis.

8.1 1300 NM ACTIVE/PASSIVE INTEGRATION PLATFORM

It is of paramount importance to realize integrated 1300 nm tunable laser for OCT for medical and biological applications, due to the low water absorption present at 1270 nm. The integration will lead to smaller and more efficient laser systems, that can perform OCT in a minimum invasive way. This thesis explains the challenges addressed to port a comprehensive foundry platform at 1550 nm to 1300 nm and to understand whether lasers realized on such platform satisfy the needs for OCT. This 1300 nm platform was developed following two main paths. Firstly, to minimize reflections at the butt-joint active/passive interfaces (< -50 dB), the effective index mismatch between the active and the passive layer stacks has been minimized. The trade-off addressed in this thesis, is between a) the performance of discrete components that can be used as functional building block inside complex photonic circuits and b) their ability of being integrated together in the platform. Secondly, a well-established InP processing scheme, deployed in Smart Photonics foundry, was used to enable that a generic approach targeting different applications through multi-project wafer (MPW) runs can be used [31]. The extension to the 1300 nm wavelength is done without increasing the fabrication complexity ensuring in this way a robust processing. The 1300 nm platform includes a passive waveguide with low propagation loss (< 3 dB/cm) which can be integrated with semiconductor optical amplifiers (SOAs) with > 60 cm⁻¹ fundamental TE mode gain and wide gain bandwidth (FWHM > 80 nm), for current densities around 7 kA/cm². The 1300 nm SOA realized on this platform presents characteristic temperature of $T_0 = 75$ K and high injection efficiency $\eta_i > 60\%$ for ridge width SOA, which leads to 30 mW output saturation power out of a 600 μ m long SOA. This confirms that the requirement of being compatible with a low loss passive waveguide does not compromise the amplifier performance. In addition, high efficiency (20° V \cdot mm) reverse bias driven electro-optic phase modulators (ERMs) have been integrated. These performance numbers are crucial to be able to reach single mode, high side mode suppression ratio (SMSR > 30 dB), and widely tunable (tuning range > 20 nm) laser systems. The realization of the platform has

been performed in parallel with the development of compact models able to describe in a parametrized way the behavior of the different components into steady state spectral models and dynamics simulation tools. Using this platform, tunable laser systems can be realized with a wide tuning range of up to 80 nm making them suitable for OCT systems with 10 μm axial resolution. On the other hand, lasers realized on this 1300 nm platform deploy the use of quite long cavities, due to the need of 2 mm ERM to achieve 2π phase shift. The introduction of ERM with higher efficiency (e.g., multi-quantum well phase modulators) can lead to lasers with shorter cavity lengths, which is beneficial to achieve high SMSR and faster wavelength switching times.

This monolithic integration platform presents an alternative solution to hybrid and heterogeneous approaches grown on Si based substrates at 1300 nm [175], [176]. Si based devices can present the advantage of leveraging a mature CMOS technology, which is high volume and presents a high lithographic quality with small fabrication tolerance [177]. However, due to the absence of Si-based light emitters, these hybrid approaches require a high precision alignment technique (e.g. flip-chip assembly or transfer printing) [178], to couple an InP optical amplifier to Si-based passive components. Alternatively, the growth of GaAs quantum dots on Si-substrate, developed at the university of Santa Barbara [179], led to the possibility of having monolithically integrated lasers on Si. In this case the high lattice mismatch between the different materials can lead to the presence of defects, which reduce the reliability of the laser performance on the same wafer. The development of the InP 1300 nm monolithic platform described in this thesis can ensure a high mode overlap between the active and the passive layer stacks ($\Delta n < 5e - 3$), which leads to the possibility of realizing extended long cavity lasers with low parasitic reflections. Moreover, it opens the possibility to co-integrate the photonic chips with InP fast electronics in the future, to drive THz electro-optic modulators, leading to a new class of photonic devices [180]. Compared to the other two techniques, the InP monolithically integration technology can obtain on-chip high density of lasers and amplifiers [181], through exploiting the energy efficient InP optoelectronics ($\approx \mu\text{W}$) [182].

To increase the capabilities of such 1300 nm platform, the development and the modelling of different functional building blocks, such as distributed Bragg reflectors (DBRs) or arrayed waveguide gratings (AWGs), could enable a different range of performance, to target different applications, in optical interconnects [183] and spectroscopy [184]. Moreover, a complete analysis of the fabrication tolerance and the performance deviation of the photonic components, within different chips and wafers, is important to improve the parametrized models and the laser simulators. This can be achieved through a high throughput testing of identical device and the creation of a performance metric through statistical analysis [68]. A complete analysis of the fabrication tolerance and the performance deviation within different chips and wafer is important to improve the parametrized models, which describe

the different components, but this goes beyond the scope of this work. For example, it was established that the wavelength dependence of the splitting ratio and the insertion losses of an MMI coupler can dramatically influence the steady state and the dynamics of the laser operation. A parametrized description of MMI as function of wavelength can improve the prediction on the laser tuning mechanism with a steady state spectral model and it allows to address some expected challenges during the design phase. Similar considerations can be done regarding the crosstalk between different ERMs inside the filters or understanding the ERM thermal behavior. The time dependent thermal behavior of the ERM at different wavelength can influence the laser wavelength switching time and its wavelength stability.

8.2 LASER SOURCES FOR OCT

The second part of the thesis focuses on the study of the suitability of monolithically integrated tunable laser systems based on voltage controlled electro-optically tuned wavelength selective filters, as sources in OCT setup schemes. Two different laser systems are studied as OCT sources. The laser designs investigated were realized on a 1550 nm integration platform for mainly practical reasons, but their analysis can be transferred to 1300 nm laser with similar cavity designs. A continuous wave (CW) single mode ring laser system based on three-stage AMZI [29] has been firstly investigated. Its use in a stepwise scan configuration within 50 nm has been tested at 1 kHz scan rates with 1000 different wavelengths per scan. The poor stability of the laser emission wavelength with time with wavelength drifts of $\approx 12 \text{ pm/h}$, is the main bottleneck hampering the performance of such laser. Therefore, a possible improvement to compensate imperfections in the chips performance and to ensure a complete control of the laser concerns the development of a fast calibration technique through the wavelength monitoring during slower laser scans that can be applied frequently, even every few seconds. This wavelength monitoring is done using a fiber bragg grating interrogator as a wavemeter with high resolution (1 pm) and sufficiently fast (19 kSa/s) sampling time. The performance of the laser scan has been investigated through the analysis of the transmission of a tunable bandpass filter at the output of the laser. The organization of the output data from laser scan according to the recorded optical wavelengths, enables the measurements of the gaussian filter FWHM in transmission from a time dependent signal. The suitability for OCT of such a laser still must be proven. The current tuning of the laser shows the presence of several gaps in the laser tuning. This can be due to the poor performance of passive components such as splitters over a wide wavelength range and to spurious reflections coming from the passive components in the laser circuit. A second issue is the imperfect reading of the wavelengths due to multimode laser operation and power fluctuations. This can be improved by multiple real-time wavelength readings with slower calibrations stepwise scan rates (1 – 5 Hz) and the use of the average reading on the

OCT measurement. The use of electronic synchronization between the laser control electronics and the wavemeter can further reduce the number of spurious readings. Moreover, as a future development, a different wavelength monitoring unit design can be implemented to discriminate between multimode configurations with 8 nm or closer lasing wavelengths, following an approach as was demonstrated using an Si arrayed waveguide grating [185]. The main limitation to the scan speed is set by the wavelength switching time inside the laser cavity of approximately 50 ns. This means for a scan with 1000 steps, a practical limit of around 10 kHz [162]. The wavelength switching time can in principle be reduced through frequent laser resets during its operation. This can be implemented using a segmented amplifier inside the laser cavity. Finally, the measurement uncertainty can be studied. By the analysis of the way the output lasing wavelengths change over time using the fast-monitoring system, it is possible to study the wavelength dependent sensitivity to the environmental conditions. Different points of the laser calibration map would have different levels of stability, and different actions can be taken.

As an alternative source, the design and the simulation of a cm-long integrated Fourier Domain Mode-Locked laser (FDML) system [132] are presented. The use of photonic integration can enhance the performance of such lasers in terms of speed (2.5 GHz repetition rates) and can enable the use of electronic waveform driving which are different than the sinusoidal one. FDML sources have enabled SS-OCT with ultrahigh A-scan rates (400 MHz) [15]. Photonic integration, if properly sustained by a sufficiently fast data acquisition [7], [186], can further increase the SS-OCT speed to the GHz level. In this thesis the use of an AMZI as a fast tunable filter, in a fiber based FDML ring laser was characterized. Highly chirped output pulses (83 ns) have been observed as a clear indication of FDML operation. Hybrid integration approaches can be implemented to exploit the use of low loss (0.1 dB/m) photonic platforms [187], inside meters-long FDML laser to obtain 100 MHz repetition rates. For OCT application, this hybrid laser design has the potential to increase the scan rate (in several MHz) and scale down the dimensions (down to few meters) of current state-of-art FD-MLLs. Moreover, wider FDML frequency comb can be generated using different arm geometrical mismatch inside AMZI integrated tunable filters. However, for a wide range of wavelength, the InP passive waveguides present a significant dispersion. For this purpose, some integrated circuits for dispersion slope compensation need to be inserted inside the FDML laser cavity [188].

APPENDIX A

RATE EQUATION FOR THE SOA DESCRIPTION

In this appendix the rate equations for the description of the SOA in the simulator used in Chapter 4 and 7 are presented. The SOA rate equations describe concentration dependent radiative and non-radiative carrier recombination rates described in [133] as well as the photon densities for two directions. The model also includes nonlinear effects such as Two Photon Absorption (TPA) and the non-linear refractive index. The SOA material gain as a function of wavelength (λ) is modelled with a logarithmic gain approximation versus carrier density. This gain approximation is validated experimentally by [103]. The gain-carrier relation used is given in (A.1), where g_{mat} is unsaturated material gain, a_N differential gain cross section and N_{tr} is transparency carrier density.

$$g_{mat}(\lambda) = a_N(\lambda) \cdot N_{tr}(\lambda) \cdot \ln \left(\frac{N}{N_{tr}(\lambda)} \right) \quad (A.1)$$

Each SOA segment is described by the rate equations for the carrier and photon density and the phase propagations.

$$\begin{aligned} \frac{dP_{\pm}}{dt} = P_{\pm} & \frac{v_g a_N \Gamma N_{tr} \ln \left(\frac{N}{N_{tr}} \right) - \varepsilon_2 (\hbar\omega)^2 v_g^3 \frac{A^2}{\Gamma^2} (P_+ + P_-)^2}{1 + \varepsilon_1 \hbar\omega v_g \frac{A}{\Gamma} (P_+ + P_-)} - 2\Gamma_2 \beta_2 \hbar\omega v_g^2 (P_{\pm}^2 + P_- P_+) - v_g \alpha_{loss} P_{\pm} - \\ & - v_g \alpha_{FC} N P_{\pm} - v_g \alpha_{FC2} N^2 P_{\pm} + \langle B \Gamma \beta N^2 \rangle \end{aligned} \quad (A.2)$$

$$\begin{aligned} \frac{d\phi_{\pm}}{dz} = -\frac{1}{2} \alpha_N a_N \Gamma N_{tr} \ln \left(\frac{N}{N_{tr}} \right) + \frac{1}{2} \alpha_T & \frac{\varepsilon_1 a_N \hbar\omega v_g A N_{tr} \ln \left(\frac{N}{N_{tr}} \right) (P_+ + P_-) + \varepsilon_2 (\hbar\omega)^2 v_g^3 \frac{A^2}{\Gamma^2} (P_+ + P_-)^2}{1 + \varepsilon_1 \hbar\omega v_g \frac{A}{\Gamma} (P_+ + P_-)} - \\ & - \Gamma'_2 n_2 \hbar\omega v_g (P_+ + P_-) \end{aligned} \quad (A.3)$$

$$\begin{aligned} \frac{dN}{dt} = -P_{\pm} & \frac{v_g a_N N_{tr} \ln \left(\frac{N}{N_{tr}} \right) - \varepsilon_2 (\hbar\omega)^2 v_g^3 \frac{A^2}{\Gamma^2} (P_+ + P_-)^2}{1 + \varepsilon_1 \hbar\omega v_g \frac{A}{\Gamma} (P_+ + P_-)} + 2 \frac{\Gamma_2}{\Gamma} \beta_2 \hbar\omega v_g^2 (P_+ + P_-)^2 + W_p - \frac{N}{\tau} - \\ & B N^2 - C N^3 - D N^{5.5} \end{aligned} \quad (A.4)$$

The evolution of the photon densities is described in (A.2) where P_+ and P_- refer to the photon densities for positive and negative propagation direction respectively. Equation (A.4) describes the phase evolution. Where v_g is group velocity, a_N is gain cross-section, A is surface of the active region, ε_1 is non-linear gain compression factor due to carrier heating and spectral hole burning, ε_2 is gain compression factor due to two photon absorption, Γ is linear confinement factor, Γ_2 is confinement factor for (TPA), Γ'_2 is confinement factor for Ultrafast Nonlinear Refraction (UNR), α_{loss} is passive propagation loss, α_{FC} is loss per carrier

per unit volume due to free carrier absorption in active region, α_{FC2} loss per carrier per unit volume due to free carrier absorption in active region (quadratic term), β_2 is the coefficient for two photon absorption, α_N is the carrier density linewidth enhancement factor, α_T is the temperature linewidth enhancement factor and n_2 is the nonlinear gain refractive index. The carrier recombination mechanism is described in (A.4), where τ is non-radiative carrier lifetime, B is the bimolecular recombination rate, C is the Auger recombination coefficient, D is carrier loss term due to leakage current and W_p is pumping rate. The above SOA rate equations are explained in more details in [174], [189].

All the rate equations parameters values used in the simulation are listed in Table. A.1. These parameters are calculated for InP-based integrated devices operating at 1550 nm. The parameters are used to model an active region that consists of a 4 MQW amplifier structure. Note that those parameters can vary for different layer structures of the SOA and passive components. It is important to mention that the effect of the gain bandwidth limitation of the SOA is not included in the rate equations of the SOA (Flat gain approximation). To include this effect an optical bandwidth limiting filter is added as a separate element in the laser design. Passive waveguides are modelled as lossy elements. The waveguide dispersion of the effective refractive index $n(\lambda)$ is not included in the model. Phase Modulators (PM) are modelled as passive waveguides where the required phase change is directly applied in radians within absolute range $[-\pi, \pi]$ which is also an approximation of the index modulation in real PMs

The simulation of the laser design is performed using PHIsim software tool. The complex field propagation for single transverse mode TE polarized light at any point in the circuit is described as:

$$E(t) = \sqrt{P_+(t)}e^{i\varphi_+(t)}e^{i\omega_0 t} + \sqrt{P_-(t)}e^{i\varphi_-(t)}e^{i\omega_0 t} \quad (2.5)$$

Where P represents the absolute power, φ the instantaneous phase and ω_0 is the central frequency of the simulation. To achieve a reasonable computational time in the simulations presented here, the length of each optical segment L_{seg} is chosen to be $8.6 \mu m$ which is 20 time the central wavelength $\lambda_0 = 1552 nm$. This value corresponds to a discretization time $T_{seg} = 103.4 fs$ at group index $n_g = 3.6$.

Table. A.1 Used parameter values in the model.

Symbol	Description	Value
a_N	Linear gain coefficient	$1.694 \times 10^{-19} \text{ m}^2$
N_{tr}	Transparency carrier density	$0.6577 \times 10^{24} \text{ m}^{-3}$
Γ	Linear confinement factor	0.053
Γ_2	Confinement factor for TPA	0.1
Γ'_2	Confinement factor for UNR	0.08
ε_1	Nonlinear gain compression factor	0.2 W^{-1}
ε_2	Nonlinear gain compression factor of TPA	$200 \text{ W}^{-2} \text{ m}^{-1}$
λ_0	Centre wavelength	1552 nm
A	Active region surface	$0.0265 \times 2 \text{ } \mu\text{m}^2$
n_2	Nonlinear gain refractive index	$-3.5 \times 10^{-16} \text{ m}^2 \text{ W}^{-1}$
β	Spontaneous emission coupling factor	10^{-5}
β_2	Coefficient for TPA	$3.7 \times 10^{-10} \text{ m/W}$
τ	Carrier lifetime	0.598 ns
B	Bimolecular recombination rate	$2.602 \times 10^{-16} \text{ m}^3/\text{s}$
C	Auger recombination coefficient	$5.269 \times 10^{-41} \text{ m}^6/\text{s}$
D	Carrier loss term due to current leakage	$5.07 \times 10^{-102} \text{ m}^{16.5}/\text{s}$
α_{loss}	Passive waveguide loss	34.5 m^{-1}
α_{FC}	Free carrier loss in active region	$2.264 \times 10^{-21} \text{ m}^2$
α_{FC2}	Free carrier loss (quadratic term)	$-2.502 \times 10^{-46} \text{ m}^5$
α_N	Carrier density linewidth enhancement factor	4
α_T	Temperature linewidth enhancement factor	2

REFERENCES

- [1] O. Carrasco, R. B. Gomez, A. Chainani, and W. E. Roper, "Hyperspectral imaging applied to medical diagnoses and food safety," *Geo-Spatial Temporal Image Data Exploit. III*, vol. 5097, no. August 2003, p. 215, 2003, doi: 10.1117/12.502589.
- [2] D. Chapman *et al.*, "Diffraction enhanced x-ray imaging," *Phys. Med. Biol.*, vol. 42, no. 11, pp. 2015–2025, 1997, doi: 10.1088/0031-9155/42/11/001.
- [3] S. Leung, "Computerized transverse axial scanning (tomography): Part I. Description of system," *Int. J. Radiat. Oncol. Biol. Phys.*, vol. 31, no. 2, pp. 393–398, 1995, doi: 10.1016/0360-3016(94)E0127-6.
- [4] S. Hughes, "Medical ultrasound imaging," *Phys. Educ.*, vol. 36, no. 6, pp. 468–475, 2001, doi: 10.1088/0031-9120/36/6/304.
- [5] P. Mansfield and A. A. Maudsley, "Medical imaging by NMR," *Br. J. Radiol.*, vol. 50, no. 591, pp. 188–194, 1977, doi: 10.1259/0007-1285-50-591-188.
- [6] A. F. Fercher, W. Drexler, C. K. Hitzenberger, and T. Lasser, "Optical coherence tomography - Principles and applications," *Reports Prog. Phys.*, vol. 66, no. 2, pp. 239–303, 2003, doi: 10.1088/0034-4885/66/2/204.
- [7] M. Wojtkowski *et al.*, "Three-dimensional retinal imaging with high-speed ultrahigh-resolution optical coherence tomography," *Ophthalmology*, vol. 112, no. 10, pp. 1734–1746, 2005, doi: 10.1016/j.ophtha.2005.05.023.
- [8] Z. Chen *et al.*, "Non-invasive multimodal optical coherence and photoacoustic tomography for human skin imaging," *Sci. Rep.*, vol. 7, no. 1, pp. 1–11, 2017, doi: 10.1038/s41598-017-18331-9.
- [9] H. Liang, B. Peric, M. Hughes, A. Podoleanu, M. Spring, and D. Saunders, "Optical coherence tomography for art conservation and archaeology," *O3A Opt. Arts, Archit. Archaeol.*, vol. 6618, no. July 2007, p. 661805, 2007, doi: 10.1117/12.726032.
- [10] L. B. Neubrand, T. G. van Leeuwen, and D. J. Faber, "Precision of attenuation coefficient measurements by optical coherence tomography," *J. Biomed. Opt.*, vol. 27, no. 08, 2022, doi: 10.1117/1.jbo.27.8.085001.
- [11] Z. H. E. C. Hen *et al.*, "Phase-stable swept source OCT angiography in human skin using an akinetic source," vol. 7, no. 8, pp. 4166–4176, 2016.
- [12] "Topcon 2000 system." <https://www.medicalworkshop.nl/producten/imaging/oct-s/topcon-3d-oct-2000/>.
- [13] L. An, P. Li, T. T. Shen, and R. Wang, "High speed spectral domain optical coherence tomography for retinal imaging at 500,000 A-lines per second," *Biomed. Opt. Express*, vol. 2, no. 10, p. 2770, 2011, doi: 10.1364/boe.2.002770.
- [14] S. Yun, G. Tearney, B. Bouma, B. Park, and J. de Boer, "High-speed spectral-domain optical coherence tomography at 13 μm wavelength," *Opt. Express*, vol. 11, no. 26, p. 3598, 2003, doi: 10.1364/oe.11.003598.
- [15] D. Huang, F. Li, Z. He, Z. Cheng, C. Shang, and P. K. A. Wai, "400 MHz ultrafast optical coherence tomography," *Opt. Lett.*, vol. 45, no. 24, p. 6675, 2020, doi:

References

- 10.1364/ol.409607.
- [16] L. An, G. Guan, and R. K. Wang, "High-speed 1310 nm-band spectral domain optical coherence tomography at 184,000 lines per second," *J. Biomed. Opt.*, vol. 16, no. 6, p. 060506, 2011, doi: 10.1117/1.3592492.
- [17] M. Göb, T. Pfeiffer, W. Draxinger, S. Lotz, J. P. Kolb, and R. Huber, "Continuous spectral zooming for in vivo live 4D-OCT with MHz A-scan rates and long coherence," *Biomed. Opt. Express*, vol. 13, no. 2, p. 713, 2022, doi: 10.1364/boe.448353.
- [18] V. J. Srinivasan *et al.*, "High-speed, high-resolution optical coherence tomography retinal imaging with a frequency-swept laser at 850 nm," *Opt. Lett.*, vol. 32, no. 4, p. 361, 2007, doi: 10.1364/ol.32.000361.
- [19] W. Wieser, W. Draxinger, T. Klein, S. Karpf, T. Pfeiffer, and R. Huber, "High definition live 3D-OCT in vivo: design and evaluation of a 4D OCT engine with 1 GVoxel/s," *Biomed. Opt. Express*, vol. 5, no. 9, p. 2963, 2014, doi: 10.1364/boe.5.002963.
- [20] N. A. Nassif *et al.*, "In vivo high-resolution video-rate spectral-domain optical coherence tomography of the human retina and optic nerve Abstract :," vol. 12, no. 3, pp. 367–376, 2004.
- [21] B. W. Tilma *et al.*, "Integrated tunable quantum-dot laser for optical coherence tomography in the 1.7 μm wavelength region," *IEEE J. Quantum Electron.*, vol. 48, no. 2, pp. 87–98, 2012, doi: 10.1109/JQE.2011.2165317.
- [22] M. Choma, M. Sarunic, C. Yang, and J. Izatt, "Sensitivity advantage of swept source and Fourier domain optical coherence tomography," *Opt. Express*, vol. 11, no. 18, p. 2183, 2003, doi: 10.1364/oe.11.002183.
- [23] W. Demtroder, *Laser Spectroscopy*, Fourth. 2008.
- [24] R. Leitgeb *et al.*, "Enhanced medical diagnosis for dOCTors : a perspective of optical coherence tomography," vol. 26, no. October 2021, pp. 1–47, 2023, doi: 10.1117/1.JBO.26.10.100601.
- [25] H. Y. Lee, H. Sudkamp, T. Marvdashti, and A. K. Ellerbee, "Interleaved optical coherence tomography," *Opt. Express*, vol. 21, no. 22, p. 26542, 2013, doi: 10.1364/oe.21.026542.
- [26] V. M. Kodach, J. Kalkman, D. J. Faber, and T. G. van Leeuwen, "Quantitative comparison of the OCT imaging depth at 1300 nm and 1600 nm," *Biomed. Opt. Express*, vol. 1, no. 1, p. 176, 2010, doi: 10.1364/boe.1.000176.
- [27] M. Smit *et al.*, "An introduction to InP-based generic integration technology," *Semicond. Sci. Technol.*, vol. 29, no. 8, 2014, doi: 10.1088/0268-1242/29/8/083001.
- [28] A. Meighan, Y. Yao, M. J. Wale, and K. A. Williams, "Design of 100 GHz-class Mach-Zehnder modulators in a generic indium phosphide platform," *2020 IEEE Photonics Conf. IPC 2020 - Proc.*, pp. 9–10, 2020, doi: 10.1109/IPC47351.2020.9252410.
- [29] S. Latkowski *et al.*, "Novel Widely Tunable Monolithically Integrated Laser Source," *IEEE Photonics J.*, vol. 7, no. 6, 2015, doi: 10.1109/JPHOT.2015.2493722.
- [30] J. Hazan, T. Couka, R. Pajkovic, K. Williams, and E. Bente, "Control strategy for a monolithically integrated widely tunable laser system on InP for optical coherence tomography," no. May, p. 21, 2022, doi: 10.1117/12.2610120.
- [31] L. M. Augustin *et al.*, "InP-Based Generic Foundry Platform for Photonic Integrated

- Circuits," *IEEE J. Sel. Top. Quantum Electron.*, vol. 24, no. 1, 2018, doi: 10.1109/JSTQE.2017.2720967.
- [32] "No Title." <https://www.zero2basiccourse.com/terminology/mpw/>.
- [33] S. P. Lerner, A. C. Goh, N. J. Tresser, and S. S. Shen, "Optical Coherence Tomography as an Adjunct to White Light Cystoscopy for Intravesical Real-Time Imaging and Staging of Bladder Cancer," *Urology*, vol. 72, no. 1, pp. 133–137, 2008, doi: 10.1016/j.urology.2008.02.002.
- [34] T. G. Van Leeuwen *et al.*, "On-chip Mach-Zehnder interferometer for OCT systems," *Adv. Opt. Technol.*, vol. 7, no. 1–2, pp. 103–106, 2018, doi: 10.1515/aot-2017-0061.
- [35] M. Bonesi *et al.*, "Akinetic all-semiconductor programmable swept-source at 1550 nm and 1310 nm with centimeters coherence length," *Opt. Express*, vol. 22, no. 3, p. 2632, 2014, doi: 10.1364/oe.22.002632.
- [36] R. Pajkovic, D. Garbi, K. Williams, and E. Bente, "Dynamic properties of wavelength switching in a widely tunable semiconductor laser for optical coherence tomography," no. April 2020, p. 19, 2020, doi: 10.1117/12.2555620.
- [37] J. Xi, L. Huo, J. Li, and X. Li, "Generic real-time uniform K-space sampling method for high-speed swept-Source optical coherence tomography," *Opt. Express*, vol. 18, no. 9, p. 9511, 2010, doi: 10.1364/oe.18.009511.
- [38] W. Yao, M. K. Smit, and M. J. Wale, "Monolithic 300 Gb/s parallel transmitter in inP-based generic photonic integration technology," *IEEE J. Sel. Top. Quantum Electron.*, vol. 24, no. 1, 2018, doi: 10.1109/JSTQE.2017.2762602.
- [39] J. Hazan, S. Andreou, D. Pustakhod, S. Kleijn, K. A. Williams, and E. A. J. M. Bente, "1300 nm Semiconductor Optical Amplifier Compatible With an InP Monolithic Active / Passive Integration Technology," *IEEE Photonics J.*, vol. 14, no. 3, pp. 1–11, 2022, doi: 10.1109/JPHOT.2022.3175373.
- [40] D. D'Agostino, "Capability extensions to the COBRA generic photonic integration platform door," 2015.
- [41] D. D'Agostino *et al.*, "Low-loss passive waveguides in a generic InP foundry process via local diffusion of zinc," *Opt. Express*, vol. 23, no. 19, p. 25143, 2015, doi: 10.1364/oe.23.025143.
- [42] "Lumerical Inc." .
- [43] S. Seifert and P. Runge, "Revised refractive index and absorption of In_{1-x}Ga_xAs_yP_{1-y} lattice-matched to InP in transparent and absorption IR-region," *Opt. Mater. Express*, vol. 6, no. 2, p. 629, 2016, doi: 10.1364/ome.6.000629.
- [44] P. U. Dow John, Redfield David, "Toward a Unified Theory of Urbach's Rule and Exponential Absorption Edges," *Phys. Rev. B*, vol. 5, no. 2, pp. 1689–1699, 1972.
- [45] J. Bolk *et al.*, "Deep UV Lithography Process in Generic InP Integration for Arrayed Waveguide Gratings," *IEEE Photonics Technol. Lett.*, vol. 30, no. 13, pp. 1222–1225, 2018, doi: 10.1109/LPT.2018.2840224.
- [46] "'Nazca,' Nazca Design."
- [47] D. Hofstetter and R. L. Thornton, "Theory of loss measurements of Fabry–Perot resonators by Fourier analysis of the transmission spectra," *Opt. Lett.*, vol. 22, no. 24, p. 1831, 1997, doi: 10.1364/ol.22.001831.

References

- [48] S. Taebi, M. Khorasaninejad, and S. S. Saini, "Modified Fabry-Perot interferometric method for waveguide loss measurement," *Appl. Opt.*, vol. 47, no. 35, pp. 6625–6630, 2008, doi: 10.1364/AO.47.006625.
- [49] Z. Li, D. Lu, and Y. He, "A waveguide loss measurement method based on the reflected interferometric pattern of a Fabry-Perot cavity," no. May, p. 64, 2018, doi: 10.1117/12.2288922.
- [50] R. W. Schafer, "What Is a Savitzky-Golay Filter?," no. July, pp. 111–117, 2011.
- [51] F. P. Payne and J. P. R. Lacey, "A theoretical analysis of scattering loss from planar optical waveguides," *Opt. Quantum Electron.*, vol. 26, no. 10, pp. 977–986, 1994, doi: 10.1007/BF00708339.
- [52] E. Kleijn, *Passive components in indium phosphide generic integration technologies*, vol. 1, no. 2014. 2014.
- [53] J. Hazan, S. Andreou, D. Pustakhod, S. Kleijn, K. Williams, and E. Bente, "1 . 3 μ m InGaAsP / InP semiconductor optical amplifier compatible with an active / passive integration technology," pp. 5–6, doi: 10.1109/3.283797.A.
- [54] S. Morasca, F. Pozzi, and C. De Bernardi, "Measurement of Group Effective Index in Integrated Semiconductor Optical Waveguides," *IEEE Photonics Technol. Lett.*, vol. 5, no. 1, pp. 40–42, 1993, doi: 10.1109/68.185054.
- [55] L. A. Bru, D. Pastor, and P. Muñoz, "Integrated optical frequency domain reflectometry device for characterization of complex integrated devices," *Opt. Express*, vol. 26, no. 23, p. 30000, 2018, doi: 10.1364/oe.26.030000.
- [56] B. J. Soller, D. K. Gifford, M. S. Wolfe, and M. E. Froggatt, "High resolution optical frequency domain reflectometry for characterization of components and assemblies," *Opt. Express*, vol. 13, no. 2, p. 666, 2005, doi: 10.1364/opex.13.000666.
- [57] I. Waveguides, U. Glombitza, and E. Brinkmeyer, "Coherent Frequency-Domain Reflectometry," vol. 11, no. 8, pp. 1377–1384, 1993.
- [58] D. Zhao, D. Pustakhod, K. Williams, and X. Leijtens, "High resolution optical frequency domain reflectometry for measurement of waveguide group refractive index," *30th Annu. Conf. IEEE Photonics Soc. IPC 2017*, vol. 2017-Janua, no. 16, pp. 537–538, 2017, doi: 10.1109/IPCon.2017.8116212.
- [59] S. Dwivedi *et al.*, "Experimental Extraction of Effective Refractive Index and Thermo-Optic Coefficients of Silicon-on-Insulator Waveguides Using Interferometers," *J. Light. Technol.*, vol. 33, no. 21, pp. 4471–4477, 2015, doi: 10.1109/JLT.2015.2476603.
- [60] E. Brinkmeyer and U. Glombitza, "Complex coherence-domain reflectometry in active laser diodes," *Opt. Lett.*, vol. 17, no. 20, p. 1441, 1992, doi: 10.1364/ol.17.001441.
- [61] A. Melloni, F. Carniel, R. Costa, and M. Martinelli, "Determination of bend mode characteristics in dielectric waveguides," *J. Light. Technol.*, vol. 19, no. 4, pp. 571–577, 2001, doi: 10.1109/50.920856.
- [62] E.-G. Neumann, "Curved dielectric optical waveguides with reduced transition losses," *IET Conf. Publ.*, vol. 129, no. 5, pp. 278–280, 1982, doi: 10.1049/ip-h-1.1982.0056.
- [63] D. Pustakhod, E. Kleijn, K. Williams, and X. Leijtens, "High-Resolution AWG-Based

- Fiber," vol. 28, no. 20, pp. 2203–2206, 2016.
- [64] L. B. Soldano and E. C. M. Pennings, "Optical Multi-Mode Interference Devices Based on Self-Imaging: Principles and Applications," *J. Light. Technol.*, vol. 13, no. 4, pp. 615–627, 1995, doi: 10.1109/50.372474.
 - [65] J. Leuthold, J. Eckner, E. Gamper, P. A. Besse, and H. Melchior, "Multimode interference couplers for the conversion and combining of zero- and first-order modes," *J. Light. Technol.*, vol. 16, no. 7, pp. 1228–1238, 1998, doi: 10.1109/50.701401.
 - [66] Y. Fu, T. Ye, W. Tang, and T. Chu, "Efficient adiabatic silicon-on-insulator waveguide taper," *Photonics Res.*, vol. 2, no. 3, p. A41, 2014, doi: 10.1364/prj.2.000a41.
 - [67] R. Hanfoug, L. M. Augustin, Y. Barbarin, J. J. G. M. Van Der Tol, and E. A. J. M. Bente, "A Multimode Interference coupler with low reflections," pp. 97–100, 2005.
 - [68] S. Latkowski, D. Pustakhod, M. Chatzimichailidis, W. Yao, and X. J. M. Leijtens, "Open Standards for Automation of Testing of Photonic Integrated Circuits," *IEEE J. Sel. Top. Quantum Electron.*, vol. 25, no. 5, pp. 1–8, 2019, doi: 10.1109/JSTQE.2019.2921401.
 - [69] J. Hazan, D. Pustakhod, S. Kleijn, S. Andreou, K. A. Williams, and E. A. J. M. Bente, "Broadband multimode interference coupler on InP substrate with flat wavelength response over the whole O-band," in *Proc. Integrated Photonics Conference*, 2021, vol. 1, no. 1, pp. 12–13, doi: 10.1109/50.372474.J.
 - [70] E. Kleijn, M. K. Smit, and X. J. M. Leijtens, "Multimode interference reflectors: A new class of components for photonic integrated circuits," *J. Light. Technol.*, vol. 31, no. 18, pp. 3055–3063, 2013, doi: 10.1109/JLT.2013.2278187.
 - [71] B. Docter, E. J. Geluk, M. J. H. Sander-Jochem, F. Karouta, and M. K. Smit, "Deep etched DBR gratings in InP for photonic integrated circuits," *Conf. Proc. - Int. Conf. Indium Phosphide Relat. Mater.*, vol. 5, no. May, pp. 226–228, 2007, doi: 10.1109/ICIPRM.2007.381164.
 - [72] Y. Huang *et al.*, "A single-directional microcavity laser with microloop mirrors and widened medium realized with quantum-well intermixing," *IEEE Photonics Technol. Lett.*, vol. 18, no. 1, pp. 130–132, 2006, doi: 10.1109/LPT.2005.860066.
 - [73] M. Hoppe *et al.*, "High speed external cavity diode laser concept based on a resonantly driven MEMS scanner for the mid-infrared region," *Appl. Opt.*, vol. 60, no. 15, p. C92, 2021, doi: 10.1364/ao.420041.
 - [74] B. Mason, J. Barton, G. A. Fish, L. A. Coldren, and S. P. DenBaars, "Design of sampled grating DBR lasers with integrated semiconductor optical amplifiers," *IEEE Photonics Technol. Lett.*, vol. 12, no. 7, pp. 762–764, 2000, doi: 10.1109/68.853492.
 - [75] L. A. Coldren, G. A. Fish, Y. Akulova, J. S. Barton, L. Johansson, and C. W. Coldren, "Tunable Semiconductor Lasers: A Tutorial," *J. Light. Technol.*, vol. 22, no. 1, pp. 193–202, 2004, doi: 10.1109/JLT.2003.822207.
 - [76] P. J. A. Thijs, T. Van Dongen, L. F. Tiemeijer, and J. J. M. Binsma, "Strained-Layer Quantum Well Lasers," vol. 12, no. 1, pp. 28–37, 1994.
 - [77] J. Jin, D. Tian, J. Shi, and T. Li, "Fabrication and complete characterization of polarization insensitive 1310 nm InGaAsP-InP quantum-well semiconductor optical amplifiers," *Semicond. Sci. Technol.*, vol. 19, no. 1, pp. 120–126, 2004, doi:

References

- 10.1088/0268-1242/19/1/020.
- [78] A. Ferrari *et al.*, "Assessment on the Achievable Throughput of Multi-Band ITU-T G.652.D Fiber Transmission Systems," *J. Light. Technol.*, vol. 38, no. 16, pp. 4279–4291, 2020, doi: 10.1109/JLT.2020.2989620.
- [79] Ł. Chorchos and J. P. Turkiewicz, "Performance comparison of the 1310nm optical amplifiers," *Photonics Appl. Astron. Commun. Ind. High-Energy Phys. Exp.* 2016, vol. 10031, no. May, p. 100311C, 2016, doi: 10.1117/12.2249337.
- [80] D. A. Ackerman *et al.*, "Analysis of Gain in Determining T0 in 1.3 μm Semiconductor Lasers," *IEEE J. Sel. Top. Quantum Electron.*, vol. 1, no. 2, pp. 250–263, 1995, doi: 10.1109/2944.401204.
- [81] L. F. Tiemeijer *et al.*, "High-gain 1310 nm semiconductor optical amplifier modules with a built-in amplified signal monitor for optical gain control," *IEEE Photonics Technol. Lett.*, vol. 9, no. 3, pp. 309–311, 1997, doi: 10.1109/68.556056.
- [82] P. J. A. Thijs, L. F. Tiemeijer, J. J. M. Binsma, and T. van Dongen, "Progress in Long-Wavelength Strained-Layer InGaAs(P) Quantum-Well Semiconductor Lasers and Amplifiers," *IEEE J. Quantum Electron.*, vol. 30, no. 2, pp. 477–499, 1994, doi: 10.1109/3.283797.
- [83] T. Higashi, T. Yamamoto, S. Ogita, and M. Kobayashi, "Experimental analysis of characteristic temperature in quantum-well semiconductor lasers," *IEEE J. Sel. Top. Quantum Electron.*, vol. 3, no. 2, pp. 513–521, 1997, doi: 10.1109/2944.605702.
- [84] A. Fiore, C. Zinoni, B. Alloing, V. Zwiller, L. H. Li, and C. Monat, "Nanoscale single quantum dot devices at 1300 nm," *Quantum Dots, Nanoparticles, Nanoclusters II*, vol. 5734, no. April 2005, p. 106, 2005, doi: 10.1117/12.598039.
- [85] S. Latkowski *et al.*, "Monolithically integrated 25 GHz extended cavity mode-locked ring laser with intracavity phase modulators," *Opt. Lett.*, vol. 40, no. 1, p. 77, 2015, doi: 10.1364/ol.40.000077.
- [86] I. M. Soganci *et al.*, "Monolithically integrated InP 1 \times 16 optical switch with wavelength-insensitive operation," *IEEE Photonics Technol. Lett.*, vol. 22, no. 3, pp. 143–145, 2010, doi: 10.1109/LPT.2009.2036859.
- [87] P. Dong *et al.*, "Novel integration technique for silicon/III-V hybrid laser," *Opt. Express*, vol. 22, no. 22, p. 26854, 2014, doi: 10.1364/oe.22.026854.
- [88] A. Y. Liu and J. Bowers, "Photonic integration with epitaxial III-V on silicon," *IEEE J. Sel. Top. Quantum Electron.*, vol. 24, no. 6, 2018, doi: 10.1109/JSTQE.2018.2854542.
- [89] L. M. M. I. T. Chen Siming *et al.*, "InAs / GaAs quantum dot lasers monolithically grown on on-axis Si (001) substrates," *Opt. Express*, vol. 25, no. 5, pp. 11381–11386, 2017.
- [90] S. Liu and A. Khope, "Latest advances in high-performance light sources and optical amplifiers on silicon," *J. Semicond.*, vol. 42, no. 4, 2021, doi: 10.1088/1674-4926/42/4/041307.
- [91] M. Buffolo *et al.*, "Degradation Mechanisms of Heterogeneous III-V/Silicon 1.55- μm DBR Laser Diodes," *IEEE J. Quantum Electron.*, vol. 53, no. 4, 2017, doi: 10.1109/JQE.2017.2714582.
- [92] A. D. Andreev and Donetsky D.V., "Analysis of temperature dependence of the AlGaAsSb quantum-well lasers," *Appl. Phys. Lett.*, vol. 2743, no. May 1999, pp. 8–11,

- 1999.
- [93] D. P. Sapkota, M. S. Kayastha, and K. Wakita, "Dependence of threshold current density on quantum well composition for compressive strained-layer Al_xGa_{1-x}As lasers," *Conf. Proc. - Int. Conf. Indium Phosphide Relat. Mater.*, pp. 261–264, 2010, doi: 10.1109/ICIPRM.2010.5516084.
 - [94] C. S. H. P. Derry, L. Figueroa, "Semiconductor lasers," in *Nature*, vol. 289, no. 5800, 1981, pp. 830–830.
 - [95] K. Hosomi, T. Mozume, H. Kashima, and K. Ouchi, "Photoluminescence investigation of InGaAs/InP quantum wells grown by gas-source molecular-beam epitaxy with source-supply interruption," *Conf. Proc. - Int. Conf. Indium Phosphide Relat. Mater.*, pp. 169–172, 1995, doi: 10.1109/iciprm.1995.522105.
 - [96] K. S. Mobarhan, "Application Note: Test and Characterization of Laser Diodes: Determination of Principal Parameters," no. ii, pp. 1–27, 2006.
 - [97] L. A. Coldren, "Diode Lasers and Photonic Integrated Circuits," *Opt. Eng.*, vol. 36, no. 2, p. 616, 1997, doi: 10.1117/1.601191.
 - [98] H. Park, P. Srinivasan, M. L. Davenport, M. N. Sysak, and R. Jones, "Experimental Investigations of Characteristic Temperatures of Hybrid Silicon Lasers," *IEEE J. Quantum Electron.*, vol. 48, no. 12, pp. 1512–1518, 2012, doi: 10.1109/JQE.2012.2222870.
 - [99] T. Tsuchiya, D. Takemoto, T. Sudou, and M. Aoki, "Low-threshold and high-temperature characteristics of 1.3- μ m InGaAlAs MQW lasers grown by metalorganic vapor-phase epitaxy," pp. 266–269.
 - [100] J. Piprek, P. Abraham, and J. E. Bowers, "Cavity length effects on internal loss and quantum efficiency of multi-quantum-well lasers," *IEEE J. Sel. Top. Quantum Electron.*, vol. 5, no. 3, pp. 643–647, 1999, doi: 10.1109/2944.788430.
 - [101] T. Cho, H. Kim, Y. Kwon, and S. Hong, "Theoretical study on intervalence band absorption in InP-based quantum-well laser structures," *Appl. Phys. Lett.*, vol. 68, no. 16, pp. 2183–2185, 1996, doi: 10.1063/1.116006.
 - [102] Y. Barbarin *et al.*, "Gain measurements of Fabry-Perot InP/InGaAsP lasers using an ultrahigh-resolution spectrometer," *Appl. Opt.*, vol. 45, no. 35, pp. 9007–9012, 2006, doi: 10.1364/AO.45.009007.
 - [103] D. Pustakhod, K. Williams, and X. Leijtens, "Fast and Robust Method for Measuring Semiconductor Optical Amplifier Gain," *IEEE J. Sel. Top. Quantum Electron.*, vol. 24, no. 1, 2018.
 - [104] J. D. Thomson, H. D. Summers, P. J. Hulyer, P. M. Snowton, and P. Blood, "Determination of single-pass optical gain and internal loss using a multisection device," *Appl. Phys. Lett.*, vol. 75, no. 17, pp. 2527–2529, 1999, doi: 10.1063/1.125066.
 - [105] S. Balle, "Simple analytical approximations for the gain and refractive index spectra in quantum-well lasers," *Asian J. Chem.*, vol. 23, no. 10, pp. 4397–4399, 2011.
 - [106] A. Tomita and A. Suzuki, "Carrier-Induced Lasing Wavelength Shift for Quantum Well Laser Diodes," *IEEE J. Quantum Electron.*, vol. 23, no. 7, pp. 1155–1159, 1987, doi: 10.1109/JQE.1987.1073481.

References

- [107] D. A. Kleinman and R. C. Miller, "Band-gap renormalization in semiconductor quantum wells containing carriers," *Phys. Rev. B*, vol. 32, no. 4, pp. 2266–2272, 1985, doi: 10.1103/PhysRevB.32.2266.
- [108] Miller.Ch, "Laser Rate Equations Dynamical System-," *Nonlinear Dyn.*, no. laser rate equations, p. 6, 2001.
- [109] R.Paschotta, "article on 'effective mode area,'" *Encyclopedia of Laser Physics and Technology*. Wiley-VCH, 2008, doi: ISBN 978-3-527-40828-3).
- [110] M. E. Prise, M. R. Taghizadeh, S. D. Smith, and B. S. Wherrett, "Picosecond measurement of Auger recombination rates in InGaAs," *Appl. Phys. Lett.*, vol. 45, no. 6, pp. 652–654, 1984, doi: 10.1063/1.95344.
- [111] P. R.Olshansky, Manning, "Measurement of Radiative and Nonradiative Recombination Rate in InGaAsP-InP LED's," *IEEE J. Quantum Electron.*, vol. 20, no. 8, pp. 1746–1750, 1984, doi: 10.1109/3.142567.
- [112] G. Pakulski *et al.*, "Transparency current density of GaInNAs lasers," *Photonics North 2004 Opt. Components Devices*, vol. 5577, no. December 2004, p. 82, 2004, doi: 10.1117/12.567550.
- [113] M. J. Connelly, "Optical amplifiers: SOAs," *Encycl. Mod. Opt.*, vol. 1–5, pp. 242–254, 2018, doi: 10.1016/B978-0-12-803581-8.09462-5.
- [114] J. C. Butcher, "history of Runge-Kutta methods," *Appl. Numer. Math.*, vol. 20, pp. 247–260, 1996.
- [115] M. L. Davenport, S. Skendzic, N. Volet, J. C. Hulme, M. J. R. Heck, and J. E. Bowers, "Heterogeneous silicon/III-V semiconductor optical amplifiers," *IEEE J. Sel. Top. Quantum Electron.*, vol. 22, no. 6, pp. 78–88, 2016, doi: 10.1109/JSTQE.2016.2593103.
- [116] J. Hazan, K. A. Williams, and E. A. J. M. Bente, "Gain spectra and saturation power measurements in a two-section InGaAsP / InP semiconductor optical amplifier at 1.3 μm ," *Proc. IEEE Photonics Benelux Symp.*, p. 4, 2021.
- [117] V. Moskalenko, "Extended cavity passively mode-locked lasers in indium phosphide generic integration technology," 2005.
- [118] S. Andreou, K. A. Williams, and E. A. J. M. Bente, "Monolithically integrated InP-based DBR lasers with an intra-cavity ring resonator," *Opt. Express*, vol. 27, no. 19, p. 26281, 2019, doi: 10.1364/oe.27.026281.
- [119] K. Hei *et al.*, "Distance Metrology with Integrated Mode-Locked Ring Laser," *IEEE Photonics J.*, vol. 11, no. 6, pp. 1–10, 2019, doi: 10.1109/JPHOT.2019.2940068.
- [120] N. R. Newbury, "Searching for applications with a fine-tooth comb," *Nat. Publ. Gr.*, vol. 5, no. April, 2011, doi: 10.1038/nphoton.2011.38.
- [121] L. Wang *et al.*, "40 Gbits/s all-optical clock recovery for degraded signals using an amplified feedback laser," vol. 49, no. 34, pp. 6577–6581, 2010.
- [122] G. Duan *et al.*, "High Performance InP-Based Quantum Dash Semiconductor Mode-Locked Lasers for Optical Communications," vol. 14, no. 3, pp. 63–84, 2009, doi: 10.1002/bltj.
- [123] B. Dong, X. C. De Labriolle, S. Liu, M. Dumont, and H. Huang, "epitaxially grown on silicon: gain properties and optical feedback stabilization Journal of Physics :

- Photonics 1 . 3- μ m passively mode-locked quantum dot lasers epitaxially grown on silicon : gain properties and optical feedback stabilization,” 2020.
- [124] V. Moskalenko, S. Latkowski, S. Tahvili, T. de Vries, M. Smit, and E. Bente, “Record bandwidth and sub-picosecond pulses from a monolithically integrated mode-locked quantum well ring laser,” *Opt. Express*, vol. 22, no. 23, p. 28865, 2014, doi: 10.1364/oe.22.028865.
 - [125] S. Garzo and M. Mendoza, “Simulation for fiber optics pulse propagation through a numerical solution of the Nonlinear Schrödinger Equation,” vol. 2, no. 7, 2020.
 - [126] E. Bente, “Photonic Integration circuit Simulator.” <https://sites.google.com/tue.nl/phisim/home>.
 - [127] M. Dong, N. Mangan, J. N. Kutz, S. T. Cundiff, and H. G. Winful, “Model for frequency comb generation in single-section quantum well diode lasers,” *2017 Conf. Lasers Electro-Optics, CLEO 2017 - Proc.*, vol. 2017-Janua, no. 6, pp. 1–2, 2017, doi: 10.1364/CLEO_AT.2017.JTu5A.102.
 - [128] J. Javaloyes and S. Balle, “Freetwm : a simulation tool for semiconductor lasers,” *Unpublished*, pp. 1–72, 2012, [Online]. Available: <http://onl.uib.eu/software>.
 - [129] M. J. R. Bente, Erwin A J M, Barbarin, Yohan, Heck and M. K. Smit, “Modeling of integrated extended cavity InP / InGaAsP semiconductor modelocked ring lasers,” pp. 131–148, 2008, doi: 10.1007/s11082-008-9184-y.
 - [130] Y. Barbarin *et al.*, “Realization and modeling of a 27-GHz integrated passively mode-locked ring laser,” *IEEE Photonics Technol. Lett.*, vol. 17, no. 11, pp. 2277–2279, 2005, doi: 10.1109/LPT.2005.857228.
 - [131] K. Y. L. and J. Paslaski, “Condition for short pulse generation in ultra-high frequency mode-locking of semiconductor lasers,” *Conf. Lasers Electro-Optics*, p. <https://news.ge/anakliis-porti-aris-qveynis-momava>, 1991.
 - [132] J. Hazan, A. Nassar, K. Williams, and E. Bente, “Monolithically integrated InP 2 . 5 GHz Fourier Domain Mode-Locked Laser at 1530nm,” no. c, pp. 2–3, doi: 10.1117/12.2610120.R.
 - [133] E. A. J. M. Bente, “Photonic Integration Circuit Simulator (PhISim),” *website*. <https://sites.google.com/tue.nl/phisim/home>.
 - [134] P. D. Ltd., “Harold.” .
 - [135] D. Pustakhod, K. Williams, and X. Leijtens, “Method for Polarization-Resolved Measurement of Electroabsorption,” *IEEE Photonics J.*, vol. 10, no. 2, pp. 1–11, 2018, doi: 10.1109/JPHOT.2018.2795250.
 - [136] A. Schlatter, S. C. Zeller, R. Grange, R. Paschotta, and U. Keller, “solid-state lasers above the Q-switching threshold,” *J. Opt. Soc. Am. B*, vol. 21, no. 8, pp. 1469–1478, 2004.
 - [137] D. A. Reid, S. G. Murdoch, and L. P. Barry, “Stepped-heterodyne optical complex spectrum analyzer,” *Opt. Express*, vol. 18, no. 19, p. 19724, 2010, doi: 10.1364/oe.18.019724.
 - [138] ITU-T, “Recommendation ITU-T G.652: Characteristics of a single-mode optical fibre and cable,” *Itu-T G.652*, no. November 2016, pp. 1–28, 2016, [Online]. Available: <https://www.itu.int/rec/T-REC-G.652-201611-l/en>.

References

- [139] S. Arahira and Y. Ogawa, "Repetition-frequency tuning of monolithic passively mode-locked semiconductor lasers with integrated extended cavities," *IEEE J. Quantum Electron.*, vol. 33, no. 2, pp. 255–264, 1997, doi: 10.1109/3.552266.
- [140] T. P. Butler *et al.*, "Direct experimental measurement of single-mode and mode-hopping dynamics in frequency swept lasers," *Opt. Express*, vol. 25, no. 22, p. 27464, 2017, doi: 10.1364/oe.25.027464.
- [141] L. O. Chua, "A nonlinear dynamics perspective of wolfram's new kind of science," *Nonlinear Dyn. Perspect. Wolfram's New Kind Sci. A - Vol. Iii*, vol. 19, no. 12, pp. 1–360, 2009, doi: 10.1142/7151.
- [142] G. Hagn, "Electro-Optic Effects and Their Application in Indium Phosphide Waveguide Devices for Fibre Optic Access by Electro-optic," *Outlook*, no. 14353, 1971.
- [143] J. F. Vinchant, J. A. Cavaillès, M. Erman, P. Jarry, and M. Renaud, "InP/GaInAsP Guided-Wave Phase Modulators Based on Carrier-Induced Effects: Theory and Experiment," *J. Light. Technol.*, vol. 10, no. 1, pp. 63–70, 1992, doi: 10.1109/50.108738.
- [144] J. P. Weber, "Optimization of the Carrier-Induced Effective Index Change in InGaAsP Waveguides-Application to Tunable Bragg Filters," *IEEE J. Quantum Electron.*, vol. 30, no. 8, pp. 1801–1816, 1994, doi: 10.1109/3.301645.
- [145] L. V. Keldysh, "The Effect of a Strong Electric Field on the Optical Properties of Insulating Crystals," *J. Exptl. Theor. Phys.*, vol. 7, no. 5, pp. 788–790, 1958, [Online]. Available: http://jetp.ac.ru/cgi-bin/dn/e_007_05_0788.pdf.
- [146] H. B. da Veiga, "On the semiconductor drift diffusion equations," *Differ. Integr. Equations*, vol. 9, no. 4, pp. 729–744, 1996.
- [147] S. Andreou, K. A. Williams, and E. A. J. M. Bente, "Steady-state analysis of the effects of residual amplitude modulation of InP-based integrated phase modulators in pound-drever-hall frequency stabilization," *IEEE Photonics J.*, vol. 11, no. 3, pp. 1–14, 2019, doi: 10.1109/JPHOT.2019.2915163.
- [148] B. R. Bennett, R. A. Soref, and J. A. Del Alamo, "Carrier-Induced Change in Refractive Index of InP, GaAs, and InGaAsP," *IEEE J. Quantum Electron.*, vol. 26, no. 1, pp. 113–122, 1990, doi: 10.1109/3.44924.
- [149] T. Kawanishi, S. Member, and H. Nakajima, "High Extinction-Ratio Integrated Mach – Zehnder Modulator With Active Y-Branch for Optical SSB Signal Generation," vol. 22, no. 12, pp. 941–943, 2010.
- [150] V. Van, *Optical Microring Resonators*. 2016.
- [151] G. Choi, "Modeling and Characterization of a Ring- Resonator based Silicon Photonic Sensor on Silicon-on-Insulator (SOI)," 2019.
- [152] T. Hansson, D. Modotto, and S. Wabnitz, "Analytical approach to the design of microring resonators for nonlinear four-wave mixing applications," *J. Opt. Soc. Am. B*, vol. 31, no. 5, p. 1109, 2014, doi: 10.1364/josab.31.001109.
- [153] S. Andreou, K. A. Williams, and E. A. J. M. Bente, "Electro-Optic Tuning of a Monolithically Integrated Widely Tuneable InP Laser with Free-Running and Stabilized Operation," *J. Light. Technol.*, vol. 38, no. 7, pp. 1887–1894, 2020, doi: 10.1109/JLT.2019.2952466.

- [154] S. Andreou, D. Zhao, K. Williams, and E. Bente, "Steady state spectral model of lasers and its experimental validation for a multi-section DBR laser," vol. 1, no. 1, pp. 22–24, 2018.
- [155] G. Griffel, "Vernier effect in asymmetrical ring resonator arrays," *IEEE Photonics Technol. Lett.*, vol. 12, no. 12, pp. 1642–1644, 2000, doi: 10.1109/68.896334.
- [156] S. Tondini, C. Castellan, M. A. Medina, and L. Pavesi, "Automatic initialization methods for photonic components on a silicon-based optical switch," *Appl. Sci.*, vol. 9, no. 9, 2019, doi: 10.3390/app9091843.
- [157] R. Pajković, Y. Tian, S. Latkowski, K. A. Williams, and E. A. J. M. Bente, "Tuning of a widely tunable monolithically integrated InP laser for optical coherence tomography," vol. 1093912, no. March 2019, p. 37, 2019, doi: 10.1117/12.2509572.
- [158] Q. Chen *et al.*, "Butterfly-packaged multi-channel interference widely tunable semiconductor laser with improved performance," *Opt. Express*, vol. 29, no. 5, p. 6344, 2021, doi: 10.1364/oe.414376.
- [159] Saša Singer and John Nelder, "Nelder-Mead algorithm," *Scholarpedia*, vol. 4, no. 7, 2009.
- [160] M. A. Luersen and R. Le Riche, "Globalized nelder-mead method for engineering optimization," *Comput. Struct.*, vol. 82, no. 23–26, pp. 2251–2260, 2004, doi: 10.1016/j.compstruc.2004.03.072.
- [161] R. Pajković, T. Reep, K. Williams, and E. Bente, "Data-driven model to extend tuning range : from 1474 nm to 1568 nm in a monolithic laser," in *ISLC 2021*, pp. 2–3.
- [162] T. Reep, "Tuning range optimisation and wavelength switching of an integrated widely tunable laser for optical coherence tomography," 2021.
- [163] R. Huber, "Fourier domain mode locking (FDML): A new laser operating regime and applications for biomedical imaging, profilometry, ranging and sensing," *Opt. InfoBase Conf. Pap.*, vol. 14, no. 8, pp. 1981–1983, 2009, doi: 10.1364/assp.2009.ma1.
- [164] S. Karpf, M. Eibl, W. Wieser, T. Klein, and R. Huber, "A Time-Encoded Technique for fibre-based hyperspectral broadband stimulated Raman microscopy," *Nat. Commun.*, pp. 6–11, 2015, doi: 10.1038/ncomms7784.
- [165] S. Slepneva, B. O'Shaughnessy, B. Kelleher, S. P. Hegarty, A. G. Vladimirov, and G. Huyet, "Dynamics of fourier domain mode locked lasers," *2017 Conf. Lasers Electro-Optics, CLEO 2017 - Proc.*, vol. 2017-Janua, no. 16, pp. 1–2, 2017, doi: 10.1364/OE.21.019240.
- [166] J. Tang, B. Zhu, W. Zhang, M. Li, S. Pan, and J. Yao, "Hybrid Fourier-domain mode-locked laser for ultra-wideband linearly chirped microwave waveform generation," *Nat. Commun.*, vol. 11, no. 1, pp. 1–8, 2020, doi: 10.1038/s41467-020-17264-8.
- [167] D. Huang, Y. Shi, F. Li, and P. K. A. Wai, "Fourier Domain Mode Locked Laser and Its Applications," *Sensors*, vol. 22, no. 9, p. 3145, 2022, doi: 10.3390/s22093145.
- [168] J. Dong, K. S. Chiang, and K. Chen, "Wavelength-tunable multi-wavelength fiber laser with an electro-optic lithium-niobate waveguide comb filter," *Asia Commun. Photonics Conf. ACPC 2015*, pp. 5–7, 2015, doi: 10.1364/acpc.2015.asu2a.51.
- [169] M. J. R. Heck and J. E. Bowers, "Integrated fourier-domain mode-locked lasers:

References

- Analysis of a novel coherent comb laser," *IEEE J. Sel. Top. Quantum Electron.*, vol. 18, no. 1, pp. 201–209, 2012, doi: 10.1109/JSTQE.2011.2113371.
- [170] "Fourier Domain Mode-Locking (incl. Parallelization)." <https://entokey.com/fdml-incl-parallelization/>.
- [171] F. Li, A. Zhang, X. Feng, and P. K. A. Wai, "Frequency synchronization of Fourier domain harmonically mode locked fiber laser by monitoring the supermode noise peaks," vol. 21, no. 25, pp. 687–693, 2013, doi: 10.1364/OE.21.030255.
- [172] T. T. M. Van Schaijk, "Feedback Insensitive Integrated Semiconductor Laser T. T. M. van Schaijk," vol. 1, no. 2019, 2019.
- [173] W. M. Laghari, M. U. Baloch, and M. A. Mengal, "Performance Analysis of Analog Butterworth Low Pass Filter as Compared to Chebyshev Type-I Filter, Chebyshev Type-II Filter and Elliptical Filter," no. September, pp. 209–216, 2014.
- [174] M. S. Tahvili, L. Du, M. J. R. Heck, R. Nötzel, M. K. Smit, and E. A. J. M. Bente, "Dual-wavelength passive and hybrid mode- quantum dot lasers," vol. 20, no. 7, pp. 8117–8135, 2012.
- [175] N. Andriolli, F. Bontempi, and G. Contestabile, "InP Monolithically Integrated Transmitters Based on High Speed Directly Modulated DFB Lasers," *IEEE J. Sel. Top. Quantum Electron.*, vol. 26, no. 5, 2020, doi: 10.1109/JSTQE.2020.2984572.
- [176] B. Corbett, C. Bower, A. Fecioru, M. Mooney, M. Gubbins, and J. Justice, "Strategies for integration of lasers on silicon," *Semicond. Sci. Technol.*, vol. 28, no. 9, 2013, doi: 10.1088/0268-1242/28/9/094001.
- [177] D. Liang and J. E. Bowers, "Photonic integration: Si or InP substrates?," *Electron. Lett.*, vol. 45, no. 12, pp. 578–581, 2009, doi: 10.1049/el.2009.1279.
- [178] G. Roelkens *et al.*, "Micro-Transfer Printing for Heterogeneous Si Photonic Integrated Circuits," *IEEE J. Sel. Top. Quantum Electron.*, vol. 29, no. 3, 2023, doi: 10.1109/JSTQE.2022.3222686.
- [179] Y. Hu *et al.*, "III/V-on-Si MQW lasers by using a novel photonic integration method of regrowth on a bonding template," *Light Sci. Appl.*, vol. 8, no. 1, 2019, doi: 10.1038/s41377-019-0202-6.
- [180] C. Mukherjee *et al.*, "Towards monolithic indium phosphide (InP)-based electronic photonic technologies for beyond 5G communication systems," *Appl. Sci.*, vol. 11, no. 5, 2021, doi: 10.3390/app11052393.
- [181] M. Smit, K. Williams, and J. Van Der Tol, "Past, present, and future of InP-based photonic integration," *APL Photonics*, vol. 4, no. 5, 2019, doi: 10.1063/1.5087862.
- [182] Y. Wang, V. Dolores-Calzadilla, K. A. Williams, M. K. Smit, and Y. Jiao, "Ultra-Compact and Efficient Microheaters on a Submicron-Thick InP Membrane," *J. Light. Technol.*, vol. 41, no. 6, pp. 1790–1800, 2022, doi: 10.1109/JLT.2022.3225110.
- [183] N. Fujioka, T. Chu, and M. Ishizaka, "Compact and low power consumption hybrid integrated wavelength tunable laser module using silicon waveguide resonators," *J. Light. Technol.*, vol. 28, no. 21, pp. 3115–3120, 2010, doi: 10.1109/JLT.2010.2073445.
- [184] T. Dennis, E. A. Curtis, C. W. Oates, L. Hollberg, and S. L. Gilbert, "Wavelength references for 1300-nm wavelength-division multiplexing," *J. Light. Technol.*, vol. 20, no. 5, pp. 804–810, 2002, doi: 10.1109/JLT.2002.1007933.

- [185] M. Muneeb *et al.*, "Silicon-on-insulator shortwave infrared wavelength meter with integrated photodiodes for on-chip laser monitoring," *Opt. Express*, vol. 22, no. 22, p. 27300, 2014, doi: 10.1364/oe.22.027300.
- [186] D. Huber *et al.*, "InP – InGaAs Single HBT Technology for Photoreceiver OEIC 's at 40 Gb / s and Beyond," vol. 18, no. 7, pp. 992–1000, 2000.
- [187] J. F. Bauters *et al.*, "Planar waveguides with less than 01 dB/m propagation loss fabricated with wafer bonding," *Opt. Express*, vol. 19, no. 24, p. 24090, 2011, doi: 10.1364/oe.19.024090.
- [188] C. K. Madsen, G. Lenz, A. J. Bruce, M. A. Cappuzzo, L. T. Gomez, and R. E. Scotti, "An All-pass Filter for Tunable Dispersion and Dispersion Slope Compensation," *Opt. InfoBase Conf. Pap.*, vol. 11, no. 12, pp. 126–128, 1999, doi: 10.1364/ipr.1999.rtua1.
- [189] E. Bente, S. Latkowski, V. Moskalenko, M. Llorens-Revul, S. Tahvili, and K. Williams, "Mode-locked lasers in InP photonic integrated circuits," *Nov. In-pl. Semicond. Lasers XVI*, vol. 10123, no. 2017, p. 101230F, 2017, doi: 10.1117/12.2251469.

LIST OF PUBLICATIONS

JOURNAL ARTICLES

J.Hazan, S. Tondini, S. Andreou, K.A. Williams and E.A.J.M. Bente, "Monolithic InP active/passive integration platform at 1300 nm: application to widely tunable laser systems", *in preparation*

J.Hazan, S. Tondini, A. Nassar, K.A. Williams and E.A.J.M. Bente "Two-section passively Mode-Locked laser as a test for amplification and absorption parameters of a quantum well based InP optical amplifier at 1300 nm", *submitted to IEEE J. Quantum Electron.*

J.Hazan, S. Andreou, D. Pustakhod, S. Kleijn, K.A. Williams and E.A.J.M. Bente "1300 nm Semiconductor Optical Amplifier compatible with an InP Monolithic Active/Passive Integration Technology", *IEEE Phot. Journal* (2022), vol. 14, no. 3, pp. 1-11.

INTERNATIONAL CONFERENCES

J. Hazan, S. Tondini, S. Andreou, K.A. Williams and E.A.J.M. Bente, "Novel 1300 nm InP monolithic active/passive integration platform: application to widely tunable lasers", in 2023 Conference on Lasers and Electro-Optics (CLEO), San José, CA (**accepted**)

S. Tondini, J. Hazan, T. Kabir and M. Heck, " Self-aligning Mach-Zehnder interferometer based filter for intra-cavity tuning on InP integrated lasers", in 2023 Conference on Lasers and Electro-Optics (CLEO), San José, CA (**accepted**)

S. Tondini, J. Zhang, J. Hazan, M. Heck and J. Chen, "Towards on-chip wavelength modulation spectroscopy at 1.5 μm via integrated photonics and low-cost driving hardware", 24th European Conference on Integrated Optics (ECIO), Enschede, April 2023 (**accepted**).

J. Hazan, A. Nassar, K. A. Williams and E.A.J.M. Bente, "Monolithically integrated InP 2.5 GHz Fourier Domain Mode-Locked laser at 1530 nm", 2022 IEEE International Semiconductor Laser Conference (ISLC), Matsue, Japan October 2022.

J.Hazan,A. Nassar, S. Kleijn, K.A. Williams and E.A.J.M. Bente,"Characterization of Passively Mode-Locked lasers and Saturable Absorbers based on an InP quantum well

List of publications

amplifier suitable for active-passive integration at 1300 nm”, 23th European Conference on Integrated Optics (ECIO), May 2022.

J. Hazan, T. Couka, R. Pajkovic, K.A. Williams and E.A.J.M. Bente “Control strategy for a monolithically integrated widely tunable laser system on InP for optical coherence tomography”, Proc. of Novel In-Plane Semiconductor Lasers XXI, SPIE OPTO, 2022 San Francisco, CA, United States, January 2022.

J. Hazan, D. Pustakhod, S. Kleijn, S. Andreou, K.A. Williams and E.A.J.M. Bente, “Broadband multimode interference coupler on InP substrate with flat wavelength response over the O-band”, IEEE Integrated Photonics Conference, Vancouver, Canada (**online**), November 2021.

J. Hazan, S. Andreou, D. Pustakhod, S. Kleijn, K.A. Williams and E.A.J.M. Bente “1.3 μ m InGaAsP/InP semiconductor optical amplifier compatible with an active/passive integration technology”, 2021 IEEE International Semiconductor Laser Conference (ISLC), Potsdam, Germany, October 2021.

REGIONAL CONFERENCES / WORKSHOPS

J. Hazan, A. Nassar, K.A. Williams and E.A.J.M. Bente, “Towards a Fourier-Domain mode-locked laser system with an integrated Mach-Zehnder interferometer as frequency filter”, Proceedings of the 26th *Annual Symposium of the IEEE Photonics Benelux Chapter*, Eindhoven, The Netherlands, Nov. 2022.

T. Kabir, S. Tondini, J. Hazan, D.M.H. Abusada, K.A. Williams and M.J.R. Heck, “Characterization of a MZI based tunable filter using an optimization algorithm”, Proceedings of the 26th *Annual Symposium of the IEEE Photonics Benelux Chapter*, Eindhoven, Nov. 2022.

J. Hazan, K.A. Williams and E.A.J.M. Bente, “Gain spectra and saturation power measurements in a two-section InGaAsP/InP semiconductor optical amplifier at 1.3 μ m”, Proceedings of the 25th *Annual Symposium of the IEEE Photonics Benelux Chapter*, Mons, Belgium, Nov. 2021.

J. Hazan, T. Couka, R. Pajkovic, K.A. Williams and E.A.J.M. Bente, “Investigation of the wavelength tuning of an integrated laser system on InP for Optical Coherence Tomography”, *Proceedings of the 2021 European Semiconductor Laser Workshop*, Paris, France (**online**), Sept. 2021.

J. Hazan, K.A. Williams and E.A.J.M. Bente, "Towards an integration technology platform at 1300 nm: ridge waveguide design", *Proceedings of the 24th Annual Symposium of the IEEE Photonics Benelux Chapter*, Amsterdam, The Netherlands, Nov. 2019.

E. Bente, S. Andreou, R. Pajkovic, J.Hazan and K. Williams," InP based integrated tunable laser systems for OCT and strain sensing", Invited talk, European Semiconductor Laser Workshop 2019, Tyndall National Institute, Cork, Ireland, Sept. 2019

ACKNOWLEDGMENTS

As I face the most difficult part of my thesis, I realize that it involves looking back at the past four years and more, acknowledging the growth process that has happened during this time. I remember arriving in Eindhoven on the 5th of July 2018, before the pandemic and more than two World Cups ago - neither of which involved Italy playing, unfortunately. The day after my arrival, Belgium was about to win a historic quarterfinal match with Brazil, marking the first time Belgium had beaten Brazil in an official match. However, that morning, I was about to play my own personal match: my first life interview. Although I had already met Erwin through Skype, this time it was different. Would my English be understandable? Would I be fit? Did I know enough about photonics to start a PhD? These were just a few of the questions that I asked myself as I walked from Markt (Eindhoven centrum) to the TU/e campus and later to Flux. At the time, I was still 24 years old, and I had found the position on the internet after attending a career day in Milan, where the master's and PhD tracks at Tilburg and Eindhoven universities were advertised.

When I arrived on the ninth floor, it was so easy to break the ice with Erwin. As soon as we met, I felt at home and safe to express my strengths and weaknesses. Erwin, I want to thank you for being my guide during this journey. Thanks to our meetings and exchanges of opinions, I have learned a lot and improved as a scientist. You also taught me to reflect on things and analyze them carefully, which is necessary to build scientific critical thinking. I have tried to bring your method to the students I have supervised, such as Tancrede Aser and Gabriel. I hope to bring these teachings into the future steps of my career.

Kevin, I admire the leadership and dedication that you put into keeping the group united and fruitful. Good luck with the future scale-up. Moreover, thanks a lot for your feedback on the papers and the thesis.

I would like to thank all the committee members for their precious comments on my thesis. Victor, thanks for the numerous chats during my PhD and for giving me the opportunity to develop a new type of active layer stack. With Al-quantum wells, the laser temperature of operation will not be an issue anymore. I want to thank also all the other PhI staff members: Xaveer for his nice effort in maintaining Nazca, and Weiming for the dedication to keeping the OLA labs a better place. Martijn, thanks for our discussion at the door of your office, and special thanks also to Jos, Yuqing, Meint, Huub, and Dan for inspiring my research.

Now I want to move to the different laser teams that passed by within the Photonic Integration (PhI) group. Stefanos, Perry, and Rastko were the first people I encountered during the PhD. Thanks for introducing me to the group, for the fruitful discussions, and the numerous suggestions during meetings. Stefano, Tasfia, Rachel, Ozan, Wenjing, and Marco, I will always smile thinking back to the moments inside the lab, making jokes, and

Acknowledgments

complaining about Smart Photonics delivery times. I am sure that the development of tunable laser systems will flourish again. I want to extend my acknowledgments to the OLA committee members. Thanks to Julian, Vikram, Jerald, and Julian.

I want to thank my office mates for creating a nice working atmosphere. Thanks to my next desk buddy Lukas, even if your radio music is terrible, I always enjoyed our chats. Thanks to Katia for taking care of the paintings in the office, and Kolsoom for the nice language jokes between Persian and Italian. Irene, our best communication officer, and the solo Dutch with an everyday "non-Dutch" lunch, and Xiao, good luck with Mode-locked laser. Thanks to Rachel for the discussions on laser systems and linewidth measurement options. Grumpy Sylvester, thanks a lot for your precious advice on photonics but also on career development at a professional and personal level. Thanks to Dima for his help with software development. Michalis, I hope you are doing great in Switzerland. Thank you for all the help and the hands-on teaching on wire bonding, chip gluing, and measurement automation. James, thanks for our Friday beer breaks and for having taught me several British expressions.

I also want to thank our PhI "competitors" of the IMOS team. Sander, looking forward to playing beach rugby again. Thank you for always organizing team-building BBQs within the group. King Rui, I am very happy that you reunited with your family in Cambridge. Still waiting for a formal invitation to Rastko so we can gather in the UK soon. Sacha, I wish you good luck with the new IMOS modulated lasers. Amir, I enjoyed the Sunday matches during lockdown. Wishing you the best at IMEC. Jasper, I hope you will bike with me again. I will bring an extra tube, don't worry. David, next time in Milan we can try a better club, I promise. Yi, I won the "PhD race," but I still hope you will pursue an academic career. You are a great scientist.

Thanks to the Italians: Stefano, Alessio, and Marco for sharing some Italian jokes and restaurant tips. Stefano, cofounder of our "Simple" journey together with Vadim. Let us hope to make lasers great again soon.

I want to thank all the rest of the PhI members: Akansha, Aura, Arezou, Bernat, Dhiman, Floris, Limeng, Ekaterina, Sara, Yunyun, Jerald, Lea, Sruja, Salim, Tarni, Ruud, Florian, Marija, and Yihui. Thanks a lot for your support.

Now, finally, I would like to thank Jolande, the spirit of PhI. Thanks for maintaining a nice environment for both new and old members. Numerous chats about football, life, and work led to several happy days even when we were not working inside the OLA labs.

I want to thank the group next door, ECO. Thanks to Rafael, Henrique, and Menno for their continuous support during my PhD. Marc, half PhI and half Eco, thanks a lot for our time in the lab, and I wish you good luck with your new bike.

Now I want to move on to my football friends: Ylia, Fede, Mauro, Dani, Dami, Marco. Thanks for playing next to me in our Brabantia Sunday matches and Wednesday trainings. Hopefully, next year we will win the championship. Thanks to the Pitolucci and Ralzone. They were at my side during these 4 years. With many dinners together, football jokes, and some nice trips,

you made my time in Eindhoven great. Please do not forget to take off your shoes when you come home 😊.

Adesso volevo ringraziare i miei amici di Milano: i phra da un'altra madre e la piazza intera. Anche se siamo dispersi in giro per il mondo so che ci saremo sempre uno per l'altro, nel bene e nel male. Voglio ringraziare la mia famiglia per essere sempre stata accanto a me in questi anni. Nonno Ico hai visto che mi sono dottorato nonostante abbia dovuto rifare analisi 1 tre volte e i quasi 50 esami del Politecnico. Nonna, tesoro, alla difesa mi vedrai senza barba come piaccio a te. Sono contento che sarai presente anche in rappresentanza di tutti e 4 (o 5?). Ricordi una parte della famiglia che purtroppo non c'è più. Sono felice che Nonno Nai sia riuscito a venire qui e vedere il mio lavoro. Spero di averti reso orgoglioso. Dalla Nonna Lilli ho sicuramente preso il carattere Kramerino per andare avanti a testa alta in ogni circostanza. André grazie mille per i tuoi continui consigli, anche se l'umorismo francese mi risulta ancora complicato.

Adesso tocca agli zii: gli strudelini (come vi chiama Camilla), i romani e lo zio Dani. Ne è passato di tempo da quando mi imboccavate, facevate funghi funghi o i campionati degli animali. Sono contento che siamo sempre rimasti uniti. Voglio anche ringraziare le mie tre donnine: Tami, Caro e Adri. Anche se c'è una differenza generazionale tra di noi, tutto quello che vi consiglio, è perché vi voglio bene e vorrei proteggervi sempre.

Adesso sono in crisi perché devo ringraziare parti di me. Mami, abbiamo passato di tutto assieme, spesso come cane e gatto. Ho sofferto per essere stato lontano forse quando avevi più bisogno ma ti guiro che presto rimedierò. Grazie per la tua infinita generosità e la tua forza. Sei la vera roccia della famiglia. Anche se mi dici che sei stanca, so benissimo che non vedi l'ora di ricominciare. Pa, le chiamate in macchina sono un must come lo erano col nonno quando ero in macchina con te. A volte la linea salta per una galleria oppure perché il telefono è volato via dal tetto 😊. Grazie per i mille consigli e le chiacchierate spensierate, spesso di calcio. In generale, vi ringrazio per avermi trasmesso il valore della famiglia, e avermi sempre supportato e sopportato tutti i miei disastri. Michi, la mia goccia d'acqua solo un po' più basso. Ancora il mio fratellino per certe cose, ma sempre un grande esempio e un modello da seguire. Invidio la tua forza d'animo e il tuo carattere, anche se a volte ci scanniamo per questo. Un abbraccio anche alla Michi, santa donna che ti sopporta.

Minna le ultime parole sono per te, la mia piccola ipocondriaca e maniaca dell'ordine. Questo viaggio ce lo siamo goduto assieme. L'immensa felicità di stare assieme e la gelosia di quando eravamo lontani. Grazie per esserti messa in discussione per me e per l'incommisurato amore che mi hai sempre dimostrato. In questi anni mi hai reso immensamente felice e hai fatto diventare Treurenburgstraat e Eindhoven casa, chi l'avrebbe mai detto? Sono certo che sarai sempre accanto a me in ogni sfida che il futuro ci offrirà.

Joel, Eindhoven, 20 Aprile 2023

BIOGRAPHY



Joel Hazan was born July 27th 1993 in Milan, Italy. He received the BSc degree in Engineering Physics from the Politecnico university of Milan in 2015, where during his bachelor final project he analyzed the non-linear effects present in a hollow core optical fiber filled with Noble gas (Ar). He obtained the MSc degrees in photonics and nano optics from the Politecnico university of Milan in 2018. During his master thesis project, Joel developed an ultraviolet ultra-fast (fs) pump probe setup to perform spectroscopic measurements on biological molecules (Tryptophan and Azurin). Since October

2018 he started as a Ph.D. candidate in the Photonic Integration Group, Eindhoven University of Technology, Eindhoven, The Netherlands. The research topic consists of the realization of an integrated widely tunable laser system at 1300 nm to be used as a swept source in an Optical Coherence Tomography setup.